Computational strategies for multiscale analysis of material behaviour.

Partovi, Maziar

Partovi, Maziar (2007) *Computational strategies for multiscale analysis of material behaviour..* thesis, Swansea University.
http://cronfa.swan.ac.uk/Record/cronfa42986

CIVIL AND COMPUTATIONAL ENGINEERING CENTRE
UNIVERSITY OF WALES SWANSEA

Computational Strategies for Multiscale Analysis of Material Behaviour

MAZIAR PARTOVI

Submitted to the University of Wales in fulfilment of the requirements for the Degree of Doctor of Philosophy of Engineering.

Swansea University

January 2007

ProQuest LLC.
789 East Eisenhower Parkway
P.O. Box 1346
Ann Arbor, MI 48106 – 1346

Summary

The main objective of this thesis is the computational implementation and assessment of multi-scale constitutive modelling strategies based on the volume averaging of the strain and stress tensors over a representative volume element (RVE) under infinitesimal strains assumption. The computational procedure is based on the finite element discretisation at both macro- and microscopic levels. Four classes of multi-scale constitutive models are considered, corresponding to: the Taylor, the linear boundary displacement, the periodic boundary displacement fluctuations and the uniform boundary traction assumptions. The corresponding finite element formulation is described in detail including the derivation of the homogenised tangent moduli which are crucial for the use of the Newton-Raphson method in the iterative solution of non-linear macro-scale problems.

The code developed possesses a recursive hierarchical structure. Under this scheme the main equilibrium procedure, operating on the macroscopic level, calls itself each time it requires to evaluate the material behaviour by homogenisation of microstructure.

A comprehensive set of numerical examples is presented. Application of the multi-scale methodology to materials with linear elastic microscopic constituents is considered first. The effect of the fibre orientation in the micro-cell and anisotropy of the RVE on the homogenised material properties are also discussed. Existing analytical methods are used to benchmark the numerical results. The effect of the topology of cavities on the homogenised material properties and the overall yield surface under different boundary conditions are also studied in the context of elasto-plastic material models. Finally, a materially non-linear fully coupled two-scale boundary value problem is solved numerically, demonstrating the suitability of the developed framework to large scale computations.

The present research shows that the adopted multi-scale methodology provides an effective tool for the constitutive modelling of heterogeneous materials in the linear and non-linear range.

DECLARATION

This work has not previously been accepted in substance for any degree and is not being concurrently submitted in candidature for any degree.

Signature ....(candidate)

Date ......31/01/2007.....................

STATEMENT 1

This thesis is being submitted in partial fulfilment of the requirements for the degree of Doctor of Philosophy in the School of Engineering.

Signature .. ..(candidate)

Date ....31/01/2007..................

STATEMENT 2

This thesis is the result of my own independent work/investigation, except where otherwise stated. Other sources are acknowledged by footnotes giving explicit references. A bibliography is appended.

Signature .. ..(candidate)

Date ....31/01/2007.....................

STATEMENT 3

I hereby give consent for my thesis, if accepted, to be available for photocopying and for inter-library loan, and for the title and summary to be made available to outside organisations

Signature .. ..(candidate)

Date ....31/01/2007......................

Contents

List of Figures

List of Tables

Acknowledgments

I would like to express my gratitude to both of my supervisors, Prof. D. Perić and Dr. E A de Souza Neto, for the help and guidance I received throughout this project. Without the valuable discussions this work would not have been possible.

I would like to express my deepest gratitude for the constant support, understanding and love that I received from my parents during the past years. I am deeply and forever indebted to them for their encouragement throughout my entire life. I am also very grateful to my only sister Dr. Mandana Partovi.

Chapter 1

Introduction

1.1 Introduction

From the dawn of human history, materials have been weapons of progress. Historical ages were even named after them: the Stone Age, Bronze Age, Iron Age and so on. Today, we cannot qualify our age after just one material, for our era is the era of choice. We have the possibility of using the right material at the right place. Composite materials are one of the well-known materials of our time. Weight/strength ratio is the main advantage of this group of materials. On the other hand, their high cost in comparison to other materials makes them suitable for industries, such as aerospace where cost is a secondary factor.

From glass fibre reinforced plastics to advanced carbon fibre reinforced epoxy, composite materials are very diverse. For instance, fibre composites are normally made of reinforcement and another material, which binds the reinforcement. This binder is called a matrix. The composite mechanical behaviour have directional properties associated with the preferred directions of the reinforcement fibres. The matrix effectively controls the mechanical properties in the transverse direction. Compared with metals, such composites have higher specific strength and higher specific elastic moduli. Generally speaking, composites are also less prone to corrosion.

Many industries such as aerospace, ship-building and automotive have used composites for several decades. However, regardless of the rate of development of composites, basic concepts are not difficult to grasp. If certain rules and principles are clearly understood and systematically followed, practicing engineers can have maximum use of these remarkable materials.

Most materials are heterogeneous at a certain scale of observation. This heterogeneity has a significant effect on the overall macroscopic behaviour. The physics and mechanics of the micro-structure affect the overall response of the macro-structure. To this end, the effect of the size, shape, spatial distribution and mechanical properties of the micro-structure on the overall behaviour of heterogeneous materials should be considered.

In many engineering applications, it is essential to determine the overall characteristics of the heterogeneous media. The understanding of the behaviour of the micro-structure and the relation between micro- and macro-structure can help us to design different composite materials such that the resulting macroscopic behaviour presents the required characteristics. However, the diversity of the possible situations, regarding the geometry, the scale and the contrast of multi-phase structures, is such that it is useful to have a guideline for choosing the appropriate modelling tool for a given application [2].

From economical points of view (time and cost), making the direct modelling of the material behaviour for different material samples with different volume fractions, sizes, various geometrical and physical properties, and loading paths is impractical. Therefore, a means of continuous interchange of information and modelling strategies between different scales is needed.

The simplest method of estimating macroscopic properties for a given heterogeneous material so-called the rule of mixtures. The overall property in this case is obtained as an average over the each individual properties of the constituents, weighted with their volume fractions. Strictly speaking, this method disregards the influence of important phenomena arising from the (often very complex) interaction between the phases and takes only the volume ratio of the different constituents into consideration.

The effective medium approximation is another method that provides the overall behaviour of heterogeneous materials. This method has been developed by a number of authors, e.g. [3–5]. The material properties are derived from the analytical method of a boundary value problem for a spherical or ellipsoidal inclusion of one material bounded in an infinite matrix of another material. The self-consistent method leans to the previous method, in which a particle of one phase is embedded into the effective material [6, 7]. This model is suitable for granular micro-structures, such as polycrystals, and can be related to the concept of complete disorder, in terms of statistical information [8]. The predicted behaviour from these methods are suitable for structures that have a geometrical regularity that typical particulate and fibre-reinforced composites do not possess [9]. In addition, this method fails to describe the behaviour of clustered structures and it is not convenient for matrix/inclusion morphologies. Moreover, self-consistent approximations should not be applied to dispersions unless the phase contrast is small enough [9]. The generalized self-consistent model (considering a continuous matrix phase) [10], can be applied to avoid the above limitations of the classical self-consistent model.

Following by the non-linear version of the self-consistent model (see Hill [11]), the variational bounding methods, [12–14] have been used to estimate the properties of composite materials. These methods are based on variational principles in the linear theory of elasticity and provide upper and lower bounds for the overall composite properties. The derived bounds from these methods are close enough when the ratio between the different phase moduli are not too large.

The asymptotic homogenisation theory is another approach to estimate the overall properties of heterogeneous materials [15]. This method applies an asymptotic expansion of displacement and stress fields in terms of the 'natural length parameter', which is the ratio of a characteristic length of the heterogeneities and a measure of the macro-structure, see [16–19]. The performance of this method usually is restricted to very simple microscopic geometries and simple material models, in context of small strains. An overview of observed situations in heterogeneous materials and different homogenisation methods have been presented in [1,2].

Over the past few years, a promising alternative approach – the so-called computational homogenisation methodology – has been developed. The basic ideas of this approach have been presented in [17,20–22] and further developed and improved in more recent works [23–29]. In these methods the relation between stress and strain could be obtained at every point of interest of the macro-structure based on the detailed modelling of the micro-level attributed correspond to that point. To show the advantage of these methods we can highlight the following items:

1. No need to have any constitutive material model at macro-level.
2. Ideal for any arbitrary material models.
3. Demonstrate the effect of the micro structural information into the macroscopic behaviour.

4. The averaging technique on the micro level could be independent from macro-level, i.e. the finite element method [22,25,28], the Voronoi cell method [20,21], a crystal plasticity framework [23, 24], or numerical methods based on Fast Fourier Transforms [14,29].
5. Enable the incorporation of finite deformations and rotations on both micro and macro levels.

One of the main concerns in the fully micro-to-macro transition technique is that, this procedure is computationally expensive. This problem can be overcome by parallel computation [25,30]. Another option is selective usage, where the model divided into critical and non-critical regions. The non-critical regions are modelled by conventional continuum closed-form homogenised constitutive relations or by the constitutive tangents obtained from the micro-structure analysis but kept constant in the elastic domain, while in the critical regions the fully coupled multi-scale analysis of the micro-structure is performed [26]. Regardless of the adapted computational strategy, the numerical homogenisation approach seems to be a flexible tool to establish micro- or macro-structure property relations in materials, where the overall behaviour of heterogeneous material is not yet possible to predict by any other method. Moreover, this micro-macro modelling technique may be used for constructing, evaluating and verifying other homogenisation methods as well as micro-mechanically based macroscopic constitutive models.

1.2 Scope and outline

This research is intended to review and implement the computational strategies for multi-scale analysis of material behaviour in the context of non-linear solid material models. Two independent algorithms are defined for the multi-scale analysis; the code corresponding to the macro-structure and the associated micro-structural code. The only link between these two structures is the macro-to-micro and the micro-to-macro transition. The hierarchical structure will be introduced for different types of variables. This structure is used to segregate the different scales from each other in multi-scale analysis.

Developing different kinematic assumptions at micro-level and study of their effect on the homogenised behaviour of the multi-phase material is another goal in this research. Finally, the effect of different factors such as topology of cavities and the prescribed boundary condition over the representative volume element on the homogenised behaviour of the cell in the context of plane-stress will be investigated.

The thesis is organised as follows: Chapter 2 reviews basic principles of continuum mechanics in large and small deformation. The constitutive theory with internal variables followed by more specific constitutive material models will be reviewed in chapter 3.

In chapter 4, the discrete boundary value problem and the finite element method (FEM) implementation in small strain for the linear and non-linear material models will be presented.

Chapter 5 focuses on the existing analytical methods and the fundamental concepts in computational homogenisation. Kinematic assumptions at micro-scale and the relevant overall tangent modulus based on the imposed kinematical constraints are discussed in detail.

Computer implementation of the multi-scale material models is the next subject covered in chapter 6. In particular, the hierarchical structure of the code and general implementation aspects are discussed in detail.

Application of the computational multi-scale methodology to materials with linear elastic micro-constituents is made in chapter 7. The analytical methods are used as benchmarks for the numerical results obtained with the computational homogenisation approach.

In chapter 8 the effect of topology of cavities on the homogenised elasto-plastic properties will be presented. The study of the effective yield surface of porous elasto-plastic media will be considered in chapter 9. The effect of anisotropy of the material at micro-level will be discussed for the elastic material models in chapter 10.

In chapter 11 some boundary value problem tests will be presented for the two-scale analysis model. Chapter 12 gives a summary of the results achieved in this thesis followed by recommendations on the practical use of the computational homogenisation techniques considered. Perspectives of future developments in computational homogenisation strategies are also discussed.

Chapter 2

Continuum mechanics

2.1 Introduction

This chapter reviews some basic principles of continuum mechanics which will be used in the later chapters of the thesis.

2.2 Kinematics of deformation

Assume $\mathscr{B}$ to be a body which occupies an open region $\mathscr{V}$ of the three-dimensional euclidean space $\mathscr{E}$ with a boundary $\partial\mathscr{V}$ in its reference configuration. A deformation of $\mathscr{B}$ is defined by a smooth one-to-one function (see figure 2.1) [31,32]

$$\varphi : \mathscr{V} \to \mathscr{E},$$

that maps each material particle $\boldsymbol{X}$ of $\mathscr{B}$ into a point

$$\boldsymbol{x} = \varphi(\boldsymbol{X}),$$

where $\boldsymbol{x}$ is a new position of the point $\boldsymbol{X}$ in the deformed configuration of $\mathscr{B}$.

The vector field $\boldsymbol{u}(\boldsymbol{X})$ is the displacement of $\boldsymbol{X}$ and

$$\boldsymbol{x} = \boldsymbol{X} + \boldsymbol{u}(\boldsymbol{X}).$$

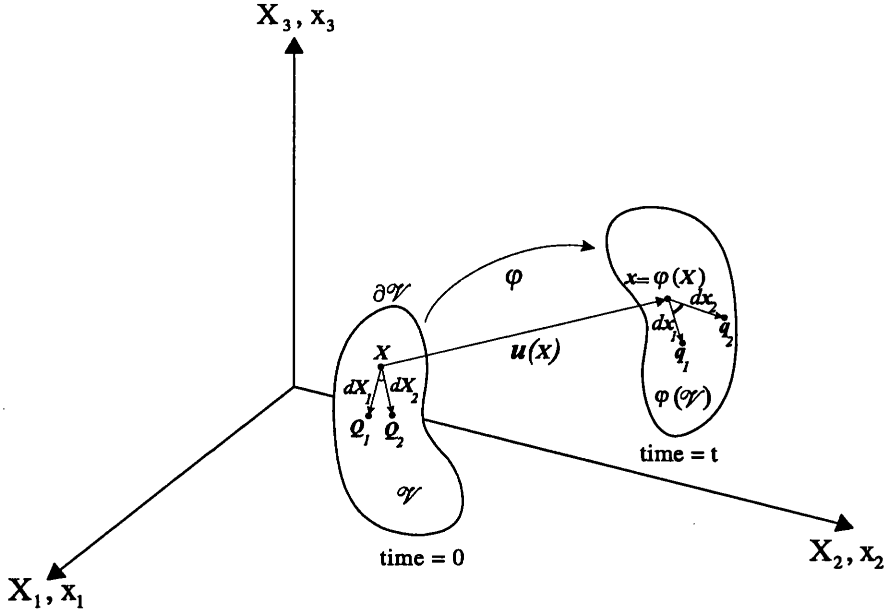

Figure 2.1: General motion of a deformable body.

2.2.1 The motion

A time-dependent deformation of $\mathscr{B}$ is called a motion of $\mathscr{B}$. During the motion φ, the new position of material point $\boldsymbol{X}$ at time t is given by:

$$\boldsymbol{x} = \varphi(\boldsymbol{X}, t).$$

Figure 2.1, shows the general motion of a deformable body. The body is shown in its initial position at $time = 0$ by the coordinates $\boldsymbol{X}$ with respect to Cartesian basis e_i and $i = 1, 2, 3$. After motion of the body, the current positions of the particles in the body are located, at $time = t$. In terms of the displacement field the motion is expressed as:

$$\varphi(\boldsymbol{X}, t) = \boldsymbol{X} + \boldsymbol{u}(\boldsymbol{X}, t). \tag{2.1}$$

Since the relation is one-to-one, φ is invertible so that we may also write [31]:

$$\boldsymbol{X} = \varphi^{-1}(\boldsymbol{x}, t).$$

2.2.2 Material and Spatial coordinates

The material or Lagrangian system is based on the current time t and the coordinates of the initial position of the material point $\boldsymbol{X}$. This identification is done with respect to the initial configuration [33].

$$\boldsymbol{X} = \sum_{i=1}^{n_{dim}} X_i e_i,$$

where X_i are the components of the point $\boldsymbol{X}$ in the reference configuration. The spatial or Eulerian variables are defined for the current coordinates of the position of the material point $\boldsymbol{X}$ at the current time t. The variables identify the current configuration are expressed by [33]:

$$\boldsymbol{x} = \sum_{i=1}^{n_{dim}} x_i e_i,$$

where x_i are the components of the point $\boldsymbol{X}$ in the current configuration.

2.2.3 The deformation gradient

The deformation gradient of the motion φ is the second order tensor $\boldsymbol{F}$ defined by [31]:

$$\boldsymbol{F}(\boldsymbol{X},t) = \nabla\varphi(\boldsymbol{X},t) = \frac{\partial \boldsymbol{x}}{\partial \boldsymbol{X}}, \tag{2.2}$$

where ∇ is the material gradient. Therefor, the elemental vector $d\boldsymbol{x}$ can be obtained in terms of $d\boldsymbol{X}$ as (see Figure 2.1) [32],

$$d\boldsymbol{x} = \boldsymbol{F} d\boldsymbol{X}. \tag{2.3}$$

In view of equation (2.1) it can be written as

$$\boldsymbol{F} = \boldsymbol{I} + \nabla \boldsymbol{u}, \tag{2.4}$$

and the cartesian components of $\boldsymbol{F}$ are given by:

$$\begin{aligned} F_{ij} &= \frac{\partial x_i}{\partial X_j} \\ &= \delta_{ij} + \frac{\partial u_i}{\partial X_j}, \end{aligned} \tag{2.5}$$

where x_i denote the components of $\boldsymbol{x}$. Further details are given in [31–37].

2.2.4 Infinitesimal deformation and strain tensor

Small or infinitesimal deformations are deformations with sufficiently small displacement gradient, $\nabla \boldsymbol{u}$. For such deformations, the description of kinematics can be substantially simplified.

As a general measure of deformation, consider the change in the scalar product of the two elemental vectors $d\boldsymbol{X}_1$ and $d\boldsymbol{X}_2$ (in the material position) that deform to $d\boldsymbol{x}_1$ and $d\boldsymbol{x}_2$ in the spatial position. This change will involve both the stretching and changes in the enclosed angle between the two vectors (see Figure 2.1).

Recalling from equation (2.3), the spatial scalar product $d\boldsymbol{x}_1 \cdot d\boldsymbol{x}_2$ can be found in terms of material vectors as [32],

$$\begin{aligned} d\boldsymbol{x}_1 \cdot d\boldsymbol{x}_2 &= d\boldsymbol{X}_1 \cdot \boldsymbol{C} d\boldsymbol{X}_2, \\ d\boldsymbol{X}_1 \cdot d\boldsymbol{X}_2 &= d\boldsymbol{x}_1 \cdot \boldsymbol{B}^{-1} d\boldsymbol{x}_2, \end{aligned} \tag{2.6}$$

where $\boldsymbol{C}$ is the right Cauchy-Green deformation tensor and $\boldsymbol{B}$ is the left Cauchy-Green tensor and are given in terms of the deformation gradient as [31],

$$\begin{aligned} \boldsymbol{C} &= \boldsymbol{F}^T \boldsymbol{F} = \boldsymbol{I} + \nabla \boldsymbol{u} + (\nabla \boldsymbol{u})^T + (\nabla \boldsymbol{u})^T \nabla \boldsymbol{u}, \\ \boldsymbol{B} &= \boldsymbol{F} \boldsymbol{F}^T = \boldsymbol{I} + \nabla \boldsymbol{u} + (\nabla \boldsymbol{u})^T + \nabla \boldsymbol{u} (\nabla \boldsymbol{u})^T. \end{aligned} \tag{2.7}$$

In general the strain measure $\boldsymbol{E}$ is the so-called Green-Lagrange strain tensor and defined as [32]:

$$\begin{aligned} \boldsymbol{E} &= \frac{1}{2}(\boldsymbol{C} - \boldsymbol{I}), \\ &= \frac{1}{2}\left[\nabla \boldsymbol{u} + (\nabla \boldsymbol{u})^T + (\nabla \boldsymbol{u})^T \nabla \boldsymbol{u}\right]. \end{aligned} \tag{2.8}$$

If the displacement gradient is sufficiently small, the second order terms in $\nabla \boldsymbol{u}$ of the expressions above can be neglected so that, under small deformations, the following approximation can be made:

$$\boldsymbol{C} \approx \boldsymbol{B} \approx \boldsymbol{I} + \nabla \boldsymbol{u} + (\nabla \boldsymbol{u})^T.$$

From the above expression and the definitions of the Green-Lagrange strain tensor $\boldsymbol{E}$ equation (2.8) it follows that, to the same order of approximation,

$$\boldsymbol{E} \approx \frac{1}{2}\left[\nabla \boldsymbol{u} + (\nabla \boldsymbol{u})^T\right].$$

This motivates the definition of the infinitesimal strain tensor to measure strains under small deformations:

$$\varepsilon \equiv \nabla^s \boldsymbol{u}, \tag{2.9}$$

where the symmetric gradient of a vector field is defined by:

$$\nabla^s(.) = sym[\nabla(.)] = \frac{1}{2}[\nabla(.) + \nabla(.)^T].$$

We should emphasize that this work has been done in the framework of small strain assumption.

2.2.5 Forces and stresses

The forces associated with the mechanical description of a body can be classed into three categories [32]:

1. Boundary forces which are applied to the boundary of the body with dimension of force per unit area.
2. Body forces which are acting in the interior of the body with dimension of force per unit mass.
3. Internal interactions between adjacent parts of a body with dimension of force per unit area.

The axiom of momentum balance

Let $\mathscr{B}$ be subjected to a system of surface boundary traction, $\boldsymbol{T}$ acting on $\varphi(\partial\mathscr{V})$, and body force, $\mathbf{f}$ acting on $\varphi(\mathscr{V})$ (see Figure 2.2). The axiom of momentum balance asserts that: for any part of the deformed configuration of $\mathscr{B}$, the balance of linear momentum [31]:

$$\int_{\varphi(\mathscr{V})} \rho\ddot{u}dv = \int_{\varphi(\mathscr{V})} \rho\mathbf{f}dv + \int_{\partial\varphi(\mathscr{V})} \boldsymbol{T}(\boldsymbol{n})da \tag{2.10}$$

is satisfied, with ρ denoting the mass density field, and $\boldsymbol{n}$ is the outward unit vector normal to the deformed boundary $\varphi(\partial\mathscr{V})$ of $\mathscr{B}$.

The left hand side of equation (2.10) contains the inertia term, with $\ddot{\boldsymbol{u}}$ denoting the acceleration field of $\mathscr{B}$ (second derivative of displacement with respect to time) [31].

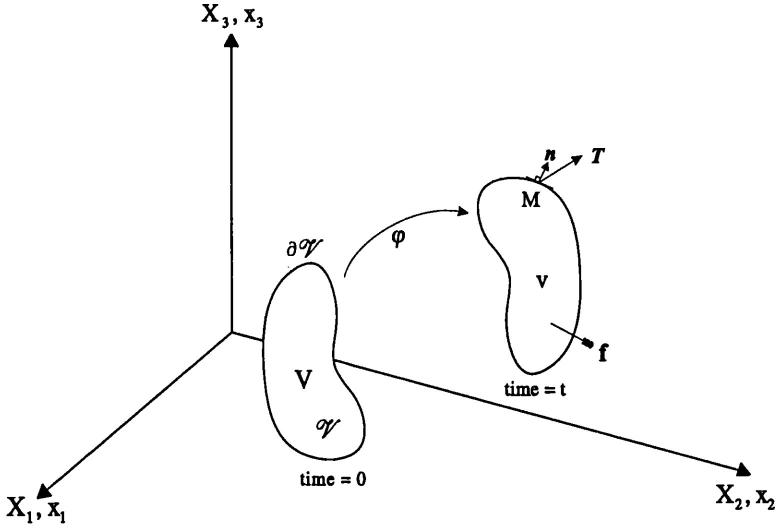

Figure 2.2: Schematic representation of body equilibrium and acting forces on the body.

The momentum balance can be expressed in its local form by the equations [31]:

$$\begin{aligned} div_x\boldsymbol{\sigma} + \mathbf{f} &= \rho\ddot{\boldsymbol{u}} \qquad in \;\; \varphi(\mathscr{V}) \\ \boldsymbol{T} &= \boldsymbol{\sigma n} \qquad in\, \varphi(\partial\mathscr{V}). \end{aligned} \tag{2.11}$$

Cauchy stress tensor

Consider a general deformable body at its current position as shown in Figure 2.3. Consider the element of area Δa normal to $\boldsymbol{n}$ in the neighborhood of spatial point $\boldsymbol{p}$ shown in Figure 2.3. If the resultant force on this area is $\Delta\boldsymbol{p}$, the traction vector $\boldsymbol{T}$ corresponding to the normal $\boldsymbol{n}$ at $\boldsymbol{p}$ is defined as [32],

$$\boldsymbol{T}(\boldsymbol{n}) = \lim_{\Delta a \to 0} \frac{\Delta \boldsymbol{p}}{\Delta a},$$

where the relationship between $\boldsymbol{T}$ and $\boldsymbol{n}$ must be such that satisfies Newton's third law of action and reaction [31],

$$\boldsymbol{T}(-\boldsymbol{n}) = -\boldsymbol{T}(\boldsymbol{n}).$$

From the axiom of momentum balance (equation (2.10)) it follows that the surface traction has a linear relation with its normal vector $\boldsymbol{n}$. This implies that there exists a tensor field $\boldsymbol{\sigma}(\boldsymbol{x})$ such that the Cauchy stress vector is given by [32],

$$\boldsymbol{T}(\boldsymbol{x}, \boldsymbol{n}) = \boldsymbol{\sigma}(\boldsymbol{x})\boldsymbol{n}. \tag{2.12}$$

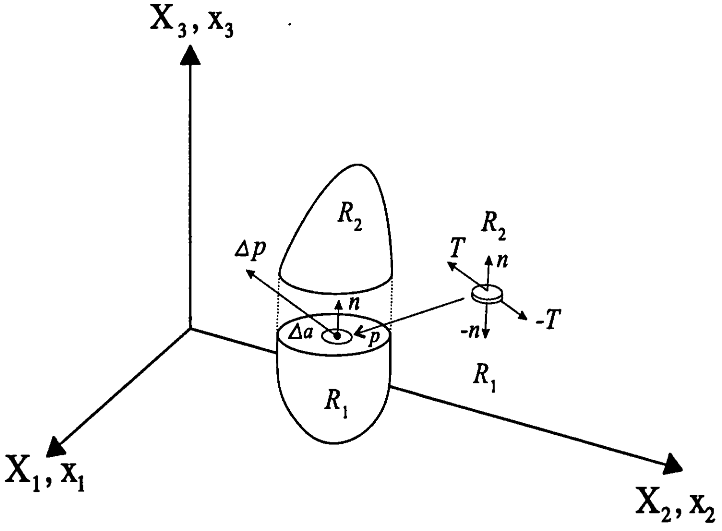

Figure 2.3: Schematic representation of a deformed body.

2.3 Weak equilibrium. The principle of virtual work

The strong form of the momentum balance have been stated in equation (2.11). In this section the momentum balance equation will be expressed in its weak form, which is the starting point of kinematically based finite element methods.

Assume the body $\mathscr{B}$ to be subjected to body forces in its interior and surface tractions on its boundary. In its deformed configuration, $\mathscr{B}$ occupies the region $\varphi(\mathscr{V})$ with boundary $\varphi(\partial\mathscr{V})$ defined through the deformation map φ [32].

Under infinitesimal deformations, reference and deformed configurations coincide and the virtual work equation reads simply [32]:

$$\int_{\mathscr{V}} [\sigma : \nabla\eta - (\mathrm{f} - \rho\ddot{u}) \cdot \eta] dV - \int_{\partial\mathscr{V}} \boldsymbol{T} \cdot \eta dA = 0 \qquad \forall\eta \in \mathfrak{V}, \tag{2.13}$$

where $\mathfrak{V}$ is the space of virtual displacements of $\mathscr{B}$.

If the stress field $\boldsymbol{\sigma}$ is sufficiently smooth, the virtual work equation is equivalent to the strong momentum balance (equation (2.11)) for more details we refer to [31,36].

2.3.1 Linearisation of the virtual work

The virtual work presented in equation (2.13), is generally nonlinear. In order to find a kinematically admissible field of displacement to satisfy the equation (2.13), it is essential to use one of the iterative procedures such as Newton-Raphson (see section 4.3.1). For this aim we need to linearize the equilibrium equation by using the general directional derivative procedure (see references [31,32,38]).

For simplicity of the procedure we assume that the stress tensor is a function of the current strain only:

$$\boldsymbol{\sigma} = \boldsymbol{\sigma}(\boldsymbol{\varepsilon}) = \boldsymbol{\sigma}(\nabla^s \boldsymbol{u}).$$

Now we want to linearize equation (2.13) with respect to the unknown $\boldsymbol{u}$ about an arbitrary argument $\hat{\boldsymbol{u}}$. That is, finding field $\boldsymbol{d}$ such that [31],

$$\mathscr{L}(\boldsymbol{d}, \boldsymbol{\eta}) \equiv G(\hat{\boldsymbol{u}}, \boldsymbol{\eta}) + DG(\hat{\boldsymbol{u}}, \boldsymbol{\eta})[\boldsymbol{d}] = 0 \quad \forall \boldsymbol{\eta} \in \mathfrak{V}, \tag{2.14}$$

where, $\mathscr{L}$ presents the linearized virtual work functional and

$$DG(\hat{\boldsymbol{u}}, \boldsymbol{\eta})[\boldsymbol{d}] = \left.\frac{d}{d\epsilon}\right|_{\epsilon=0} G(\hat{\boldsymbol{u}} + \epsilon \boldsymbol{d}, \boldsymbol{\eta}), \tag{2.15}$$

is the directional derivative of G at $\hat{\boldsymbol{u}}$ in the direction of $\boldsymbol{d}$.

The directional derivative of G is given by,

$$\begin{aligned} DG(\hat{\boldsymbol{u}}, \boldsymbol{\eta})[\boldsymbol{d}] &= \left.\frac{d}{\epsilon}\right|_{\epsilon=0} \int_{\mathscr{V}} [\boldsymbol{\sigma}(\boldsymbol{\varepsilon}(\epsilon)) : \nabla\boldsymbol{\eta} - \mathbf{f}\cdot\boldsymbol{\eta}]\, dV - \int_{\partial\mathscr{V}} \boldsymbol{T}\cdot\boldsymbol{\eta} dA \\ &= \left.\frac{d}{\epsilon}\right|_{\epsilon=0} \int_{\mathscr{V}} [\boldsymbol{\sigma}(\boldsymbol{\varepsilon}(\epsilon)) : \nabla\boldsymbol{\eta} - \mathbf{f}\cdot\boldsymbol{\eta}]\, dV. \end{aligned} \tag{2.16}$$

In above,

$$\boldsymbol{\varepsilon}(\epsilon) = \nabla^s(\hat{\boldsymbol{u}} + \epsilon \boldsymbol{d}) = \hat{\boldsymbol{\varepsilon}} + \epsilon \nabla^s \boldsymbol{d}. \tag{2.17}$$

Straightforward application of the chain rule to the functional $\boldsymbol{\sigma}$ in equation (2.16) yields,

$$DG(\hat{\boldsymbol{u}}, \boldsymbol{\eta})[\boldsymbol{d}] = \int_{\mathscr{V}} [\boldsymbol{C} : \nabla^s \boldsymbol{d} : \nabla\boldsymbol{\eta}]\, dV. \tag{2.18}$$

The fourth order tensor $\boldsymbol{C}$ in the context of small strain is known as the tangent modulus and defined as,

$$\boldsymbol{C} \equiv \frac{\partial \boldsymbol{\sigma}}{\partial \boldsymbol{\varepsilon}}. \tag{2.19}$$

The above definition will be used to achieve the consistent overall tangent modulus for the multi-scale material models.

2.3.2 Principal directions; principal stresses

For any symmetric stress tensor $\boldsymbol{\sigma}$, the eigenvectors of the tensor represent three principle directions. The planes having these directions as their normals are known as principle planes. The stress vectors which are normal to these planes are principle stresses. The principle stresses are the maximum and minimum values of normal stresses among all planes passing through a given point.

To determine the principle stresses, from the continuum mechanics (determination of the eigenvalues and eigenvectors - see reference [33]), the following system of equations should be solved,

$$det(\boldsymbol{\sigma} - \lambda \mathbf{I}) = 0,$$

where the obtained eigenvalues from the solution of the above equation, present the principal stresses for the stress tensor $\boldsymbol{\sigma}$. Figure 2.4 illustrates the transformation of the normal stresses to the principal directions.

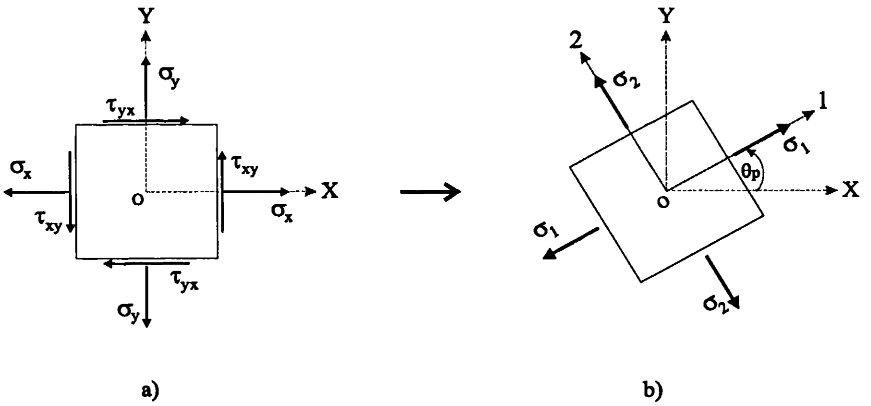

Figure 2.4: a) Stresses in given coordinate system. b) Principal stresses

2.3.3 State of plane stress and plane strain

If a thin plate is loaded by forces applied at the boundary, parallel to the plane of the plate and distributed uniformly over the thickness (see Figure 2.5), the stress components, σ_{33}, σ_{13}, σ_{23}, are zero on both faces of the plate. The state of stress is then specified by σ_{11}, σ_{22}, σ_{12}, only and,, is called the *plane stress.* [39].

Assume that the dimension of the prismatic body in the third direction (perpendicular to the plane) is very large and is loaded by forces that are perpendicular to the longitudinal elements. Assume that these forces do not vary along the length and it may be assumed that all cross sections are in the same condition. It is supposed that the end sections are confined between fixed smooth rigid planes, so that displacement in the axial direction is prevented (see Figure 2.5). In such a case, the components of strain ε_{33}, ε_{13}, ε_{23}, are zero and the state of strain is then specified by ε_{11}, ε_{22}, ε_{12}. Such strain case is called the *plane strain* [39].

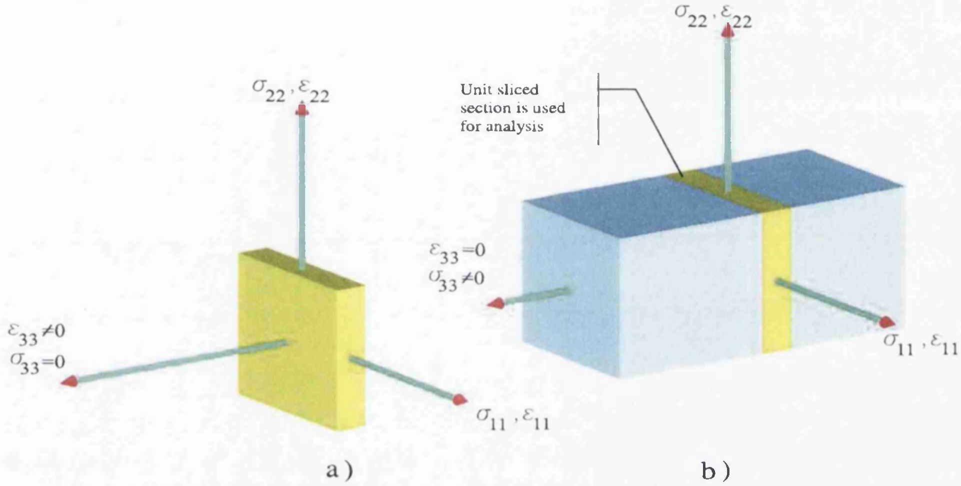

Figure 2.5: Plane problems. a) Plane stress. b) Plane strain

2.4 Conclusion

In this chapter, we reviewed some basic concepts of continuum mechanics in the context of large and small deformation, such as, the concepts of kinematics of deformation, motion, deformation gradient, infinitesimal strain tensor, the axiom of momentum balance and definition of Cauchy stress tensor. In addition, the concept of weak equilibrium and the principle of virtual work and linearisation of the virtual work were presented.

Moreover, the definition of principal directions and principal stresses were explained and at the end of this chapter the plane strain and the plane stress problems were reviewed.

Chapter 3

Constitutive material models

3.1 Introduction

Constitutive material models are defined to link the deformation of a continuum body to the forces acting on it and to illustrate the physical characteristic of different materials. The first constitutive model we consider is the linear isotropic elastic material followed by anisotropic elastic models and, at the end of this chapter, the von Mises elasto-plastic model is described.

3.2 Constitutive theory with internal variables

The principle of constitutive determinism restricted to the purely mechanical theory postulates that for a simple material undergoing small straining, the local history of the strain tensor $\boldsymbol{\varepsilon}^t$ (see equation (2.9)) at any point of interest up to instant t suffices to determine the history of the stress tensor $\boldsymbol{\sigma}$ at that point [40]. Therefore, there exists a symmetric tensor-valued constitutive functional $\mathfrak{F}$ such that, at an arbitrary instant t [41],

$$\boldsymbol{\sigma}(t) = \mathfrak{F}(\boldsymbol{\varepsilon}^t). \tag{3.1}$$

The constitutive theory with internal variables is based on the hypothesis that at any instant the thermodynamic state at a given point can be completely determined by the knowledge of a finite number of *state variables.* The thermodynamic state depends only on the instantaneous value of the state variables and not on their past history. It is assumed that the thermodynamic state at any time t for a given point is determined by the following set of state variables [31]:

$$\{\boldsymbol{\varepsilon}, \boldsymbol{\alpha}\},$$

where $\boldsymbol{\varepsilon}$ and $\boldsymbol{\alpha}$ represent, respectively, the instantaneous values of the strain tensor and the set of internal variables,

$$\boldsymbol{\alpha} = \{\alpha_k\},$$

generally containing scalar, vectorial and tensorial variables associated with dissipative mechanism (for more detail we refer to [36]). In this case, the specific free energy is assumed to have the form [31]:

$$\psi = \psi(\boldsymbol{\varepsilon}, \boldsymbol{\alpha}),$$

and the constitutive behaviour of the material is described by the following general set of equations:

$$\begin{cases} \boldsymbol{\sigma} = \frac{\partial \psi}{\partial \boldsymbol{\varepsilon}} \\ \dot{\boldsymbol{\alpha}} = f(\boldsymbol{\varepsilon}, \boldsymbol{\alpha}) \end{cases}, \tag{3.2}$$

Effectively, any model of the present type is completely defined by specifying the functions ψ and f.

3.3 Linear elastic material model

Within this framework, the simplest material model is the linear elastic one (for more detail we refer to i.e. [36,39,42,43]), for which the free-energy is expressed as,

$$\psi = \frac{1}{2}\boldsymbol{C} : \boldsymbol{\varepsilon} : \boldsymbol{\varepsilon},$$

or in index form,

$$\psi = \frac{1}{2} C_{ijkl} \varepsilon_{kl} \varepsilon_{ij}. \tag{3.3}$$

where, $\boldsymbol{C}$ is the fourth order tensor of elastic moduli (*the elasticity tensor*).

The linear stress-strain relation can be derived from equation (3.3) as

$$\sigma_{ij} = \frac{\partial \psi}{\partial \varepsilon_{ij}} = C_{ijkl} \varepsilon_{kl}, \qquad \text{or} \qquad \boldsymbol{\sigma} = \boldsymbol{C} : \boldsymbol{\varepsilon}. \tag{3.4}$$

The stress and strain tensors are required to be symmetric. In the most general case, a fourth order tensor has 81 independent components. However, the symmetry of $\boldsymbol{\sigma}$ and $\boldsymbol{\varepsilon}$ reduces the number of independent components to 36. On the other hand, due to symmetry of stress and strain tensor and from strain energy relation, it can be concluded that the stiffness tensor should also be a symmetric tensor, i.e,

$$C_{ijkl} = C_{klij}.$$

With the above restriction for the stiffness tensor, the number of independent components of stiffness tensor is reduced to 21. Any further reduction in the number of independent components can only be made through restrictions imposed by the symmetry properties of the material.

To present C_{ijkl} in compact form, it is convenient to introduce a contracted notation.

Stresses		Strain	
Tensor notation	*Contracted notation*	*Tensor notation*	*Contracted notation*
σ_{11}	σ_1	ε_{11}	ε_1
σ_{22}	σ_2	ε_{22}	ε_2
σ_{33}	σ_3	ε_{33}	ε_3
$\tau_{23} = \sigma_{23}$	σ_4	$\gamma_{23} = 2\varepsilon_{23}$	ε_4
$\tau_{31} = \sigma_{31}$	σ_5	$\gamma_{31} = 2\varepsilon_{31}$	ε_5
$\tau_{12} = \sigma_{12}$	σ_6	$\gamma_{12} = 2\varepsilon_{12}$	ε_6

Table 3.1: Notation for stresses and strains

In Table 3.1, γ_{ij} for $i \neq j$ presents engineering shear strain whereas ε_{ij} for $i \neq j$ represents tensor shear strain components.

With this notation the stress-strain relations, equation (3.4) with 21 independent components for C_{ijkl}, can be written as [43],

$$\begin{bmatrix} \sigma_1 \\ \sigma_2 \\ \sigma_3 \\ \sigma_4 \\ \sigma_5 \\ \sigma_6 \end{bmatrix} = \begin{bmatrix} C_{11} & C_{12} & C_{13} & C_{14} & C_{15} & C_{16} \\ & C_{22} & C_{23} & C_{24} & C_{25} & C_{26} \\ & & C_{33} & C_{34} & C_{35} & C_{36} \\ & & & C_{44} & C_{45} & C_{46} \\ & sym. & & & C_{55} & C_{56} \\ & & & & & C_{66} \end{bmatrix} \begin{bmatrix} \varepsilon_1 \\ \varepsilon_2 \\ \varepsilon_3 \\ \varepsilon_4 \\ \varepsilon_5 \\ \varepsilon_6 \end{bmatrix},$$

or in index notation,

$$\sigma_i = C_{ij}\varepsilon_j \qquad\qquad i,j = 1...6.$$

For symmetry with respect to a plane, C_{ij} has 13 independent components as,

$$C_{ij} = \begin{bmatrix} C_{11} & C_{12} & C_{13} & 0 & 0 & C_{16} \\ & C_{22} & C_{23} & 0 & 0 & C_{26} \\ & & C_{33} & 0 & 0 & C_{36} \\ & & & C_{44} & C_{45} & 0 \\ & sym. & & & C_{55} & 0 \\ & & & & & C_{66} \end{bmatrix},$$

where the plane of symmetry is $e_3 = 0$. For an orthotropic material (symmetry with respect to three mutually orthogonal planes), $\boldsymbol{C}$ has nine independent components and C_{ij} is written as,

$$C_{ij} = \begin{bmatrix} C_{11} & C_{12} & C_{13} & 0 & 0 & 0 \\ & C_{22} & C_{23} & 0 & 0 & 0 \\ & & C_{33} & 0 & 0 & 0 \\ & & & C_{44} & 0 & 0 \\ & sym. & & & C_{55} & 0 \\ & & & & & C_{66} \end{bmatrix}.$$

For a transversely isotropic material one of the planes for the orthotropic case is taken to be a plane of isotropy. Letting e_1 be normal to the plane of isotropy, we then have five independent components as [43],

$$C_{ij} = \begin{bmatrix} C_{11} & C_{12} & C_{12} & 0 & 0 & 0 \\ & C_{22} & C_{23} & 0 & 0 & 0 \\ & & C_{22} & 0 & 0 & 0 \\ & & & \frac{1}{2}(C_{22} - C_{23}) & 0 & 0 \\ & sym. & & & C_{66} & 0 \\ & & & & & C_{66} \end{bmatrix}.$$

Finally, in the case of complete isotropy there are only two independent components of C_{ij}, and we have [43],

$$C_{ij} = \begin{bmatrix} C_{11} & C_{12} & C_{12} & 0 & 0 & 0 \\ & C_{11} & C_{12} & 0 & 0 & 0 \\ & & C_{11} & 0 & 0 & 0 \\ & & & \frac{1}{2}(C_{11}-C_{12}) & 0 & 0 \\ & sym. & & & \frac{1}{2}(C_{11}-C_{12}) & 0 \\ & & & & & \frac{1}{2}(C_{11}-C_{12}) \end{bmatrix}.$$

In this case the stress-strain relations can be equivalently written as,

$$\sigma_{ij} = \lambda \varepsilon_{kk} \delta_{ij} + 2\mu \varepsilon_{ij},$$

where λ and μ are the *Lamé* coefficients and δ_{ij} is the Krönecker delta symbol. Alternatively, the stress-strain relations can be written compactly in terms of deviatoric and dilatational (volumetric) components. Let s_{ij} and $(\varepsilon_d)_{ij}$ be the deviatoric components of stress and strain, defined as [43],

$$\begin{aligned} s_{ij} &= \sigma_{ij} - \frac{1}{3}\delta_{ij}\sigma_{kk} \\ (\varepsilon_d)_{ij} &= \varepsilon_{ij} - \frac{1}{3}\delta_{ij}\varepsilon_{kk}. \end{aligned} \tag{3.5}$$

With equation (3.5) the stress-strain relations take the form,

$$s_{ij} = 2\mu(\varepsilon_d)_{ij},$$

and

$$\sigma_{kk} = 3k\varepsilon_{kk},$$

where μ in particular, is the shear modulus and constant k is the bulk modulus, which governs volumetric changes. Alternatively, the elastic relation may be expressed in terms of the Young's modulus,

$$E = \frac{9k\mu}{3k+\mu},$$

and Poisson's ratio,

$$\nu = \frac{3k-2\mu}{2(3k+\mu)}.$$

The elasticity tensor for plane stress models and based on the elastic modulus is expressed by [44],

$$C = \frac{E}{1-\nu^2}\begin{bmatrix} 1 & \nu & 0 \\ \nu & 1 & 0 \\ 0 & 0 & (1-\nu)/2 \end{bmatrix},$$

and for plane strain problems as,

$$C = \frac{E}{(1+\nu)(1-2\nu)}\begin{bmatrix} 1-\nu & \nu & 0 \\ \nu & 1-\nu & 0 \\ 0 & 0 & (1-2\nu)/2 \end{bmatrix}.$$

3.4 Anisotropic plane elasticity models

From equation (3.4), the linear elastic law for isotropic material model is expressed as [45],

$$\begin{aligned} \sigma_{ij} &= C_{ijkl}\varepsilon_{kl}, \\ \varepsilon_{ij} &= S_{ijkl}\sigma_{kl}, \end{aligned} \tag{3.6}$$

where $\boldsymbol{S}$ is compliance tensor. The reduced stiffness and compliance matrices for the plane stress condition and a unidirectional lamina model are expressed by [46],

$$\boldsymbol{C} = \begin{bmatrix} C_{11} & C_{12} & 0 \\ C_{12} & C_{22} & 0 \\ 0 & 0 & C_{66} \end{bmatrix}, \boldsymbol{S} = \begin{bmatrix} S_{11} & S_{12} & 0 \\ S_{12} & S_{22} & 0 \\ 0 & 0 & S_{66} \end{bmatrix}. \tag{3.7}$$

For an isotropic lamina, the components of stiffness and compliance matrices in equation (3.7) can be written in terms of engineering constants [46],

$$\boldsymbol{C} = \begin{bmatrix} \frac{E}{1-v^2} & \frac{vE}{1-v^2} & 0 \\ \frac{vE}{1-v^2} & \frac{E}{1-v^2} & 0 \\ 0 & 0 & G \end{bmatrix}, \boldsymbol{S} = \begin{bmatrix} \frac{1}{E} & -\frac{v}{E} & 0 \\ -\frac{v}{E} & \frac{1}{E} & 0 \\ 0 & 0 & \frac{1}{G} \end{bmatrix}, \tag{3.8}$$

where E and v are respectively Young's modulus and Poisson's ratio.

We can rewrite the components of the stiffness and compliance matrices for an orthotropic lamina containing unidirectional fibres at a fibre orientation angle of $\theta = 0$ or $\theta = 90$ (see Figure 3.1) in terms of the engineering constants by [46],

$$\begin{aligned}
C_{11} &= \frac{E_{11}}{1-\upsilon_{12}\upsilon_{21}},\\
C_{22} &= \frac{E_{22}}{1-\upsilon_{12}\upsilon_{21}},\\
C_{12} &= \frac{\upsilon_{12}E_{22}}{1-\upsilon_{12}\upsilon_{21}},\\
C_{21} &= \frac{\upsilon_{21}E_{11}}{1-\upsilon_{12}\upsilon_{21}},\\
C_{66} &= G_{12}.
\end{aligned} \tag{3.9}$$

$$\begin{aligned}
S_{11} &= \frac{1}{E_{11}},\\
S_{22} &= \frac{1}{E_{22}},\\
S_{12} &= \frac{-\upsilon_{12}}{E_{11}},\\
S_{21} &= \frac{-\upsilon_{21}}{E_{22}},\\
S_{66} &= \frac{1}{G_{12}}.
\end{aligned} \tag{3.10}$$

The general form of stiffness and compliance matrices for a general orthotropic lamina ($\theta \neq 0$ or $\theta \neq 90$) could be expressed as,

$$\bar{\boldsymbol{C}} = \begin{bmatrix} \bar{C}_{11} & \bar{C}_{12} & \bar{C}_{16} \\ \bar{C}_{12} & \bar{C}_{22} & \bar{C}_{26} \\ \bar{C}_{16} & \bar{C}_{26} & \bar{C}_{66} \end{bmatrix}, \bar{\boldsymbol{S}} = \begin{bmatrix} \bar{S}_{11} & \bar{S}_{12} & \bar{S}_{16} \\ \bar{S}_{12} & \bar{S}_{22} & \bar{S}_{26} \\ \bar{S}_{16} & \bar{S}_{26} & \bar{S}_{66} \end{bmatrix}. \tag{3.11}$$

Elements in the $\bar{\boldsymbol{C}}$ matrix could be expressed in terms of the material properties in the principal material directions in the following form [46],

$$\begin{aligned}
\bar{C}_{11} &= C_{11}cos^4\theta + 2(C_{12}+2C_{66})sin^2\theta cos^2\theta + C_{22}sin^4\theta,\\
\bar{C}_{12} &= C_{12}(sin^4\theta + cos^4\theta) + (C_{11}+C_{22}-4C_{66})sin^2\theta cos^2\theta,\\
\bar{C}_{22} &= C_{11}sin^4\theta + 2(C_{12}+2C_{66})sin^2\theta cos^2\theta + C_{22}cos^4\theta,\\
\bar{C}_{16} &= (C_{11}-C_{12}-2C_{66})sin\theta cos^3\theta + (C_{12}-C_{22}+2C_{66})sin^3\theta cos\theta,\\
\bar{C}_{26} &= (C_{11}-C_{12}-2C_{66})sin^3\theta cos\theta + (C_{12}-C_{22}+2C_{66})sin\theta cos^3\theta,\\
\bar{C}_{66} &= (C_{11}+C_{22}-2C_{12}-2C_{66})sin^2\theta cos^2\theta + C_{66}(sin^4\theta + cos^4\theta).
\end{aligned} \tag{3.12}$$

Figure 3.1 shows lamina with unidirectional fibres at a local fibre orientation angle θ with respect to the global material axes. Figure 3.1-(a) is a 2-D representation in the plane of the fibres. The angle θ is measured positive counter clockwise from the global xx axis to the local *11* axis. Figure 3.1-(b) shows 3-D schematic view of the lamina when the local fibre axes coincide with the global material axes.

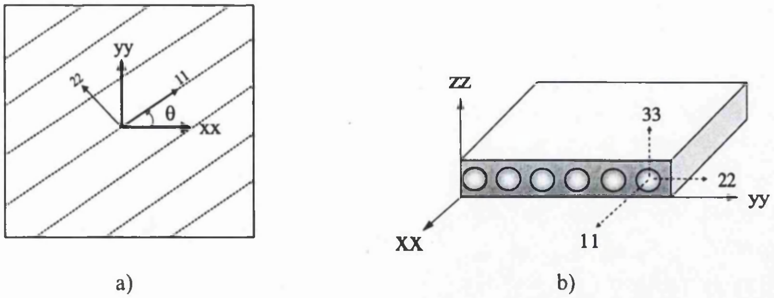

a) b)

Figure 3.1: a) Fibre orientation angle in plane of fibres. b) 3-D view of the principal material directions and local fibre directions.

By introducing the transformation matrix $\boldsymbol{T}$ as [45–47],

$$\boldsymbol{T} = \begin{bmatrix} m^2 & n^2 & 2mn \\ n^2 & m^2 & -2mn \\ -mn & mn & m^2 - n^2 \end{bmatrix}, \tag{3.13}$$

where $m = cos\theta$ and $n = sin\theta$, the equations (3.12) can be written as [45–47],

$$\begin{aligned}
\bar{C}_{11} &= C_{11}m^4 + 2(C_{12} + 2C_{66})n^2m^2 + C_{22}n^4, \\
\bar{C}_{12} &= C_{12}(n^4 + m^4) + (C_{11} + C_{22} - 4C_{66})n^2m^2, \\
\bar{C}_{22} &= C_{11}n^4 + 2(C_{12} + 2C_{66})n^2m^2 + C_{22}m^4, \\
\bar{C}_{16} &= (C_{11} - C_{12} - 2C_{66})nm^3 + (C_{12} - C_{22} + 2C_{66})n^3m, \\
\bar{C}_{26} &= (C_{11} - C_{12} - 2C_{66})n^3m + (C_{12} - C_{22} + 2C_{66})nm^3, \\
\bar{C}_{66} &= (C_{11} + C_{22} - 2C_{12} - 2C_{66})n^2m^2 + C_{66}(n^4 + m^4).
\end{aligned} \tag{3.14}$$

3.5 Elasto-plastic material model

The initial idea of plasticity theory could be traced back to the nineteenth century. Following the substantial developments during the last century, today we take advantage of the most successful and well-known phenomenological constitutive models of solid materials. The theory of plasticity is expressed for solid materials which after loading and unloading show a plastic/irreversible deformation.

In particular, this theory is restricted to predict the behaviour of materials for which the permanent deformations do not depend on the rate of application of loads and is often referred to as the rate-independent plasticity. Materials whose behaviour can be adequately described by the theory of plasticity are called plastic (or rate-independent plastic) materials.

To determine the general mathematical formulation for this theory the experimental observations have been done for the behaviour of metals under the uniform states of combined stresses. In contrast to the elastic materials, for which the state of strain depends only on the final state of stress, the deformation that occurs in a plastic solid is determined by the complete history of the loading. The plasticity problem is, therefore, essentially incremental in nature, and the final displacement of the solid obtains as the sum of the incremental displacements following the strain path.

3.5.1 Phenomenological aspect of plasticity

The uniaxial tension test is commonly used to assess the behaviour of ductile metals. This presentation of the material behaviour is generally known as the stress-strain curve (see Figure 3.2). In the schematic diagram of Figure 3.2, where the axial stress, σ, is plotted against the axial strain, ε, the imposed loading to the bar has been increased gradually such that the axial stress changes from zero to prescribed value, σ_0. The bar is then unloaded back to an unstressed state and subsequently reloaded to a higher stress level, σ_1. From this test some important phenomenological properties can be identified:

1. The elastic domain is the range of stresses within which the behaviour of the material remains purely elastic. The elastic domain is defined by the so-called yield stress.

2. By increasing the load, at the yield stress point the evolution of plastic strain takes place. This phenomena is known as *plastic yielding.*

3. The evolution of the yield stress is known as *hardening* (see the difference between two points Y_0, and, Y_1).

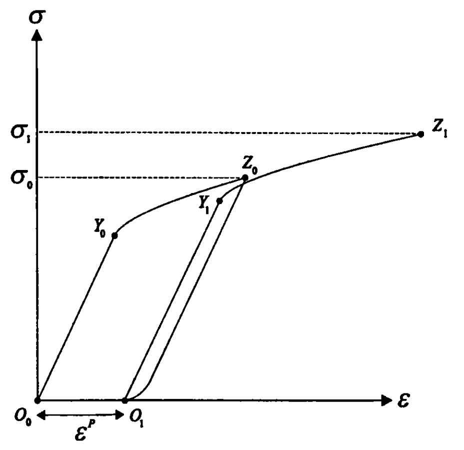

Figure 3.2: Uniaxial tension experiment with ductile metals [31].

The object of the mathematical theory of plasticity is to provide continuum constitutive models capable of describing (qualitatively and quantitatively) the phenomenological behaviour of materials that possess the characteristics discussed above with sufficient accuracy. Various criteria have been suggested in the past to predict the yielding of metals under complex stresses. Two widely used criteria are those due to Tresca and von Mises. From a series of experiments on the extrusion of metals [48], Tresca concluded that '*plastic deformation occurs when the maximum shear stress over all planes attains a critical value given by the yield stress in shear denoted by,* k_Y' [49].

Von Mises suggested that '*plastic deformation occurs when the maximum octahedral shear stress reaches its critical value* '. Because of the direct relation between the maximum octahedral shear stress and the distortional energy, this criterion is sometimes termed the *maximum distortional energy criterion.*

The Tresca criterion is expressed as [49,50]:

$$\Phi(\boldsymbol{\sigma}) = 4J_2^3 - 27J_3^2 - 36k_Y^2 J_2^2 + 96k_Y^4 J_2 - 64k_Y^4, \tag{3.15}$$

where, $J_2(\boldsymbol{s})$, and, $J_3(\boldsymbol{s})$, are respectively, the *second* and *third invariant* of the *deviatoric stress tensor,*

$$\boldsymbol{s} := dev[\boldsymbol{\sigma}] = \boldsymbol{\sigma} - \frac{1}{3}tr[\boldsymbol{\sigma}]. \tag{3.16}$$

Also the von Mises criterion is expressed by

$$\Phi(\boldsymbol{\sigma}) \;=\; \sqrt{3J_2} - \sigma_y, \tag{3.17}$$

where,

$$\sigma_y = \sqrt{3}k_Y, \tag{3.18}$$

indicates the relation between the uniaxial and *shear yield stress.* From equation (3.17), the von Mises effective stress is expressed by

$$\sigma_{eff} = \sqrt{3J_2} = \sqrt{\sigma_{xx}^2 + \sigma_{yy}^2 + 3\sigma_{xy}^2 - \sigma_{xx}\sigma_{yy}}. \tag{3.19}$$

Figure 3.3 illustrates the Tresca and the von Mises criteria in the deviatoric plane. The Tresca yield locus is a hexagon with distances of $\sqrt{2/3}Y$, from origin to apex on the deviatoric plane whereas the von Mises yield surface is a circle of radius $\sqrt{2}k_Y$ ($\sqrt{J_2} = k_Y$). The constant Y may be chosen such that, the von Mises and the Tresca criteria to be in agree with each other. It is conventional to make the circle pass through the apices of the hexagon by taking the constant $Y = \sqrt{3}k_Y$, the uniaxial yield stress (see 3.18) [51].

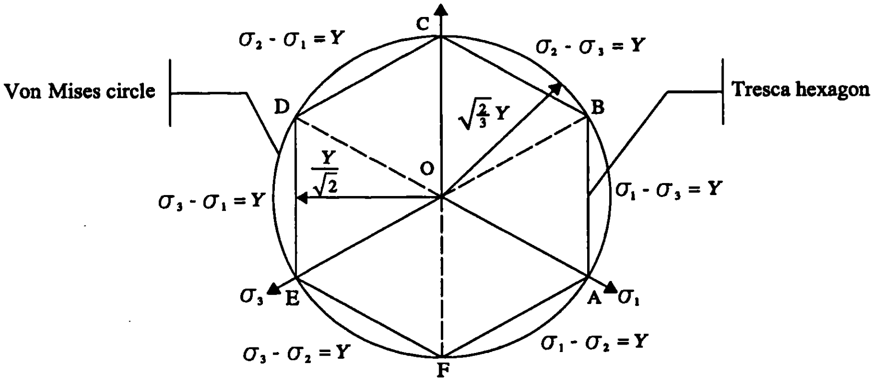

Figure 3.3: Tresca and von Mises yield criteria in deviatoric plane.

We should emphasize that the von Mises elasto-plastic material model has been considered in this research and for more detail about other models, criteria, and plastic behaviour, we refer to [31,36,48,50,52].

3.5.2 Von Mises yield criterion

It should be mentioned that, in the von Mises yield criterion, the volumetric components of stress do not take part in the definition of the von Mises criterion and only the deviatoric stress can influence the plastic yielding [31, 49]. 3-D view in the principal stress space of the von Mises model is illustrated in Figure 3.4.

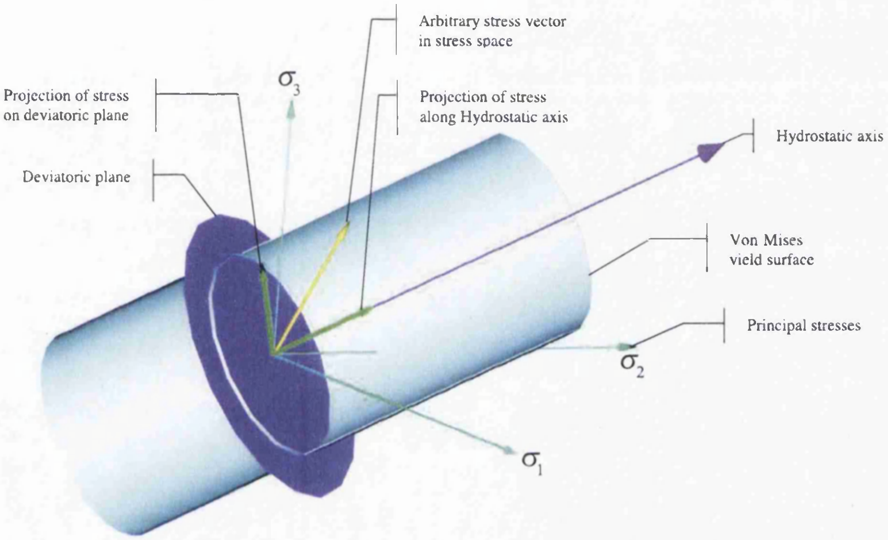

Figure 3.4: 3-D representation of the yield criterion in principal stress space.

Constitutive equations for the von Mises elasto-plastic material model

The general constitutive equations in framework of elaso-plastic materials have been explained in detail in [31, 36, 48–50, 52]. Consider a point p, of a generic elasto-plastic body, $\mathscr{B}$, in a configuration at time t_0 and assume that, at this instant, the plastic strain tensor, $\boldsymbol{\varepsilon}^p(t_0)$, and all elements of the set $\boldsymbol{\alpha}(t_0)$ of internal variables are known. Furthermore, let the motion of $\mathscr{B}$ be prescribed between t_0 and a subsequent instant, t_1. The prescribed motion defines the history of the strain tensor, $\boldsymbol{\varepsilon}(t)$, at the material point of intrest between instants t_0 and t_1. The basic elasto-plastic initial value problem is stated in the following [31],

$$\dot{\varepsilon}(t) = \dot{\varepsilon}^e(t) + \dot{\varepsilon}^p(t), \tag{3.20}$$

$$\dot{\varepsilon}^p(t) = \dot{\gamma}(t)\mathbf{N}(\boldsymbol{\sigma}(t), \mathbf{A}(t)), \tag{3.21}$$

$$\dot{\boldsymbol{\alpha}}(t) = \dot{\gamma}(t)\mathbf{H}(\boldsymbol{\sigma}(t), \mathbf{A}(t)), \tag{3.22}$$

$$\Phi(\boldsymbol{\sigma}(t), \mathbf{A}(t)) \leq 0, \quad \dot{\gamma}(t) \geq 0, \quad \dot{\gamma}(t).\Phi(\boldsymbol{\sigma}(t), \mathbf{A}(t)) = 0, \tag{3.23}$$

$$\dot{\Phi}(\boldsymbol{\sigma}(t), \mathbf{A}(t)).\dot{\gamma} = 0, \tag{3.24}$$

where Φ is the yield function, $\dot{\varepsilon}^p$ is the rate of the plastic strain, $\dot{\gamma}$ is the rate of plastic multiplier, $\dot{\boldsymbol{\alpha}}$ is the rate of the internal variable for the strain hardening and $\mathbf{A}$ is the hardening thermo-dynamical force [31].

The rate of plastic multiplier $\dot{\gamma}$, is defined by,

$$\dot{\gamma} = \dot{\bar{\varepsilon}}^p = \sqrt{\frac{2}{3}}\,\|\dot{\varepsilon}^p\|\,.$$

In equation (3.21) $\mathbf{N}$ is the flow vector and $\mathbf{H}$ in equation (3.22) is the generalized hardening modulus, which defines the evolution of the hardening variables [31].

By taking the von Mises yield function, equation (3.17), as the flow potential, from the Prandtl-Reuss plasticity law [31], the flow vector $\mathbf{N}$ is given by [31],

$$\boldsymbol{N} = \partial_\sigma \Phi = \frac{\partial}{\partial \sigma}\left[\sqrt{3J_2}\right] = \sqrt{\frac{3}{2}}\frac{\boldsymbol{s}}{\|\boldsymbol{s}\|}, \tag{3.25}$$

and the corresponding flow rule in equation (3.21), is expressed by,

$$\dot{\varepsilon}^p = \dot{\gamma}\sqrt{\frac{3}{2}}\frac{\boldsymbol{s}}{\|\boldsymbol{s}\|}. \tag{3.26}$$

Hardening laws

The phenomenon of hardening has been identified in the uniaxial experiment. Hardening is characterised by a dependence of yield stress level upon the history of plastic straining to which the body has been subjected. In the two- and three -dimensional situations, hardening is represented by changes in the hardening thermo dynamical force, **A**, [31], during plastic yielding. These changes may, in general, affect the size, shape and orientation of the yield surface, which is defined by:

$$\Phi(\sigma, \mathbf{A}). \tag{3.27}$$

In this section we will have a brief review of different types of hardening such as perfect plasticity (no hardening) and isotropic hardening.

Perfect plasticity

A material model is said to be *perfectly plastic* if *no hardening* is allowed, that is, the yield stress level does not depend in any way on the degree of plastification. In this case, the yield surface remains fixed regardless of any deformation process so that the elasto-plastic modulus, E^{ep}, vanishes and in the von Mises model, this type of hardening responds to constant uniaxial yield stress, σ_y.

Figure 3.5, shows the stress-strain curve of typical uniaxial cyclic test with a perfectly plastic von Mises model along with the corresponding deviatoric plane representation of the yield surface.

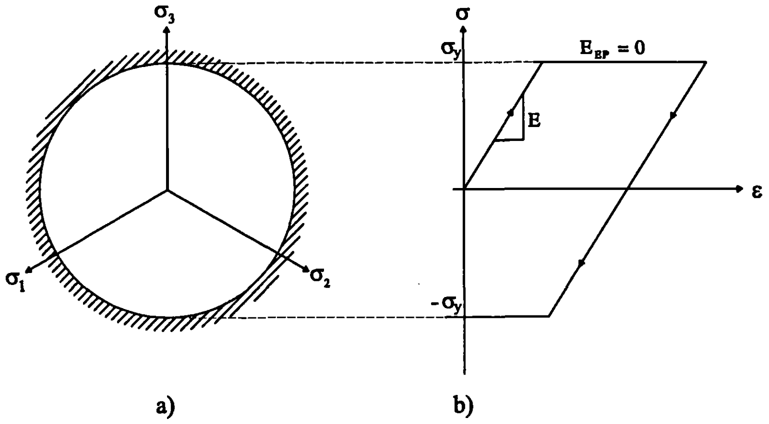

Figure 3.5: Perfect plasticity. Uniaxial cyclic test and deviatoric plane representation. a) Deviatoric plane. b) Stress-strain curve for uniaxial cyclic test

Isotropic hardening

A material model is said to be *Isotropic hardening* if the evolution of the yield surface is such that, at any state of hardening, it corresponds to a uniform (isotropic) expansion of the initial yield surface, without translation [31].

During plastic flow, the elastic domain expands equally in both tension and compression. The expansion of the yield surface and the stress-strain curve for uniaxial cyclic test with an isotropic hardening for the von Mises model is shown in Figure 3.6.

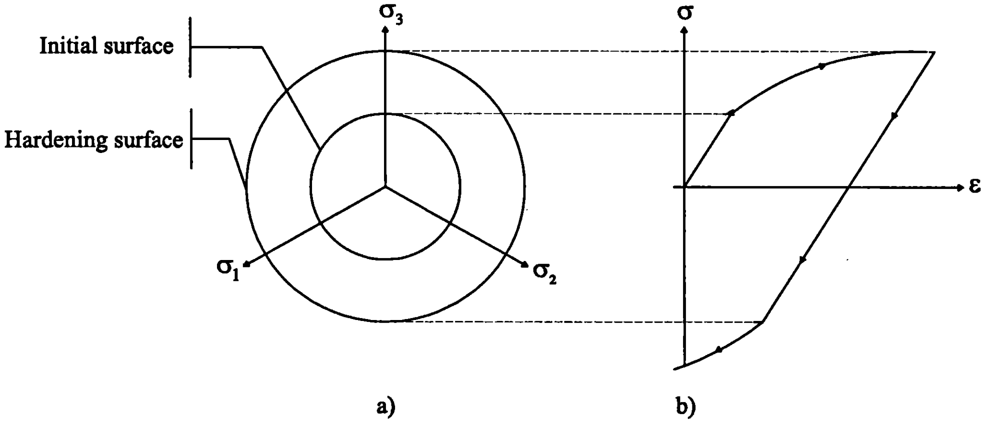

Figure 3.6: Isotropic hardening. Uniaxial cyclic test and deviatoric plane representation.
a) Deviatoric plane. b) Stress-strain curve for uniaxial cyclic test.

The choice of a suitable set of hardening internal variables, $\boldsymbol{\alpha}$, must be obviously dependent on the specific characteristics of the material under consideration. The set $\boldsymbol{\alpha}$ normally contains a single scalar variable, which determines the size of the yield surface. The most popular approach is called strain hardening for which the effective strain defined by,

$$\bar{\varepsilon}^p \equiv \int_0^t \sqrt{\frac{2}{3}\dot{\varepsilon}^p : \dot{\varepsilon}^p dt} = \int_0^t \sqrt{\frac{2}{3}} \left\| \dot{\varepsilon}^p \right\| dt, \tag{3.28}$$

is chosen as the internal variable associated with isotropic hardening. The variable $\bar{\varepsilon}^p$ is also known as accumulated plastic strain and its evolution law for $\bar{\varepsilon}^p$ is given by [31]:

$$\dot{\bar{\varepsilon}}^p = \sqrt{\frac{2}{3}\dot{\varepsilon}^p : \dot{\varepsilon}^p} = \sqrt{\frac{2}{3}} \left\| \dot{\varepsilon}^p \right\|. \tag{3.29}$$

The effect of the hardening variables on the size of the yield surface is introduced by making the yield stress dependent on $\bar{\varepsilon}^p$. For the von Mises criteria, one has for the uniaxial yield stress,

$$\sigma_y = \sigma_y(\bar{\varepsilon}^p). \tag{3.30}$$

The function (3.30) define the co-called hardening curve, which is the only experimentally determined plastic property required by isotropic hardening materials. If σ_y is a linear function of $\bar{\varepsilon}^p$, the model is said to be linear hardening. Otherwise, it is a non-linear hardening model [31].

3.5.3 Return mapping in the elasto-plastic problem

Due to the additive structure of the total strain rate (see equation (3.20)), the numerical integration of the von Mises constitutive initial value problem for the elasto-plasticity is split into a sequence of two sub problems: the elastic predictor and the plastic corrector.

The procedure starts by solving the system of equations (3.20) - (3.24) for the elastic predictor problem, in which the material is assumed to behave purely elastic between time t_n and t_{n+1}, with the internal variables frozen at the beginning of the time interval. The elastic predictor problem is defined by the following steps [31]:

Given the strain history $\varepsilon(t)$ within the time interval $[t_n, t_{n+1}]$, find $\varepsilon^{e\ trial}$, $\varepsilon^{p\ trial}$ and α^{trial}, that satisfy [31,49]:

$$\begin{aligned} \dot{\varepsilon}^{e\ trial} &= \dot{\varepsilon}, & (3.31)\\ \dot{\varepsilon}^{p\ trial} &= 0, & (3.32)\\ \dot{\alpha}^{trial} &= 0, & (3.33) \end{aligned}$$

with the same initial conditions, as the original elasto-plastic problem:

$$\begin{aligned} \varepsilon^{e\ trial}(t_n) &= \varepsilon^e_n, & (3.34)\\ \varepsilon^{p\ trial}(t_n) &= \varepsilon^p_n, & (3.35)\\ \alpha^{trial}(t_n) &= \alpha_n. & (3.36) \end{aligned}$$

The solution of the elastic predictor problem at time t_{n+1}, denoted $\varepsilon^{e\ trial}_{n+1}$, $\varepsilon^{p\ trial}_{n+1}$ and α^{trial}_{n+1}, defines the so-called elastic trial state. The next step in the elasto-plastic operator split algorithm is to take the elastic trial state as initial condition for the plastic corrector problem [31].

In the plastic corrector (the return mapping) the objective is to find ε^e, ε^p and α, such that the following equations are satisfied [31,49]:

$$\dot{\varepsilon}^e(t) = -\dot{\varepsilon}^p(t), \tag{3.37}$$

$$\dot{\varepsilon}^p = \dot{\gamma}\mathbf{N}, \tag{3.38}$$

$$\dot{\alpha} = -\dot{\gamma}\mathbf{H}, \tag{3.39}$$

$$\Phi(\sigma, \mathbf{A}) \leq 0, \quad \dot{\gamma} \geq 0, \quad \dot{\gamma}\Phi(\sigma, \mathbf{A}) = 0, \tag{3.40}$$

where the stress σ and the hardening force $\mathbf{A}$ are given by [31]:

$$\sigma = \bar{\rho}\frac{\partial \psi}{\partial \varepsilon^e}, \qquad \mathbf{A} = \bar{\rho}\frac{\partial \psi}{\partial \alpha}, \tag{3.41}$$

where ψ, is the free potential energy.

The initial conditions are:

$$\begin{aligned} \varepsilon^e(t_n) &= \varepsilon_{n+1}^{e\ trial}, & (3.42)\\ \varepsilon^p(t_n) &= \varepsilon_{n+1}^{p\ trial}, & (3.43)\\ \alpha(t_n) &= \alpha_{n+1}^{trial}. & (3.44) \end{aligned}$$

Finally, the solution obtained for the plastic corrector at t_{n+1}, denoted,

$$\{\sigma_{n+1}, \varepsilon_{n+1}^e, \varepsilon_{n+1}^p, \alpha_{n+1}\} \tag{3.45}$$

is an approximation to the solution of the actual elasto-plastic initial value problem at t_{n+1} [31].

To sum up, the approximated solution of the initial value problem of elasto-plasticity has resulted in a numerical algorithm that involves two steps: The elastic predictor, which in the evolution problem is solved as if the material were purely elastic within the time interval considered, followed by the return mapping, which ensures plastic admissibility of the converged state. The return mapping procedure is executed only if the elastic trial state violates plastic admissibility [31].

The fully implicit elastic predictor and return mapping algorithm for numerical integration of general elasto-plastic constitutive equations, has been summarized in the Box 3.1:

1. *Elastic predictor.* For given $\Delta\varepsilon$ and the state variables at time t_n, evaluate the elastic trial state:

$$\begin{aligned} \varepsilon^{e\,trial}_{n+1} &= \varepsilon^{e}_{n} + \Delta\varepsilon, \\ \alpha^{trial}_{n+1} &= \alpha^{trial}_{n}, \end{aligned}$$

$$\sigma^{trial}_{n+1} = \bar{\rho}\frac{\partial\psi}{\partial\varepsilon^{e}}\Big|^{trial}_{n+1}, \qquad \mathbf{A}^{trial}_{n+1} = \bar{\rho}\frac{\partial\psi}{\partial\alpha}\Big|^{trial}_{n+1},$$

2. *Check for plastic admissibility,*
   IF $\Phi(\sigma^{trial}_{n+1}, \mathbf{A}^{trial}_{n+1}) \leq 0$,
   THEN set $(.)_{n+1} = (.)^{trial}_{n+1}$ and EXIT

3. *Return mapping.* Solve the non-linear system of equations,

$$\begin{aligned} \varepsilon^{e}_{n+1} - \varepsilon^{e\,trial}_{n+1} + \Delta\gamma \boldsymbol{N}_{n+1} &= 0 \\ \alpha_{n+1} - \alpha^{trial}_{n+1} - \Delta\gamma \boldsymbol{H}_{n+1} &= 0 \\ \Phi(\sigma_{n+1}, \mathbf{A}_{n+1}) &= 0 \end{aligned}$$

   for ε^{e}_{n+1}, α_{n+1}, and $\Delta\gamma$, with,

$$\sigma_{n+1} = \bar{\rho}\frac{\partial\psi}{\partial\varepsilon^{e}}\Big|_{n+1}, \qquad \mathbf{A}_{n+1} = \bar{\rho}\frac{\partial\psi}{\partial\alpha}\Big|_{n+1},$$

4. *EXIT*

Box 3.1. Implicit elastic predictor and return mapping algorithm for numerical integration of general elasto-plastic constitutive equations

For further details, readers are referred to [31, 36, 48–50, 52]. A geometric interpretation of the elastic predictor and plastic corrector is given in Figure 3.7 [49].

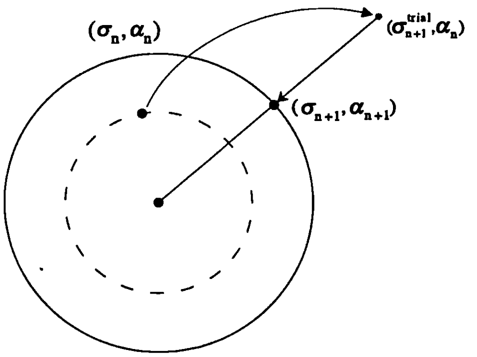

Figure 3.7: The elastic predictor-plastic corrector scheme for the von Mises yield criterion. Return mapping for the trial stress, σ_{n+1}^{trial}, to the current yield surface, $\Phi_{n+1} = \Phi(\sigma_{n+1}, \alpha_{n+1})$.

3.6 Continuum models for materials with microstructures

Composite materials have many characteristics that are different from more conventional engineering materials. Some characteristics are merely modifications of conventional behaviour; others are totally new and require new analytical and experimental procedures. Often, the predicted results from the modelling of such materials based on the purely macroscopic theories are in disagreement with the observed constitutive response. By increasing in demand for new composite materials with complex structures, the phenomenological theories stretched to their limit of applicability. A possible alternative to improve accuracy in this case is by identifying new internal variables. However, the disadvantage of this approach is the difficulty for identification of states and evolution laws for the extra internal variables. A second alternative to solve the problem consists in the adoption of so-called multi-scale models. In this method because of the inherent heterogeneous nature of composite materials, they are conveniently studied from two points of view: micro-mechanics and macro-mechanics and the constitutive description of the macroscopic behaviour is determined by means of homogenisation techniques.

Micro-mechanics is the study of composite material behaviour where the interaction of the constituent materials is examined on a microscopic scale. On the other hand, macro-mechanics is the study of composite material behaviour in which the material is assumed homogeneous and the effect of the constituent materials are considered only as averaged apparent properties of the composite [53].

3.7 Conclusion

In the first part of this chapter, we reviewed the basics of constitutive theory with internal variables in small strain.

In the second part, three types of constitutive material models were explained: The linear elastic material model, anisotropic elasticity model, and the elasto-plastic material model. For the second material model, the concept of anisotropy was explained for the plane stress condition and a unidirectional lamina material model.

In addition, for the elasto-plastic material model, the uniaxial tension experiment with ductile metals was discussed. For predicting the yielding of metals under complex stresses, two satisfactory and widely used criteria were described, the Tresca and von Mises yield criterion. In the following, the phenomenon of hardening was identified in terms of the perfect plasticity and isotropic hardening. In addition, the constitutive equations for the von Mises elasto-plastic material model were explained.

Finally the necessity of introducing a new approach to cope with new complex material models was presented.

Chapter 4

Basics of Finite element (FE) and implementation

4.1 Introduction

This chapter reviews some basics of the finite element method (FEM) for 2-D solid mechanics problems under small strains. For more details about finite element methods refer to standard textbooks such as [31,32,51,54–56].

The finite element method has become a powerful tool for the numerical solution of a wide range of engineering problems. The finite element method relies essentially on the discretization of the virtual work (equation 2.13) by means of finite element bases interpolation (or shape) functions whose parameters are the nodal displacements. This is described in the following.

4.1.1 Discrete boundary value problem

To drive the discretised form of the virtual work equation it is convenient to introduce some standard matrix notations. Firstly we define global interpolation matrix [31]:

$$\boldsymbol{N}^g(\boldsymbol{x}) = \Big[diag[N_1^g(\boldsymbol{x})] \;\; diag[N_2^g(\boldsymbol{x})] \;\; \cdots \;\; diag[N_{n_{point}}^g(\boldsymbol{x})] \;\; \Big], \tag{4.1}$$

where $diag[N_i^g]$ denotes the $n_{dim} \times n_{dim}$ diagonal matrix [31]. We also define the global vector of displacements [31]:

$$\boldsymbol{u} = \left[u_1^1, ..., u_{n_{dim}}^1, ..., u_1^{n_{point}}, ..., u_{n_{dim}}^{n_{point}}\right]^T, \tag{4.2}$$

and analogously, the vector of virtual nodal displacement [31]:

$$\boldsymbol{\eta} = \left[\eta_1^1, \ldots, \eta_{n_{dim}}^1, \ldots, \eta_1^{n_{point}}, \ldots, \eta_{n_{dim}}^{n_{point}}\right]^T, \tag{4.3}$$

It is also convenient to introduce the global *strain-displacement matrix*, which is defined in two dimensions for plane strain and plane stress for all nodes and elements by [31],

$$\boldsymbol{B}^g = \begin{bmatrix} N_{1,1}^g & 0 & N_{2,1}^g & 0 & \cdots & N_{n_{npoint},1}^g & 0 \\ 0 & N_{1,2}^g & 0 & N_{2,2}^g & \cdots & 0 & N_{n_{npoint},2}^g \\ N_{1,2}^g & N_{1,1}^g & N_{2,2}^g & N_{2,1}^g & \cdots & N_{n_{npoint},2}^g & N_{n_{npoint},1}^g \end{bmatrix}. \tag{4.4}$$

By generating the finite-dimensional sets [31] we are ready to discretize the virtual work equation:

$$\mathfrak{K}^{\mathfrak{finite}} \equiv \left\{ \boldsymbol{u}^{finite}(\boldsymbol{x}) = \sum_{i=1}^{n_{point}} \boldsymbol{u}^i N_i^g(\boldsymbol{x}) \mid \boldsymbol{u}^i = \bar{\boldsymbol{u}}(\boldsymbol{x}^i) \;\; if \;\; \boldsymbol{x}^i \in \mathscr{V} \right\}, \tag{4.5}$$

and

$$\mathfrak{V}^{\mathfrak{finite}} \equiv \left\{ \boldsymbol{\eta}^{finite}(\boldsymbol{x}) = \sum_{i=1}^{n_{point}} \boldsymbol{\eta}^i N_i^g(\boldsymbol{x}) \mid \boldsymbol{\eta}^i = \boldsymbol{0} \;\; if \;\; \boldsymbol{x}^i \in \partial\mathscr{V} \right\}. \tag{4.6}$$

Assume that the underlying material is elastic and the stress tensor is a function of the strain only and according to the quasi-static formulation [31], where inertia effects are ignored, we recall the virtual work expression (equation (2.13)),

$$\int_{\mathscr{V}} [\boldsymbol{\sigma}(\nabla^s \boldsymbol{u}) : \nabla^s \boldsymbol{\eta} - \mathbf{f} \cdot \boldsymbol{\eta}] dV - \int_{\partial\mathscr{V}} \boldsymbol{T} \cdot \boldsymbol{\eta} dA = 0 \qquad \forall \boldsymbol{\eta} \in \mathfrak{V}. \tag{4.7}$$

By replacing our domains to the new finite-dimensional sets (equations (4.5)-(4.6)), equation (4.7) can be written as [31]:

$$\int_{\mathscr{V}} [\boldsymbol{\sigma} : \boldsymbol{B}^g \boldsymbol{\eta} - \mathbf{f} \cdot \boldsymbol{N}^g \boldsymbol{\eta}] dV - \int_{\partial\mathscr{V}} \boldsymbol{T} \cdot \boldsymbol{N}^g \boldsymbol{\eta} dA = 0 \qquad \forall \boldsymbol{\eta} \in \mathfrak{V}^{\mathfrak{finite}}, \tag{4.8}$$

or it can be rearranged as [31]:

$$\left\{ \int_{\mathscr{V}} [(\boldsymbol{B}^g)^T \boldsymbol{\sigma} - (\boldsymbol{N}^g)^T \mathbf{f}] dV - \int_{\partial\mathscr{V}} (\boldsymbol{N}^g)^T \boldsymbol{T} dA \right\} \cdot \boldsymbol{\eta} = 0 \qquad \forall \boldsymbol{\eta} \in \mathfrak{V}^{\mathfrak{finite}}. \tag{4.9}$$

Since the above equation is satisfied for all virtual displacements, the term within the curly brackets must vanish. Therefore, following the general equations for equilibrium, the finite element discrete boundary value problem is formulated as followed [31],

$$\mathbf{F}^{int}(\mathbf{u}) - \mathbf{F}^{ext} = \mathbf{0}, \tag{4.10}$$

where, $\mathbf{F}^{ext}$, is external global force vectors and, $\mathbf{F}^{int}$, represents internal force vectors, given as,

$$\mathbf{F}^{int} = \int_{\mathscr{V}} (\boldsymbol{B}^g)^T \boldsymbol{\sigma} dV, \tag{4.11}$$

$$\mathbf{F}^{ext} = \int_{\mathscr{V}} [\boldsymbol{N}^g]^T \mathbf{f} dV + \int_{\partial\mathscr{V}} [\boldsymbol{N}^g]^T \boldsymbol{T} dA, \tag{4.12}$$

Here, $\boldsymbol{\sigma}$, is the stress tensor and, dV, corresponds to global domain. In equation (4.12), $\mathbf{f}$, is body force vector, $\boldsymbol{T}$, is traction force acting on the domain, dA.

In finite element computations, internal and external force vectors (equations (4.11) and (4.12)) are obtained by assembling the element force vectors [31],

$$\mathbf{F}^{int} = \mathop{\mathsf{A}}_{e=1}^{n_{elem}} (\mathbf{F}_e^{int}), \tag{4.13}$$

$$\mathbf{F}^{ext} = \mathop{\mathsf{A}}_{e=1}^{n_{elem}} (\mathbf{F}_e^{ext}). \tag{4.14}$$

In equations (4.13) and (4.14), $\mathbf{F}^{int}$, $\mathbf{F}^{ext}$, are obtained respectively for each element from equations (4.11) and (4.12).

4.2 Finite element model for the linear elastic problems

A simple example of application of the finite element method is given in isotropic linear elasticity, where the stress tensor is a linear function of the strain tensor:

$$\boldsymbol{\sigma} = \boldsymbol{C} : \boldsymbol{\varepsilon}, \tag{4.15}$$

and the fourth order isotropic elasticity tensor has the classical general format [57]:

$$\boldsymbol{C} = 3k\boldsymbol{I}^{vol} + 2\mu\boldsymbol{I}^{dev}, \tag{4.16}$$

where μ and k are, respectively, the shear and bulk modulus. Let the symbols $\hat{\boldsymbol{I}}$ and $\boldsymbol{I}$ designate the second- and fourth-order symmetric identity tensors [57],

$$\hat{I}_{ij} = \delta_{ij},$$
$$I_{ijkl} = \frac{1}{2}(\delta_{ik}\delta_{jl} + \delta_{il}\delta_{jk}).$$

In equation (4.16), $\boldsymbol{I}^{vol}$ and $\boldsymbol{I}^{dev}$ are spherical and deviatoric part of the identity tensor $\hat{\boldsymbol{I}}$, respectively given by [57],

$$\boldsymbol{I}^{vol} \equiv \frac{1}{3}\hat{\boldsymbol{I}} \otimes \hat{\boldsymbol{I}},$$
$$\boldsymbol{I}^{dev} \equiv \boldsymbol{I} - \boldsymbol{I}^{vol}.$$

4.2.1 The finite element equilibrium equation

From the definition of the strain-displacement matrix (see equation (4.4)), it follows that,

$$\boldsymbol{\varepsilon} = \boldsymbol{B}^g\boldsymbol{u}, \tag{4.17}$$

so that, in view of the linear elastic constitutive law for $\boldsymbol{\sigma}$, we have,

$$\boldsymbol{\sigma} = \boldsymbol{C}\boldsymbol{B}^g\boldsymbol{u}. \tag{4.18}$$

With the substitution of the above relation into equation (4.11), the global internal force vector reduces to the following linear function of $\boldsymbol{u}$:

$$\mathrm{F}^{int}(\boldsymbol{u}) = \left[\int_{\mathcal{V}}(\boldsymbol{B}^g)^T\boldsymbol{C}\boldsymbol{B}^g dV\right]\boldsymbol{u}, \tag{4.19}$$

or, equivalently,

$$\mathrm{F}^{int}(\boldsymbol{u}) = \boldsymbol{K}\boldsymbol{u}, \tag{4.20}$$

where $\boldsymbol{K}$ is the global stiffness matrix assembled from element stiffnesses:

$$\mathrm{K} = \mathop{\mathsf{A}}_{e=1}^{n_{elem}} \mathrm{K}^e. \tag{4.21}$$

Finally, with equation (4.20), the discrete boundary value problem defined by the equilibrium equation (4.10) is reduced to the solution of the following linear system of algebraic equations for the global nodal displacement vector $\boldsymbol{u}$:

$$\mathbf{K}\boldsymbol{u} = \mathbf{F}^{ext}. \tag{4.22}$$

4.3 The non-linear incremental finite element procedure

In common path-dependent model (see section 3.5.1), the solution of the constitutive initial value problem for a given set of initial conditions is usually not known for complex strain paths, $\boldsymbol{\varepsilon}(t)$. In context of the non-linear incremental finite element equation, the target is to find the nodal displacement vector, $\mathbf{u}_{n+1}$, at time (pseudo-time), t_{n+1}, such that the incremental finite element equilibrium equation [31],

$$\mathbf{R}(\mathbf{u}_{n+1}) \equiv \mathbf{F}^{int}(\mathbf{u}_{n+1}) - \mathbf{F}^{ext}_{n+1}, \tag{4.23}$$

is satisfied. In equation (4.23),

$$\mathbf{F}^{int}_e = \int_{\mathcal{V}} (\boldsymbol{B}^g)^T \boldsymbol{\sigma}(\boldsymbol{\alpha}_n, \boldsymbol{\varepsilon}(\mathbf{u}_{n+1}))dV, \tag{4.24}$$

$$\mathbf{F}^{ext}_e = \int_{\mathcal{V}^e} [\boldsymbol{N}^g]^T \mathbf{f}_{n+1} dV + \int_{\partial\mathcal{V}^e} [\boldsymbol{N}^g]^T \boldsymbol{T}_{n+1} dA, \tag{4.25}$$

The non-linearity of the incremental constitutive function takes part in the definition of the element internal force vector (equation (4.24)).

In equation (4.24), $\boldsymbol{\sigma}$, represents the stress tensor based on internal variables, $\boldsymbol{\alpha}$, at time, t_n, and strain tensor based on new displacement at time t_{n+1}. Moreover, in equation (4.25), $\boldsymbol{N}$, $\mathbf{f}$, $\boldsymbol{T}$, respectively represent, global shape function, body force and traction force vector acting on relevant domains, dV, dA, at time t_{n+1}, [31].

The loading curve, is often in FE code defined by a load factor, λ_{n+1}, at arbitrary time, t_{n+1}. The proportional loading acting as body force and surface traction are given by using load factor,

$$\mathbf{f}_{n+1} = \lambda_{n+1}\bar{\mathbf{f}}, \tag{4.26}$$

$$\boldsymbol{T}_{n+1} = \lambda_{n+1}\overline{\boldsymbol{T}}. \tag{4.27}$$

In equations (4.26) and (4.27), λ_{n+1}, represents load factor at time, t_{n+1}, and, $\bar{\mathbf{f}}$, $\overline{\boldsymbol{T}}$, are prescribed body force vector and traction force and are constant with respect to time. Therefore the external force can be written in the form of,

$$\mathbf{F}^{ext}_{n+1} = \lambda_{n+1}\overline{\mathbf{F}}^{ext}, \tag{4.28}$$

where, $\overline{\mathbf{F}}^{ext}$, is calculated only once.

4.3.1 The Newton-Raphson method

There exists a range of methods that can be employed in solution of the non-linear set of algebraic equations such as, fixed point iteration, bisection, etc [49]. For solving the incremental non-linear equation (4.23), the most effective method is the Newton-Raphson method. This method is interesting because of its quadratic rate of asymptotic convergence [31].

If k denotes iteration number, then the basic steps of the Newton-Raphson iterative procedure may be summarized in Box 4.1 [49].

```
Starting loop while, $[\|\mathbf{R}^{k+1}_{n+1}\| > \epsilon_{tol}]$, and, $[k < N_{max}]$.
    $\mathbf{K}^{k}_{n+1}\delta\mathbf{u}^{k+1}_{n+1} = -\mathbf{R}^{k}_{n+1}$,
    $\mathbf{u}^{k}_{n+1} + \delta\mathbf{u}^{k+1}_{n+1} \rightarrow \mathbf{u}^{k+1}_{n+1}$,
    Update stress and state-variables
    $\mathbf{F}^{int}_{n+1}(\sigma^{k+1}_{n+1}) - \mathbf{F}^{ext}_{n+1} \rightarrow \mathbf{R}^{k+1}_{n+1}$,
    $k + 1 \rightarrow k$,
End of the loop
```

Box 4.1. The Newton-Raphson iterative procedure.

In Box 4.1, ϵ_{tol}, is the prescribed equilibrium convergence tolerance, N_{max} is maximum number of iteration, $\delta\mathbf{u}$ is incremental displacement, $\mathbf{K}$ represents the global tangent stiffness, $\boldsymbol{\sigma}$ is stress and superscript k and subscript, n, represent iteration number and relevant time, respectively. The method is schematically illustrated in Figure 4.1 [31].

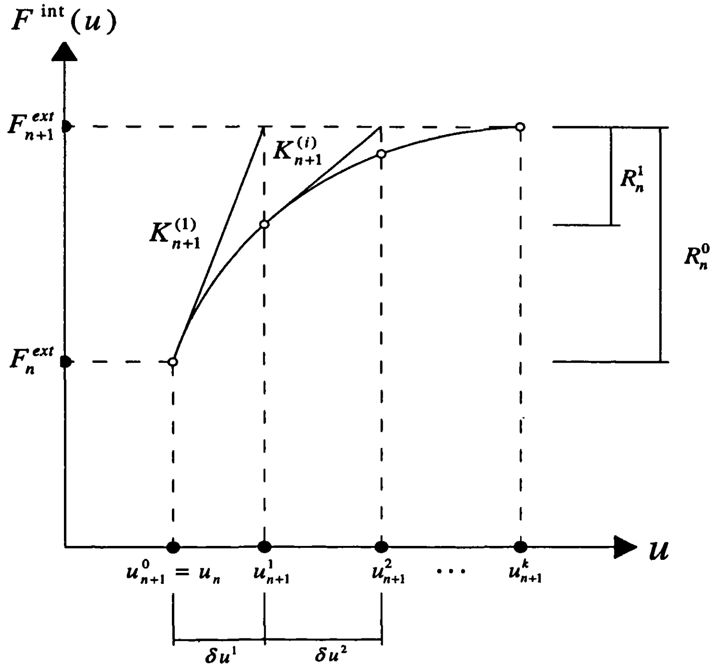

Figure 4.1: The Newton-Raphson algorithm for the incremental finite element equilibrium equation.

As can be seen from Figure 4.1, in time interval, $[t_n, t_{n+1}]$, the procedure is repeated until the convergence is obtained (see Box 4.1).

4.4 Conclusion

In this chapter, the finite element formulations were used to present the discrete form of the boundary value problem in terms of internal forces and external forces. Moreover, discrete form of the linear elastic problems was explained. The non-linear incremental finite element procedure was reviewed for path-dependent materials such as the von Mises elasto-plastic material models.

The Newton-Raphson method was explained as one of the efficient methods for solving the non-linear problems.

Chapter 5

Computational homogenisation

5.1 Introduction

In the first part of this chapter, different types of analytical methods for the effective elastic material properties will be discussed. Among them, the analytical solutions presented by Nemat-Nasser [1] for dilute distribution of cavities/inclusions in the cell, Taylor assumption, Reuss assumption and Hashin and Shtrikman bounds for the effective elastic material properties. In the second part, the computational homogenisation concepts are presented. Among them the formulation at micro-level and the micro- to macro-transition based on the averaging theory are explained in detail. We should emphasize that the first order computational homogenisation is used in the following formulation. Therefore, the effect of second gradient of displacement is not considered in the macro-strain tensor.

The multi-scale technique is used to determine the macroscopic constitutive variables from the solution of the boundary value problem at micro-level. General procedure for this method, can be expressed by [18,27,58,59],

1. Definition of a representative volume element (RVE) at micro-level with known constitutive material models for each constituents.
2. Prescribing the different boundary conditions over the RVE based on the imposed macro-strain.
3. Obtaining the macro-variables from the solution of the micro-structure boundary value problem.

Using homogenisation theory has some advantages, among them we refer to the out standing one in which by using this theory there is no need to define any constitutive material model at macro-level. We should emphasize that although the multi-scale model may be defined as a linear or non-linear problem, for simplicity of the formulation we will present the formula in one of the iterations of the non-linear incremental procedure.

5.2 Analytical solution for a dilute distribution of cavities

This section reviews briefly the analytical methods for porous elastic materials used in the assessment of the computational multi-scale approach. These methods assume that the elastic homogeneous solid contains a dilute distribution of cavities, with typical cavities being sufficiently far apart so that their interaction may be neglected [1]. In addition, a very brief review on the damage theory is provided.

5.2.1 Void volume fraction theory

This method has been throughly discussed by Nemat-Nasser in [1]. It predicts the effective isotropic elastic properties of a porous material in plane strain and plane stress under two basic assumptions: prescribed macro-stress and prescribed macro-strain. Two different cases are considered in the woer of Nemat-Nasser: 1) the elastic solids contains a dilute distribution of cavities; and 2) the cavities are randomly distributed. In the latter case, the approach is based on the so-called self-consistent method which we do not consider it in this study. The range of validity for the two cases is limited to relatively small volume fractions of voids [1]. Since only plane problems are considered, an RVE with unit thickness in the out-of-plane direction is used and all field quantities are assumed to be uniformly distributed throughout the thickness.

Figure 5.1, displays a typical portion of an RVE in a 3-D view. The circular holes for the dilute distribution of cavities are assumed to be far apart. Let n be the number of holes in the RVE and let Ω_i denotes the volume of a typical hole bounded by the surface area $\partial\Omega_i$. The void volume fraction, f, is given by

$$f \equiv \sum_{i=1}^{n} \frac{\Omega_i}{V}, \tag{5.1}$$

with V being the total volume of the RVE.

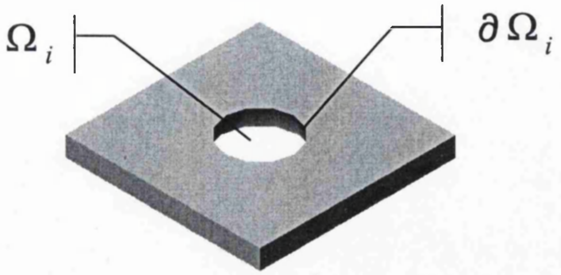

Figure 5.1: 3-D view of a typical portion of an RVE containing microcavities.

Let κ be defined as

$$\kappa = \begin{cases} 3-4\upsilon & For\ plane\ strain, \\ (3-\upsilon)/(1+\upsilon) & For\ plane\ stress, \end{cases} \tag{5.2}$$

where υ is the Poisson's ratio. Under the prescribed macro-stress assumption, the effective shear modulus $\bar{\mu}$ and the effective Poisson ratio $\bar{\upsilon}$ (see equation 5.2), are obtained as,

$$\frac{\bar{\mu}}{\mu} = \{1+f(\kappa+1)\}^{-1} = 1-f(\kappa+1)+O(f^2), \tag{5.3}$$

$$\begin{aligned} \frac{\bar{\kappa}}{\kappa} &= \left\{1+f\frac{2(\kappa+1)}{\kappa}\right\}\{1+f(\kappa+1)\}^{-1} \\ &= 1-f\frac{(\kappa+1)(\kappa-2)}{\kappa}+O(f^2). \end{aligned} \tag{5.4}$$

For plane stress, the effective Young modulus, $\bar{E}$, and Poisson ratio, $\bar{\upsilon}$, are,

$$\frac{\bar{E}}{E} = (1+3f)^{-1} = 1-3f+O(f^2), \tag{5.5}$$

$$\begin{aligned} \frac{\bar{\upsilon}}{\upsilon} &= (1+f\frac{1}{\upsilon})(1+3f)^{-1} \\ &= 1-(3-\frac{1}{\upsilon})f+O(f^2). \end{aligned} \tag{5.6}$$

where $O(.)$ represents the higher order terms of the expansions.

Under the prescribed macro-strain assumption, the effective shear modulus $\bar{\mu}$, and the effective Poisson ratio $\bar{v}$, are given as

$$\frac{\bar{\mu}}{\mu} = 1 - f(\kappa + 1), \tag{5.7}$$

$$\begin{aligned}\frac{\bar{\kappa}}{\kappa} &= \left\{1 - f\frac{(\kappa+1)(\kappa^2 - 2\kappa + 2)}{\kappa(\kappa - 1)}\right\}(1 - f\frac{\kappa+1}{\kappa-1})^{-1}, \\ &= 1 - f\frac{(\kappa+1)(\kappa-2)}{\kappa} + O(f^2),\end{aligned} \tag{5.8}$$

For plane stress conditions, the effective Young modulus, $\bar{E}$, and Poisson ratio, $\bar{v}$, are,

$$\begin{aligned}\frac{\bar{E}}{E} &= (1 - f\frac{4}{1+v})(1 - f\frac{2}{1-v})\left(1 - f\frac{3 - 2v + 3v^2}{1 - v^2}\right)^{-1} \\ &= 1 - 3f + O(f^2),\end{aligned} \tag{5.9}$$

$$\begin{aligned}\frac{\bar{v}}{v} &= \left\{1 + f\frac{1 - 6v + v^2}{v(1 - v^2)}\right\}\left(1 - f\frac{3 - 2v + 3v^2}{1 - v^2}\right)^{-1} \\ &= 1 - (3 - \frac{1}{v})f + O(f^2).\end{aligned} \tag{5.10}$$

5.2.2 Damage theory

A very brief review on this theory is provided in this section and for more details we refer to [36,60]. The phenomenon of damage represents surface discontinuities in the form of micro-cracks, or volume discontinuities in the form of cavities. There are several types of damage measurement. We focused on the measurement at the scale of micro-structure. Measurement at the scale of micro-structure (density of micro-cracks or cavities) leads to microscopic models that can be integrated over the macroscopic volume element with the help of mathematical homogenisation techniques [36]. To use this theory for obtaining the properties of damage in continuum mechanics analysis we need to define damage variable D.

In order to define this variable we need to introduce some relations: Let A be the virgin area of a section of the volume element and A_0 be an area of the void, which is located inside the volume element. We define the effective area as

$$\tilde{A} = A - A_0. \tag{5.11}$$

Figure 5.2, shows the virgin and effective area of the cell.

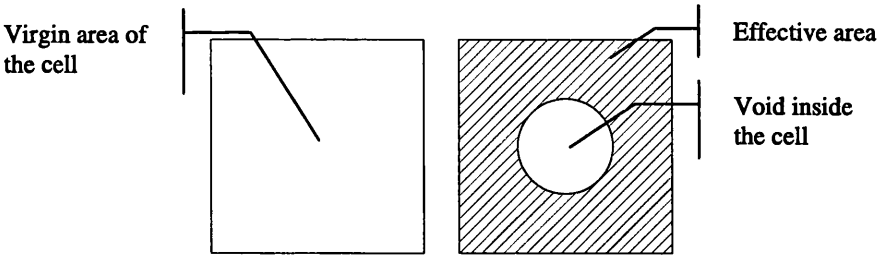

Figure 5.2: Effective area. Defining a void as cavities.

We define Damage variable as

$$D = 1 - \frac{\tilde{A}}{A}. \tag{5.12}$$

It is obvious that $0 \leq D < 1$ characterizes the damaged state. The value $D = 0$ corresponds to the non-damaged or virgin state, and $D = 1$ corresponds to the total loss of load bearing capacity [36, 60]. In addition, we can define the effective Young's modulus by,

$$\bar{E} = E(1 - D). \tag{5.13}$$

The damage theory affects only the value of the Young's modulus.

5.3 Analytical solution for a dilute distribution of micro-inclusions

In this section all analytical methods described by Nemat-Nasser [1] for microstructures with elastic inclusions will be briefly reviewed.

Suppose all micro-inclusions in an RVE are of cylindrical shape (Figure 5.3), or they can be approximated as cylinders. Assume that the matrix and the inclusions are linearly elastic and isotropic, and have the distinct elastic parameters. In order to express the overall elasticity tensor, it suffices to obtain two independent overall elastic moduli as functions of the volume fraction of the inclusions (equation (5.1)) and the elastic moduli of the matrix and the inclusions.

We should emphasize that the present method assumes a dilute distribution of inclusions. The interaction effects are completely neglected [1].

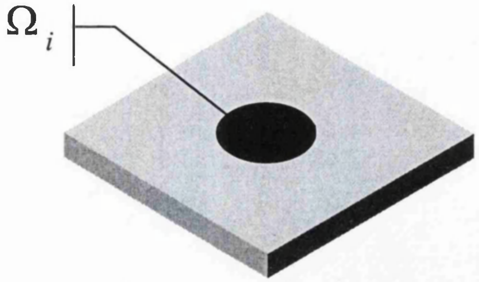

Figure 5.3: 3-D view of the typical portion of an RVE with micro-inclusion.

5.3.1 Dilute distribution of fibres

First consider an RVE, which contains a random and dilute distribution of aligned reinforcing microfibres, and assume that the interaction between neighboring fibres is negligible. In order to estimate the overall elastic parameters of the RVE in plane problems, the concept of the Eshelby tensor, S (this tensor has been proposed by Eshelby for the elasticity problem of an ellipsoidal inclusion embedded in an unbounded matrix loaded uniformly at infinity [61]) for an isolated infinitely long circular cylindrical inclusion embedded in an unbounded homogeneous solid is performed.

The average strain and stress of each fibre can be determined by the uniform strain and stress in an isolated infinitely long circular cylindrical inclusion embedded in an unbounded homogeneous solid which has the matrix elasticity and compliance tensors $\boldsymbol{C}$ and $\boldsymbol{S}$. When the overall stress and strain, $\boldsymbol{\sigma}^0$, $\boldsymbol{\varepsilon}^0$, which satisfy $\boldsymbol{\sigma}^0 = \boldsymbol{C} : \boldsymbol{\varepsilon}^0$ or $\boldsymbol{\varepsilon}^0 = \boldsymbol{S} : \boldsymbol{\sigma}^0$, are prescribed for this unbounded solid, the exact uniform strain and stress in the isolated microfibre can be calculated from the associated Eshelby tensor, $\mathbf{S}^I$. Hence, the average stress and strain of a typical microfibre in the composite, denoted by, $\bar{\boldsymbol{\sigma}}^I$ and $\bar{\boldsymbol{\varepsilon}}^I$, are approximated by [1],

$$\bar{\boldsymbol{\varepsilon}}^I = \mathbf{A}^I : (\mathbf{A}^I - \mathbf{S}^I)^{-1} : \boldsymbol{\varepsilon}^0, \tag{5.14}$$

$$\bar{\boldsymbol{\sigma}}^I = \boldsymbol{C}^I : \mathbf{A}^I : (\mathbf{A}^I - \mathbf{S}^I)^{-1} : \boldsymbol{S} : \boldsymbol{\sigma}^0, \tag{5.15}$$

where, $\mathbf{A}^I$, is the two-dimensional fourth-order tensor,

$$\mathbf{A}^I = (\boldsymbol{C} - \boldsymbol{C}^I)^{-1} : \boldsymbol{C}. \tag{5.16}$$

The overall compliance and elasticity tensors, $\bar{S}$ and $\bar{C}$, are determined from the equations (5.14) and (5.15), when the macro-stress $\bar{\sigma} = \sigma^0$, is prescribed [1],

$$\bar{S} = \{\mathbf{1}^{(4s)} + f(\mathrm{A}^I - \mathrm{S}^I)^{-1}\} : S, \tag{5.17}$$

and when the macro-strain $\bar{\varepsilon} = \varepsilon^0$, is prescribed the overall elasticity tensor is defined by [1],

$$\bar{C} = C : \{\mathbf{1}^{(4s)} - f(\mathrm{A}^I - \mathrm{S}^I)^{-1}\}, \tag{5.18}$$

where, f, is the volume fraction of the microfibres (equation (5.1)), and the two-dimensional fourth-order identity tensor, $(\delta_{ik}\delta_{jl} + \delta_{il}\delta_{jk})/2$, is denoted by $\mathbf{1}^{(4s)}$.

Assume that an isotropic fourth-order tensor can be expressed in terms of two basic isotropic fourth-order tensors in two-dimensions [1]

$$\begin{aligned} E^1_{ijkl} &\equiv \frac{1}{2}\delta_{ij}\delta_{kl}, && (5.19)\\ E^2_{ijkl} &\equiv -\frac{1}{2}\delta_{ij}\delta_{kl} + \frac{1}{2}(\delta_{ik}\delta_{jl} + \delta_{il}\delta_{jk}). && (5.20)\end{aligned}$$

Based on, $\mathbf{E}^1$ and $\mathbf{E}^2$, the tensorial equation (5.17) can be reduced to,

$$\begin{aligned} \frac{1}{3\bar{K}'}\mathbf{E}^1 + \frac{1}{2\bar{\mu}}\mathbf{E}^2 &= \frac{1}{3K'}\{1 + f(\frac{K'}{K' - K'^I} - s_1)^{-1}\}\mathbf{E}^1 + \\ &\quad \frac{1}{2\mu}\{1 + f(\frac{\mu}{\mu - \mu^I} - s_2)^{-1}\}\mathbf{E}^2, \end{aligned} \tag{5.21}$$

and equation (5.18) becomes,

$$\begin{aligned} 3\bar{K}'\mathbf{E}^1 + 2\bar{\mu}\mathbf{E}^2 &= 3K'\{1 - f(\frac{K'}{K' - K'^I} - s_1)^{-1}\}\mathbf{E}^1 + \\ &\quad 2\mu\{1 - f(\frac{\mu}{\mu - \mu^I} - s_2)^{-1}\}\mathbf{E}^2, \end{aligned} \tag{5.22}$$

where, $s_1 = \frac{2}{1+\kappa}$, $s_2 = \frac{\kappa}{1+\kappa}$ and κ, is defined in equation (5.2). Here K', and K'^I, are defined by [1],

$$\frac{1}{3K'} \equiv \begin{cases} (1 - v - 2v^2)/E & For\ plane\ strain, \\ (1 - v)/E & For\ plane\ stress, \end{cases} \tag{5.23}$$

$$\frac{1}{3K'^I} \equiv \begin{cases} (1 - v^I - 2(v^I)^2)/E^I & For\ plane\ strain, \\ (1 - v^I)/E^I & For\ plane\ stress. \end{cases} \tag{5.24}$$

Therefore, the overall elastic moduli K', and overall shear moduli $\bar{\mu}$, are obtained, when $\bar{\sigma} = \sigma^0$ is prescribed as [1],

$$\begin{aligned}\frac{\bar{K}'}{K'} &= \left\{1 + f\left(\frac{K'}{K' - K'^I} - s_1\right)^{-1}\right\}^{-1} \\ &= 1 - f\left(\frac{K'}{K' - K'^I} - s_1\right)^{-1} + O(f^2),\end{aligned} \tag{5.25}$$

$$\begin{aligned}\frac{\bar{\mu}}{\mu} &= \left\{1 + f\left(\frac{\mu}{\mu - \mu^I} - s_2\right)^{-1}\right\}^{-1} \\ &= 1 - f\left(\frac{\mu}{\mu - \mu^I} - s_2\right)^{-1} + O(f^2),\end{aligned} \tag{5.26}$$

and when $\bar{\varepsilon} = \varepsilon^0$ is prescribed as [1],

$$\frac{\bar{K}'}{K'} = 1 - f\left(\frac{K'}{K' - K'^I} - s_1\right)^{-1}, \tag{5.27}$$

$$\frac{\bar{\mu}}{\mu} = 1 - f\left(\frac{\mu}{\mu - \mu^I} - s_2\right)^{-1}. \tag{5.28}$$

5.4 Taylor assumption

In the Taylor (or Voigt) assumption [62, 63], it is assumed that different material phases in a local mixture, share the same history of the imposed macro-strain, $\dot{\bar{\varepsilon}} = \dot{\varepsilon}_{fibre} = \dot{\varepsilon}_{matrix}$. This assumption is used to achieve a rough estimate for the upper boundary of the effective material properties. The only constraint in this assumption is based on the summation of the direct effect of the volume fraction of the different material phases inside the unit cell.

If we assume that M_i is one of the material properties for material phase i with volume fraction equal to f_i and we have n different phases inside the unit cell, the effective material properties based on the Taylor assumption could be expressed by [64],

$$\bar{M}_{eff} = \sum_{i=1}^{n} f_i M_i.$$

5.5 Reuss assumption

In contrast to the Taylor assumption in the Reuss assumption it is assumed that different material phases at a fixed point, satisfy the uniform stress requirements [65], $\bar{\sigma} = \sigma_{fibre} = \sigma_{matrix}$. This assumption is used to achieve a rough estimate for the lower boundary of the effective material properties. The only constraint in this assumption is based on the summation of the inverse effect of the volume fraction of the different material phases inside the unit cell.

If we assume that M_i is one of the material properties for material phase i with volume fraction equal to f_i and we have n different phases inside the unit cell, the effective material properties based on the Reuss assumption could be expressed by [64]

$$\bar{M}_{eff} = \left(\sum_{i=1}^{n} \frac{f_i}{M_i}\right)^{-1}.$$

5.6 Hashin and Shtrikman bounds

As pointed out by Hill [66], neither Taylor nor Reuss assumptions are correct. The tractions at the interfaces are not in equilibrium under the Taylor condition; the interface could not remain bonded under the Reuss condition. The effective material properties could be obtained from the Taylor assumption only when the Poisson's ratio of the different phases is the same.

The Taylor and Reuss bounds are relatively wide apart, and modifications have accordingly been proposed by many researchers such as Hashin and Shtrikman [12]. Their model has received wide attention.

Hashin and Shtrikman treated the system containing one particulate phase and one continuous matrix phase. They employed the 'minimum energy' principle and introduced bounds of the bulk modulus, K and shear modulus, G as [12],

$$\begin{aligned} K^L_{eff} &= K_m + \frac{f_p}{\frac{1}{K_p - K_m} + \frac{3f_m}{3K_m + 4G_m}}, \\ K^U_{eff} &= K_p + \frac{f_m}{\frac{1}{K_m - K_p} + \frac{3f_p}{3K_p + 4G_p}}, \end{aligned}$$

$$
\begin{aligned}
G^L_{eff} &= G_m + \frac{f_p}{\frac{1}{G_p - G_m} + \frac{6(K_m + 2G_m) f_m}{5G_m(3K_m + 4G_m)}}, \\
G^U_{eff} &= G_p + \frac{f_m}{\frac{1}{G_m - G_p} + \frac{6(K_p + 2G_p) f_p}{5G_p(3K_p + 4G_p)}},
\end{aligned}
$$

The superscripts U and L denote, upper and lower bounds and the subscripts m and p denote, matrix and particle, respectively.

5.7 Homogenisation procedure

Homogenisation procedure is used to determine the effective properties of structures with micro-structural heterogeneities like inclusions or voids at smaller microscopic length scales. The micro-structures define representative volumes of linear and non-linear heterogeneous materials such as inelastic composites, polycrystalline aggregates or particle assemblies. The definition of an overall macroscopic response of a heterogeneous material with complex micro-structure in an averaged or homogenised sense is often referred to micro-to-macro transition.

5.7.1 Multi-scale analysis and Representative Volume Element (RVE)

Hierarchical multi-scale modelling, differentiating between regions requiring different resolutions, is becoming a progressively more useful tool for modelling deformation and damage in heterogeneous materials. Sub-structuring in these models enables pure macroscopic analysis in some parts of the domain using homogenised or effective material properties and changing the scale to the microscopic modelling at a different scale in other regions of the domain [18].

The multi-scale model may be categorized into two essential levels:

1. Purely macroscopic domain (level-1), with homogenised material parameters.

2. Purely microscopic domain (level-2), where the RVE exists and extended micro-structural regions with spatial distribution of heterogeneities needs to be modelled.

Figure 5.4 is a schematic representation of the above cited levels.

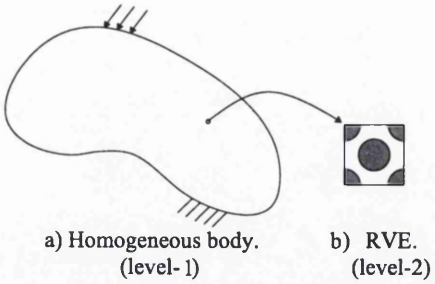

Figure 5.4: Schematic representation of the multi-scale levels.

The domain of the RVE is assumed to consist in general of a solid part, Ω^s, and a void part, Ω^v, (see Figure 5.5)

$$\Omega = \Omega^s \cup \Omega^v.$$

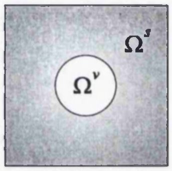

Figure 5.5: Schematic representation of different parts of RVE.

For simplicity, in this research we consider only RVEs whose void part does not intersect the RVE boundary,

$$\Omega \cap \Omega^v = \emptyset.$$

5.7.2 Homogenisation and Localization

For introducing the concept of homogenisation, first, we will have a brief review of some fundamental concepts in this area. According to overall properties of highly heterogeneous medium, as cited in previous section, two different scales are concerned: the macroscopic scale (with coordinate, $\mathbf{x}$) at which the size of the heterogeneities is very small, and the so-called 'microscopic' scale (with coordinate, $\mathbf{y}$), of dimensions of the order of the heterogeneities. For example, in the homogenisation theory of periodic media, the RVE is the unit cell, which generates the complete structure of the composite by periodicity. Figure 5.6, is a schematic representation of macro-structure with periodic micro-structure.

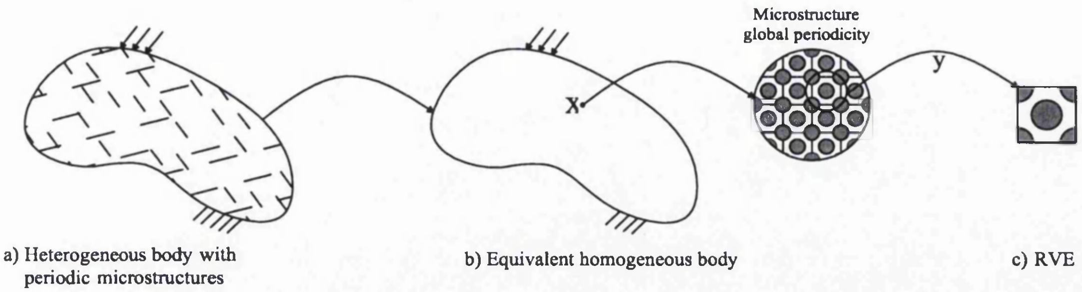

Figure 5.6: Schematic representation of macro-structure with periodic micro-structure.

At a macroscopic point $\mathbf{x}$ of the macro-continuum we must consider two different groups of variables:

1. The macroscopic variables, which stand in the homogeneous body.
2. The microscopic variables defined over the entire domain of the RVE.

In the approach followed in this thesis the essential assumption underlying the relationship between macro- and micro-variables is the volume averaging of the strain and stress tensors with $\bar{\boldsymbol{\sigma}}$ and $\bar{\boldsymbol{\varepsilon}}$ denoting, respectively, the macro-stress and strain fields.

$$\bar{\sigma}_{ij} = \frac{1}{\mid V \mid} \int_V \sigma_{ij} dV = \langle \sigma_{ij} \rangle, \tag{5.29}$$

$$\bar{\varepsilon}_{ij} = \frac{1}{\mid V \mid} \int_V \varepsilon_{ij}(\mathbf{u}) dV = \langle \varepsilon_{ij}(\mathbf{u}) \rangle, \tag{5.30}$$

in which, $\mid V \mid = \int_V dV$, is a domain that is defined over the RVE and, $\langle \cdot \rangle = \frac{1}{V} \int_V \cdot \, dV$, stands for the averaging operator. Moreover, all the mechanical quantities are usually assumed to be additive functions and are averaged when proceeding from the microscopic level to the macroscopic one [15]. The procedure that relates mechanical quantities like stress and strain and the micro constitutive laws to macroscopic quantities by averaging equations (5.29)-(5.30) is termed *homogenisation*, $\boldsymbol{\sigma}(\mathbf{y}), \boldsymbol{\varepsilon}(\mathbf{y}) \rightarrow \bar{\boldsymbol{\sigma}},\ \bar{\boldsymbol{\varepsilon}}$. The inverse procedure is termed *localization*, that is amounts to a micromechanics problem, which permits to determine microscopic quantities, $\bar{\boldsymbol{\sigma}},\ \bar{\boldsymbol{\varepsilon}} \rightarrow \boldsymbol{\sigma}(\mathbf{y}),\ \boldsymbol{\varepsilon}(\mathbf{y})$ [15], where $\boldsymbol{\sigma}$ and $\boldsymbol{\varepsilon}$ are the micro-stress and strain fields defined over the RVE.

Equation (5.29) can be written in another form,

$$\bar{\sigma}(\boldsymbol{x},t) = \frac{1}{V}\int_{\Omega}\sigma(\boldsymbol{y},t)dV = \frac{1}{V}\int_{\Omega^s}\sigma(\boldsymbol{y},t)dV + \frac{1}{V}\int_{\Omega^v}\sigma(\boldsymbol{y},t)dV. \qquad (5.31)$$

By using the integration by parts formula [67],

$$\int_{\Omega}\boldsymbol{S}(\nabla\boldsymbol{v})^T dV = \int_{\partial\Omega}(\boldsymbol{S}\boldsymbol{n})\otimes\boldsymbol{v}dA - \int_{\Omega}(div\boldsymbol{S})\otimes\boldsymbol{v}dV, \qquad (5.32)$$

and with the replacement of $\boldsymbol{S}$ with $\boldsymbol{\sigma}$, $\boldsymbol{v}$ with $\boldsymbol{y}$ and combined with identity $\nabla\boldsymbol{y} = \boldsymbol{I}$, we can rewrite the equation (5.31) to the new form,

$$\begin{aligned}\int_{\Omega}\boldsymbol{\sigma}dV &= \int_{\Omega^s}\boldsymbol{\sigma}dV + \int_{\Omega^v}\boldsymbol{\sigma}dV \\ &= \int_{\partial\Omega}(\boldsymbol{\sigma}\boldsymbol{n})\otimes\boldsymbol{y}dA - \int_{\Omega^s}(div\boldsymbol{\sigma})\otimes\boldsymbol{y}dV - \\ &\quad \int_{\Omega^v}(div\boldsymbol{\sigma})\otimes\boldsymbol{y}dV + \int_{\partial\Omega^v}[\boldsymbol{\sigma}\boldsymbol{n}]\otimes\boldsymbol{y}dA, \qquad (5.33)\end{aligned}$$

where $[\boldsymbol{\sigma}\boldsymbol{n}]$, denotes the jump of vector field $\boldsymbol{\sigma}\boldsymbol{n}$ across the solid-void interface, $\partial\Omega^v$.

5.7.3 Minimum RVE kinematical constraints

Equation (5.30) naturally places a constraint on the possible displacement field of the RVE. That is, only fields $\boldsymbol{u}$ that satisfy Equation (5.30), can be said to be kinematically admissible. The necessary condition for a micro-displacement field $\boldsymbol{u}$ to be kinematically admissible is,

$$\boldsymbol{u} \in \mathscr{K}^*,$$

where the minimally constrained set of kinematically admissible microscopic displacements, $\mathscr{K}^*$, is defined by [41],

$$\mathscr{K}^* \equiv \left\{\boldsymbol{v}, \text{sufficiently regular} \,\middle|\, \int_{\Omega}\nabla^s\boldsymbol{v}dV = V\bar{\boldsymbol{\varepsilon}}\right\} \qquad (5.34)$$

In domain (5.34), sufficiently regular fields refers to the functional fields that all operations in the present context make sense.

An equivalent expression for the above constraint can be obtained in terms of RVE boundary displacements. By definition of integration by part for the general tensor form (see equation (5.32)) and by specialising the cited formula and identifying the generic tensor $\boldsymbol{S}$ with $\boldsymbol{I}$, the vector field $\boldsymbol{v}$ with $\boldsymbol{u}$ and the domains with the RVEs domains, in the absence of voids ($\Omega^v = \emptyset$), equation (5.34) can be written as [41],

$$\bar{\boldsymbol{\varepsilon}} = \frac{1}{V}\int_{\partial\Omega} \boldsymbol{u} \otimes_s \boldsymbol{n} dA. \tag{5.35}$$

where the definition of symmetry tensor product for any arbitrary vector field is given by,

$$\boldsymbol{u} \otimes_s \boldsymbol{v} \equiv \frac{1}{2}(\boldsymbol{u} \otimes \boldsymbol{v} + \boldsymbol{v} \otimes \boldsymbol{u}),$$

and $\partial\Omega$ presents the boundary for the RVE (see Figure 5.5).

In the presence of voids ($\Omega^v \neq \emptyset$), when the strain is not defined in the sub domain $\Omega^v \subset \Omega$, constraint (5.34) is generalized as,

$$\begin{aligned} V\bar{\boldsymbol{\varepsilon}} &= \int_{\partial\Omega^s} \boldsymbol{u} \otimes_s \boldsymbol{n}^s dA + \int_{\partial\Omega^v} \boldsymbol{u} \otimes_s \boldsymbol{n}^v dA \\ &= \int_{\partial\Omega} \boldsymbol{u} \otimes_s \boldsymbol{n}^s dA + \int_{\partial\Omega^s \cap \partial\Omega^v} \boldsymbol{u} \otimes_s \boldsymbol{n}^s dA + \int_{\partial\Omega^v \cap \partial\Omega^s} \boldsymbol{u} \otimes_s \boldsymbol{n}^v dA, \end{aligned} \tag{5.36}$$

where $\boldsymbol{n}^s$ and $\boldsymbol{n}^v$ are, respectively, the outward unit normals to the solid and void domains at their boundaries. From Figure 5.5, by observing that $\boldsymbol{n}^s = -\boldsymbol{n}^v$ at the intersection $\partial\Omega^s \cap \partial\Omega^v$, it can be concluded that in equation (5.36) the two last integrals on the right hand side of equation cancel each other so that the generalized expression (5.36) recovers equation (5.35). An alternative for the expression (5.34) is [41],

$$\mathscr{K}^* \equiv \left\{ \boldsymbol{v}, \text{sufficiently regular} \,\middle|\, \int_{\partial\Omega} \boldsymbol{v} \otimes_s \boldsymbol{n} dA = V\bar{\boldsymbol{\varepsilon}} \right\} \tag{5.37}$$

5.7.4 Additive split of the microscopic displacement

Any microscopic displacement field, $\boldsymbol{u}$ may be split into [41],

$$\boldsymbol{u}(\boldsymbol{y},t) = \bar{\boldsymbol{\varepsilon}}(\boldsymbol{x},t)\boldsymbol{y} + \tilde{\boldsymbol{u}}(\boldsymbol{y},t), \tag{5.38}$$

which is a sum of a linear displacement $\bar{\boldsymbol{\varepsilon}}\boldsymbol{y}$, (varies linearly in $\boldsymbol{y}$), and a displacement fluctuation, $\tilde{\boldsymbol{u}}$. Accordingly, the microscopic strain field is decomposed into,

$$\boldsymbol{\varepsilon}(\boldsymbol{y},t) = \bar{\boldsymbol{\varepsilon}}(\boldsymbol{x},t) + \tilde{\boldsymbol{\varepsilon}}(\boldsymbol{y},t), \tag{5.39}$$

a sum of a homogeneous strain (constant in $\boldsymbol{y}$) which is the same as macroscopic strain, $\bar{\boldsymbol{\varepsilon}}$, and a strain fluctuation field [41],

$$\tilde{\boldsymbol{\varepsilon}} = \nabla^s \tilde{\boldsymbol{u}}, \tag{5.40}$$

that generally varies in $\boldsymbol{y}$. From equation (5.38) and with regard to the constraint (5.37), it can be concluded that any kinematically admissible displacement fluctuation, $\tilde{\boldsymbol{u}}$, satisfies,

$$\tilde{\boldsymbol{u}} \in \tilde{\mathscr{K}}^*, \tag{5.41}$$

where [41],

$$\tilde{\mathscr{K}}^* \equiv \left\{ \boldsymbol{v}, \text{sufficiently regular} \,\middle|\, \int_{\partial\Omega} \boldsymbol{v} \otimes_s \boldsymbol{n} dA = \boldsymbol{0} \right\}, \tag{5.42}$$

is the minimally constrained set of kinematically admissible displacement fluctuations of the RVE. This constraint will be used in one of the classical boundary conditions over the micro cell.

To show that the integral of the obtained tensor from the symmetric tensor product in equation (5.42) is equal to zero, recall (5.34) and equation (5.30). As a result, the overall strain tensor is defined by,

$$\bar{\boldsymbol{\varepsilon}} = \frac{1}{V} \int_\Omega \nabla^s \boldsymbol{u} dV. \tag{5.43}$$

From the additive split of the microscopic displacement (see equation (5.38)), the above equation can be written as,

$$\bar{\boldsymbol{\varepsilon}} = \frac{1}{V} \int_\Omega \nabla^s (\bar{\boldsymbol{u}} + \tilde{\boldsymbol{u}}) \, dV = \frac{1}{V} \int_\Omega \nabla^s (\bar{\boldsymbol{u}}) \, dV + \frac{1}{V} \int_\Omega \nabla^s (\tilde{\boldsymbol{u}}) \, dV. \tag{5.44}$$

In equation (5.44), the gradient of macro-displacement, $\bar{\boldsymbol{u}}$, is equal to macro strain, $\bar{\boldsymbol{\varepsilon}}$, and the integral over the volume will be canceled by the volume averaging. As a result,

$$\frac{1}{V} \int_\Omega \nabla^s (\tilde{\boldsymbol{u}}) \, dV = 0. \tag{5.45}$$

Equation (5.45) can be rewritten by Green's formula as,

$$\frac{1}{V}\int_{\partial\Omega} \tilde{\boldsymbol{u}} \otimes_s \boldsymbol{n} dA = 0. \tag{5.46}$$

Assume that $\tilde{\mathscr{K}}$ is a subspace of vector space $\tilde{\mathscr{K}}^*$,

$$\tilde{\mathscr{K}} \subset \tilde{\mathscr{K}}^*.$$

Accordingly, for a given macroscopic strain $\bar{\boldsymbol{\varepsilon}}$, the set $\mathscr{K}$, is the translation of space $\tilde{\mathscr{K}}$ given by [41],

$$\mathscr{K} = \left\{ \boldsymbol{u} = \bar{\boldsymbol{\varepsilon}}\boldsymbol{y} + \tilde{\boldsymbol{u}} \,\middle|\, \tilde{\boldsymbol{u}} \in \tilde{\mathscr{K}} \right\} \tag{5.47}$$

By definition, the space of virtual displacements in solid mechanics is the set of all variations of kinematically admissible displacement fields of the problem in question. Here $\mathscr{V}$ denotes the space of virtual displacements at micro-cell and is defined by,

$$\mathscr{V} \equiv \left\{ \boldsymbol{\eta} = \boldsymbol{v}_1 - \boldsymbol{v}_2 \,|\, \boldsymbol{v}_1, \boldsymbol{v}_2 \in \mathscr{K} \right\}. \tag{5.48}$$

From the definition of translation space and the space of virtual displacement at micro-level (constraint (5.48)) we can write,

$$\begin{aligned} \boldsymbol{v}_1 &= \bar{\boldsymbol{\varepsilon}}\boldsymbol{y} + \tilde{\boldsymbol{v}}_1 \\ \boldsymbol{v}_2 &= \bar{\boldsymbol{\varepsilon}}\boldsymbol{y} + \tilde{\boldsymbol{v}}_2. \end{aligned} \tag{5.49}$$

By subtracting $\boldsymbol{v}_1$ and $\boldsymbol{v}_2$, from equation (5.49), we have,

$$\boldsymbol{\eta} = \tilde{\boldsymbol{v}}_1 - \tilde{\boldsymbol{v}}_2. \tag{5.50}$$

The space of virtual displacement at micro-level (constraint (5.48)) can be expressed as,

$$\mathscr{V} = \tilde{\mathscr{K}}. \tag{5.51}$$

The same arguments applied to the rate form of additive split of the micro-displacements,

$$\dot{\boldsymbol{u}} = \dot{\boldsymbol{\varepsilon}} \boldsymbol{y} + \dot{\tilde{\boldsymbol{u}}}. \tag{5.52}$$

By using the same procedure (5.48)-(5.51) for the rate of the micro-displacements (velocity), we can show that any kinematically admissible fluctuation velocity, $\dot{\tilde{\boldsymbol{u}}}$, satisfies,

$$\dot{\tilde{\boldsymbol{u}}} \in \mathscr{V}$$

5.7.5 Formulation of the two-scale boundary value problem

In this section, based on the previous section, we present only the results, which are obtained for the micro-and macro-scale principal equations, while the detailed formulations are given in [15,18,19,30]. First the principal of virtual work (see section 2.3) is considered to show the RVE is in equilibrium if and only if the variational equation [41],

$$\int_{\Omega} \boldsymbol{\sigma}(\boldsymbol{y},t) : \nabla^s \boldsymbol{\eta} dV - \int_{\Omega} \mathrm{f}(\boldsymbol{y},t) \cdot \boldsymbol{\eta} dV - \int_{\partial\Omega} \boldsymbol{T}(\boldsymbol{y},t) \cdot \boldsymbol{\eta} dA = 0 \qquad \forall \boldsymbol{\eta} \in \mathscr{V}, \tag{5.53}$$

holds at each t.

For sufficiently regular fields $\boldsymbol{\sigma}$, the variational equations of equilibrium (5.53), for the void and solid parts of the RVE, can be equivalently written in differential form as,

$$\begin{cases} div\boldsymbol{\sigma}(\boldsymbol{y},t) = \mathrm{f}(\boldsymbol{y},t) & \forall \boldsymbol{y} \in \Omega^s, \\ div\boldsymbol{\sigma}(\boldsymbol{y},t) = \mathrm{f}(\boldsymbol{y},t) & \forall \boldsymbol{y} \in \Omega^v, \\ \boldsymbol{\sigma}(\boldsymbol{y},t)\boldsymbol{n} = \boldsymbol{T}(\boldsymbol{y},t) & \forall \boldsymbol{y} \in \partial\Omega, \\ [\boldsymbol{\sigma}(\boldsymbol{y},t)\boldsymbol{n}] = 0 & \forall \boldsymbol{y} \in \partial\Omega^v, \end{cases} \tag{5.54}$$

The equations (5.54) are called *the strong form of equilibrium* over the RVE at micro-level.

The average stress (equation (5.33)) can be expressed in terms of boundary traction and body force with introducing the strong form of equilibrium equation, (equation (5.54)), as,

$$\bar{\sigma}(\boldsymbol{x},t)=\frac{1}{V}\left[\int_{\partial\Omega}\boldsymbol{T}(\boldsymbol{y},t)\otimes_s\boldsymbol{y}dA-\int_{\Omega^s}\mathrm{f}(\boldsymbol{y},t)\otimes_s\boldsymbol{y}dV\right], \tag{5.55}$$

The micro-scale boundary value problem for a unit cell yields the following variation forms [30]: Find, $\mathbf{u}(\boldsymbol{y})\in\mathscr{V}^{micro}$, such that:

$$\begin{aligned}\int_{\Omega}\nabla\boldsymbol{\eta}:\boldsymbol{\sigma}dv &= 0, \qquad \forall\boldsymbol{\eta}\in\mathscr{V}^{micro},\\ \boldsymbol{\sigma} &= \frac{\partial\psi}{\partial\boldsymbol{\varepsilon}},\\ \boldsymbol{\varepsilon} &= \nabla\bar{\boldsymbol{u}}(\mathrm{x})+\nabla\tilde{\boldsymbol{u}},\end{aligned} \tag{5.56}$$

where, the first equation in (5.56) is the part of the equilibrium condition for the RVE in absence of body force and external traction acting on the boundary of void in RVE. The solution for, $\mathbf{u}(\boldsymbol{y})$, is expressed by [30],

$$\boldsymbol{u}=\nabla\bar{\boldsymbol{u}}(\mathrm{x}).\boldsymbol{y}+\tilde{\boldsymbol{u}}. \tag{5.57}$$

On the other hand, the macro-scale problem is given as follows:

Find, $\mathbf{u}(\boldsymbol{x})\in\mathscr{U}$, such that:

$$\begin{aligned}\int_{\mathscr{V}}\bar{\sigma}:\nabla\eta dV &= \int_{\mathscr{V}}\mathrm{f}.\eta dV+\int_{\partial\mathscr{V}}\mathrm{T}.\eta dA, \qquad \forall\eta\in\mathscr{V}^{macro},\\ \bar{\sigma} &= \frac{1}{\mid V\mid}\int_{\Omega}\sigma dV,\\ \bar{\varepsilon} &= \frac{1}{\mid V\mid}\int_{\Omega}\varepsilon dV=\nabla\bar{\boldsymbol{u}},\end{aligned} \tag{5.58}$$

where, $\mathscr{U}$, is the space of admissible macroscopic displacement vectors and, $\mathscr{V}^{macro}$, is the space of admissible variational macroscopic displacement.

Finally, the two-scale boundary value problem for the elasto-plastic body is defined as follows:

Find the set of macroscopic state variables,

$$\mathcal{X}^{macro}:=\Big\{\mathrm{u}(\boldsymbol{x}),\bar{\sigma}(\boldsymbol{x}),\bar{\varepsilon}(\boldsymbol{x})\Big\}, \tag{5.59}$$

that satisfies the macro-scale boundary value problems equations (5.58), so that the set of microscopic variables,

$$\mathcal{X}^{micro}:=\Big\{\mathrm{u}(\boldsymbol{y}),\varepsilon(\boldsymbol{y}),\varepsilon^{p}(\boldsymbol{y}),\sigma(\boldsymbol{y}),\boldsymbol{\alpha}(\boldsymbol{y}),\gamma(\boldsymbol{y})\Big\}, \tag{5.60}$$

would satisfy the set of governing equations (5.56), at the micro-scale [30]. Note that, the macro-scale material model is embedded in the average relationship and each micro structural response plays a role of constitutive laws.

5.7.6 The Hill-Mandel principle of macro-homogeneity

The Hill-Mandel principle of macro-homogeneity [6], implies that macroscopic stress power must be equal to the volume average of the microscopic stress power over the RVE corresponding to the macroscopic point. Therefore, for any state of the RVE which characterized by a stress field $\boldsymbol{\sigma}$ is in equilibrium, we have,

$$\bar{\boldsymbol{\sigma}} : \dot{\bar{\boldsymbol{\varepsilon}}} = \frac{1}{V}\int_{\Omega} \boldsymbol{\sigma} : \dot{\boldsymbol{\varepsilon}} dV. \tag{5.61}$$

The identity (5.61) must hold for any kinematically admissible microscopic strain rate field, $\dot{\boldsymbol{\varepsilon}}$ (see equation (5.39)). The Hill-Mandel principle holds if and only if the virtual work of the external surface traction $\boldsymbol{T}$, and body force field, $\mathbf{f}$, of the RVE vanish. Therefore, the Hill-Mandel principle is equivalent to the following variational equations,

$$\int_{\partial\Omega} \boldsymbol{T} \cdot \boldsymbol{\eta} dA = 0, \qquad \int_{\Omega^s} \mathbf{f} \cdot \boldsymbol{\eta} dV = 0 \qquad \forall \boldsymbol{\eta} \in \mathscr{V}. \tag{5.62}$$

The constraints (5.62) could be proved as follows: By having the equations (5.39) and (5.40) and replacing them into the equation (5.61) we obtain,

$$\frac{1}{V}\int_{\Omega} \boldsymbol{\sigma} : \dot{\boldsymbol{\varepsilon}} dV = \frac{1}{V}\int_{\Omega} \boldsymbol{\sigma} : (\dot{\boldsymbol{\varepsilon}} + \nabla^s \dot{\tilde{\boldsymbol{u}}}) dV \tag{5.63}$$

$$= \bar{\boldsymbol{\sigma}} : \dot{\bar{\boldsymbol{\varepsilon}}} + \frac{1}{V}\int_{\Omega} \boldsymbol{\sigma} : \nabla^s \dot{\tilde{\boldsymbol{u}}} dV. \tag{5.64}$$

Hence, identity (5.61) hold if and only if [41],

$$\int_{\Omega} \boldsymbol{\sigma} : \nabla^s \dot{\tilde{\boldsymbol{u}}} dV = 0 \qquad \forall \dot{\tilde{\boldsymbol{u}}} \in \mathscr{V}. \tag{5.65}$$

By using the integration by part formula (5.32) into the equation (5.65) and in the presence of voids, we obtain,

$$\int_{\Omega} \boldsymbol{\sigma} : \nabla^s \dot{\tilde{\boldsymbol{u}}} dV = \int_{\partial\Omega} \boldsymbol{\sigma n} \cdot \dot{\tilde{\boldsymbol{u}}} dA - \int_{\Omega^s} (div \boldsymbol{\sigma}) \cdot \dot{\tilde{\boldsymbol{u}}} dV$$

$$- \int_{\Omega^v} (div \boldsymbol{\sigma}) \cdot \dot{\tilde{\boldsymbol{u}}} dV + \int_{\partial\Omega^v} [\boldsymbol{\sigma n}] \cdot \dot{\tilde{\boldsymbol{u}}} dA. \tag{5.66}$$

From the strong equilibrium equations (5.54), and in the absence of body force acting on the void section of the RVE [41],

$$\mathbf{f}(\boldsymbol{y}, t) = 0 \qquad \forall \boldsymbol{y} \in \Omega^v,$$

equation (5.66) can be written in condensed form as,

$$\int_{\Omega} \boldsymbol{\sigma} : \nabla^s \dot{\tilde{\boldsymbol{u}}} dV = \int_{\partial\Omega} \boldsymbol{T} \cdot \dot{\tilde{\boldsymbol{u}}} dA - \int_{\Omega^s} \mathbf{f} \cdot \dot{\tilde{\boldsymbol{u}}} dV. \tag{5.67}$$

Thus, from equation (5.65) and equation (5.67), the Hill-Mandel principle is equivalent to the following variational equation [41]:

$$\int_{\partial\Omega} \boldsymbol{T} \cdot \dot{\tilde{\boldsymbol{u}}} dA - \int_{\Omega^s} \mathbf{f} \cdot \dot{\tilde{\boldsymbol{u}}} dV = 0 \qquad \forall \dot{\tilde{\boldsymbol{u}}} \in \mathscr{V}. \tag{5.68}$$

The above equation holds if and only if each of its integrals vanish individually. Hence, the constraint (5.62) is proved.

5.8 Kinematic assumptions at micro-scale

The imposition of the macroscopic strain $\bar{\varepsilon}$ on the micro-cell (RVE) can be done by means of different kinematic assumptions. The simplest hypothesis is to assume that all the micro structural constituents undergo a constant deformation identical to the macroscopic one. This commonly referred to as the Taylor assumption which is an extension of Voigt [62] method to crystal plasticity [63]. Another common strategy is to assume a uniform stress over the RVE which indeed is equal to the macro-stress [64, 65]. This is called the Reuss assumption. The Taylor assumption provides an upper bound to the overall stiffness, while the Reuss assumption provides a lower bound. Classically four types of conditions are used to solve the problem at micro-level: prescribed uniform deformation (or the Taylor) assumption, the linear boundary displacement condition, the periodic boundary displacement fluctuations condition and anti-periodic tractions on the boundary, and the uniform boundary traction assumption .

Figure 5.7, illustrates RVE's deformed configurations (with exaggerated deformation) for three cited boundary conditions. Before explaining the different boundary conditions at micro-level, the microscopic constitutive response and equilibrium are reviewed.

By using the axiom of constitutive determinism (see 3.1) in micro-equilibrium equation (5.53), the equilibrium problem can be stated in terms of the displacement fluctuation field as follows: Find $\tilde{\boldsymbol{u}} \in \mathscr{V}$ such that, for each t,

$$\int_{\Omega^s} \mathfrak{F}\{[\bar{\varepsilon}(\boldsymbol{x}, t) + \nabla^s \tilde{\boldsymbol{u}}(\boldsymbol{y}, t)]^t\} : \nabla^s \boldsymbol{\eta} dV - \int_{\partial\Omega^v} \boldsymbol{T}^v(\boldsymbol{y}, t) \cdot \boldsymbol{\eta} dA = 0 \qquad \forall \boldsymbol{\eta} \in \mathscr{V}. \tag{5.69}$$

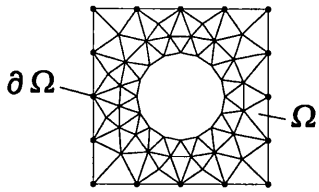

Undeformed cell with internal and boundary domains.

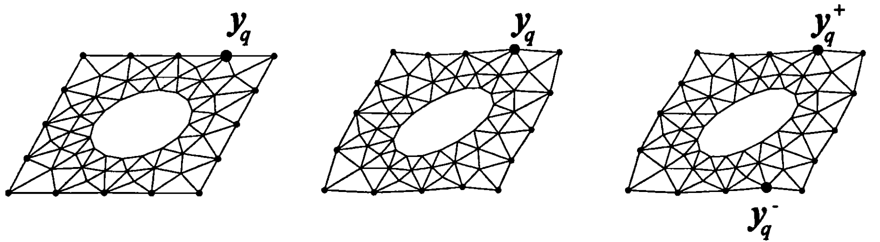

a) Linear displacements.

b) Uniform tractions.

c) Periodic displacements and antiperiodic tractions.

Figure 5.7: RVE boundary conditions. a) the linear displacement boundary condition; b) the uniform boundary traction assumption and c) the periodic displacement fluctuations boundary condition.

After solving the above problem, with $\tilde{\boldsymbol{u}}$ in hand, the macroscopic stress can be obtained from equation (5.31) which,

$$\boldsymbol{\sigma}(\boldsymbol{y},t) = \mathfrak{F}\{[\bar{\boldsymbol{\varepsilon}}(\boldsymbol{x},t) + \nabla^s\tilde{\boldsymbol{u}}(\boldsymbol{y},t)]^t\}.$$

Alternatively, in this step one may determine the reaction forces $\boldsymbol{T}$ and f by freeing the space of virtual displacements after solving equation (5.69) and then obtaining the macroscopic stress from expression (5.55) exclusively in terms of external forces.

5.9 The Taylor assumption

This model is obtained by choosing the space of virtual displacements at micro-cell (equation (5.48)) as [41],

$$\mathscr{V} = \mathscr{V}^{Taylor} \equiv \{\boldsymbol{0}\}, \tag{5.70}$$

That is, the kinematical constraint on the RVE is,

$$\tilde{\boldsymbol{u}} = \boldsymbol{0} \qquad \forall \boldsymbol{y} \in \Omega^s. \tag{5.71}$$

Equation (5.71) is the solution for the micro-equilibrium equation (5.69). This choice implies that the associated total microscopic displacement field is linear in $\boldsymbol{y}$,

$$\boldsymbol{u}(\boldsymbol{y},t) = \bar{\boldsymbol{\varepsilon}}(\boldsymbol{x},t)\boldsymbol{y} \qquad \forall \boldsymbol{y} \in \Omega^s, \tag{5.72}$$

and the micro-cell strain is homogeneous [41],

$$\boldsymbol{\varepsilon}(\boldsymbol{y},t) = \bar{\boldsymbol{\varepsilon}}(\boldsymbol{x},t), \tag{5.73}$$

The above equation implies that, the strain at each micro-element is identical to the imposed macro-strain;

$$\bar{\boldsymbol{\varepsilon}} = \boldsymbol{\varepsilon}_{elem}.$$

The microscopic stress is obtained from the micro-cell constitutive equation with prescribed strain, $\bar{\boldsymbol{\varepsilon}}$:

$$\boldsymbol{\sigma}(\boldsymbol{y},t) = \mathfrak{F}(\bar{\boldsymbol{\varepsilon}}^t(\boldsymbol{x},t)). \tag{5.74}$$

This method usually overestimates the overall behaviour of the model. Therefore, the results, which are obtained from this method, are rough and are not realistic. Another point in this assumption is application of a macroscopic strain field on the micro-structure leads to a local stress field that cannot be in equilibrium.

In conclusion, from equations (5.31) and (5.74) the homogenised stress tensor under the Taylor assumption is obtained as,

$$\bar{\boldsymbol{\sigma}}(\boldsymbol{x},t) \; = \; \frac{1}{V}\int_{\Omega} \boldsymbol{\sigma}(\boldsymbol{y},t)dV = \frac{1}{V}\int_{\Omega^s} \boldsymbol{\sigma}(\boldsymbol{y},t)dV = v^s\boldsymbol{\sigma}, \tag{5.75}$$

where v^s presents the solid volume fraction and defined by, $v^s \equiv \frac{V^s}{V}$.

If the solid part of the unit-cell composed with k different solid constituents with different volume fractions, equation (5.75) is rewritten as

$$\bar{\boldsymbol{\sigma}} = \sum_{i=1}^{k} v_i^s \boldsymbol{\sigma}_i, \tag{5.76}$$

where the solid volume fraction of phase i is presented by v_i^s.

From equation (5.75) and by using the definition for the overall tangent modulus, we have,

$$\bar{\mathbb{C}} = \frac{\partial \bar{\sigma}}{\partial \bar{\varepsilon}} = \frac{1}{V}\sum_{i=1}^{n} \frac{\partial \sigma_i^{elem}}{\partial \varepsilon_i^{elem}} dV_i = \frac{1}{V}\sum_{i=1}^{n} \mathbb{C}_i^{elem} dV_i. \tag{5.77}$$

Equation (5.77), presents the overall tangent modulus for the Taylor assumption that is a volume average of the weighted tangent modulus for n elements at RVE.

5.10 The linear displacement boundary assumption

The linear displacement boundary condition is another classical boundary condition which is prescribed at micro-level. This boundary condition shows softer and more realistic behaviour for the micro-structures and the overall properties with respect to the Taylor assumption.

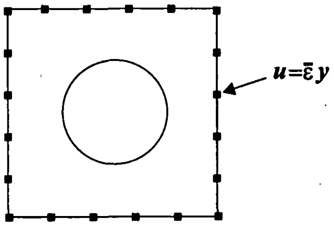

Figure 5.8: Schematic representation of the nodes on the boundary of RVE in the linear displacement assumption.

This class of boundary assumption is derived by assuming that the micro-cell boundary displacement fluctuations vanish. In other words, the set $\mathscr{V}$, taking part in equation (5.69) is chosen as [41],

$$\mathscr{V} = \mathscr{V}^{Linear} \equiv \{\tilde{\boldsymbol{u}}, \text{sufficiently regular} \,|\, \tilde{\boldsymbol{u}}(\boldsymbol{y},t) = \boldsymbol{0} \qquad \forall \boldsymbol{y} \in \partial\Omega\}. \tag{5.78}$$

By having the above choice, the equation (5.38) is expressed as,

$$\boldsymbol{u}^* = \boldsymbol{u}(\boldsymbol{y},t) = \bar{\boldsymbol{\varepsilon}}(\boldsymbol{x},t)\boldsymbol{y} \qquad on\ \partial\Omega, \tag{5.79}$$

Moreover, the constraint (5.78) satisfies the first part of the variational statement of the Hill-Mandel principle over the $\partial\Omega$ (equations (5.62)). For the rest of the domain at RVE, Ω, the Hill-Mandel principle implies that,

$$\mathbf{f}(\boldsymbol{y}, t) = \mathbf{0} \qquad in\, \Omega. \tag{5.80}$$

The RVE has been divided into the following (see Figure 5.8):

- Interior nodes (whose degrees of freedom will be denoted by the subscript i).
- Nodes which belong to the boundary of the cell (subscript b).

The pseudo code format for this assumption is illustrated in Box 5.1.

```
1- Set the nodal displacements on the surface of the micro-structure
   (see Figure 5.8),
       $\mathbf{u}_b = \mathbb{D}_b^T \bar{\boldsymbol{\varepsilon}},$
2- Get the current internal force vector, $\mathbf{F}^{int}(\mathbf{u})$, and the associated tangent,
   stiffness, $\mathbf{K}(\mathbf{u})$, of the micro-structure, based on the discretized nodes,
   $\boldsymbol{y}_i \in \Omega$, and, $\boldsymbol{y}_b \in \partial\Omega$,
       $\mathbf{F}^{int} = \begin{bmatrix} \mathbf{F}_i \\ \mathbf{F}_b \end{bmatrix}, \quad \mathbf{K} = \begin{bmatrix} \mathbf{K}_{ii} & \mathbf{K}_{ib} \\ \mathbf{K}_{bi} & \mathbf{K}_{bb} \end{bmatrix},$
3- Update the displacements in the interior domain by solving the equations
       $\boldsymbol{F}^{ext} = \boldsymbol{K}\boldsymbol{U},$
       $\mathbf{u}_i - \mathbf{K}_{ii}^{-1}\mathbf{F}_i \Rightarrow \mathbf{u}_i,$
4- Check for convergence: if , $\| \mathbf{F}_i \| > tol$, go to 2.
5- Compute the condensed stiffness matrix associated with the boundary,
   $\partial\Omega$ [27],
       $\widetilde{\mathbf{K}}_{bb} := \mathbf{K}_{bb} - \mathbf{K}_{bi}\mathbf{K}_{ii}^{-1}\mathbf{K}_{ib}$
6- Compute the macroscopic stress components and the overall
   tangent modulus,
       $\bar{\boldsymbol{\sigma}}(\boldsymbol{x}, t) = \frac{1}{V}\left[\int_{\partial\Omega} \boldsymbol{T}(\boldsymbol{y}, t) \otimes_s \boldsymbol{y} dA\right],$
       $\bar{\mathbb{C}} = \frac{1}{V}\mathbb{D}_b \widetilde{\mathbf{K}}_{bb} \mathbb{D}_b^T,$
```

Box 5.1. Micro-to-macro transition for linear displacement.

Box 5.1, shows an iterative procedure for the computation of the equilibrium state within a typical incremental step, including the setting up of new matrix representations of the homogenised stress and the overall tangent modulus [27]. $\mathbb{D}_b \in \mathscr{R}^3 \times \mathscr{R}^{2.M}$, is defined as a global coordinate matrix and for an arbitrary node, q, with material coordinate (y_1, y_2), is defined by [27],

$$\mathbb{D}_q := \frac{1}{2}\begin{bmatrix} 2y_1 & 0 \\ 0 & 2y_2 \\ y_2 & y_1 \end{bmatrix}_q . \tag{5.81}$$

M is number of nodes on the boundary, $\partial\Omega$, therefore, global coordinate matrix can be expressed by,

$$\mathbb{D}_b := \begin{bmatrix} \mathbb{D}_1 & \mathbb{D}_2 & \cdots & \mathbb{D}_3 \end{bmatrix} . \tag{5.82}$$

The projection matrices, which define the interior contribution and the contributions on the boundary, are defined as,

$$\mathbb{P}_i \in \mathscr{R}^{(N-M).n_{dim}} \times \mathscr{R}^{N.n_{dim}}, \tag{5.83}$$

$$\mathbb{P}_b \in \mathscr{R}^{M.n_{dim}} \times \mathscr{R}^{N.n_{dim}}, \tag{5.84}$$

N is the total number of nodes for micro-structure and $n_{dim} = 1,\ 2,\ 3$, indicates the dimension for the micro-structure problem. $\mathbb{P}$ is defined as Boolean matrix, i.e. it consists of integers 0 and 1.

The contributions for the overall tangent matrix are defined as,

$$\mathbf{K} = \begin{bmatrix} \mathbf{K}_{ii} & \mathbf{K}_{ib} \\ \mathbf{K}_{bi} & \mathbf{K}_{bb} \end{bmatrix} := \begin{bmatrix} \mathbb{P}_i\mathbf{K}\mathbb{P}_i^T & \mathbb{P}_i\mathbf{K}\mathbb{P}_b^T \\ \mathbb{P}_b\mathbf{K}\mathbb{P}_i^T & \mathbb{P}_b\mathbf{K}\mathbb{P}_b^T \end{bmatrix} . \tag{5.85}$$

In other words, the condensed stiffness matrices are assembled from the corresponding degrees of freedom for the internal nodes, $\mathbf{K}_{ii}$, boundary nodes, $\mathbf{K}_{bb}$, or combination of them, $\mathbf{K}_{ib}$ and $\mathbf{K}_{bi}$, from the global stiffness $\mathbf{K}$.

The matrix $\mathbb{D}_q$ for an arbitrary node $q \in \partial\Omega$, with coordinate (y_1, y_2) is obtained as follows: Equation (5.78) in matrix form is expressed by,

$$\begin{bmatrix} u_1 \\ u_2 \end{bmatrix} = \begin{bmatrix} \varepsilon_{11} & \varepsilon_{12} \\ \varepsilon_{21} & \varepsilon_{22} \end{bmatrix} \begin{bmatrix} y_1 \\ y_2 \end{bmatrix}. \tag{5.86}$$

From Box 5.1 and the first step, we have,

$$\mathbf{u}_b = \mathbb{D}_b^T \bar{\varepsilon}, \tag{5.87}$$

where the equation (5.87), for the unknown matrix, $\mathbb{D}_b$, is written as,

$$\begin{bmatrix} u_1 \\ u_2 \end{bmatrix} = \begin{bmatrix} a_1 & a_2 & a_3 \\ a_4 & a_5 & a_6 \end{bmatrix} \begin{bmatrix} \varepsilon_{11} \\ \varepsilon_{22} \\ 2\varepsilon_{12} \end{bmatrix}, \tag{5.88}$$

By making equation (5.86) equal to equation (5.88), and by solving the obtained system of equations for the unknown variables $a_1 \ldots a_6$, we have,

$$\begin{bmatrix} a_1 & a_2 & a_3 \\ a_4 & a_5 & a_6 \end{bmatrix} = \begin{bmatrix} y_1 & 0 & \frac{1}{2}y_2 \\ 0 & y_2 & \frac{1}{2}y_1 \end{bmatrix} = \frac{1}{2} \begin{bmatrix} 2y_1 & 0 \\ 0 & 2y_2 \\ y_2 & y_1 \end{bmatrix}^T \equiv \mathbb{D}_q, \tag{5.89}$$

5.10.1 The overall tangent modulus for the linear displacement boundary condition

The overall tangent modulus presented in Box 5.1 is based on the procedure explained by Miehe in [27]. We present an alternative approach for calculating the overall tangent modulus.

From Box 5.1 and step 3, the general form of the equilibrium equation is,

$$\boldsymbol{K}\boldsymbol{U} = \boldsymbol{F}^{ext}. \tag{5.90}$$

Equation (5.90) in matrix form is expressed by,

$$\begin{bmatrix} \boldsymbol{K}_{ii} & \boldsymbol{K}_{ib} \\ \boldsymbol{K}_{bi} & \boldsymbol{K}_{bb} \end{bmatrix} \begin{bmatrix} \boldsymbol{u}_i^* + \tilde{\boldsymbol{u}}_i \\ \boldsymbol{u}_b^* + \tilde{\boldsymbol{u}}_b \end{bmatrix} = \begin{bmatrix} \boldsymbol{F}_i \\ \boldsymbol{F}_b \end{bmatrix}. \tag{5.91}$$

The linear displacement boundary constraint (5.78), and the equilibrium condition at micro-level (see Box 5.1, step 4), are used to rewrite the equation (5.91) as a system of equations,

$$\left\{\begin{array}{l} \boldsymbol{K}_{ii}(\boldsymbol{u}_i^* + \tilde{\boldsymbol{u}}_i) + \boldsymbol{K}_{ib}\boldsymbol{u}_b^* = \boldsymbol{F}_i, \\ \boldsymbol{K}_{bi}(\boldsymbol{u}_i^* + \tilde{\boldsymbol{u}}_i) + \boldsymbol{K}_{bb}\boldsymbol{u}_b^* = \boldsymbol{F}_b, \end{array}\right. \Rightarrow \left\{\begin{array}{l} \boldsymbol{K}_{ii}\tilde{\boldsymbol{u}}_i = -(\boldsymbol{K}_{ii}\boldsymbol{u}_i^* + \boldsymbol{K}_{ib}\boldsymbol{u}_b^*), \\ \boldsymbol{K}_{bi}\tilde{\boldsymbol{u}}_i + \boldsymbol{K}_{bi}\boldsymbol{u}_i^* + \boldsymbol{K}_{bb}\boldsymbol{u}_b^* = \boldsymbol{F}_b, \end{array}\right. \tag{5.92}$$

The second system of equations in equation (5.92) can be written in the form of

$$\left\{\begin{array}{l} \tilde{\boldsymbol{u}}_i = -\boldsymbol{K}_{ii}^{-1}\boldsymbol{K}_I\boldsymbol{U}^*, \\ \boldsymbol{K}_{bi}\tilde{\boldsymbol{u}}_i + \boldsymbol{K}_{II}\boldsymbol{U}^* = \boldsymbol{F}_b, \end{array}\right. \tag{5.93}$$

In equation (5.93), $\boldsymbol{U}^*$ stands for, $[\boldsymbol{u}_i^* \;\; \boldsymbol{u}_b^*]^T$ and $\boldsymbol{K}_I$ and $\boldsymbol{K}_{II}$ are defined by,

$$\boldsymbol{K}_I = \begin{bmatrix} \boldsymbol{K}_{ii} & \boldsymbol{K}_{ib} \end{bmatrix} \begin{bmatrix} \boldsymbol{u}_i^* \\ \boldsymbol{u}_b^* \end{bmatrix}, \tag{5.94}$$

$$\boldsymbol{K}_{II} = \begin{bmatrix} \boldsymbol{K}_{bi} & \boldsymbol{K}_{bb} \end{bmatrix} \begin{bmatrix} \boldsymbol{u}_i^* \\ \boldsymbol{u}_b^* \end{bmatrix}. \tag{5.95}$$

By substituting $\tilde{\boldsymbol{u}}_i$, from equation (5.93) into the second part of the same equation, we have,

$$(\boldsymbol{K}_{II} - \boldsymbol{K}_{bi}\boldsymbol{K}_{ii}^{-1}\boldsymbol{K}_I)\boldsymbol{U}^* = \boldsymbol{F}_b, \tag{5.96}$$

or in condensed form,

$$\boldsymbol{K}_{III}\boldsymbol{U}^* = \boldsymbol{F}_b, \tag{5.97}$$

where,

$$\boldsymbol{K}_{III} = (\boldsymbol{K}_{II} - \boldsymbol{K}_{bi}\boldsymbol{K}_{ii}^{-1}\boldsymbol{K}_I),$$

and

$$\boldsymbol{U}^* = \mathbb{D}_{global}^T\bar{\boldsymbol{\varepsilon}},$$

where $\mathbb{D}_{global}$ is assembled for all the internal and boundary nodes at RVE.

On the other hand, from Box 5.1 and step 6, we can rewrite the average stress formula with,

$$\bar{\boldsymbol{\sigma}} = \frac{1}{V}\sum_{i=1}^{n_b} sym(\boldsymbol{F}_i^{ext} \otimes \boldsymbol{y}_i), \tag{5.98}$$

or by definition (5.81), equation (5.98) can be written as,

$$\bar{\sigma} = \frac{1}{V}\sum_{i=1}^{n_b} \mathbb{D}_i \boldsymbol{F}_i^{ext} \equiv \frac{1}{V}\mathbb{D}_b \boldsymbol{F}_b^{ext}. \tag{5.99}$$

From definition of the overall tangent modulus, we have,

$$\bar{\mathbb{C}} = \frac{\partial \bar{\sigma}}{\partial \bar{\varepsilon}}. \tag{5.100}$$

By using expression (5.97) for the boundary force vector, into the equation (5.99), we have,

$$\bar{\mathbb{C}} = \frac{1}{V}\mathbb{D}_b \frac{\partial \boldsymbol{F}_b^{ext}}{\partial \bar{\varepsilon}} = \frac{1}{V}\mathbb{D}_b \boldsymbol{K}_{III} \mathbb{D}^T_{global}. \tag{5.101}$$

5.11 The periodic boundary displacement fluctuations assumption

The third possible definition of well-posed microscopic equilibrium problems consists in imposing periodic displacement fluctuations along the unit-cell boundary. In this particular model, the boundary is decomposed into two parts, Γ^+ and Γ^-, with outward normals $\boldsymbol{n}_i^+$ and $\boldsymbol{n}_i^-$. Boundary sides of the RVE have been equally sized into pair nodes $\{\boldsymbol{y}^+, \boldsymbol{y}^-\}$. In other words, each point $\boldsymbol{y}^+ \in \Gamma^+$ has a corresponding pair $\boldsymbol{y}^- \in \Gamma^-$. For an arbitrary pair of node i, we can write,

$$\begin{aligned} \Gamma_i^+ \cup \Gamma_i^- &\in \partial\Omega, \\ \boldsymbol{n}_i^+ &= -\boldsymbol{n}_i^-. \end{aligned}$$

The kinematical assumption in this boundary condition is defined as,

$$\mathscr{V} = \mathscr{V}^{Periodic} \equiv \left\{ \tilde{\boldsymbol{u}}, \text{sufficiently regular} \left| \tilde{\boldsymbol{u}}(\boldsymbol{y}^+, t) = \tilde{\boldsymbol{u}}(\boldsymbol{y}^-, t) \quad \forall \boldsymbol{y}_{Pairs} \in \partial\Omega \right. \right\} \tag{5.102}$$

By defining the admissible virtual displacement space $\mathscr{V}$ as a constraint in (5.102), equation (5.42) can be written as [41],

$$\sum_{i}^{n_{pairs}} \left(\int_{\Gamma_i^+} \tilde{\boldsymbol{u}} \otimes_s \boldsymbol{n}_i^+ dA + \int_{\Gamma_i^-} \tilde{\boldsymbol{u}} \otimes_s \boldsymbol{n}_i^- dA \right) = \boldsymbol{0}, \tag{5.103}$$

where i stands for the number of pairs of nodes, over the boundary of RVE.

The external surface traction, $\boldsymbol{T}$, depends on the outward normals on the boundary of the cell. Moreover, the external boundary traction is orthogonal to $\mathscr{V}^{Periodic}$, as a result, we can write [41],

$$\int_{\partial\Omega} \boldsymbol{T} \cdot \eta dA = 0 \qquad \forall \eta \in \mathscr{V}^{Periodic}. \tag{5.104}$$

The above equation implies that $\boldsymbol{T}$, is anti-periodic on the $\partial\Omega$ and we can write,

$$\boldsymbol{T}(\boldsymbol{y}^{+}, t) = -\boldsymbol{T}(\boldsymbol{y}^{-}, t) \qquad \forall \boldsymbol{y}_{Pairs} \in \partial\Omega. \tag{5.105}$$

Same as the linear displacement boundary condition, the constraint (5.104), satisfies the first part of the variational statement of the Hill-Mandel principle over the $\partial\Omega$ (equations (5.62)). For the rest of the nodes of the RVE, the above constraint implies that,

$$\mathrm{f}(\boldsymbol{y}, t) = \mathbf{0} \qquad in\, \Omega. \tag{5.106}$$

To obtain the homogenised stress tensor and the overall tangent modulus under the periodic boundary displacement fluctuations condition, the RVE has been divided into the following (see Figure 5.9):

- Interior nodes (whose degrees of freedom will be denoted by the subscript I).
- Nodes which belong to Γ^{+} (subscript P).
- Nodes which belong to Γ^{-} (subscript M).
- Corner nodes (subscript C).

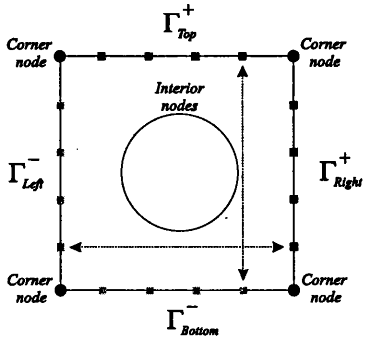

Figure 5.9: Schematic representation of the nodes on the boundary of RVE - The periodic boundary displacement fluctuations assumption.

The general solution procedure for this boundary condition comprises the following steps:

Recall additive split of the microscopic displacement (equation (5.38)),

$$\boldsymbol{u} = \boldsymbol{u}^* + \tilde{\boldsymbol{u}}, \tag{5.107}$$

where, $\boldsymbol{u}^*$ is given by,

$$\boldsymbol{u}^* = \bar{\varepsilon}(\boldsymbol{x}, t)\boldsymbol{y}, \tag{5.108}$$

The next step is to assemble and solve the equation (5.90), for unknown displacement fluctuations:

$$\boldsymbol{K}\boldsymbol{U} = \boldsymbol{F}^{ext}$$

$$\begin{bmatrix} \boldsymbol{K}_{II} & \boldsymbol{K}_{IP} & \boldsymbol{K}_{IM} & \boldsymbol{K}_{IC} \\ \boldsymbol{K}_{PI} & \boldsymbol{K}_{PP} & \boldsymbol{K}_{PM} & \boldsymbol{K}_{PC} \\ \boldsymbol{K}_{MI} & \boldsymbol{K}_{MP} & \boldsymbol{K}_{MM} & \boldsymbol{K}_{MC} \\ \boldsymbol{K}_{CI} & \boldsymbol{K}_{CP} & \boldsymbol{K}_{CM} & \boldsymbol{K}_{CC} \end{bmatrix} \begin{bmatrix} \boldsymbol{u}_I^* + \tilde{\boldsymbol{u}}_I \\ \boldsymbol{u}_P^* + \tilde{\boldsymbol{u}}_P \\ \boldsymbol{u}_M^* + \tilde{\boldsymbol{u}}_M \\ \boldsymbol{u}_C^* + \tilde{\boldsymbol{u}}_C \end{bmatrix} = \begin{bmatrix} \boldsymbol{F}_I \\ \boldsymbol{F}_P \\ \boldsymbol{F}_M \\ \boldsymbol{F}_C \end{bmatrix}. \tag{5.109}$$

From equation (5.108), we can write known prescribed displacements as follows:

$$\boldsymbol{u}_I^* = \bar{\varepsilon}\boldsymbol{y}_I, \quad \boldsymbol{u}_P^* = \bar{\varepsilon}\boldsymbol{y}_P, \quad \boldsymbol{u}_M^* = \bar{\varepsilon}\boldsymbol{y}_M, \quad \boldsymbol{u}_C^* = \bar{\varepsilon}\boldsymbol{y}_C, \tag{5.110}$$

where $\boldsymbol{y}$ is the coordinate of the nodes at micro-cell,

$$\boldsymbol{y} = [\boldsymbol{y}_I \;\; \boldsymbol{y}_P \;\; \boldsymbol{y}_M \;\; \boldsymbol{y}_C]^T.$$

To obtain the unknown displacement fluctuations from equation (5.109) we can rewrite the cited relation as,

$$\boldsymbol{K}(\boldsymbol{U}^* + \tilde{\boldsymbol{U}}) = \boldsymbol{F} \rightarrow \boldsymbol{K}\tilde{\boldsymbol{U}} = \boldsymbol{F} - \boldsymbol{K}\boldsymbol{U}^*,$$

or in matrix components form,

$$\begin{bmatrix} \boldsymbol{K}_{II} & \boldsymbol{K}_{IP} & \boldsymbol{K}_{IM} & \boldsymbol{K}_{IC} \\ \boldsymbol{K}_{PI} & \boldsymbol{K}_{PP} & \boldsymbol{K}_{PM} & \boldsymbol{K}_{PC} \\ \boldsymbol{K}_{MI} & \boldsymbol{K}_{MP} & \boldsymbol{K}_{MM} & \boldsymbol{K}_{MC} \\ \boldsymbol{K}_{CI} & \boldsymbol{K}_{CP} & \boldsymbol{K}_{CM} & \boldsymbol{K}_{CC} \end{bmatrix} \begin{bmatrix} \tilde{\boldsymbol{u}}_I \\ \tilde{\boldsymbol{u}}_P \\ \tilde{\boldsymbol{u}}_M \\ \tilde{\boldsymbol{u}}_C \end{bmatrix} = \begin{bmatrix} \boldsymbol{F}_I \\ \boldsymbol{F}_P \\ \boldsymbol{F}_M \\ \boldsymbol{F}_C \end{bmatrix} - \boldsymbol{K}\boldsymbol{U}^*. \tag{5.111}$$

The prescribed domain for the admissible displacement fluctuations, (relation (5.102)), implies,

$$\tilde{\boldsymbol{u}}_P = \tilde{\boldsymbol{u}}_M. \tag{5.112}$$

Moreover, to avoid rigid body motion, the fluctuations part of the displacement at corners were assumed equal to zero,

$$\tilde{\boldsymbol{u}}_C = \boldsymbol{0}. \tag{5.113}$$

By substituting the above assumptions (relations (5.112)-(5.113)) into equation (5.111) and after some easy manipulations we have,

$$\begin{bmatrix} \boldsymbol{K}_{II} & \boldsymbol{K}_{IP} + \boldsymbol{K}_{IM} \\ \boldsymbol{K}_{PI} & \boldsymbol{K}_{PP} + \boldsymbol{K}_{PM} \\ \boldsymbol{K}_{MI} & \boldsymbol{K}_{MP} + \boldsymbol{K}_{MM} \\ \boldsymbol{K}_{CI} & \boldsymbol{K}_{CP} + \boldsymbol{K}_{CM} \end{bmatrix} \begin{bmatrix} \tilde{\boldsymbol{u}}_I \\ \tilde{\boldsymbol{u}}_P \end{bmatrix} = \begin{bmatrix} \boldsymbol{F}_I \\ \boldsymbol{F}_P \\ \boldsymbol{F}_M \\ \boldsymbol{F}_C \end{bmatrix} - \boldsymbol{K}\boldsymbol{U}^*. \tag{5.114}$$

From equation (5.106) and the strong form of the micro-equilibrium equations (equations (5.54)), we can say,

$$\boldsymbol{F}_I = \boldsymbol{0}.$$

Moreover, the anti-periodicity of traction on the $\partial\Omega$ (equation (5.105)) is used in terms of boundary reactions,

$$\boldsymbol{F}_P = -\boldsymbol{F}_M.$$

By replacing the above relations into the equation (5.114), the reduced system of equations can be written as,

$$\begin{aligned} &\boldsymbol{K}_{II}\tilde{\boldsymbol{u}}_I + (\boldsymbol{K}_{IP} + \boldsymbol{K}_{IM})\tilde{\boldsymbol{u}}_P = -(\boldsymbol{K}_{II}\boldsymbol{u}_I^* + \boldsymbol{K}_{IP}\boldsymbol{u}_P^* + \boldsymbol{K}_{IM}\boldsymbol{u}_M^* + \boldsymbol{K}_{IC}\boldsymbol{u}_C^*), \\ &\boldsymbol{K}_{PI}\tilde{\boldsymbol{u}}_I + (\boldsymbol{K}_{PP} + \boldsymbol{K}_{PM})\tilde{\boldsymbol{u}}_P + (\boldsymbol{K}_{PI}\boldsymbol{u}_I^* + \boldsymbol{K}_{PP}\boldsymbol{u}_P^* + \boldsymbol{K}_{PM}\boldsymbol{u}_M^* + \boldsymbol{K}_{PC}\boldsymbol{u}_C^*) = \boldsymbol{F}_P, \\ &\boldsymbol{K}_{MI}\tilde{\boldsymbol{u}}_I + (\boldsymbol{K}_{MP} + \boldsymbol{K}_{MM})\tilde{\boldsymbol{u}}_P + (\boldsymbol{K}_{MI}\boldsymbol{u}_I^* + \boldsymbol{K}_{MP}\boldsymbol{u}_P^* + \boldsymbol{K}_{MM}\boldsymbol{u}_M^* + \boldsymbol{K}_{MC}\boldsymbol{u}_C^*) = -\boldsymbol{F}_P, \\ &\boldsymbol{K}_{CI}\tilde{\boldsymbol{u}}_I + (\boldsymbol{K}_{CP} + \boldsymbol{K}_{CM})\tilde{\boldsymbol{u}}_P + (\boldsymbol{K}_{CI}\boldsymbol{u}_I^* + \boldsymbol{K}_{CP}\boldsymbol{u}_P^* + \boldsymbol{K}_{CM}\boldsymbol{u}_M^* + \boldsymbol{K}_{CC}\boldsymbol{u}_C^*) = \boldsymbol{F}_C. \end{aligned} \tag{5.115}$$

By summing up the left side of the equations, associated with $\boldsymbol{F}_P$, from equation (5.115), we can write,

$$\begin{aligned} &\begin{bmatrix} \boldsymbol{K}_{II} & \boldsymbol{K}_{IP} + \boldsymbol{K}_{IM} \\ \boldsymbol{K}_{PI} + \boldsymbol{K}_{MI} & \boldsymbol{K}_{PP} + \boldsymbol{K}_{PM} + \boldsymbol{K}_{MP} + \boldsymbol{K}_{MM} \end{bmatrix} \begin{bmatrix} \tilde{\boldsymbol{u}}_I \\ \tilde{\boldsymbol{u}}_P \end{bmatrix} = - \\ &\begin{bmatrix} \boldsymbol{K}_{II} & \boldsymbol{K}_{IP} & \boldsymbol{K}_{IM} & \boldsymbol{K}_{IC} \\ \boldsymbol{K}_{PI} + \boldsymbol{K}_{MI} & \boldsymbol{K}_{PP} + \boldsymbol{K}_{MP} & \boldsymbol{K}_{PM} + \boldsymbol{K}_{MM} & \boldsymbol{K}_{PC} + \boldsymbol{K}_{MC} \end{bmatrix} \boldsymbol{U}^*. \end{aligned} \tag{5.116}$$

Equation (5.116) is solved for unknown fluctuations displacements, $[\tilde{\boldsymbol{u}}_I \; \tilde{\boldsymbol{u}}_P]^T$. By having $\tilde{\boldsymbol{u}}_I$ and $\tilde{\boldsymbol{u}}_P$ in hand, and from equation (5.115), other external forces, $\boldsymbol{F}_C$, $\boldsymbol{F}_P$ and $\boldsymbol{F}_M$, can be obtained.

By implementing the constraint (5.106), into the equation (5.55), the homogenised stress tensor is obtained by,

$$\bar{\boldsymbol{\sigma}}(\boldsymbol{x},t) = \frac{1}{V}\int_{\partial\Omega} \boldsymbol{T}(\boldsymbol{y},t) \otimes_s \boldsymbol{y} dA = \frac{1}{V}\int_{\partial\Omega} \boldsymbol{T}(\boldsymbol{y},t)\boldsymbol{y}^T dA. \tag{5.117}$$

From the finite element method and by using the interpolation functions, element displacement can be presented as,

$$\boldsymbol{u} = \sum_{i=1}^{b} \boldsymbol{N}_i \boldsymbol{u}_i, \tag{5.118}$$

From micro-equilibrium equation (5.69), and equation (5.118), the traction part of the micro-equilibrium equation on the boundary can be written as

$$\begin{aligned}
\int_{\partial\Omega} \boldsymbol{T}(\boldsymbol{y},t)\cdot\boldsymbol{\eta} dA &= \int_{\partial\Omega} \boldsymbol{T}(\boldsymbol{y},t)\cdot(\sum_{i=1}^{b} \boldsymbol{N}_i\boldsymbol{\eta}_i)dA \\
&= \int_{\partial\Omega} \sum_{i=1}^{b} \boldsymbol{N}_i \boldsymbol{T}(\boldsymbol{y},t)\cdot\boldsymbol{\eta}_i dA \\
&= \sum_{i=1}^{b}\Big(\int_{\partial\Omega} \boldsymbol{N}_i\boldsymbol{T}(\boldsymbol{y},t)dA\Big)\cdot\boldsymbol{\eta}_i \\
&= \sum_{i=1}^{b} \boldsymbol{F}_i\cdot\boldsymbol{\eta}_i.
\end{aligned} \tag{5.119}$$

From equations (5.117) and (5.119), the overall stress tensor is expressed by,

$$\bar{\boldsymbol{\sigma}}(\boldsymbol{x},t) = \frac{1}{V} sym\left[\sum_{i=1}^{b} \boldsymbol{F}_i \boldsymbol{y}_i^T\right]. \tag{5.120}$$

Note that the external forces, $\boldsymbol{F}$, on the boundary of the cell, for this particular boundary condition, are expressed by,

$$\boldsymbol{F}_b = [\boldsymbol{F}_P \; \boldsymbol{F}_M \; \boldsymbol{F}_C]^T. \tag{5.121}$$

5.11.1 The overall tangent modulus for the periodic boundary displacement fluctuations assumption

In computational homogenisation method, because of implicit approach, the tangent modulus should be determined numerically by relations between variations of the macroscopic stress and macroscopic strain at associated integration point at macro-level [68].

$$\bar{\mathbb{C}} = \frac{\partial \bar{\sigma}}{\partial \bar{\varepsilon}}.$$

In this section the consistent overall tangent modulus under the periodic boundary displacement fluctuations assumption is achieved by reducing the total unit-cell system of equations (see equation (5.111)) to the relation between the forces acting on the boundary, $\partial\Omega$, and the displacement on the boundary.

From equation (5.116), fluctuation part of displacements, $\tilde{\boldsymbol{U}} = [\tilde{\boldsymbol{u}}_I \;\; \tilde{\boldsymbol{u}}_P]^T$, can be obtained as follows,

$$\tilde{\boldsymbol{U}} = -\boldsymbol{K}_1^{-1}\boldsymbol{K}_2\boldsymbol{U}^*, \tag{5.122}$$

where,

$$\boldsymbol{K}_1 = \begin{bmatrix} \boldsymbol{K}_{II} & \boldsymbol{K}_{IP} + \boldsymbol{K}_{IM} \\ \boldsymbol{K}_{PI} + \boldsymbol{K}_{MI} & \boldsymbol{K}_{PP} + \boldsymbol{K}_{PM} + \boldsymbol{K}_{MP} + \boldsymbol{K}_{MM} \end{bmatrix}, \tag{5.123}$$

and

$$\boldsymbol{K}_2 = \begin{bmatrix} \boldsymbol{K}_{II} & \boldsymbol{K}_{IP} & \boldsymbol{K}_{IM} & \boldsymbol{K}_{IC} \\ \boldsymbol{K}_{PI} + \boldsymbol{K}_{MI} & \boldsymbol{K}_{PP} + \boldsymbol{K}_{MP} & \boldsymbol{K}_{PM} + \boldsymbol{K}_{MM} & \boldsymbol{K}_{PC} + \boldsymbol{K}_{MC} \end{bmatrix}. \tag{5.124}$$

Moreover, from equation (5.115), external forces acting on boundary of the cell, are obtained as,

$$\begin{aligned} \boldsymbol{F}_P &= [\boldsymbol{K}_{PI} \quad \boldsymbol{K}_{PP} + \boldsymbol{K}_{PM}]\tilde{\boldsymbol{U}} + [\boldsymbol{K}_{PI} \quad \boldsymbol{K}_{PP} \quad \boldsymbol{K}_{PM} \quad \boldsymbol{K}_{PC}]\boldsymbol{U}^*, \\ \boldsymbol{F}_P &= \boldsymbol{K}_3\tilde{\boldsymbol{U}} + \boldsymbol{K}_4\boldsymbol{U}^*. \end{aligned} \tag{5.125}$$

Because of anti-periodicity condition we can write,

$$\begin{aligned} \boldsymbol{F}_M &= -\boldsymbol{F}_P, \\ \boldsymbol{F}_M &= -(\boldsymbol{K}_3\tilde{\boldsymbol{U}} + \boldsymbol{K}_4\boldsymbol{U}^*), \end{aligned} \tag{5.126}$$

and finally,

$$\begin{aligned} \boldsymbol{F}_C &= [\boldsymbol{K}_{CI} \quad \boldsymbol{K}_{CP} + \boldsymbol{K}_{CM}]\tilde{\boldsymbol{U}} + [\boldsymbol{K}_{CI} \quad \boldsymbol{K}_{CP} \quad \boldsymbol{K}_{CM} \quad \boldsymbol{K}_{CC}]\boldsymbol{U}^*, \\ \boldsymbol{F}_C &= \boldsymbol{K}_5\tilde{\boldsymbol{U}} + \boldsymbol{K}_6\boldsymbol{U}^*. \end{aligned} \tag{5.127}$$

By replacing $\tilde{\boldsymbol{U}}$ from equation (5.122) into equations (5.125)-(5.127), we have,

$$\begin{aligned}
\boldsymbol{F_P} &= \left(\boldsymbol{K}_4 - \boldsymbol{K}_3\boldsymbol{K}_1^{-1}\boldsymbol{K}_2\right)\boldsymbol{U}^*, \\
\boldsymbol{F_C} &= \left(\boldsymbol{K}_6 - \boldsymbol{K}_5\boldsymbol{K}_1^{-1}\boldsymbol{K}_2\right)\boldsymbol{U}^*, \\
\boldsymbol{F_P} &= \tilde{\boldsymbol{K}}_{\boldsymbol{P}}\boldsymbol{U}^*, & (5.128) \\
\boldsymbol{F_M} &= -\tilde{\boldsymbol{K}}_{\boldsymbol{P}}\boldsymbol{U}^*, & (5.129) \\
\boldsymbol{F_C} &= \tilde{\boldsymbol{K}}_{\boldsymbol{C}}\boldsymbol{U}^*. & (5.130)
\end{aligned}$$

From equation (5.121), it can be written,

$$\boldsymbol{F_b} = \begin{bmatrix} \boldsymbol{F_P} \\ \boldsymbol{F_M} \\ \boldsymbol{F_C} \end{bmatrix} = \begin{bmatrix} \tilde{\boldsymbol{K}}_{\boldsymbol{P}} \\ -\tilde{\boldsymbol{K}}_{\boldsymbol{P}} \\ \tilde{\boldsymbol{K}}_{\boldsymbol{C}} \end{bmatrix} \boldsymbol{U}^*, \tag{5.131}$$

or in condensed form,

$$\boldsymbol{F_b} = \tilde{\boldsymbol{K}}_{Periodic}\boldsymbol{U}^* = \tilde{\boldsymbol{K}}_{Periodic}\mathbb{D}_{global}^T\bar{\boldsymbol{\varepsilon}}. \tag{5.132}$$

Following the same procedure for the linear displacement boundary condition, (see equations (5.99)-(5.101)), the homogenised tangent modulus for the periodic fluctuations displacement boundary assumption is obtained. Therefore, the tangent modulus can be written [68],

$$\bar{\mathbb{C}} = \frac{1}{V}\mathbb{D}_b\frac{\partial \boldsymbol{F}_b^{ext}}{\partial \bar{\boldsymbol{\varepsilon}}} = \frac{1}{V}\mathbb{D}_b\tilde{\boldsymbol{K}}_{Periodic}\mathbb{D}_{global}^T. \tag{5.133}$$

5.12 The uniform boundary traction assumption

The final class of multi-scale models is derived under the assumption of minimum kinematical constraint on the RVE (see the defined space in (5.42)). For this constraint, the space $\mathscr{V}$ is defined such as [41],

$$\mathscr{V} = \mathscr{V}^{Traction} \equiv \left\{ \tilde{\boldsymbol{u}}, \text{sufficiently regular} \,\middle|\, \int_{\partial\Omega} \tilde{\boldsymbol{u}} \otimes_s \boldsymbol{n} dA = \boldsymbol{0} \right\}. \tag{5.134}$$

With the same explanation for the linear displacement boundary condition and the periodic fluctuations displacement assumption, from the above choice we have,

$$\mathrm{f}(\boldsymbol{y}, t) = \boldsymbol{0} \qquad in\ \Omega. \tag{5.135}$$

The external surface traction compatible with the present model is given by

$$\boldsymbol{T}(\boldsymbol{y},t) = \boldsymbol{\sigma}(\boldsymbol{y},t)\boldsymbol{n}(\boldsymbol{y}) = \bar{\boldsymbol{\sigma}}(\boldsymbol{x},t)\boldsymbol{n}(\boldsymbol{y}) \qquad \forall \boldsymbol{y} \in \partial\Omega, \tag{5.136}$$

where $\bar{\boldsymbol{\sigma}}(\boldsymbol{x},t)$ is a macro-stress at corresponding point $\boldsymbol{x}$ of macro-structure.

To obtain the homogenised stress tensor and the overall tangent modulus under the uniform boundary traction assumption, the nodes on the boundary of the cell have been decomposed as follows:

- Interior nodes, I.
- Corner nodes with dependent degrees of freedom, with subscript d.
- Boundary nodes and corner node with independent degrees of freedom (free nodes), with subscript f.
- Corner nodes with prescribed degrees of freedom, with subscript p.

Figure (5.10) is a schematic representation of the above decomposition of the micro-cell.

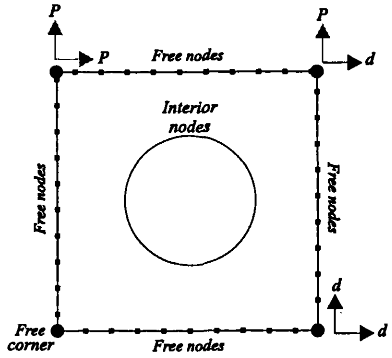

Figure 5.10: Schematic representation of the nodes on the boundary of RVE - The uniform boundary traction assumption.

Assume the system is in equilibrium, thus we can write,

$$\boldsymbol{F}^{int} = \boldsymbol{F}^{ext}. \tag{5.137}$$

From equation (5.90) and the variational form of the system we have,

$$\begin{aligned} \boldsymbol{F}^{int}.\boldsymbol{\eta} &= \boldsymbol{F}^{ext}.\boldsymbol{\eta} \\ \boldsymbol{K}\boldsymbol{U}.\boldsymbol{\eta} &= \boldsymbol{F}^{ext}.\boldsymbol{\eta} \qquad \forall \boldsymbol{\eta} \in \mathscr{V}^{Traction}. \end{aligned} \tag{5.138}$$

The developed form of equation (5.138), based on the boundary decomposition, is expressed by,

$$\begin{bmatrix} \boldsymbol{K}_{II} & \boldsymbol{K}_{If} & \boldsymbol{K}_{Id} & \boldsymbol{K}_{Ip} \\ \boldsymbol{K}_{fI} & \boldsymbol{K}_{ff} & \boldsymbol{K}_{fd} & \boldsymbol{K}_{fp} \\ \boldsymbol{K}_{dI} & \boldsymbol{K}_{df} & \boldsymbol{K}_{dd} & \boldsymbol{K}_{dp} \\ \boldsymbol{K}_{pI} & \boldsymbol{K}_{pf} & \boldsymbol{K}_{pd} & \boldsymbol{K}_{pp} \end{bmatrix} \begin{bmatrix} \boldsymbol{u}_I^* + \tilde{\boldsymbol{u}}_I \\ \boldsymbol{u}_f^* + \tilde{\boldsymbol{u}}_f \\ \boldsymbol{u}_d^* + \tilde{\boldsymbol{u}}_d \\ \boldsymbol{u}_p^* + \tilde{\boldsymbol{u}}_p \end{bmatrix} \cdot \begin{bmatrix} \eta_I \\ \eta_f \\ \eta_d \\ \eta_p \end{bmatrix} = \begin{bmatrix} \boldsymbol{F}_I \\ \boldsymbol{F}_f \\ \boldsymbol{F}_d \\ \boldsymbol{F}_p \end{bmatrix} \cdot \begin{bmatrix} \eta_I \\ \eta_f \\ \eta_d \\ \eta_p \end{bmatrix}. \tag{5.139}$$

To avoid the rigid body motion, the imposed constraints, over the cell are,

$$\begin{cases} \tilde{\boldsymbol{u}}_p = 0, \\ \eta_p = 0. \end{cases} \tag{5.140}$$

By substituting the constraints (5.140) into (5.139) and by eliminating the last row from the system of equations, we have,

$$\left\{ \begin{bmatrix} \boldsymbol{K}_{II} & \boldsymbol{K}_{If} & \boldsymbol{K}_{Id} & \boldsymbol{K}_{Ip} \\ \boldsymbol{K}_{fI} & \boldsymbol{K}_{ff} & \boldsymbol{K}_{fd} & \boldsymbol{K}_{fp} \\ \boldsymbol{K}_{dI} & \boldsymbol{K}_{df} & \boldsymbol{K}_{dd} & \boldsymbol{K}_{dp} \end{bmatrix} \begin{bmatrix} \boldsymbol{u}_I^* \\ \boldsymbol{u}_f^* \\ \boldsymbol{u}_d^* \\ \boldsymbol{u}_p^* \end{bmatrix} + \begin{bmatrix} \boldsymbol{K}_{II} & \boldsymbol{K}_{If} & \boldsymbol{K}_{Id} \\ \boldsymbol{K}_{fI} & \boldsymbol{K}_{ff} & \boldsymbol{K}_{fd} \\ \boldsymbol{K}_{dI} & \boldsymbol{K}_{df} & \boldsymbol{K}_{dd} \end{bmatrix} \begin{bmatrix} \tilde{\boldsymbol{u}}_I \\ \tilde{\boldsymbol{u}}_f \\ \tilde{\boldsymbol{u}}_d \end{bmatrix} \right\} \cdot \begin{bmatrix} \eta_I \\ \eta_f \\ \eta_d \end{bmatrix}$$

$$= \begin{bmatrix} \boldsymbol{F}_I \\ \boldsymbol{F}_f \\ \boldsymbol{F}_d \end{bmatrix} \cdot \begin{bmatrix} \eta_I \\ \eta_f \\ \eta_d \end{bmatrix}. \tag{5.141}$$

From defined space (5.134), we can write,

$$\int_{\partial\Omega} \tilde{\boldsymbol{u}} \otimes_s \boldsymbol{n} dA = \int_{\partial\Omega} \boldsymbol{N} \tilde{\boldsymbol{u}} \otimes_s \boldsymbol{n} dA = 0, \tag{5.142}$$

where $\boldsymbol{N}$ is a vector of shape functions over the boundary of cell.

To define a relation between any arbitrary displacement fields belonging to the space $\mathscr{V}^{Traction}$ such as, $\boldsymbol{v}_f$ and $\boldsymbol{v}_d$, on the boundary of RVE, assume boundary of RVE could be divided into two sub-domains, Γ^+ and Γ^-, where,

$$\Gamma^+ \cup \Gamma^- = \partial\Omega,$$

and $\tilde{\boldsymbol{u}}$ is constant in each domain. Equation (5.142) for all the boundary elements is expressed by,

$$\mathop{\mathsf{A}}_{i=1}^{b\_ele} \left[\tilde{\boldsymbol{u}}^{+} \int_{\Gamma+} \boldsymbol{N} dA \otimes_s \boldsymbol{n}^{+} + \tilde{\boldsymbol{u}}^{-} \int_{\Gamma+} \boldsymbol{N} dA \otimes_s \boldsymbol{n}^{-} \right] = 0, \tag{5.143}$$

or,

$$\boldsymbol{C} \tilde{\boldsymbol{u}} = 0. \tag{5.144}$$

The matrix $\boldsymbol{C}$, in above, is specified for free, dependent and prescribed degrees of freedom on the boundary $\partial\Omega$. Thus, equation (5.144) can be rewritten as,

$$[\boldsymbol{C}_f \;\; \boldsymbol{C}_d \;\; \boldsymbol{C}_p] \, [\boldsymbol{v}_f \;\; \boldsymbol{v}_d \;\; \boldsymbol{v}_p]^T = 0. \tag{5.145}$$

The prescribed degrees of freedom for the *Prescribed* nodes on the boundary, assumed to be zero,

$$\boldsymbol{v}_p = [0 \;\; 0 \;\; 0] \, . \tag{5.146}$$

Therefore, equation (5.145), could be written as,

$$[\boldsymbol{C}_f \;\; \boldsymbol{C}_d \;\; \boldsymbol{C}_p] \, [\boldsymbol{v}_f \;\; \boldsymbol{v}_d \;\; 0]^T = 0, \tag{5.147}$$

or,

$$\boldsymbol{C}_f \boldsymbol{v}_f = -\boldsymbol{C}_d \boldsymbol{v}_d \Rightarrow \boldsymbol{v}_d = -\boldsymbol{C}_d^{-1} \boldsymbol{C}_f \boldsymbol{v}_f. \tag{5.148}$$

Assume that,

$$\boldsymbol{R} = -\boldsymbol{C}_d^{-1} \boldsymbol{C}_f. \tag{5.149}$$

Thus, by substituting $\boldsymbol{R}$ from equation (5.149) into equation (5.148) we have,

$$\boldsymbol{v}_d = \boldsymbol{R} \boldsymbol{v}_f. \tag{5.150}$$

By using the above relation between any admissible displacement field belonging to $\mathcal{V}^{Traction}$, we have,

$$\boldsymbol{\eta}_d = \boldsymbol{R} \boldsymbol{\eta}_f, \qquad \tilde{\boldsymbol{u}}_d = \boldsymbol{R} \tilde{\boldsymbol{u}}_f. \tag{5.151}$$

By replacing (5.151) into equation (5.141), we have,

$$\left\{\begin{bmatrix} \boldsymbol{K}_{II} & \boldsymbol{K}_{If} & \boldsymbol{K}_{Id} & \boldsymbol{K}_{Ip}\\ \boldsymbol{K}_{fI} & \boldsymbol{K}_{ff} & \boldsymbol{K}_{fd} & \boldsymbol{K}_{fp}\\ \boldsymbol{K}_{dI} & \boldsymbol{K}_{df} & \boldsymbol{K}_{dd} & \boldsymbol{K}_{dp}\end{bmatrix}\begin{bmatrix}\boldsymbol{u}_I^*\\ \boldsymbol{u}_f^*\\ \boldsymbol{u}_d^*\\ \boldsymbol{u}_p^*\end{bmatrix} + \begin{bmatrix}\boldsymbol{K}_{II} & \boldsymbol{K}_{If}+\boldsymbol{K}_{Id}\boldsymbol{R}\\ \boldsymbol{K}_{fI} & \boldsymbol{K}_{ff}+\boldsymbol{K}_{fd}\boldsymbol{R}\\ \boldsymbol{K}_{dI} & \boldsymbol{K}_{df}+\boldsymbol{K}_{dd}\boldsymbol{R}\end{bmatrix}\begin{bmatrix}\tilde{\boldsymbol{u}}_I\\ \tilde{\boldsymbol{u}}_f\end{bmatrix}\right\}\cdot\begin{bmatrix}\boldsymbol{\eta}_I\\ \boldsymbol{\eta}_f\\ \boldsymbol{R}\boldsymbol{\eta}_f\end{bmatrix}$$

$$= \begin{bmatrix}\boldsymbol{F}_I\\ \boldsymbol{F}_f\\ \boldsymbol{F}_d\end{bmatrix}\cdot\begin{bmatrix}\boldsymbol{\eta}_I\\ \boldsymbol{\eta}_f\\ \boldsymbol{R}\boldsymbol{\eta}_f\end{bmatrix} \qquad (5.152)$$

To eliminate $\boldsymbol{R}$ from $\boldsymbol{R}\boldsymbol{\eta}_f$ in the last row of equation (5.152), a general index form for the last row of the above equation is written, such that,

$$K_{ij}U_jR_{jk}\eta_k \equiv R^T_{kj}K_{ij}U_j\eta_k. \qquad (5.153)$$

As a result, equation (5.152) can be written as,

$$\left\{\begin{bmatrix} \boldsymbol{K}_{II} & \boldsymbol{K}_{If} & \boldsymbol{K}_{Id} & \boldsymbol{K}_{Ip}\\ \boldsymbol{K}_{fI} & \boldsymbol{K}_{ff} & \boldsymbol{K}_{fd} & \boldsymbol{K}_{fp}\\ \boldsymbol{R}^T\boldsymbol{K}_{dI} & \boldsymbol{R}^T\boldsymbol{K}_{df} & \boldsymbol{R}^T\boldsymbol{K}_{dd} & \boldsymbol{R}^T\boldsymbol{K}_{dp}\end{bmatrix}\begin{bmatrix}\boldsymbol{u}_I^*\\ \boldsymbol{u}_f^*\\ \boldsymbol{u}_d^*\\ \boldsymbol{u}_p^*\end{bmatrix} + \right.$$

$$\left.\begin{bmatrix}\boldsymbol{K}_{II} & \boldsymbol{K}_{If}+\boldsymbol{K}_{Id}\boldsymbol{R}\\ \boldsymbol{K}_{fI} & \boldsymbol{K}_{ff}+\boldsymbol{K}_{fd}\boldsymbol{R}\\ \boldsymbol{R}^T\boldsymbol{K}_{dI} & \boldsymbol{R}^T\boldsymbol{K}_{df}+\boldsymbol{R}^T\boldsymbol{K}_{dd}\boldsymbol{R}\end{bmatrix}\begin{bmatrix}\tilde{\boldsymbol{u}}_I\\ \tilde{\boldsymbol{u}}_f\end{bmatrix}\right\}\cdot\begin{bmatrix}\boldsymbol{\eta}_I\\ \boldsymbol{\eta}_f\\ \boldsymbol{\eta}_f\end{bmatrix} =$$

$$\begin{bmatrix}\boldsymbol{F}_I\\ \boldsymbol{F}_f\\ \boldsymbol{R}^T\boldsymbol{F}_d\end{bmatrix}\cdot\begin{bmatrix}\boldsymbol{\eta}_I\\ \boldsymbol{\eta}_f\\ \boldsymbol{\eta}_f\end{bmatrix}. \qquad (5.154)$$

Adding up the correspondent rows to $\boldsymbol{\eta}_f$, leads to,

$$\left\{\begin{bmatrix} \boldsymbol{K}_{II} & \boldsymbol{K}_{If} & \boldsymbol{K}_{Id} & \boldsymbol{K}_{Ip}\\ \boldsymbol{K}_{fI}+\boldsymbol{R}^T\boldsymbol{K}_{dI} & \boldsymbol{K}_{ff}+\boldsymbol{R}^T\boldsymbol{K}_{df} & \boldsymbol{K}_{fd}+\boldsymbol{R}^T\boldsymbol{K}_{dd} & \boldsymbol{K}_{fp}+\boldsymbol{R}^T\boldsymbol{K}_{dp}\end{bmatrix}\begin{bmatrix}\boldsymbol{u}_I^*\\ \boldsymbol{u}_f^*\\ \boldsymbol{u}_d^*\\ \boldsymbol{u}_p^*\end{bmatrix} + \right.$$

$$\left.\begin{bmatrix}\boldsymbol{K}_{II} & \boldsymbol{K}_{If}+\boldsymbol{K}_{Id}\boldsymbol{R}\\ \boldsymbol{K}_{fI}+\boldsymbol{R}^T\boldsymbol{K}_{dI} & \boldsymbol{K}_{ff}+\boldsymbol{K}_{fd}\boldsymbol{R}+\boldsymbol{R}^T\boldsymbol{K}_{df}+\boldsymbol{R}^T\boldsymbol{K}_{dd}\boldsymbol{R}\end{bmatrix}\begin{bmatrix}\tilde{\boldsymbol{u}}_I\\ \tilde{\boldsymbol{u}}_f\end{bmatrix}\right\}\cdot\begin{bmatrix}\boldsymbol{\eta}_I\\ \boldsymbol{\eta}_f\end{bmatrix} =$$

$$\begin{bmatrix}\boldsymbol{F}_I\\ \boldsymbol{F}_f+\boldsymbol{R}^T\boldsymbol{F}_d\end{bmatrix}\cdot\begin{bmatrix}\boldsymbol{\eta}_I\\ \boldsymbol{\eta}_f\end{bmatrix} \qquad (5.155)$$

In case of equilibrium, the system of equations obtained from (5.155) should be solved for unknown fluctuation displacements from,

$$\left\{ \begin{bmatrix} K_{II} & K_{If} & K_{Id} & K_{Ip} \\ K_{fI}+R^TK_{dI} & K_{ff}+R^TK_{df} & K_{fd}+R^TK_{dd} & K_{fp}+R^TK_{dp} \end{bmatrix} \begin{bmatrix} u_I^* \\ u_f^* \\ u_d^* \\ u_p^* \end{bmatrix} = -\begin{bmatrix} K_{II} & K_{If}+K_{Id}R \\ K_{fI}+R^TK_{dI} & K_{ff}+K_{fd}R+R^TK_{df}+R^TK_{dd}R \end{bmatrix} \begin{bmatrix} \tilde{u}_I \\ \tilde{u}_f \end{bmatrix} \right\} \tag{5.156}$$

Same as the periodic fluctuations displacement boundary assumption, the homogenised stress is obtained from equations (5.117) and (5.119) after assembling the boundary reaction forces.

$$F_b = [F_f \;\; F_d \;\; F_p]^T, \tag{5.157}$$

$$\bar{\sigma}(x,t) = \frac{1}{V} sym\left[\sum_{i=1}^{b} F_i y_i^T\right]. \tag{5.158}$$

5.12.1 The overall tangent modulus for the uniform boundary traction assumption

The procedure to determine the consistent overall tangent modulus for this particular boundary assumption, follows the same steps as in the periodic boundary displacement fluctuations assumption. From equation (5.156), we have,

$$\tilde{U} = -K_b^{-1}K_aU^*, \tag{5.159}$$

where,

$$\begin{aligned} K_a &= \begin{bmatrix} K_{II} & K_{If} & K_{Id} & K_{Ip} \\ K_{fI}+R^TK_{dI} & K_{ff}+R^TK_{df} & K_{fd}+R^TK_{dd} & K_{fp}+R^TK_{dp} \end{bmatrix} \\ K_b &= \begin{bmatrix} K_{II} & K_{If}+K_{Id}R \\ K_{fI}+R^TK_{dI} & K_{ff}+K_{fd}R+R^TK_{df}+R^TK_{dd}R \end{bmatrix}. \end{aligned} \tag{5.160}$$

By using (5.159) and from equation (5.156), we can obtain the correspondent external forces for the boundary nodes, such as,

$$\boldsymbol{F}_f = \left(\boldsymbol{K}_{f1} - \boldsymbol{K}_{f2}\boldsymbol{K}_b^{-1}\boldsymbol{K}_a\right)\boldsymbol{U}^* = \boldsymbol{K}_F\boldsymbol{U}^*, \tag{5.161}$$

$$\boldsymbol{F}_d = \left(\boldsymbol{K}_{d1} - \boldsymbol{K}_{d2}\boldsymbol{K}_b^{-1}\boldsymbol{K}_a\right)\boldsymbol{U}^* = \boldsymbol{K}_D\boldsymbol{U}^*, \tag{5.162}$$

$$\boldsymbol{F}_p = \left(\boldsymbol{K}_{p1} - \boldsymbol{K}_{p2}\boldsymbol{K}_b^{-1}\boldsymbol{K}_a\right)\boldsymbol{U}^* = \boldsymbol{K}_P\boldsymbol{U}^*, \tag{5.163}$$

where in above equations,

$$\begin{aligned}
\boldsymbol{K}_{f1} &= \left[\boldsymbol{K}_{fI}\ \boldsymbol{K}_{ff}\ \boldsymbol{K}_{fd}\ \boldsymbol{K}_{fp}\right], \quad \boldsymbol{K}_{f2} = \left[\boldsymbol{K}_{fI}\ \boldsymbol{K}_{ff} + \boldsymbol{K}_{fd}\boldsymbol{R}\right], \\
\boldsymbol{K}_{d1} &= \left[\boldsymbol{K}_{dI}\ \boldsymbol{K}_{df}\ \boldsymbol{K}_{dd}\ \boldsymbol{K}_{dp}\right], \quad \boldsymbol{K}_{d2} = \left[\boldsymbol{K}_{dI}\ \boldsymbol{K}_{df} + \boldsymbol{K}_{dd}\boldsymbol{R}\right], \\
\boldsymbol{K}_{p1} &= \left[\boldsymbol{K}_{pI}\ \boldsymbol{K}_{pf}\ \boldsymbol{K}_{pd}\ \boldsymbol{K}_{pp}\right], \quad \boldsymbol{K}_{p2} = \left[\boldsymbol{K}_{pI}\ \boldsymbol{K}_{pf} + \boldsymbol{K}_{pd}\boldsymbol{R}\right].
\end{aligned} \tag{5.164}$$

Boundary force vector is assembled from equations (5.161)-(5.163),

$$\boldsymbol{F}_b = \left[\boldsymbol{F}_f \quad \boldsymbol{F}_d \quad \boldsymbol{F}_p\right]^T = \left[\boldsymbol{K}_F \quad \boldsymbol{K}_D \quad \boldsymbol{K}_P\right]^T \boldsymbol{U}^*, \tag{5.165}$$

or in condensed form,

$$\boldsymbol{F}_b = \tilde{\boldsymbol{K}}_{Traction}\boldsymbol{U}^* = \tilde{\boldsymbol{K}}_{Traction}\mathbb{D}^T_{global}\bar{\varepsilon}. \tag{5.166}$$

The same procedure as other boundary conditions is used to obtain the overall tangent modulus. Therefore, it can be written,

$$\bar{\mathbb{C}} = \frac{1}{V}\mathbb{D}_b\frac{\partial \boldsymbol{F}_b^{ext}}{\partial \bar{\varepsilon}} = \frac{1}{V}\mathbb{D}_b\tilde{\boldsymbol{K}}_{Traction}\mathbb{D}^T_{global}, \tag{5.167}$$

where, for the uniform boundary traction assumption, $\mathbb{D}_{global}$ and $\mathbb{D}_b$ are defined as,

$$\mathbb{D}_{global} = \left[\mathbb{D}_I\ \mathbb{D}_f\ \mathbb{D}_d\ \mathbb{D}_p\right],$$

and,

$$\mathbb{D}_b = \left[\mathbb{D}_f\ \mathbb{D}_d\ \mathbb{D}_p\right].$$

5.13 Conclusion

In this chapter we presented the analytical methods for the effective material properties. In addition, we introduced the concepts of computational homogenisation. Initially, two concepts related to the homogenisation procedure were expressed: homogenisation and localization. In addition formulation for two-scale boundary value problem was explained.

Four kinematic assumptions at the micro-scale were described. The Taylor assumption for which the macro strain is imposed uniformly over the whole micro cell, the linear boundary displacement assumption explained directly in terms of prescribed displacements on the boundary nodes, the periodic fluctuations displacement boundary condition and, finally, the uniform boundary traction assumption. These last two assumptions require a non-conventional treatment of the RVE boundary degrees of freedom.

The consistent overall tangent moduli were also derived from the reduced system of equilibrium equations for the different kinematic assumptions.

Chapter 6

Computer implementation of multi-scale material models

6.1 Introduction

The theory of the homogenisation (reviewed in chapter 5) represents a potentially very accurate modelling methodology for characterizing the mechanical behaviour of heterogeneous media in general. In summary, multi-scale methodologies of the present type evaluate the actual stress and strain over a representative volume element (RVE), and by means of a homogenisation procedure, transfer those values to the macroscopic scale. The two-scale boundary value problem involves two distinct equilibrium conditions, at the macro- and micro-scales, which must be satisfied simultaneously (see Box 6.1). Figure 6.1 shows the flow diagram for two-scale analysis. In general, the resulting coupled mechanical problem can not be solved analytically. Numerical methods based on FEM are particularly well suited for actual computations.

This chapter describes the structure of a multi-scale finite element computer program. The code described here – written in MATLAB language – has been developed for two-scale analysis of generally dissipative non-linear solid under the small strain assumption.

Macro-level		***Micro-level***
• Initialize the macro and micro model		
• Specify an RVE to every macro elements at GP	→	• Assemble the RVE's stiffness
		• Prescribe boundary condition
• Assemble global stiffness and obtain incremental displacement	←	• Calculate the overall tangent modulus
• Obtain the incremental macro strain for each element at each GP	→	• Solve the boundary condition for imposed macro strain
• Assemble global internal force	←	• Obtain the average stress
• Check for convergence		

Box 6.1. Two-scale analysis procedure.

6.2 The `MULTISCALE` function

The multi-scale code is organised in three main parts: data input, analysis, and output. The main function is named `MULTISCALE`. It calls the (sub-)functions listed in Table 6.1 [69].

Name of the function	Description
`READ_DATA`	For reading the data.
`RESET_VARIABLES`	For resetting and initializing the variables.
`Load_incr_loop`	For solving the single or multi-scale problems.
`PLOTTING_MESH`	For plotting the initial and deformed meshes and relevant contour plots.

Table 6.1: List of functions called by main program `MULTISCALE`.

A general flowchart of the program is shown in Figure 6.1.

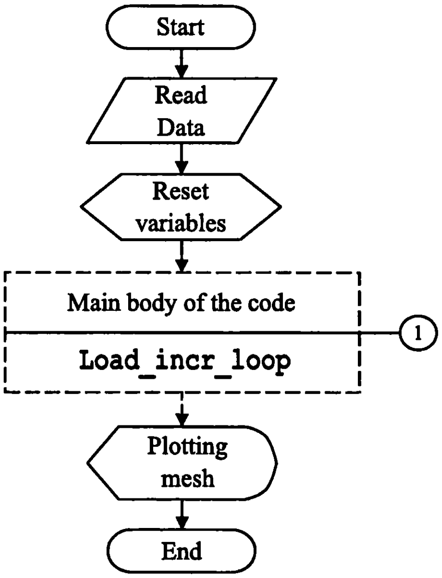

Figure 6.1: Flow chart for Multi-scale code.

Data input is carried out by function `READ_DATA`. Program variables are divided variables into two groups;

1. The variables that are fixed during the process.
2. The variables that may be updated during the process.

The first group contains: material types (elastic, plastic, visco-plastic), analysis type (plane strain, plane stress or axisymmetric), information about geometry of the macro-structures or micro-structures, material properties and element groups (for multi-material models), types of element and element properties (number of gauss points), thickness (for plane stress), load history which includes the number of load increment, load factors, time history (for visco-plastic materials), convergence tolerances and number of iterations for Newton-Raphson method, prescribed displacements, external loads, rotation angle (for some models which rotation of the structure is required) and amplification factor for plotting deformed meshes.

The variables like internal forces, accumulated load factors, total time and relevant variables for each load increment, from load history, total displacements, reactions, prescribed values for nodes (for solving the boundary conditions problems for macro- or micro-structure) and state-variables belong to the second group.

All fixed are stored in a structure named `ibvp`, and variables that may be updated are stored in structure `variables`.

In this way, the code can be organised with a recursive structure which, in principle, may contain as many scales as necessary (see Figure 6.2).

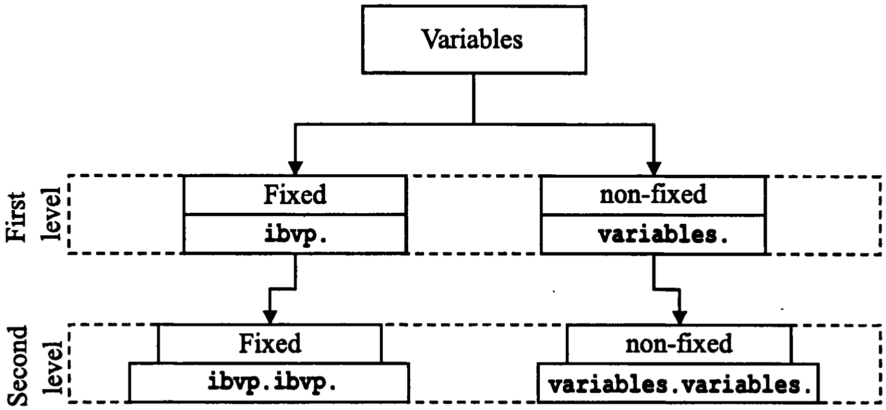

Figure 6.2: Hierarchical structure for variables.

The `Load_incr_loop` function is the main body of the code. All calculations for single- and multi-scale problems are performed in this function.

After the `Load_incr_loop` function is executed, the `plot_mesh` function will plot the initial and deformed meshes, different stress contour plots, and the effective plastic strain contour plot (for elasto-plastic material models) for the macro-structure. In the next sections we will briefly review these sub-functions.

6.2.1 The `Load_incr_loop` function

As mentioned above, this function works as a main body for the multi-scale code. This function contains two main loops; the outer loop over load increments, and the inner loop, which iterates for the solution of incremental equilibrium equations using the Newton-Raphson algorithm.

Figure 6.3, shows the flowchart of the macro-scale computation at the two-scale analysis method (see section 5.7.5), which has been defined in `Load_incr_loop` function. The numerical algorithm for the macro-scale analysis has the same structure as that of the standard FEM. This structure has been defined in a way that for the multi-scale analysis the calculation for the overall tangent modulus and the average stress are performed through the associated sub-functions.

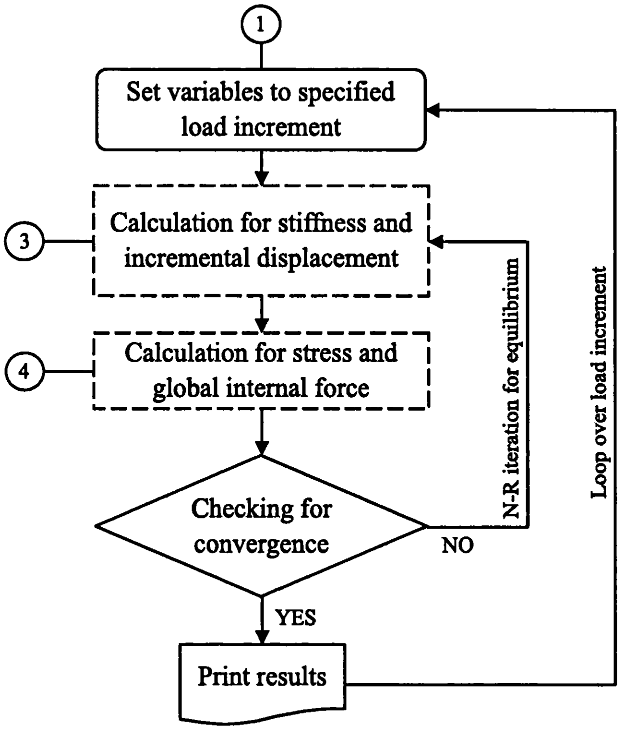

Figure 6.3: Flow chart for `Load_incr_loop` function. Two main loops over load increment and over N-R algorithm.

Two points should be considered during the multi-scale analysis:

1. *The estimation process for the macroscopic stress and strain.* As shown in equations (5.29) and (5.30), these macroscopic values are evaluated as the volume-average quantities of the corresponding microscopic ones, which are actually the solutions of the micro-scale self-equilibrium problem. In other words, the non-linear material responses at macro-scale are evaluated at Gauss points in the macroscopic domain, at which the micro-scale problem is solved for the self-equilibrated stress state. Accordingly, the micro-scale problem plays the role of the macro-scale constitutive relation in an implicit manner. More specifically, the macroscopic FE (finite element) model identifies the microscopic FE analysis results with 'the material property at a macro-scale integration point'. In the actual macroscopic FE algorithm, a macroscopic FE is assigned an ID number of the corresponding cell model instead of the material ID in the usual FE analysis. Such treatment is schematically illustrated in Figure 6.4 [30].

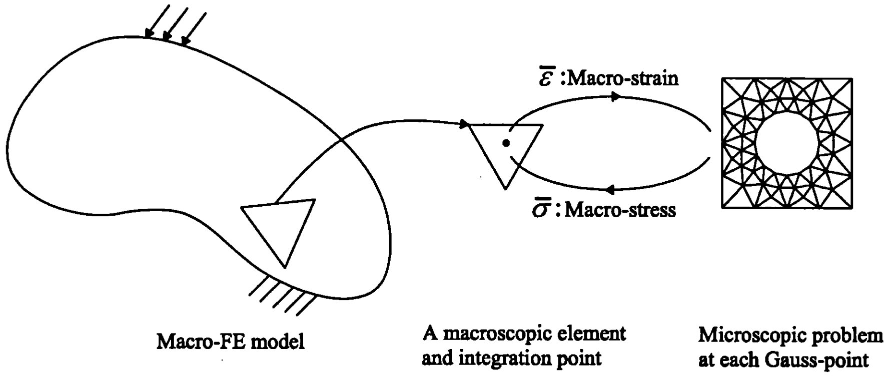

Figure 6.4: Illustration of the algorithmic structure of two-scale analysis.

2. *The macroscopic tangent modulus of the linearized equation for the macro structure.* This homogenised tangent modulus naturally arises along with the requirement of the consistency between micro-and macro equilibrium states [30],

$$\mathbf{C}_n^i := \frac{\partial \bar{\sigma}_n^i}{\partial \bar{\varepsilon}_n^i}, \tag{6.1}$$

In equation (6.1), the superscript, i, illustrates the number of the iteration in Newton-Raphson algorithm and the subscript, n, indicates the time or loading step [30].

By setting the variables into the relevant load history values, the code calculates the stiffness and incremental displacement by calling the relevant functions. Based on the total displacement, the elemental displacements, strain and incremental strain are obtained.

These variables will be used in the subsequent steps, which are the functions for updating state-variables and estimating the global internal forces. The cited subfunctions are defined in `global_internal_force` function (see Figure 6.3).

Checking for convergence is the next step in `load_incr_loop` function. This function is used to check [31],

$$\mathbf{R}(\mathbf{U}_{n+1}) \equiv \mathbf{F}^{int}(\mathbf{U}_{n+1}) - \mathbf{F}_{n+1}^{ext} = 0, \tag{6.2}$$

where the global internal and external forces at time, t_{n+1}, and nodal displacement, $\mathbf{U}_{n+1}$, are represented respectively by, $\mathbf{F}^{int}(\mathbf{U}_{n+1})$, and, $\mathbf{F}_{n+1}^{ext}$.

The norm of the residual, $\| \mathbf{R}^{i+1}_{n+1} \|$, may be less or more than the predefined tolerance, therefore the flag for convergence will be set to the relevant situation. If the iterative method converged after, $i + 1$, iterations, the results will be printed into the output text file and the procedure will be repeated by new values for load increment, otherwise same procedure will be continued for the next iteration till the obtained results by the Newton-Raphson method satisfied the equilibrium equations.

We should emphasize that if the numerical solution is converged, the state-variables are reset to the converged values, which are cited as `old` values and at the multi-scale problems, if the solution for macro-structure is converged, the convergence flag for macro-structure will be set to `true`, otherwise as mentioned, the procedure will be repeated as long as the equilibrium is obtained. [69].

6.3 Automatic load increment cutting

Due to non-linearity of the proposed problem, the converged results may not be obtained from the solution of the equilibrium equations at macro- or micro-level. To cope with this problem and make the structure of the code robust, the load increment cutting facility has been defined. This function, can be activated by the following reasons:

1. Not getting the converged solution at macro-level within the maximum allowed number of the Newton-Raphson iterations. In this case load increment cutting flag will be set to active sign inside the convergence function and all the variables will be reset to the last converged results.

2. Failure due to the iterative procedure at micro-level to get the converged solution within the total number of the Newton-Raphson iterations. In this case load increment cutting flag will be set to active sign at micro averaging stress function and at macro-level all the variables (macro- and micro-levels) will be reset to the last converged results.

3. Failure in stress update functions (at macro- or micro-level). In this case load increment cutting flag will be set to active sign inside the stress update function and all the variables will be reset to the last converged results.

The load increment cutting has been defined to reset and restart the new procedure by taking the half of the failed load step. MATLAB's facilities have been used to call the main function, `Load_incr_loop`, to solve the same problem at the failed time step for the new load steps. Figure 6.5, shows the check points for the load increment cutting function in the main multi-scale algorithm.

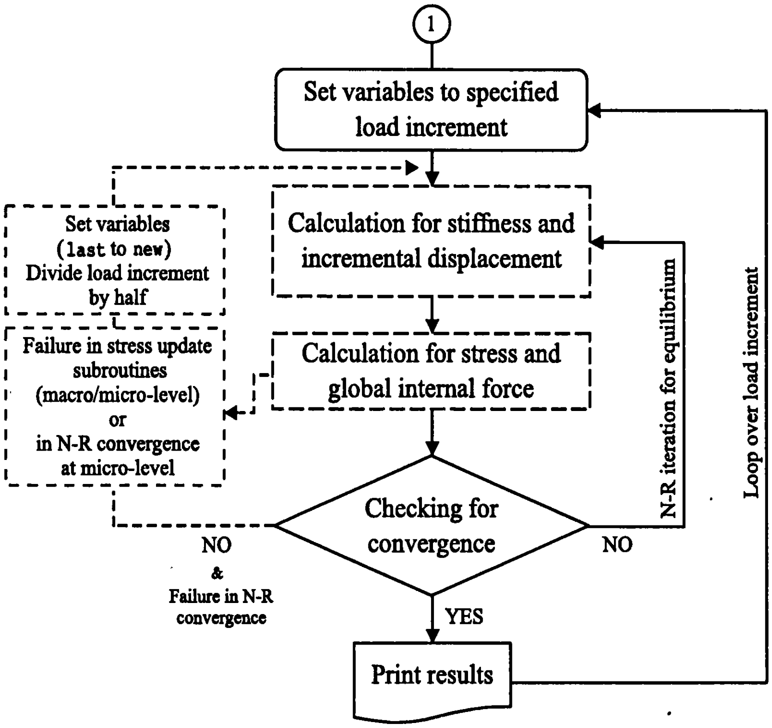

Figure 6.5: Functional position for load increment cutting facility.

6.4 Macro-and micro-scale coupling

The goal in this part is to develop and implement a single structure for solving the single- and multi-scale problems concurrently. The procedure is for estimating the state-variables at Gauss-points at the macro-level and respectively the micro-structures, which are defined in these points. The code should solve a new problem at micro-level. Therefore, for solving the micro-structures under the prescribed boundary condition at micro-level, an independent routine has been implemented to solve the problem at micro-level and pass the averaged stresses to macro-level. Based on the first supposition, hierarchical structure for the variables (see Figure 6.2), the new problem is defined by passing the specified level's variables into the cited function. This process is illustrated in Figure 6.6. The advantage of this method is that the code is completely independent at the different scales. Therefore, the defined structure for variables plays the main role at the multi-scale analysis.

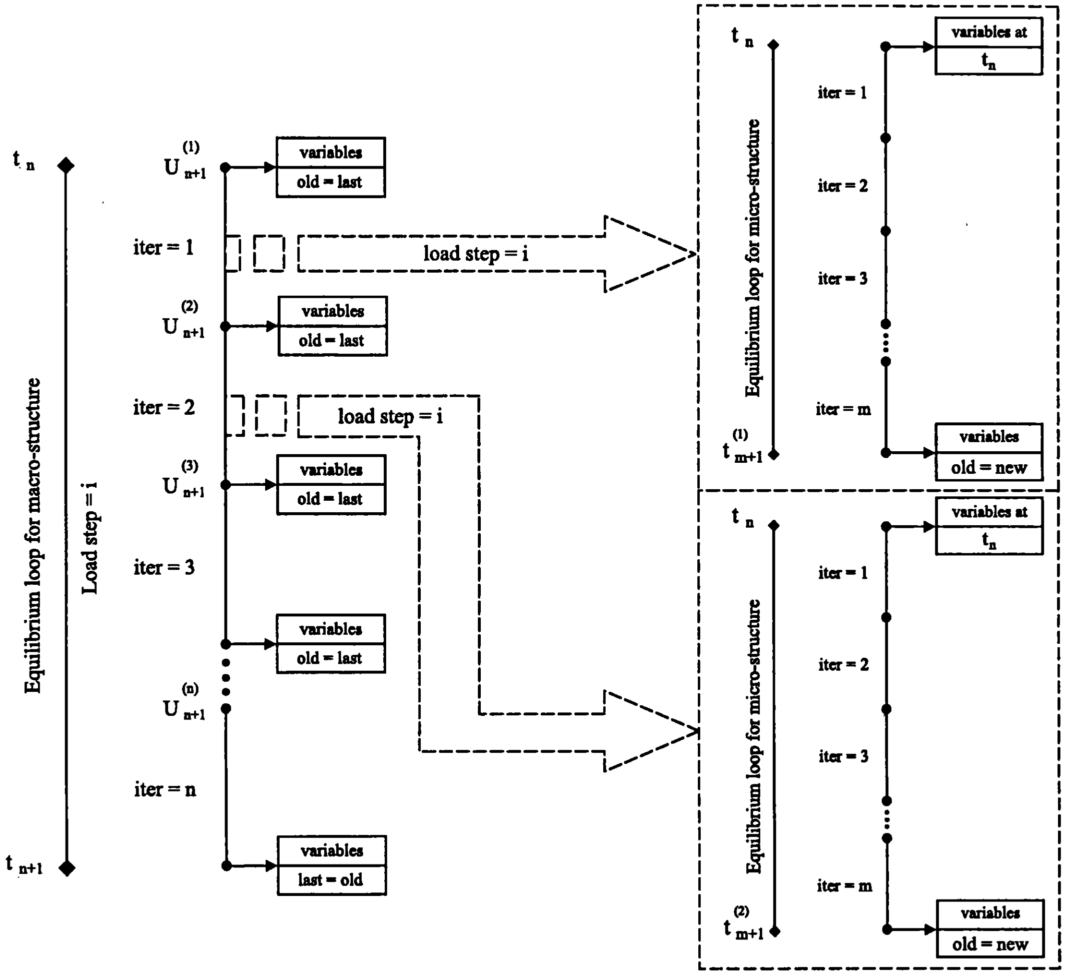

Figure 6.6: Illustration of the concurrent algorithm for two-scale analysis.

Figure 6.6, shows conjugacy of the multi-scale analysis. Initially, the code starts to analyze the macro level. In different iterations at macro-level, the new problem is defined at the micro-level by specified boundary condition. After this stage, the new problem is solved as single-scale problem. As can be seen from Figure 6.6, the micro-levels have the same pattern and the same solver for non-linear problems as macro-level. The obtained results based on the homogenisation theory (see section 5.7.2) are transferred to macro-level at the relevant integration points.

An important point at the multi-scale analysis is that, although the solution at the micro-level may converge in m iterations, the macro-level solution may still not be converged. In this case the obtained homogenised results for integration points at macro-level, based on the converged results at micro-level, should not be assumed as converged and final results. Therefore, because these results are temporary, they are located in `new` part of the structural variables (`old` at micro-level is defined as `new` at macro-level). As long as the results are converged at macro-level after, n, iteration, the converged results are saved into the `last` part of the structural variables. As cited in section 6.2, for the subsequent load step, these values will be used as initial values for the variables [69].

6.5 Multi-scale analysis for the overall stiffness matrix and state-variables

This part reviews the structure of the code in the case of assembling the overall stiffness matrix, estimating the homogenised tangent modulus and the state-variables. As mentioned in section 6.2.1, in the multi-scale analysis, the relevant variables are used to solve the problem in two main sub-functions: assembling the global stiffness and updating the global internal force based on the homogenised stress field (see Figure 6.3). According to Figure 6.3, the first sub-function is used for estimating the homogenised tangent modulus, overall stiffness matrix and calculating the overall incremental displacement which is obtained from [69],

$$\mathbf{K}^{i}_{n+1} \triangle \mathbf{u}^{i+1}_{n+1} = -\mathbf{R}^{i}_{n+1}, \tag{6.3}$$

where $\mathbf{K}$ is the global stiffness, $\triangle\mathbf{u}$ is incremental displacement and $\mathbf{R}$ indicates the residual. Integers i and n represent the number of iterations and relevant time steps respectively.

According to Figure 6.3, the first step is to estimate the tangent modulus, assembling the global stiffness and in addition, solving the equation (6.3). These calculations are performed in `assemble_solve` function and relevant sub-functions. These series of calculation are shown in Figure 6.7 [69].

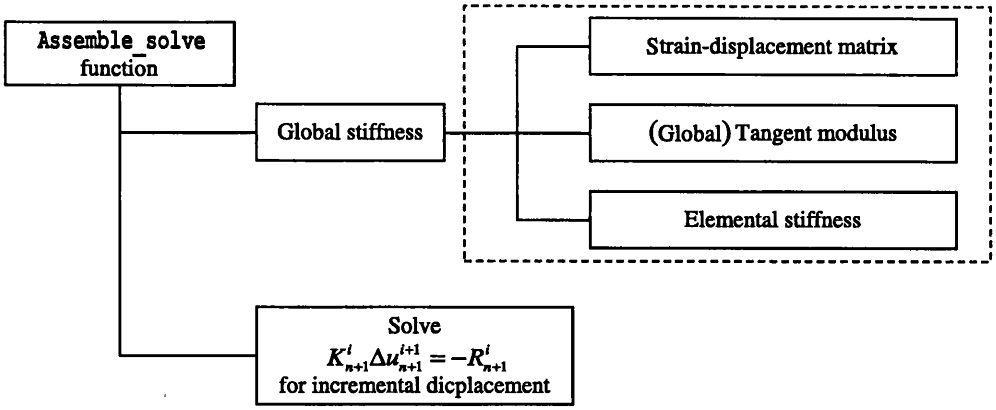

Figure 6.7: Process of assembling the global stiffness and calculating the incremental displacement.

It can be seen from Figure 6.7 that, the main function has been divided into two parts. The first section is used for assembling the global stiffness while, the second section is used to solve the equation (6.3).

In the first part of this division, the code has been organized to determine the tangent modulus for different types of material from separate sub-functions (material routines). Note that the homogenisation of the tangent stiffness matrix is obtained from the consistency between micro-and macro-scale equilibrium states.

Importantly, in this stage we have implemented a strategy for solving the multi-scale problems. We have defined the '*multi-scale*', as a type of material models. Therefore, material type '*multi-scale*' is recognized by the multi-scale code as material models, such as, linear elastic material model or elasto-plastic von Mises material model.

The advantage of this assumption is that, after solving the relevant boundary condition, over the cell, for obtaining the stiffness at the micro-level, the unique procedure is followed by the code for calculating the tangent modulus and stiffness in the same fashion as when solving the problem for the single-scale material models. This procedure is illustrated as a flowchart in Figure 6.8. It should be mentioned that in the multi-scale analysis and for obtaining the homogenised tangent modulus based on different boundary conditions at micro-level, a switch function `CTMULT`, has been defined. The function of `CTMULT` is to call the relevant sub-routines for calculating the overall tangent modulus at micro-level and based on the prescribed boundary condition over the cell [69].

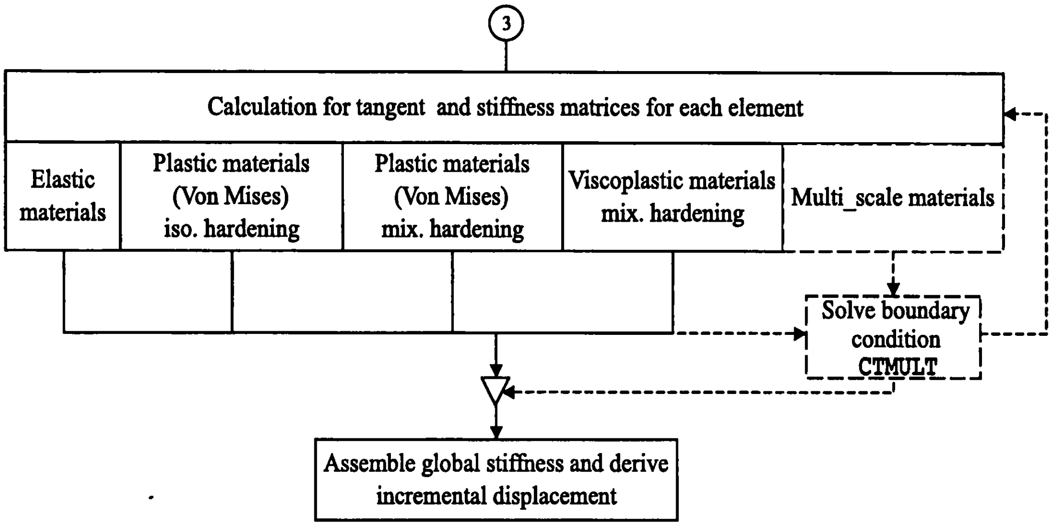

Figure 6.8: Flow chart for assembling the global stiffness and relevant variables. Multi-scale is defined as a type of material model.

Figure 6.8, shows different sections, based on different types of material. The sub-functions (material routines), which are defined in `MULTISCALE` code, are completely independent and they are detached, based on different types of material and type of analyses (plane-stress, plane-strain or axisymmetric (only for single-scale analysis)).

As can be seen from Figure 6.8, in the case of multi-scale analysis, we defined a '*multi-scale*' material model. When the code reaches from macro-level to this stage, by solving the prescribed boundary condition over the cell at micro-level, the homogenised tangent modulus is obtained for the corresponding integration point at macro-level. The procedure, which the code follows for the multi-scale analysis, is the same as the single-scale analysis' procedure, except the part, which is defined for solving the boundary conditions at micro-level.

The second part of the multi-scale code according to Figure 6.3, relates to the updating stress components, the state-variables and assembling the global internal forces. These calculations are performed in `global_internal_force` function and relevant sub-functions. In this part of the code we followed the same detachment as in the previous section; that is defining the '*multi-scale*' as a new type of material. As already mentioned, the independent material routines have been applied for updating the state-variables as the ones used in estimation of the tangent modulus.

Figure 6.9, shows this procedure for updating the state-variables and assembling the global internal forces [69].

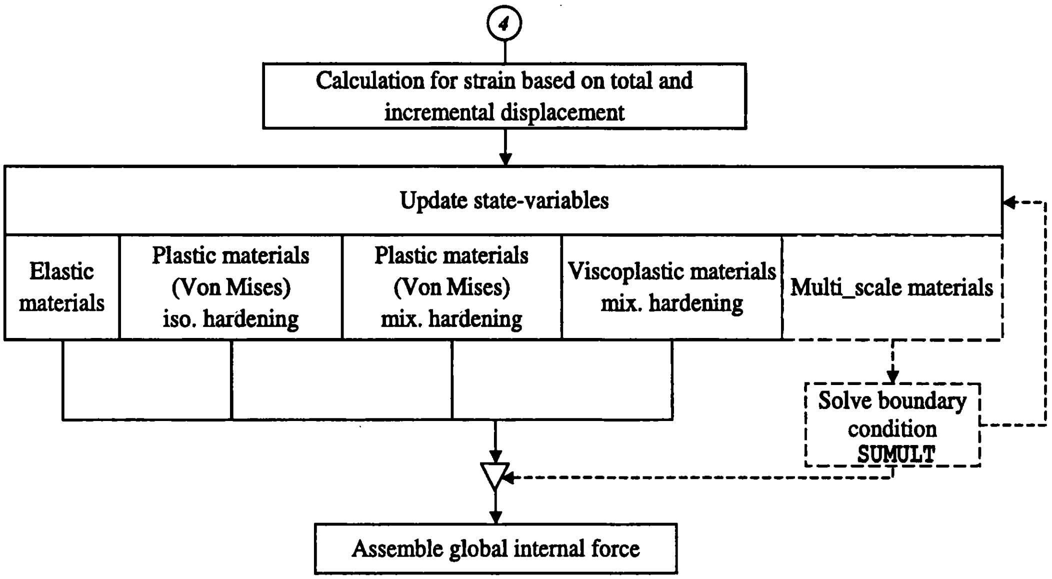

Figure 6.9: Flow chart for updating state-variables and assembling global internal forces. Multi-scale is defined as a type of material model.

For updating the state-variables, such as stress components, at each Gauss point, the strain tensor is required. The procedure in the multi-scale code has been design to obtain the strain tensor and the material properties before updating and calculating the state-variables from the relevant material routines. In the multi-scale analysis, the main transition between macro- and micro-scale analysis is done by passing the macro-strain for the specific integration point at the macro-level to the micro-level and by solving the prescribed boundary condition over the cell at micro-level. The macroscopic variables and the homogenised stress tensor are then obtained and returned to the integration point at the macro-level (see Figure 6.4).

As can be seen from Figure 6.9, in the section 'multi-scale material models', the variables, with regard to the last converged flag or the load increment cutting flag for the macro-structure, will be reset to the relevant variables structures at micro-level. After resetting the variables for the micro-level, the independent function is called from macro-level to solve the prescribed boundary condition over the cell and calculate the homogenised stress field at micro-level. Note that this function is called for each integration point at the macro-structure.

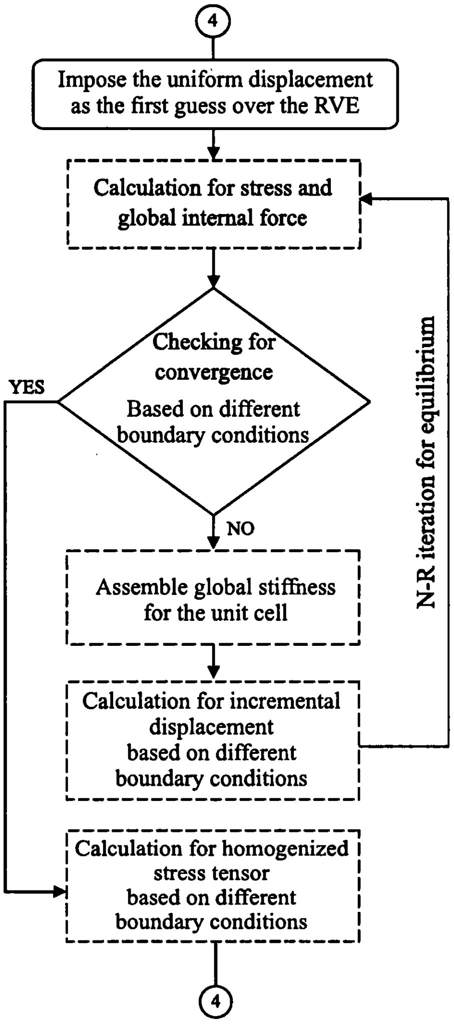

Figure 6.10: Flow chart for updating state-variables and calculating the homogenised stress tensor at micro-level.

Figure 6.10 shows a flowchart for the function used to solve the prescribed boundary condition at micro-level and the homogenised stress field. This function has been called `SUMULT` in multi-scale code, which represents the stress update for multi-scale material models.

Note that the new problem is defined at micro-level for relevant macro-iteration number (see Figure 6.6). Based on the obtained results from micro to macro transition and FEM (see chapter 4), the global forces will be assembled.

Figure 6.11 illustrate the main structure and the links between substructures of the multi-scale code. Different paths have been indicated by 1, 2, 3 and 4.

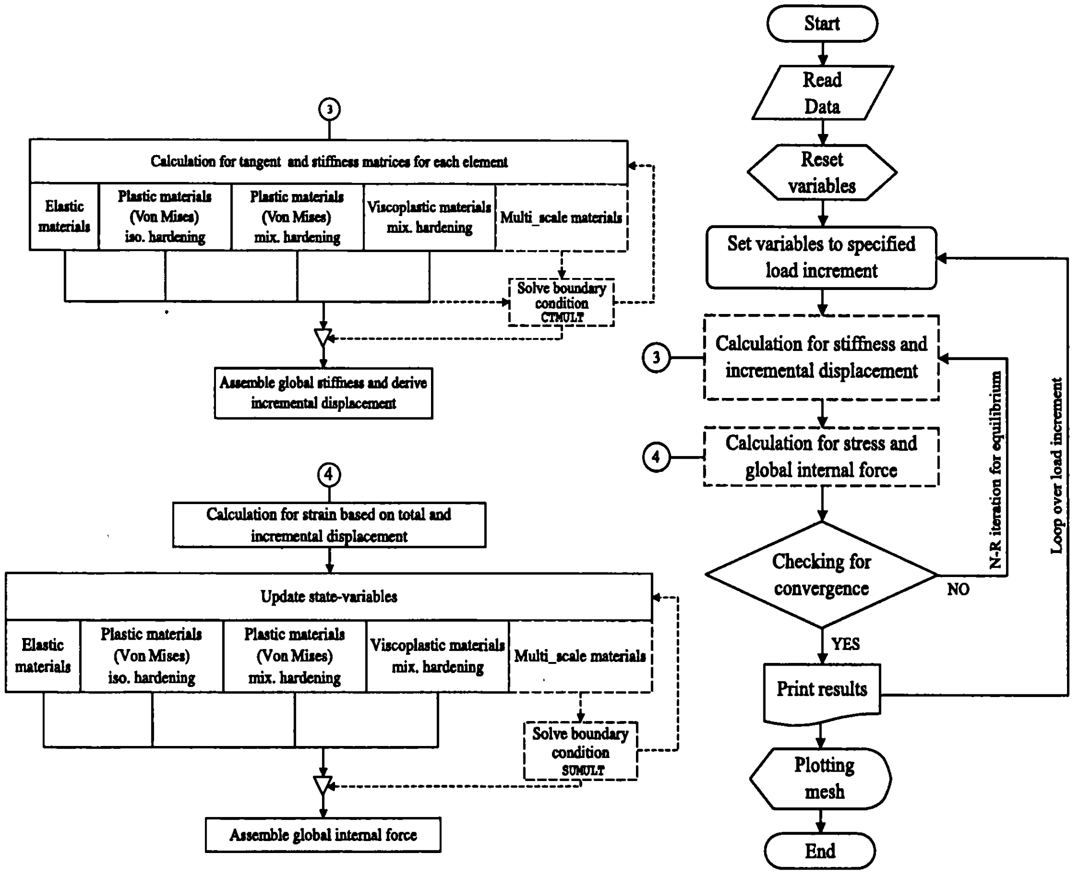

Figure 6.11: Flow charts for multi-scale analysis.

6.6 Conclusion

In this chapter implementation of the multi-scale finite element code has been described. The code is based on an incremental procedure for general dissipative materials coupled with a full Newton-Raphson scheme for equilibrium iterations. A key feature of the multi-scale program is its recursive hierarchical structure whereby the main equilibrium procedure calls itself when, at the Gauss point, computational homogenisation is used to describe the material behaviour.

Also worth nothing is, its data structure in which the macro-problem description contains all micro-information stored with a similar structure compatible with the recursive nature of the equilibrium problem.

Chapter 7

Comparison between analytical and numerical methods for the overall response of the elastic material models

7.1 Introduction

This chapter presents numerical examples to validate the elastic part of the multi-scale code. The analysis has been focused on two types of micro-structures: dilute distribution of cavities in the cell and dilute distribution of fibres in the RVE. It should be mentioned that the dilute distribution of cavities/fibres is an additional restriction in analytical analysis to avoid the effect of interaction between cavities/fibres and this restriction is not applicable to computational homogenisation. The accuracy and the validity of the numerical results for the effective material properties have been assessed by comparison with analytical solutions presented in chapter 5. Some of the presented solutions are based on the different types of micro-structures under the plane strain or plane stress assumptions. In addition, for dilute distribution of cavities in the cell, the numerical results have been compared with the numerical results based on the damage theory.

7.1.1 Void volume fraction theory

This theory has been discussed in section 5.2.1. Table 7.1 contains the estimated effective values for Young's modulus and Poisson's ratio based on equations (5.2)-(5.10) for a material whose matrix properties are $E = 70\ GPa$ and, $v = 0.2$.

Macro-stress prescribed		
f	$\bar{E}$	$\bar{v}$
5%	60.86956522	0.2173913
10%	53.84615385	0.23076923
15%	48.27586207	0.24137931
20%	43.75	0.25
30%	36.84210526	0.26315789
40%	31.81818182	0.27272727
50%	28	0.28
60%	25	0.28571429
70%	22.58064516	0.29032258

Macro-strain prescribed		
f	$\bar{E}$	$\bar{v}$
5%	59.4660194	0.22330097
10%	48.8372093	0.25581395
15%	38.0434783	0.30434783
20%	26.9230769	0.38461538
30%	0	1
40%	0	-1
50%	-28	-0.28
60%	-50	-0.14285714
70%	-71.1864407	-0.08474576

Table 7.1: Effective material properties based on analytical estimates [1].

The values in Table 7.1, are given for both the prescribed macro-stress and macro-strain assumptions. The effective Young's modulus $\bar{E}$ and Poisson's ratio $\bar{v}$ are displayed against the values for percentage of the void volume fraction f. As can be seen from Table 7.1, material properties under the prescribed macro-strain assumption are acceptable up to 30% of void volume fraction of the RVE.

7.1.2 Damage theory

Table 7.2 contains the values for the effective Young's modulus, $\bar{E}$, and damage variable, D, with respect to the percentage of the void volume fraction, f, based on the equations (5.11)-(5.13). Note that the initial values for material properties are: $E = 70\ GPa$, and $v = 0.2$.

f	D	$\bar{E}$
5%	0.05	66.5
10%	0.1	63
15%	0.15	59.5
20%	0.2	56
30%	0.3	49
40%	0.4	42
50%	0.5	35
60%	0.6	28
70%	0.7	21

Table 7.2: Effective material properties based on damage theory.

7.2 Dilute distribution of fibres

Table 7.3 contains the effective values for Young's modulus and Poisson's ratio based on equations (5.25)-(5.28). The material properties for the matrix are: $E = 70\ GPa$ and, $v = 0.2$, and for the inclusion, $E^I = 210\ GPa$ and $v^I = 0.3$.

Macro-stress prescribed			Macro-strain prescribed		
f	$\bar{E}$	$\bar{v}$	f	$\bar{E}$	$\bar{v}$
5%	73.182	0.205	5%	73.042	0.205
10%	76.667	0.21	10%	76.081	0.209
15%	80.5	0.216	15%	79.118	0.213
20%	84.737	0.223	20%	82.152	0.216
30%	94.706	0.239	30%	88.215	0.222
40%	107.334	0.258	40%	94.271	0.228
50%	123.847	0.284	50%	100.322	0.233
60%	146.366	0.319	60%	106.369	0.237
70%	178.892	0.37	70%	112.412	0.241

Table 7.3: Effective material properties based on analytical solutions for dilute distribution of micro-inclusions.

7.3 Numerical tests with elastic assumption

In this section we consider two groups of micro-structures. The first group is the micro-structure with a hole, and the second group is the micro-structure with the elastic inclusions instead of the holes and elastic material in the matrix.

In general, we defined four types of micro-structure for each group. Each group contains different void or inclusion volume fraction (VVF or IVF) values in RVE. The side length of the cube-shaped representative micro-structure under the consideration is $1\mu m$. Table 7.4 shows different numerical models of micro-structure in both groups.

Micro groups	Number of Elements	Number of Nodes	Void Volume Fraction
Model 1	878	487	5%
Model 2	816	459	10%
Model 3	785	446	15%
Model 4	736	424	20%
Micro groups	Number of Elements	Number of Nodes	Inclusion Volume Fraction
Model 1	922	502	5%
Model 2	918	500	10%
Model 3	930	506	15%
Model 4	912	497	20%

Table 7.4: Different models of micro-structure.

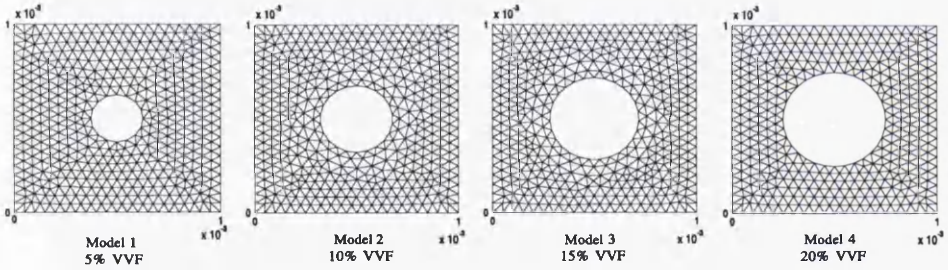

Model 1
5% VVF

Model 2
10% VVF

Model 3
15% VVF

Model 4
20% VVF

Figure 7.1: Different FE models of micro-structure based on various values of void volume fraction (VVF).

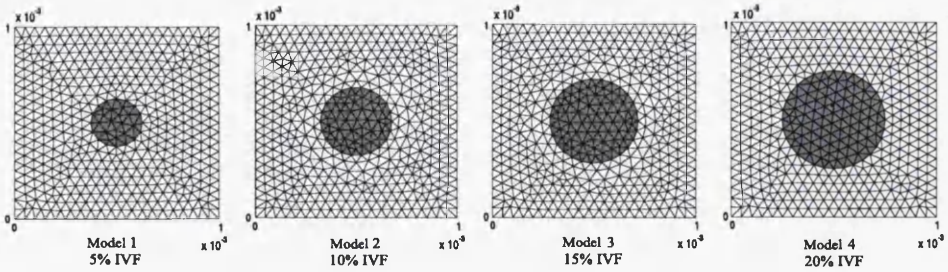

Model 1
5% IVF

Model 2
10% IVF

Model 3
15% IVF

Model 4
20% IVF

Figure 7.2: Different FE models of micro-structure based on various values of inclusion volume fraction (IVF).

Figure 7.1 shows different FE models of micro-structure based on various values of void volume fraction and Figure 7.2 shows different types of micro-structure based on various values of inclusion volume fraction.

As a first numerical test to obtain the homogenised properties of micro-structures and based on the first group of micro-structures, a single square macro-structure is defined with suitable boundary condition and by imposing the prescribed displacement on the RVE the variation of the effective shear modulus, $\bar{\mu}$, from multi-scale analysis, with respect to the matrix shear modulus, μ, has been plotted (see Figure 7.3). In the same figure the graphs for the prescribed macro-stress and macro-strain based on the void volume fraction theory have been illustrated.

Figure 7.3 shows the variation of the homogenised shear modulus, $\bar{\mu}$, with respect to the void volume fraction, f, for plane stress analysis with $\upsilon = 0.2$.

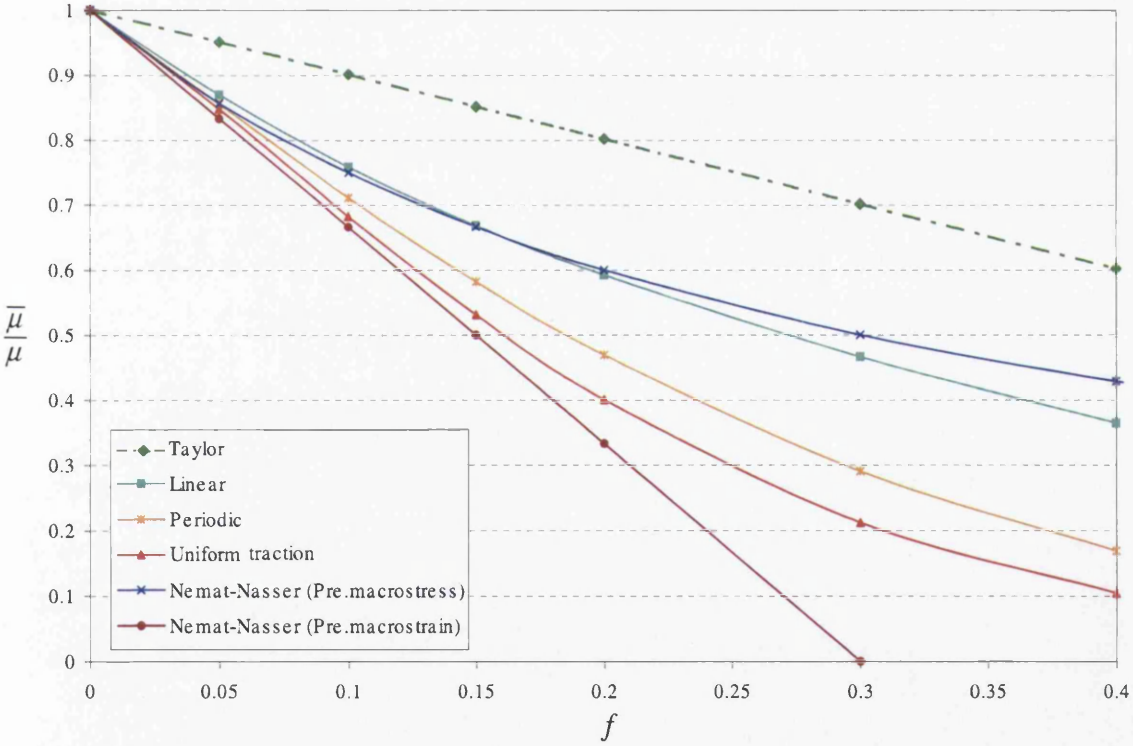

Figure 7.3: Normalized overall shear modulus for $\upsilon = 0.2$.

Since a dilute distribution of cavities is assumed, the applicability of these results is limited to small values of the void volume fraction, f [1]. As can be seen from Figure 7.3, the Taylor assumption presents the upper bound for the homogenised material properties. The closest curve to the linear displacement boundary assumption is the prescribed macro-stress curve. The results obtained for the periodic boundary displacement fluctuations condition are located between the prescribed macro-stress and macro-strain curves. On the other hand, the softest behaviour, which is obtained by the uniform boundary traction assumption, tends to the analytical curve which has been plotted based on the prescribed macro-strain assumption. Therefore from Figure 7.3 it can be concluded that the proposed assumptions by Nemat-Nasser [1], the prescribed macro-stress and macro-strain prescribed, respectively give the upper limit and lower limit for the overall elastic material properties for porous media.

In the second part of the elastic tests, we used the micro-structures with inclusions (group two). Figure 7.4 illustrates the graphs obtained from equations (5.25) - (5.28) based on the prescribed macro-stress and macro-strain. In the same figure we plot variation of the effective shear modulus, $\bar{\mu}$, from multi-scale analysis, with respect to the matrix shear modulus, μ (see Figure 7.4).

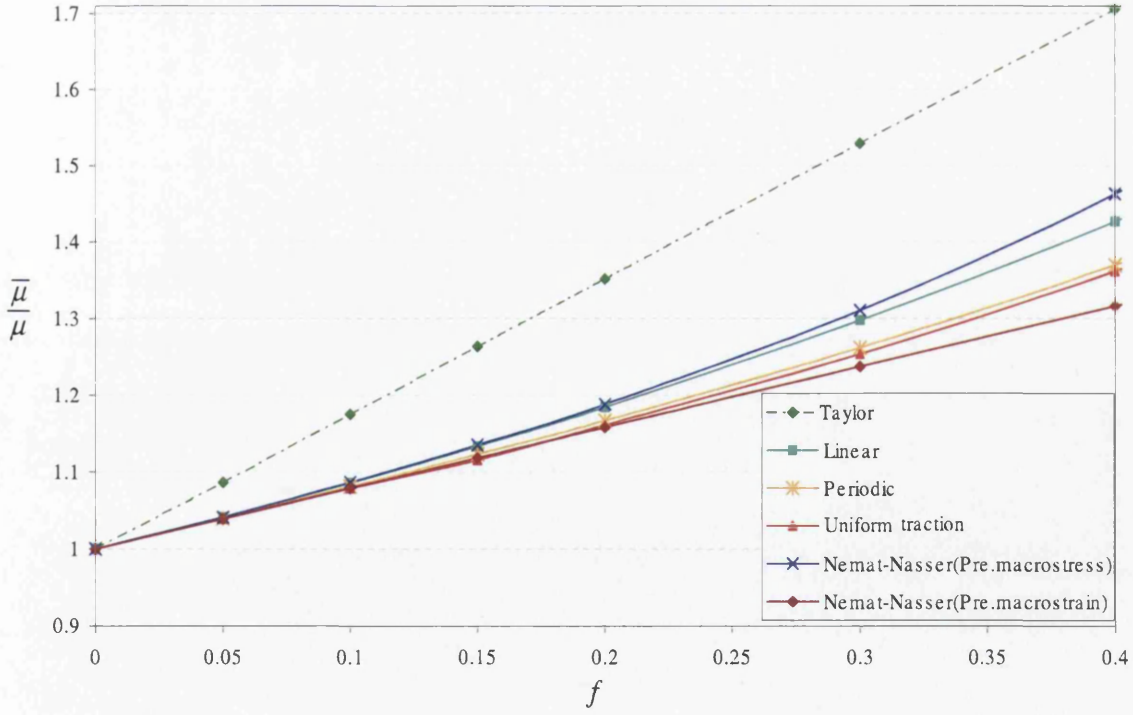

Figure 7.4: Two-dimensional overall shear moduli of an RVE with dilute distributed inclusion. $\upsilon^I = 0.3$ and $\upsilon = 0.2$.

We note that analytical results based on a dilute distribution of micro-inclusion are strictly applicable to small values of the micro-inclusion volume fraction f [1]. As can be seen from Figure 7.4, the graph obtained from the linear displacement boundary condition presents the closest curve to the graph obtained from the prescribed macro-stress assumption. On the other hand, the lower bound is presented by the curve based on the prescribed macro-strain assumption and the closest curve is obtained from the uniform boundary traction assumption.

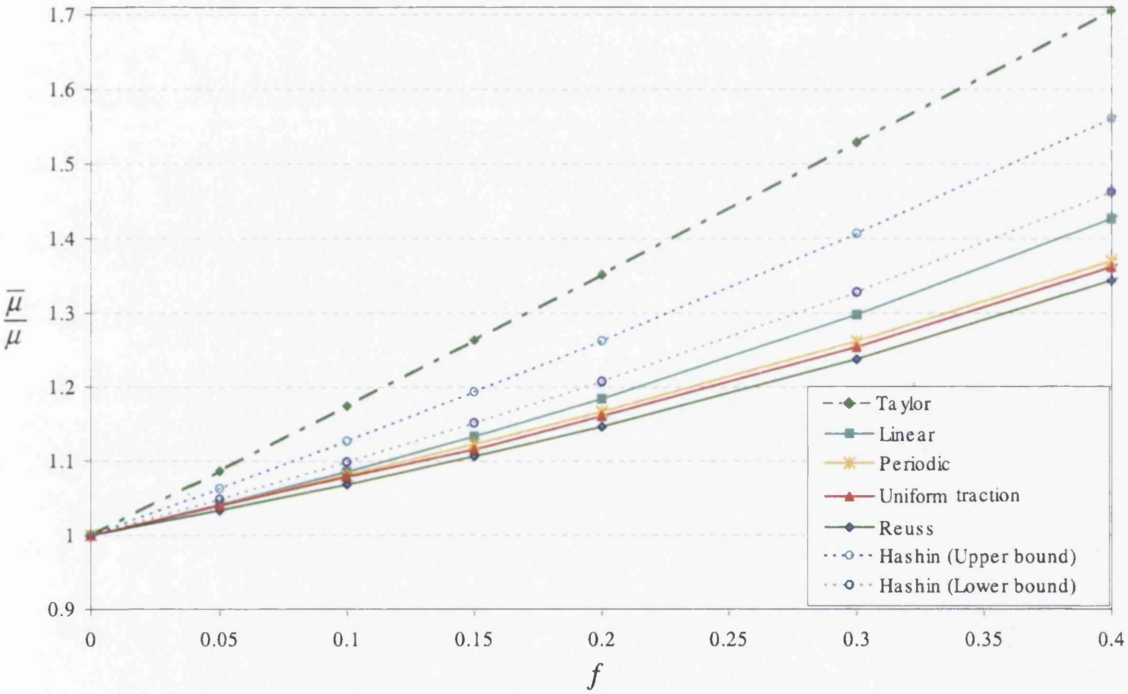

Figure 7.5: Two-dimensional overall shear moduli of an RVE with dilute distributed inclusion. $\upsilon^I = 0.3$ and $\upsilon = 0.2$.

Figure 7.5 shows the numerical results based on the multi-scale analysis and the analytical results based on; the Taylor, Reuss, and Hashin - Shrikman assumptions. From Figure 7.5 it can be seen that the stiffest behaviour is obtained by the Taylor assumption from numerical analysis. Both Hashin - Shrikman assumptions (upper bound and lower bound) show softer behaviour with respect to the Taylor assumption. Both Hashin - Shrikman assumptions show stiffer behaviour in comparison with the other assumptions. As can be seen from Figure 7.5 among the analytical methods, the Reuss method presents the lower bound for the homogenised material properties while, in numerical methods the lower bound has been presented by the uniform boundary traction assumption.

7.4 Conclusion

In this chapter we presented the different numerical examples for the multi-scale analysis. Firstly, based on the analytical solution for the dilute distribution of micro-cavities, and damage theory, and for the dilute distribution of fibres at micro-level, from the theory presented by Nemat-Nasser [1], we obtained the effective material properties for different values of void/inclusion volume fraction at micro-cell. The analytical solutions were used to obtain the upper and lower bounds for the overall elastic material properties.

Numerical multi-scale tests were performed to validate the accuracy of the obtained homogenised elastic material properties with the analytical obtained results from the above theories. For the multi-scale tests, two types of micro-structures were considered: The RVE with different percentage of the micro-cavities and the unit cell with different size of the micro-inclusions.

Different boundary conditions were assumed over the RVE: The Taylor assumption, the linear displacement boundary condition, the periodic boundary displacement fluctuations condition, and the uniform boundary traction assumption.

The important observations are:

- The obtained overall behaviour of the multi-scale analysis from the micro-cavity models under the uniform boundary traction assumption shows the closest response to the analytical behaviour obtained from the macro-prescribed strain assumption. On the other hand, the obtained homogenised behaviour from the linear displacement boundary condition shows closest response to the prescribed macro-stress assumption in void volume fraction theory.

- The obtained overall behaviour of the multi-scale analysis from the micro-inclusion models under the uniform boundary traction assumption shows the closest response to the analytical behaviour obtained from the prescribed macro-strain assumption. On the other hand, the obtained homogenised behaviour from the linear displacement boundary condition shows closest response to the prescribed macro-stress assumption in void volume fraction theory.

- Among the analytical methods, the Taylor assumption provides the upper limit for the homogenised elastic material behaviour while, the Reuss assumption shows the lower limit for the overall response for the elastic material models.

Chapter 8

Study of the effect of distribution of cavities on the homogenised elasto-plastic properties

8.1 Introduction

In this chapter the homogenised elasto-plastic response of the RVE will be considered. In the first part of this chapter, basic numerical tests will be performed to benchmark the developed computational framework. In the second part, the effect of distribution of cavities on the homogenised behaviour will be considered.

8.2 Homogenised elasto-plastic response

The effect of the shape of the RVE on the homogenised behaviour of the micro-cell has been investigated by many authors. The shape of the RVE has been considered as square, hexagonal (honeycombs) and random. Among others, results have been presented by S. Ghosh, K. Lee and S. Moorthy [21], S. Ghosh, K. Lee [70], D. B. Zahil, S. Schmauder and M. McMeeking [71], V. Carvelli ans A. Taliercio [72]. The mechanical and transport properties of two-dimensional cellular solids consisting of either hexagonal, triangular, square or Voroni cells have been discussed by S. Torquato, L.V. Gibiansky, M.J. Silva and L.J. Gibson [73].

The effect of the size of the RVE on the rate of the convergence has been presented by P. Ladeveze, A. Nouy and O. Loiseau [74] and V. Kouznetsova [59].

8.3 Models specification

Two different models are considered: regular cavity model, and irregular cavity model with random distribution of voids. Two different cells are considered for each group: a single cell (reference RVE) and an RVE which is modified by repetition of the reference cell in two directions (see Figure 8.1). For all models the void volume fraction of the RVE is taken as 15%. For convenience the models are labeled as:

Reg.m-1 = 1 μm, Reg.m-2 = 2 μm (4-blocks with 4-voids),
Irreg.m-1 = 1 μm, Irreg.m-2 = 2 μm (4-blocks).

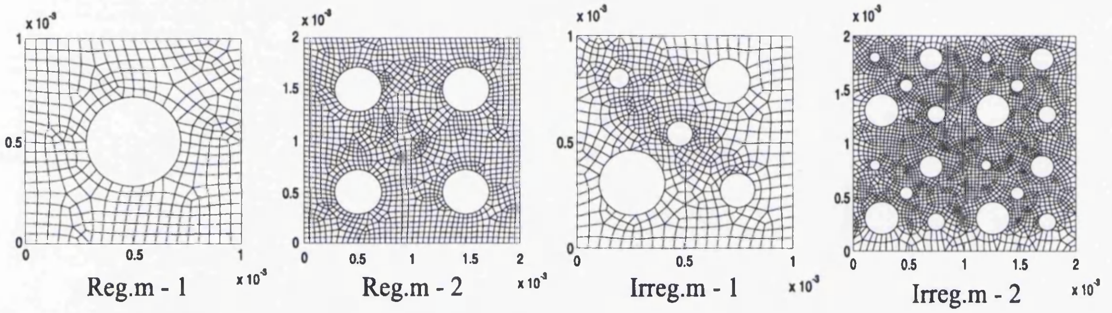

Reg.m - 1 Reg.m - 2 Irreg.m - 1 Irreg.m - 2

Figure 8.1: Different regular cavity models belong to the first group.

The 8-noded quadrilateral element with 4-Gauss points is used in all cases. The matrix in all models is assumed to be composed of the von Mises elasto-plastic material with linear strain hardening. The material properties assigned are; Young's modulus $E = 70\ GPa$, Poisson ratio $\upsilon = 0.2$, the initial yield stress $\sigma_{y_0} = 0.243\ GPa$ and strain hardening modulus $H = 0.2$.

The overall response of the RVE is considered under three assumptions; (*i*) the linear displacement boundary condition, (*ii*) the periodic boundary displacement fluctuations condition and (*iii*) the uniform boundary traction.

8.3.1 Analysis approach

All simulations have been performed by employing the computational homogenisation under plane-stress. The average stress is obtained by imposing the macro-strain over the unit cell and solving the problem for defined boundary condition over the RVE. An arbitrary imposed macro-strain tensor is expressed by:

$$[\bar{\varepsilon}_{11}, \bar{\varepsilon}_{22}, 2\bar{\varepsilon}_{12}] = [0.001, 0.001, 0.0034].$$

To obtain the load step at each load increment, the generic strain tensor is multiplied the by the relevant load factor. The multiplication factors (load factors) are defined by:

$$\lambda = [0, 0.1, ..., 4].$$

To illustrate the overall behaviour of the models, different graphs have been presented based on the effective homogenised stress,

$$\bar{\sigma}_{eff} = \sqrt{3\bar{J}_2},$$

against the Euclidean norm of the imposed macro-strain tensor,

$$\|\bar{\varepsilon}\| = \sqrt{\bar{\varepsilon}_{11}^2 + \bar{\varepsilon}_{22}^2 + 2\bar{\varepsilon}_{12}^2}.$$

Figure 8.2 shows the effective stress - strain norm graphs for the regular models under the aforementioned boundary conditions. As can be seen from Figure 8.2 the models show different responses for different imposed boundary conditions. The important point to observe is that as expected from the definition of the RVE and the periodic boundary displacement fluctuations condition, changing in the geometry of the cell, by means of the repetition of the reference cell, does not affect the homogenised behaviour of the cell.

Figure 8.3 shows the equivalent plastic strain distribution for both regular models under the periodic boundary displacement fluctuations assumption at the last converged load factor multiplied by the original strain tensor. The occurrence of localised bands with significant plastic straining can be observed on both contour plots. In addition, the growth path for the effective plastic strain for the model Reg.m-2 shows the same pattern (each block) and magnitude as the evolution path of the reference block model Reg.m-1.

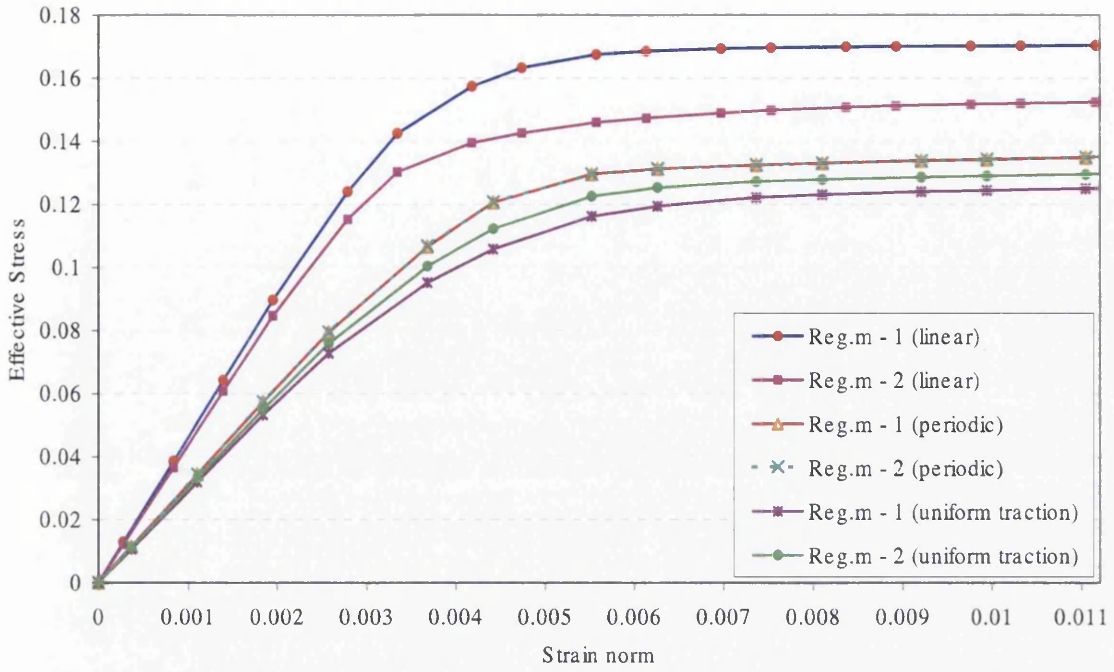

Figure 8.2: Effective stress - strain norm graphs for the regular models under different boundary conditions.

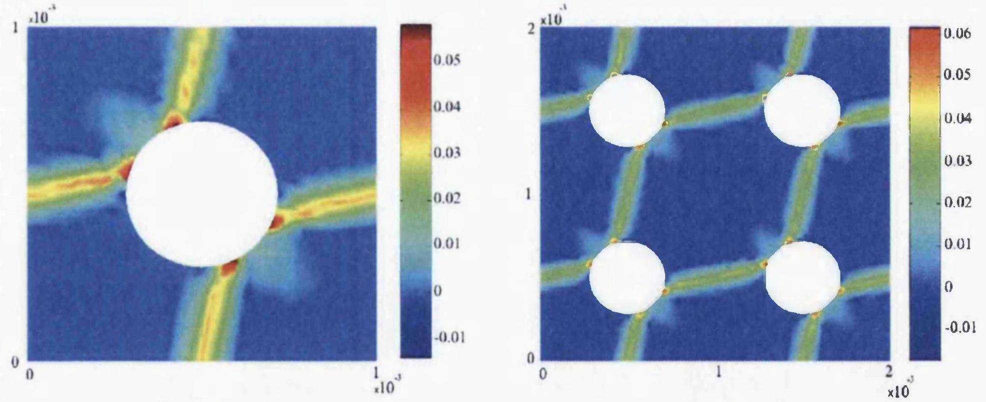

Reg.m - 1

Reg.m - 2

Figure 8.3: Effective plastic strain contour plots for the regular models under the periodic boundary displacement fluctuations assumption.

The same observations have been made from the simulations of the irregular cavity models. Figure 8.4 shows the effective stress - strain norm graphs for the irregular cavity models under different boundary conditions while the growth of the effective plastic strain has been illustrated in Figure 8.5 at the last converged load factor multiplied by the original strain tensor.

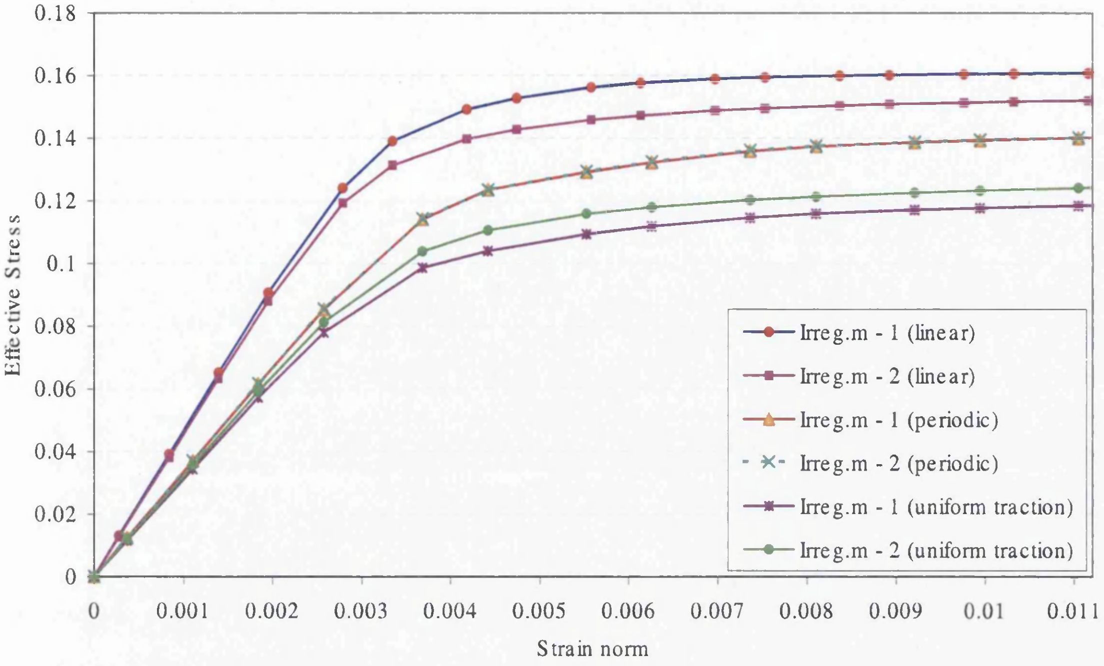

Figure 8.4: Effective stress - strain norm graphs for the irregular models under different boundary conditions.

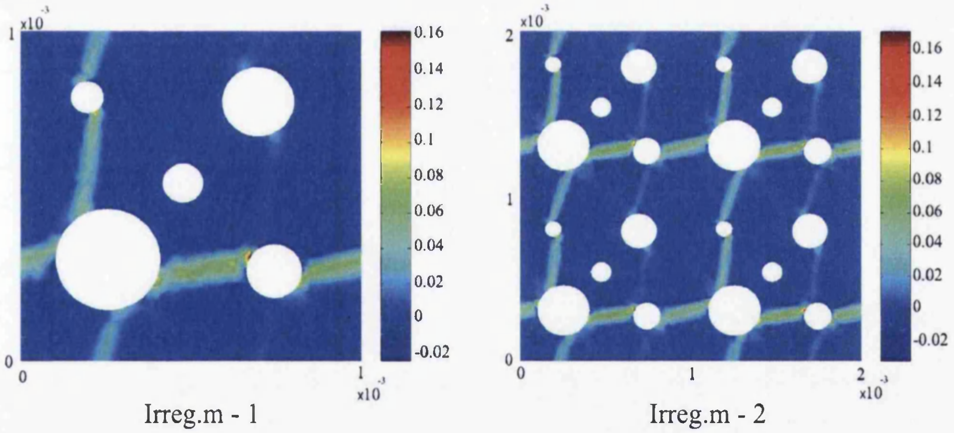

Figure 8.5: Effective plastic strain contour plots for the irregular models under the periodic boundary displacement fluctuations assumption.

In conclusion, the above results show that, for the heterogeneous media with a periodic micro-structure, the overall behaviour of the cell, as we expected, remains unchanged when the imposed constraint over the RVE is the periodic boundary displacement fluctuations.

8.4 The effect of distribution of cavities on the overall behaviour of the RVE

Porous materials with complex internal void structures have many uses in science and industry (e.g. geophysics, civil engineering, ocean engineering, petroleum engineering and environmental engineering). The relative performance of different porous solids in these applications is highly dependent on the internal pore structure of each material. Deriving the physical and mechanical properties of a porous medium from parameters describing the structure of the medium (e.g., porosity, cavity's distribution, and effective surface area) is an ongoing challenge for scientists.

In this section we validate our results for homogenised behaviour of the composite materials by comparison with other authors results. Firstly, we considered the effect of the regularity and irregularity of cavities in the micro-cell. Several works consider the effect of the regular and irregular distribution of the fibres. Among them we mention R. Foye [75], A.R. Zecca and D.R. Hay [76]. Inelastic behaviour of fibre composite materials have been investigated by T.I. Zohdi [77], N. Ohno, X. Wu and T. Matsuda [78], C.W. Nan and D.R. Clarke [79]. Reference [79] studies the effect of particle size and distribution and volume fraction on the homogenised deformation. The overall behaviour of the non-linear composites with complex micro-strutures have been studied by H. Moulinec and P. Suquet [80, 81] in which the Fast Fourier Transformation method has been implemented to avoid meshing and provide direct use of micro-structure images.

The effect of the regularity, irregularity and density of the cavities at micro-level for porous media is another research area which has been considered in many publications. R.J.M. Smit, W.A.M. Brekelmans and H.E.H. Meijer [82] have shown that the irregular void distribution causes a radical change in deformation behaviour. A continuum level elastic-plastic constitutive modeling method has been used for composite and porous materials by L. Lee and S. Ghosh [80]. The micro-structural morphology, e.g. spatial distributions, shapes, sizes, and properties of the individual phases at both macro and micro-level has been investigated for composite materials and porous media. They have shown that the anisotropy caused by the morphology and induced plastic flow in the micro-structure can be the source of the distinctly different overall responses. Finally, a complete study on the effects of the size, regularity and irregularity of distributed cavities at two scales have been performed by Kouznetsova [59].

In this section our aim is to study the overall behaviour of the RVE under two different assumptions; firstly, regular distribution of the cavities in the unit cell and secondly, randomly distribution of the cavities in the RVE.

8.5 Problem specifications

For this section we defined a square unit cell containing; (*i*) a single circular hole embedded in a soft matrix for the regular structure and (*ii*) several voids surrounded by a matrix for modelling the random structure. Ten different unit cells with non-regular arrangements of voids are considered. The side length of the unit cell is $1\mu m$ and the void volume fraction is kept at 15% of the RVE. Note that in all randomly distributed cavity models, we use the fixed void volume fraction with different pore size distribution.

Two types of element have been chosen for this section; linear 3-noded triangle element and 8-noded quadrilateral element with 4-Gauss points. The imposed macro-strain and material properties for this section are identical to the previous examples in this chapter.

The analysis has been done under three different boundary conditions; (*i*) the linear displacement boundary condition, (*ii*) the periodic boundary displacement fluctuations condition and (*iii*) the uniform boundary traction assumption.

To illustrate the growth of the plastic zone and principal stress components inside the cell and circumference of the cavities different contour plots have been used.

8.5.1 Linear Triangle element models

For the examples in this section the linear triangle element is used. To increase the accuracy of the results we use relatively fine meshes. Table 8.1 shows the relevant information about the number of the elements and nodes for each example. Figure 8.6 gives a schematic representation of different models obtained by random distribution of cavities.

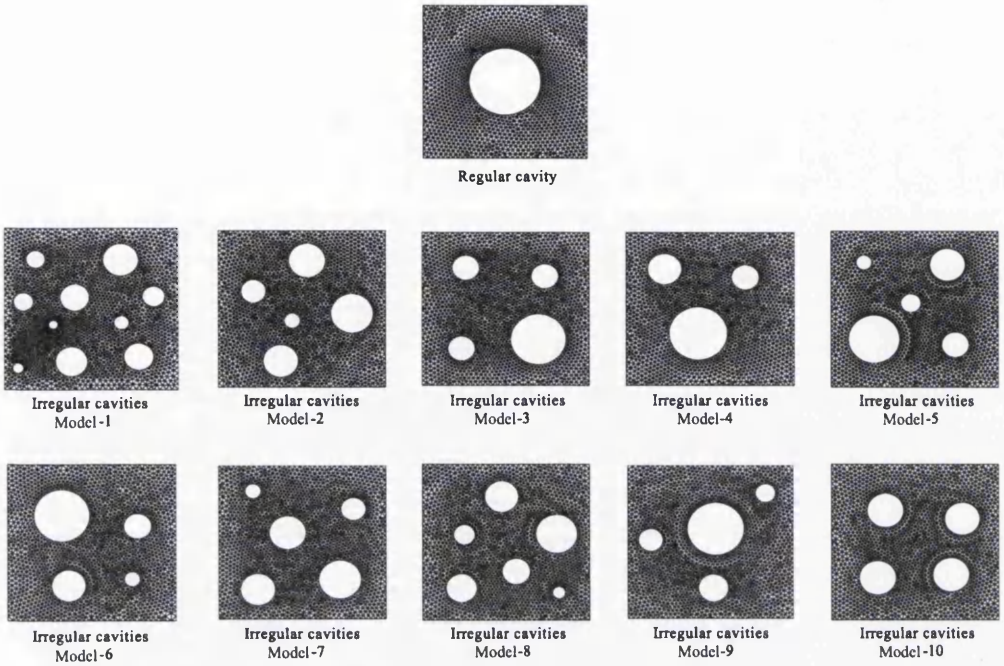

Regular cavity

Irregular cavities Model-1

Irregular cavities Model-2

Irregular cavities Model-3

Irregular cavities Model-4

Irregular cavities Model-5

Irregular cavities Model-6

Irregular cavities Model-7

Irregular cavities Model-8

Irregular cavities Model-9

Irregular cavities Model-10

Figure 8.6: Regular an irregular distribution of cavities for triangle element models.

Model Type	*Number of Elements*	*Number of Nodes*
Regular	2889	1545
Irreg. Model – 1	4407	2357
Irreg. Model – 2	3809	2040
Irreg. Model – 3	3760	2008
Irreg. Model – 4	3497	1869
Irreg. Model – 5	3653	1958
Irreg. Model – 6	3588	1920
Irreg. Model – 7	3891	2081
Irreg. Model – 8	3868	2075
Irreg. Model – 9	3685	1968
Irreg. Model – 10	3636	1949

Table 8.1: Different models for triangle element.

In the first test we obtain the average stress for all models under the linear displacement boundary condition. Figure 8.7 shows the effective stress - strain norm curves for all different micro-models. As can be seen from Figure 8.7, the main difference between the regular and irregular cavity models becomes more obvious in the elasto-plastic range.

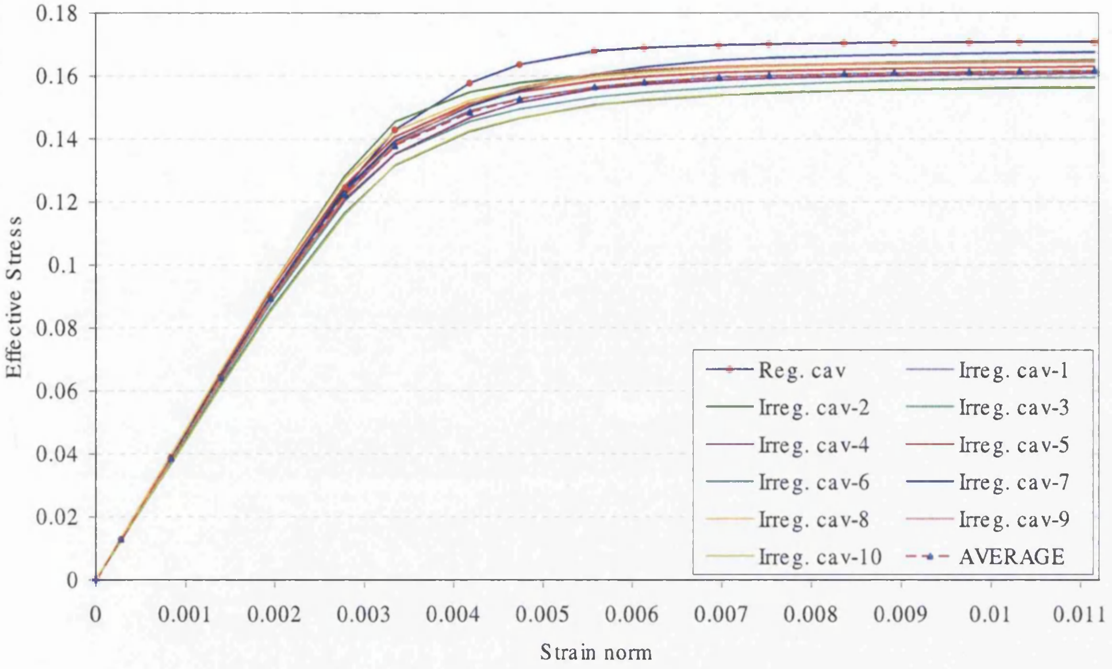

Figure 8.7: Effective stress - strain norm curve for all triangle element models under the linear displacement assumption.

From this observation we can say that the overall response of the regular cavity model with linear displacement boundary assumption shows yielding at higher stresses than the irregular cavity models.

The average stress-strain curves have also been obtained for all models under the periodic boundary displacement fluctuations condition. This is shown in Figure 8.8. It can be seen that, in contrast to the linear displacement boundary condition, deviation of the overall response for all irregular models takes place on both sides of the regular cavity model. In general, under the periodic boundary displacement fluctuations condition, it may be concluded that calculations performed on the simplest regular unit cell usually provide an answer within an acceptable tolerance with respect to the average response from all irregular models.

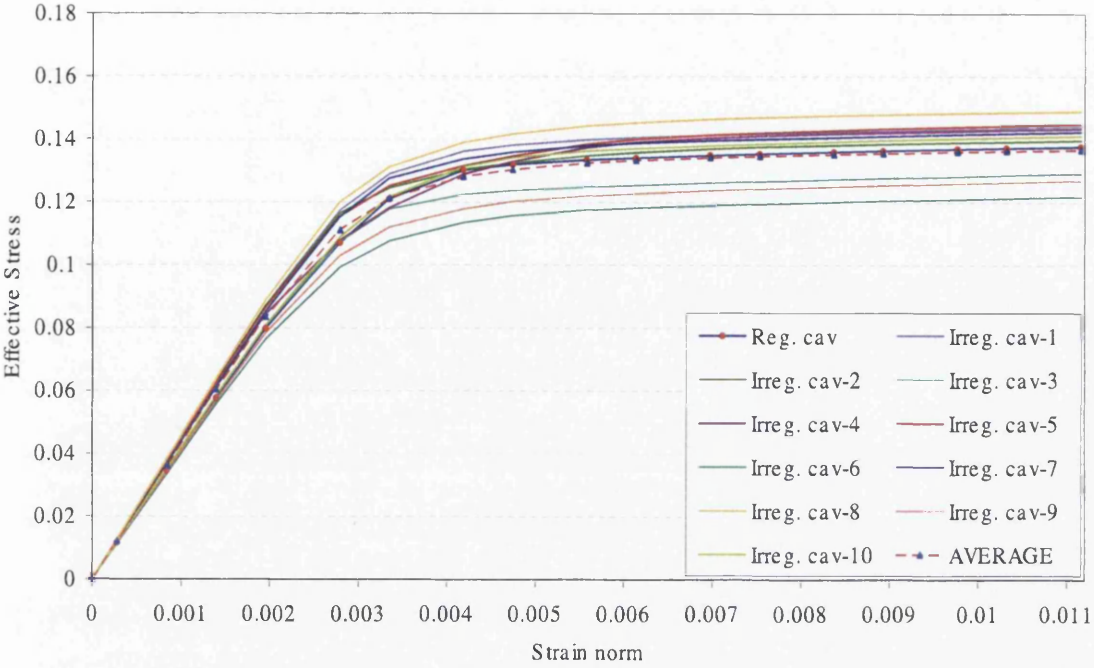

Figure 8.8: Effective stress - strain norm curve for all triangle element models under the periodic assumption.

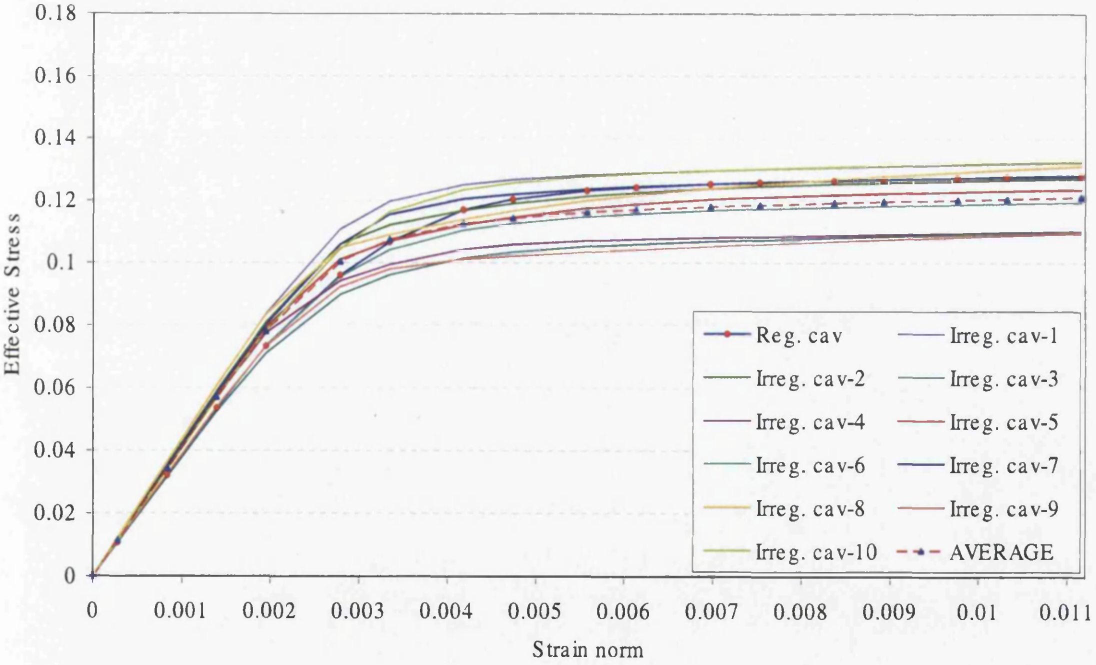

Figure 8.9: Effective stress - strain norm curve for all triangle element models under the uniform boundary traction assumption.

Finally the effective homogenised stress - strain norm graphs for the regular and irregular cavity models have been plotted in Figure 8.9 under the uniform boundary traction assumption. In the elastic zone the irregular cavity models show different behaviour from the regular cavity model. After the yielding point the effect of the regularity and irregularity of cavities on the homogenised behaviour of the RVE is more pronounced. In general, under the uniform boundary traction assumption the regular cavity model shows yielding at higher stresses than the average yielding stresses from all the irregular cavity models.

In the next section we consider the same examples by using 8-noded quadrilateral element.

8.5.2 Quadrilateral 8-node element models

In this section we use 8-node quadrilateral element with 4-Gauss points for the regular and irregular cavity models. Table 8.2 shows the relevant information about the number of the elements and nodes for each model. Figure 8.10 is a schematic representation of different models obtained by random distribution of cavities.

Model Type	*Number of Elements*	*Number of Nodes*
Regular	350	1158
Irreg. Model – 1	2581	8052
Irreg. Model – 2	573	1869
Irreg. Model – 3	372	1249
Irreg. Model – 4	369	1231
Irreg. Model – 5	690	2222
Irreg. Model – 6	553	1798
Irreg. Model – 7	638	2062
Irreg. Model – 8	638	2065
Irreg. Model – 9	477	1566
Irreg. Model – 10	370	1243

Table 8.2: Different models for 8-node quadrilateral element.

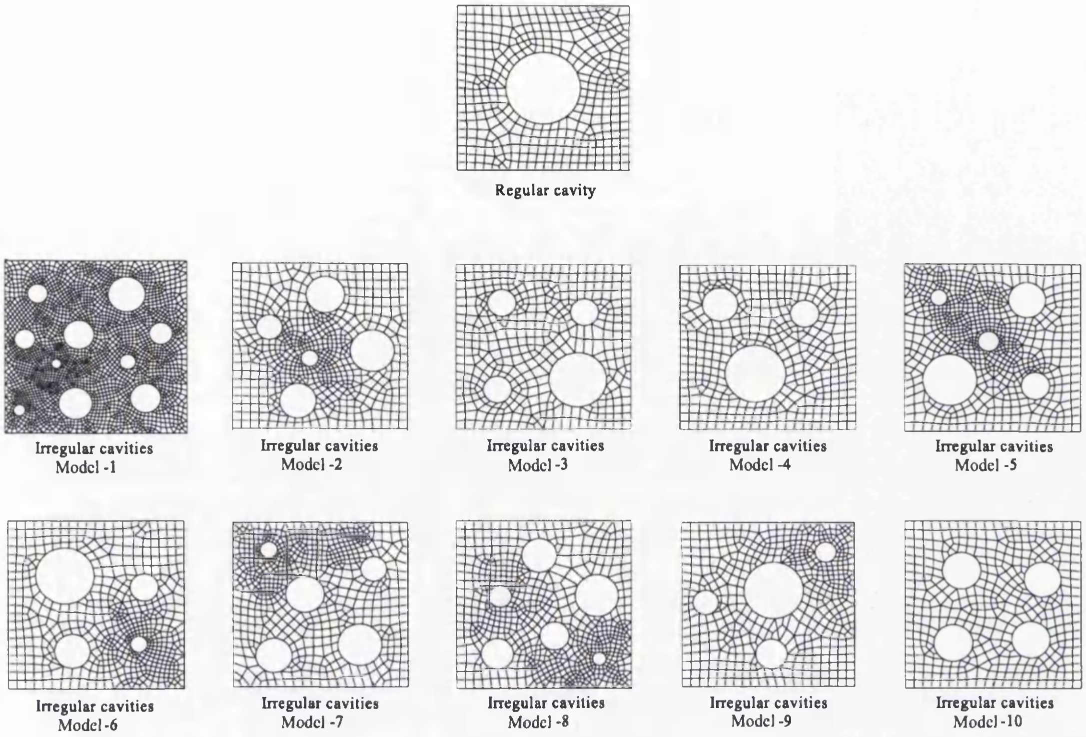

Regular cavity

Irregular cavities Model -1

Irregular cavities Model -2

Irregular cavities Model -3

Irregular cavities Model -4

Irregular cavities Model -5

Irregular cavities Model -6

Irregular cavities Model -7

Irregular cavities Model -8

Irregular cavities Model -9

Irregular cavities Model -10

Figure 8.10: Regular and irregular distribution of cavities for 8-node quadrilateral element models.

Figure 8.11 shows the effective stress - strain norm curve for all models under the linear displacement boundary condition. The overall behaviour of the micro-models with 8-noded quadrilateral element shows the same response as the unit-cells with linear triangle element under the linear displacement boundary condition. The homogenised response from the regular cavity model gives an upper bound in comparison with the irregular cavity models behaviour. In other words, the obtained overall behaviour from the irregular cavity models show softer response with respect to the regular cavity model behaviour.

In addition we have obtained the average stress for all models under the periodic boundary displacement fluctuations condition. Figure 8.12 shows the effective stress - strain norm curve for all models under the periodic boundary displacement fluctuations condition.

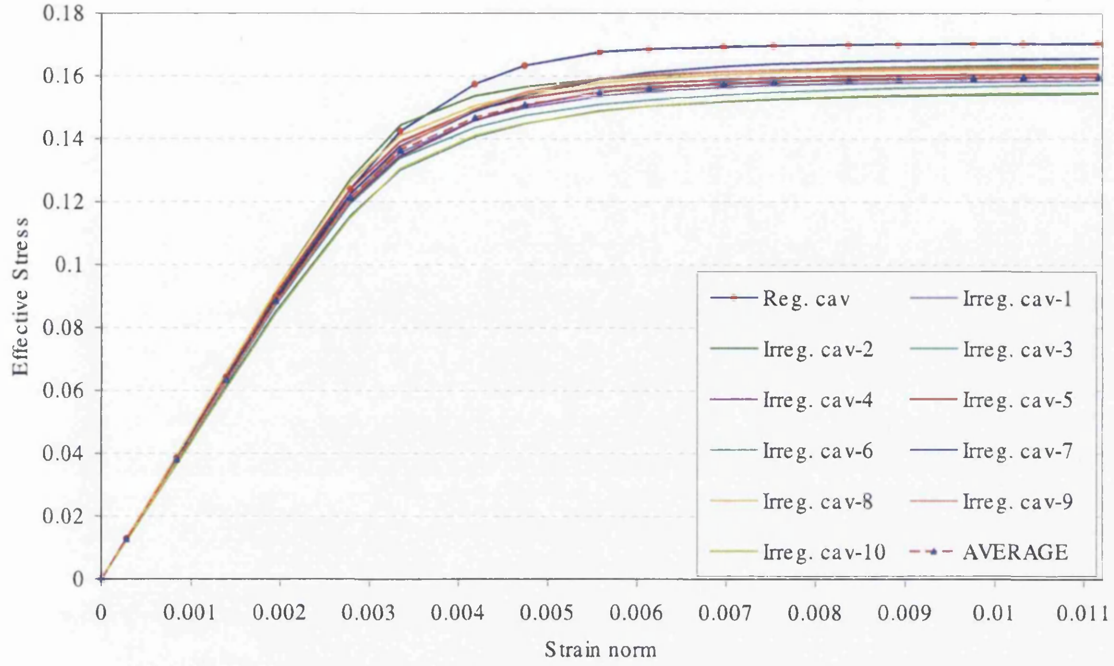

Figure 8.11: Effective stress - strain norm curve for all quadrilateral element models under the linear displacement assumption.

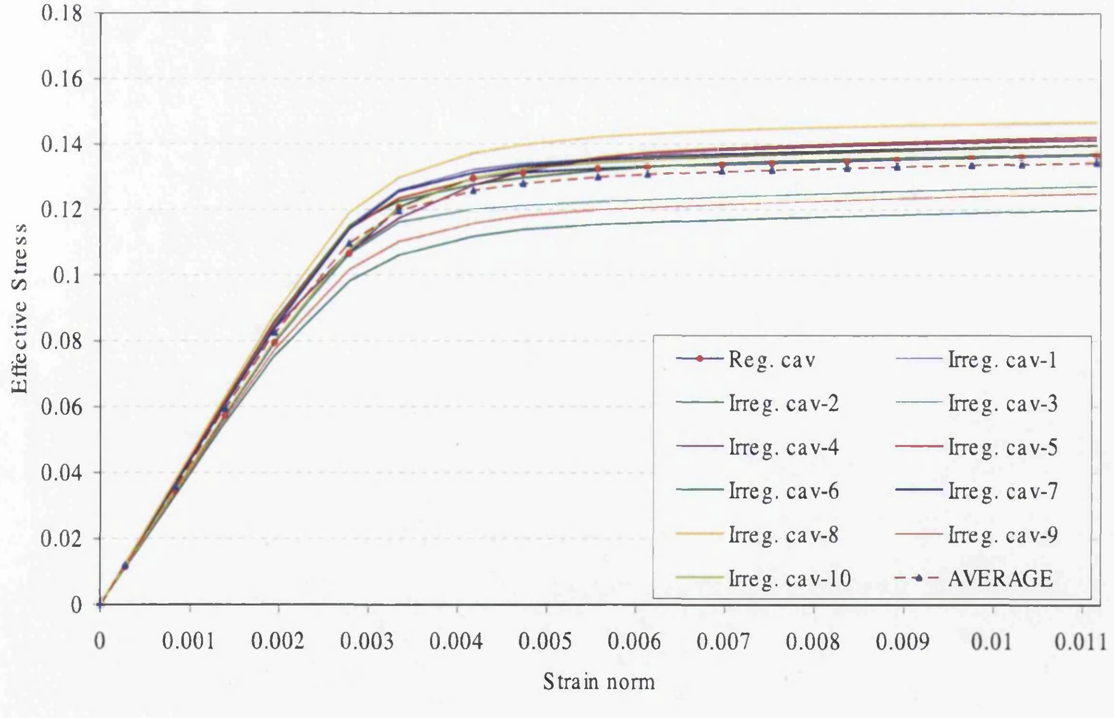

Figure 8.12: Effective stress - strain norm curve for all quadrilateral element models under the periodic assumption.

From Figures 8.11 and 8.12, it may be concluded that, with respect to the defined boundary condition, for the linear displacement boundary condition, the overall response of the regular cavity model shows yielding at higher stresses than the irregular cavity models. On the other hand, under the periodic boundary displacement fluctuations condition, deviation of the overall response for all irregular models takes place on both sides of the regular cavity model. One might consider that the results for the regular cavity model under the periodic boundary displacement fluctuations assumption provide acceptable approximation for overall behaviour of randomly distributed cavity models.

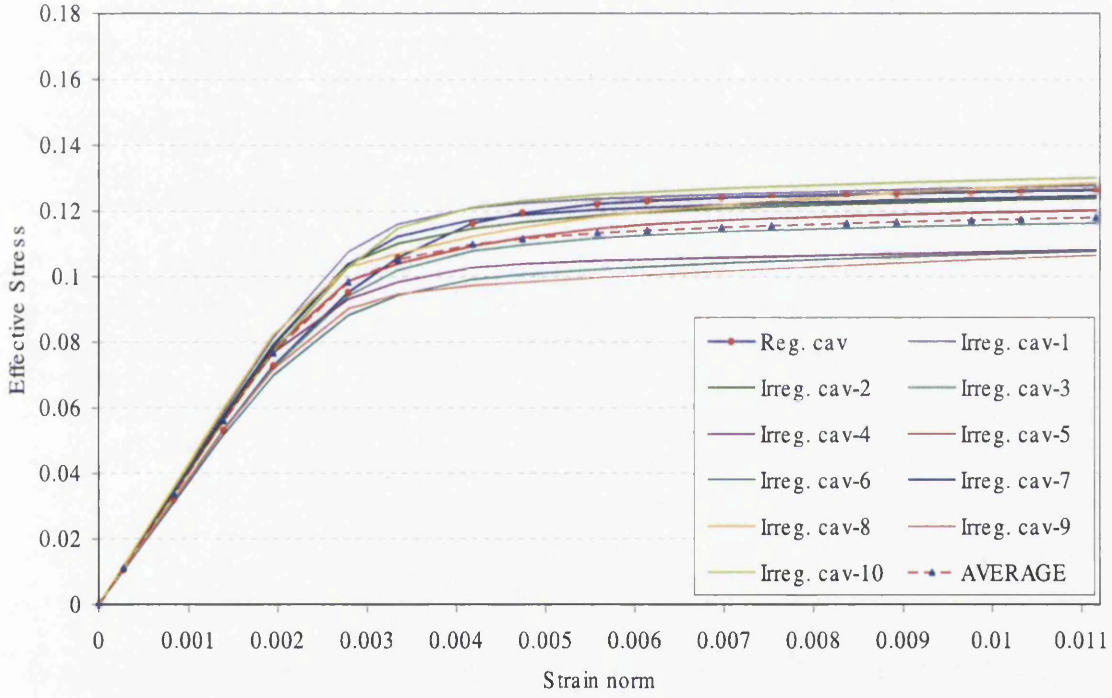

Figure 8.13: Effective stress - strain norm curve for all quadrilateral element models under the uniform boundary traction assumption.

Figures 8.13 shows the effective stress - strain norm graphs for the regular and irregular cavity models under the uniform boundary traction assumption. From these graphs it may be concluded that except for three irregular models, the yielding point for the regular cavity model has a higher value than the irregular cavity models. Although the averaged behaviour for the irregular cavity models shows stiffer behaviour in elastic zone, they show softer behaviour in the plastic range.

8.5.3 The effect of different element types on the homogenised response

In this part our aim is to compare the overall behaviour of the unit cell with respect to the performance of the different element types with full and reduced integration points. The unit cell with the regular cavity model is the model which has been selected for this part of the test. We have analysed the model with linear triangle element, 8-noded quadrilateral element with 4-Gauss points, and finally the same quadrilateral element model with full integration points (9-Gauss points).

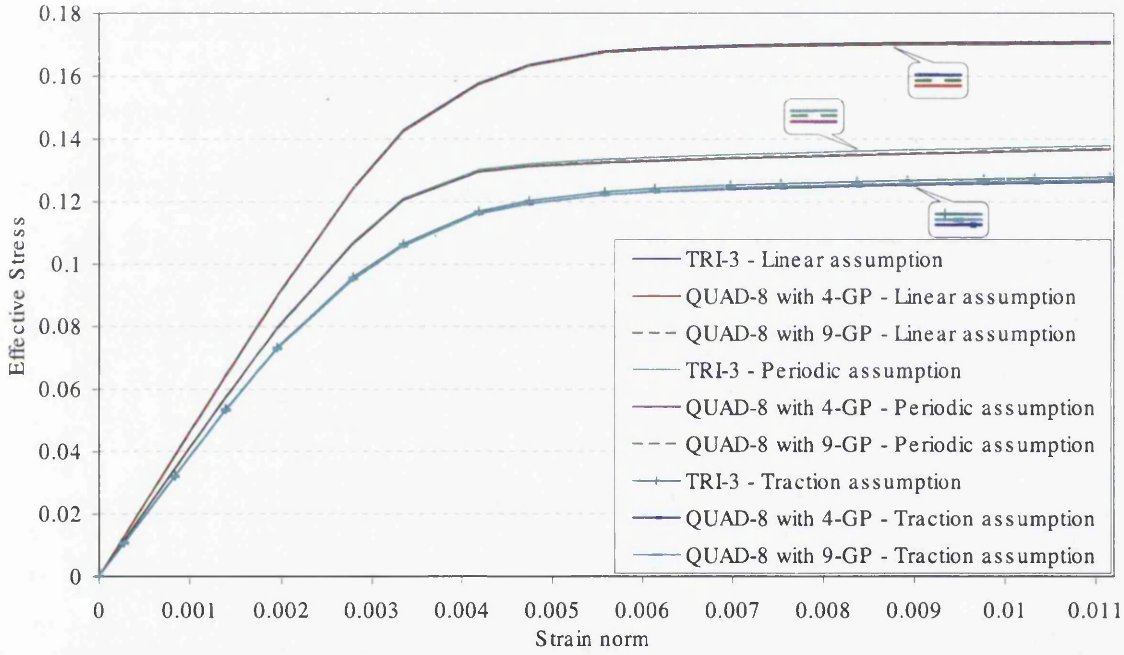

Figure 8.14: Effective stress - strain norm curves for all element types under the linear displacement boundary condition, the periodic boundary displacement fluctuations condition and the uniform boundary traction assumption.

Figure 8.14 shows the effective homogenised stress - strain norm for the regular cavity model under three different boundary conditions; the linear displacement boundary condition, the periodic boundary displacement fluctuations condition and the uniform boundary traction assumption.

As can be seen, the overall response of the linear displacement assumption shows yielding at higher stresses compared with the unit cell under the periodic boundary displacement fluctuations assumption. On the other hand, the uniform boundary traction presents the lower bound for the homogenised behaviour of the regular cavity models.

By comparing the observed responses from different elements with various numerical integration points, it may be concluded that the softest behaviour is shown by 8-noded quadrilateral element with 4-Gauss points. Slightly stiffer behaviour is shown by the same element but with full integration points and finally the stiffest response is obtained by using linear triangle elements. Note that because of defining fine meshes for the models with linear triangle element, the obtained results are close to the 8-node quadrilateral element model results.

8.6 Study of the models

In this section we focus on the behaviour of the unit cell in more detail. We chose two models: (*i*) regular cavity model and (*ii*) Irregular cavity model-5 with random voids. 8-noded quadrilateral element with reduced number of Gauss points is employed in all simulations. Imposed macro-strain follows the same pattern as the above examples.

The effect of the regularity of voids inside the RVE on the average stress components and also growth of the plastic zone inside the RVE will be considered. We present the graphs for the normal components of the average stress and the effective stress graph (calculated from average stress components). Several snap-shots of the effective stress graphs are used to study the different responses of the unit cell before and after the yielding point.

8.6.1 Regular cavity model under the linear displacement boundary assumption

First we focus on the results obtained from the linear displacement boundary assumption. Figure 8.15 shows the normal stress components against the strain norm. From Figure 8.15 it can be seen that the stress components of the homogenised stress show quite similar behaviour. The similarity of the components of the average stress is because of the symmetry of the unit cell, regular distribution of cavities at micro level and finally equal components of the imposed strain in x and y directions.

Figure 8.15 also shows a graph which is based on the effective stress (equation (3.19)). The data for this graph have been calculated based on the normal average stress components and have been plotted against the strain-norm.

We chose four different stages on the graph to show the growth of the plastic regime inside the unit cell (see Figure 8.16). These points are assigned as $a - d$, and are shown at the different stages of the loading process before the plastic yielding point and after the plastic yielding point. To clarify the growth of the plastic zone inside the unit cell at each stage, we plot the deformed shapes of the unit cell together with the relevant effective plastic strain contour plots.

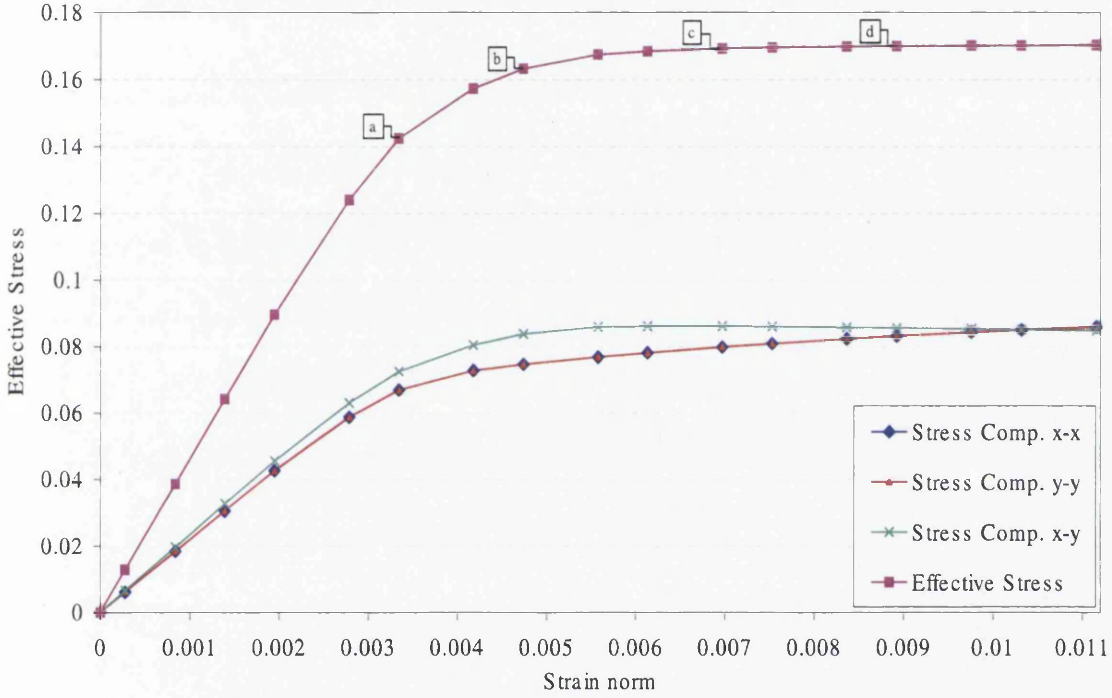

Figure 8.15: Effective stress - strain norm curves for the regular model under the linear displacement boundary assumption.

From Figure 8.16, it is clear that for this regular cavity model and under the linear displacement boundary assumption, the growth path of the plastic zone starts from the boundary of the void and it develops along the diagonal side of the cell up to the boundary of the RVE.

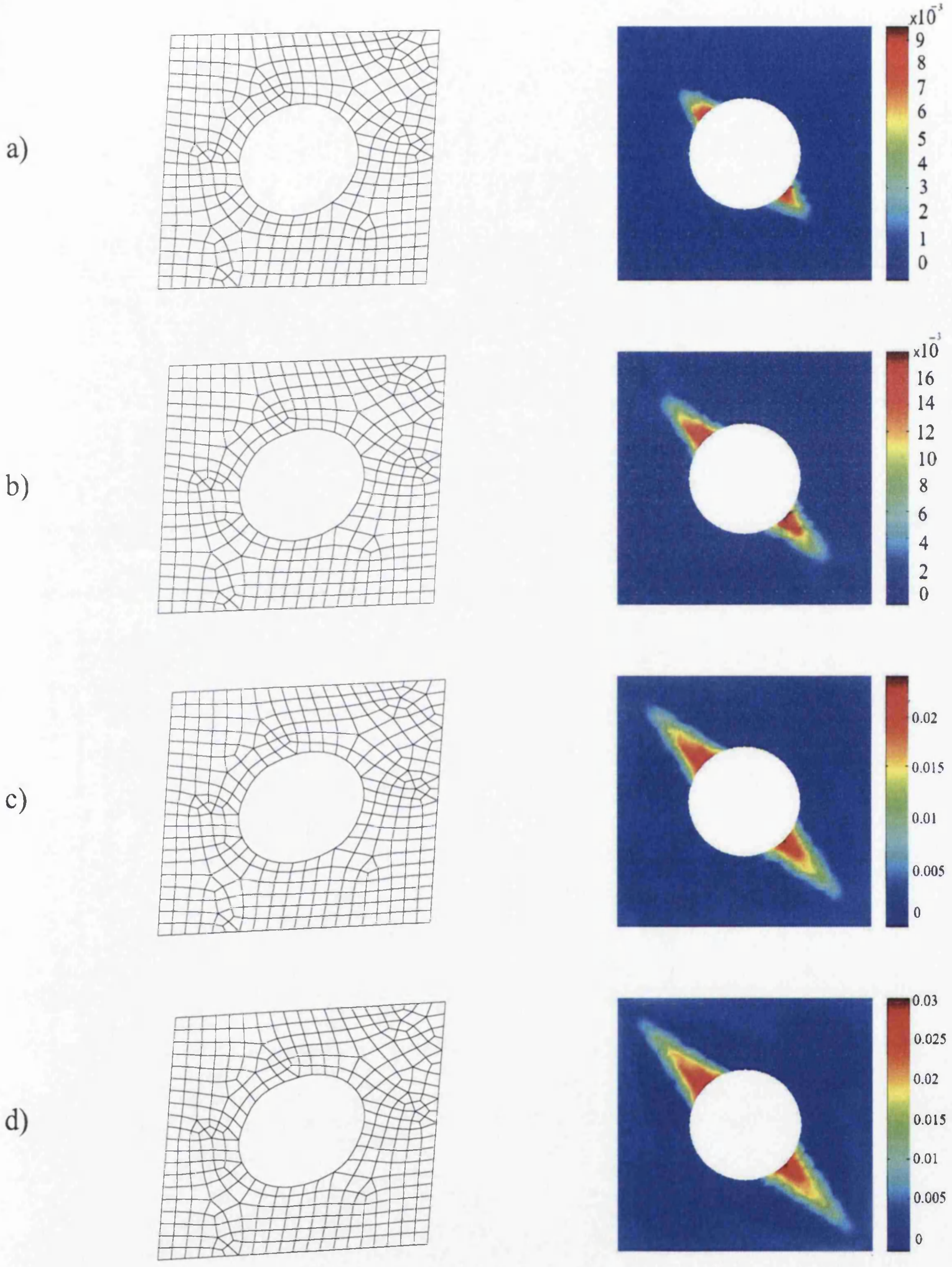

Figure 8.16: Effective plastic strain contour plots for the regular model under the linear displacement assumption.

Figure 8.17 shows the growth of the homogenised normal stress components $\bar{\sigma}_{xx}$, $\bar{\sigma}_{yy}$ and $\bar{\sigma}_{xy}$.

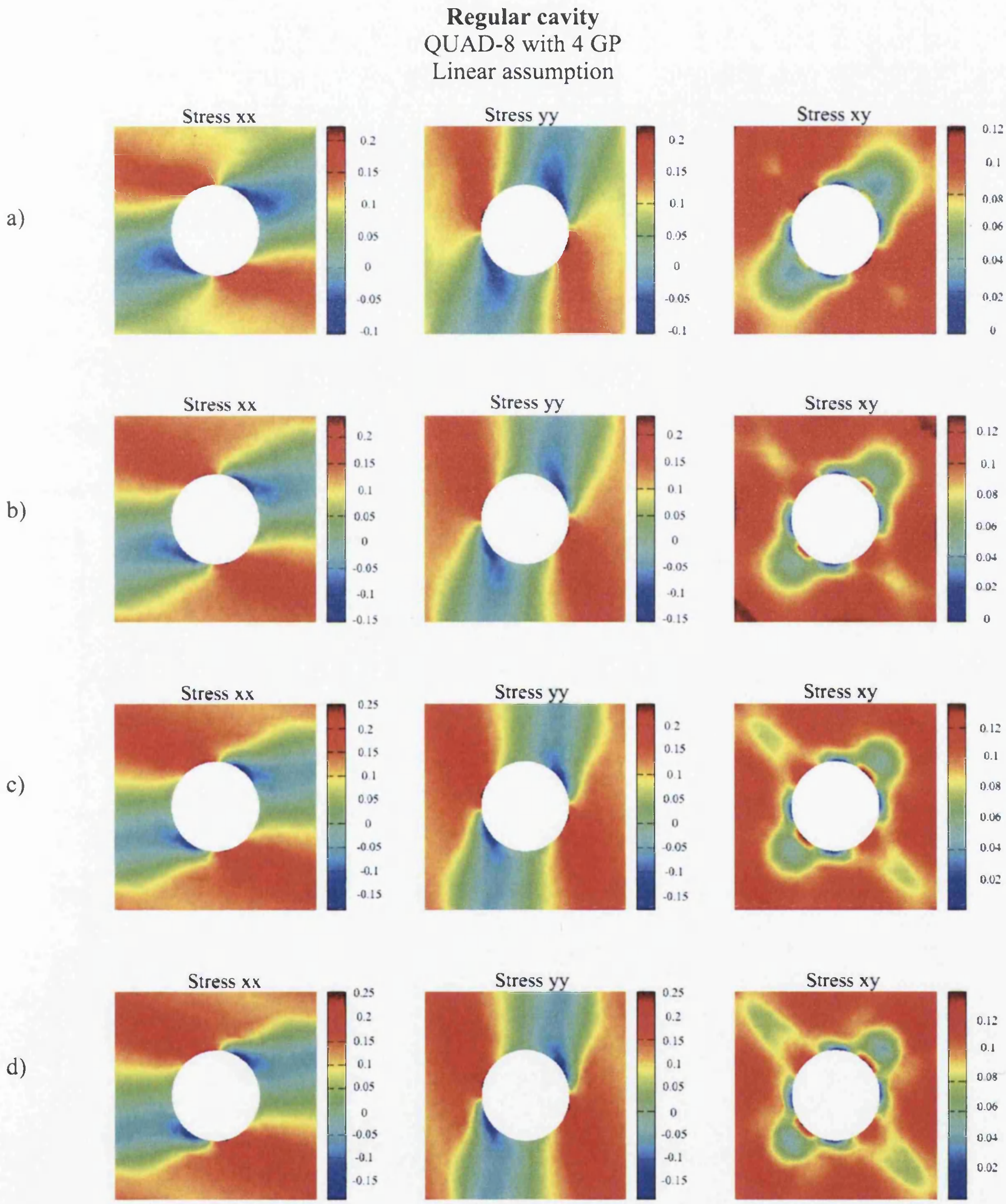

Figure 8.17: Stress contour plots for the regular cavity model under the linear displacement assumption.

8.6.2 Regular cavity model under the periodic boundary displacement fluctuations assumption

In this section we consider the results obtained from the periodic boundary displacement fluctuations condition. Figure 8.18 shows the normal stress components against the strain norm. From Figure 8.18 it can be seen that the stress components of the average stress $\bar{\sigma}_{xx}$ and $\bar{\sigma}_{yy}$ show quite similar behaviour. The similarity of the components of the average stress is related to the symmetry of the unit cell, regular distribution of the the cavities at micro-level and equal components of the imposed strain in x and y directions.

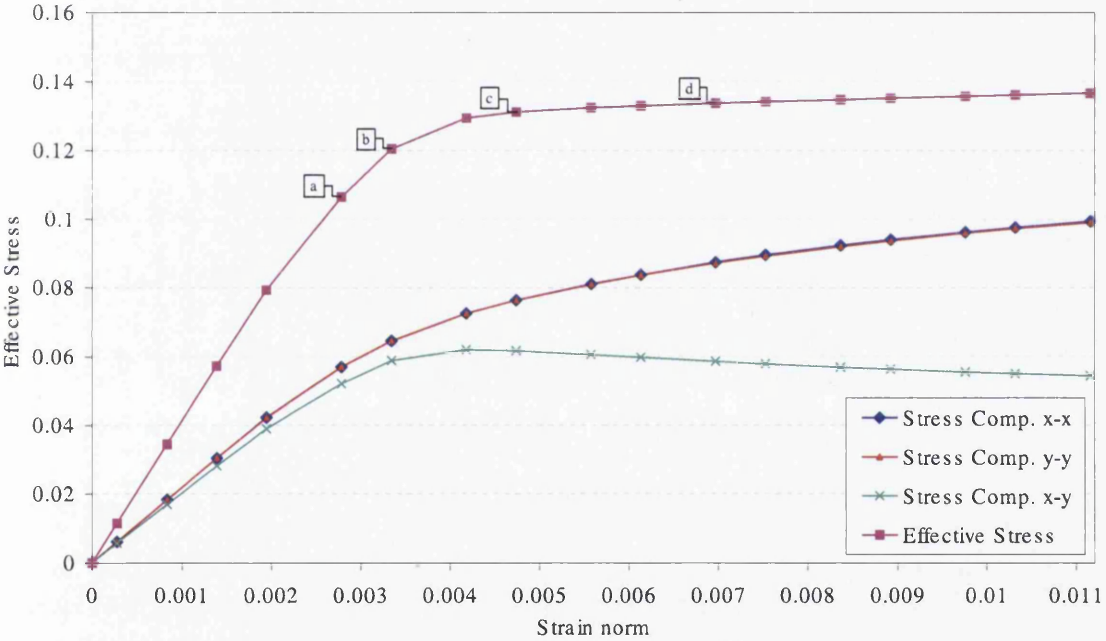

Figure 8.18: Effective stress - strain norm curves for the regular model under the periodic boundary displacement fluctuations assumption.

Figure 8.18 also shows a graph which is based on the effective stress. The data for this graph have been calculated based on the average stress components and have been plotted against the strain-norm. We chose four different stages on the graph and used contour plots to show the evolution of the plastic zone inside the unit cell (see Figure 8.19). These points are denoted as $a - d$, and are shown at different stages of the loading process before the plastic yielding point and after the plastic yielding point.

To clarify the growth of the plastic zone inside the unit cell at each stage, we plot the deformed shapes of the unit cell together with the relevant effective plastic strain contours at each stage. From Figure 8.19, it can be seen that the growth path of the plastic zone follows the deformed shape of the unit cell and resembles hyperbolic curves.

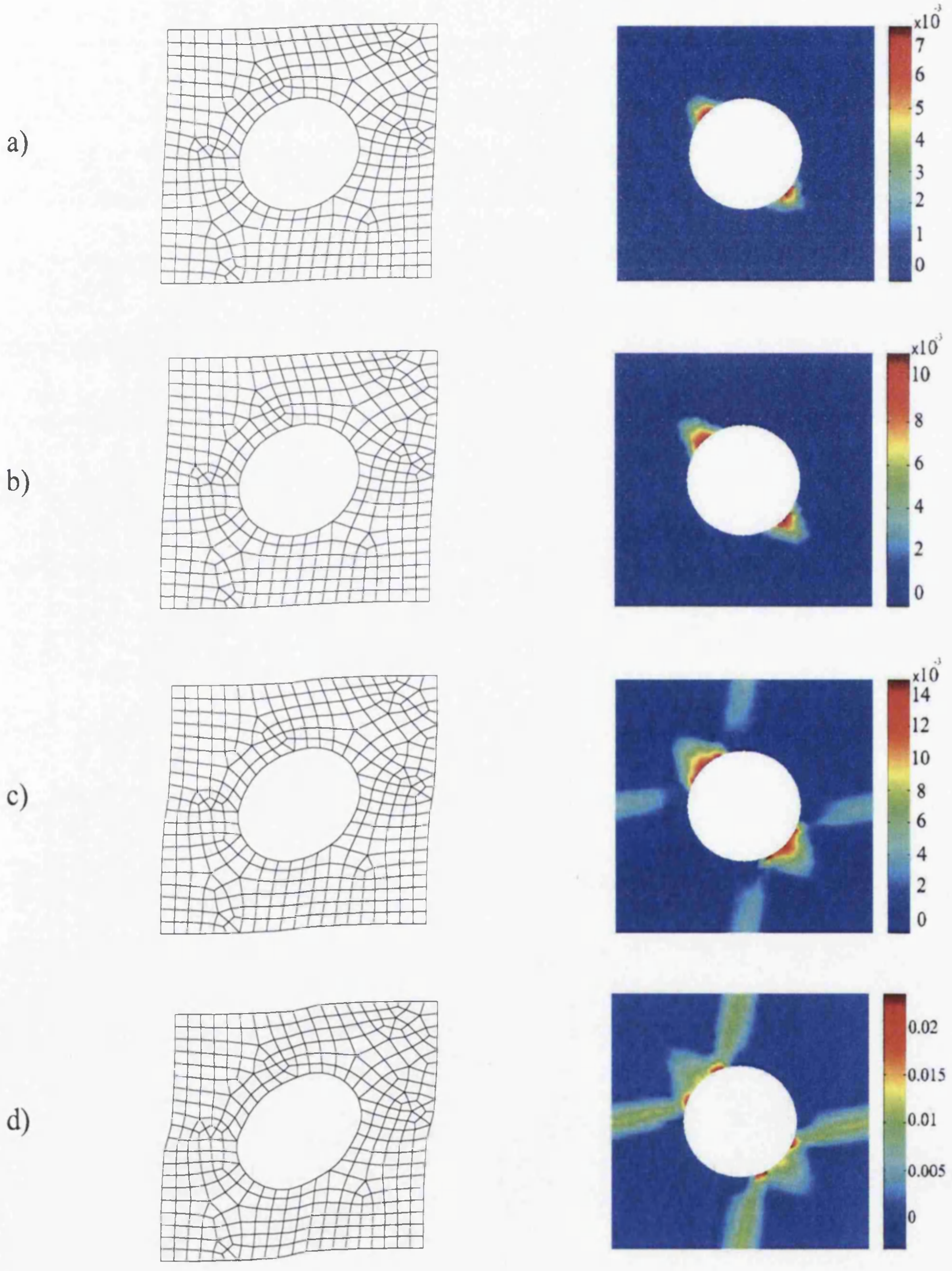

Figure 8.19: Effective plastic strain contour plots for the regular model under the periodic boundary displacement fluctuations assumption.

Figure 8.20 shows the growth of the overall normal stress components $\bar{\sigma}_{xx}$, $\bar{\sigma}_{yy}$ and $\bar{\sigma}_{xy}$.

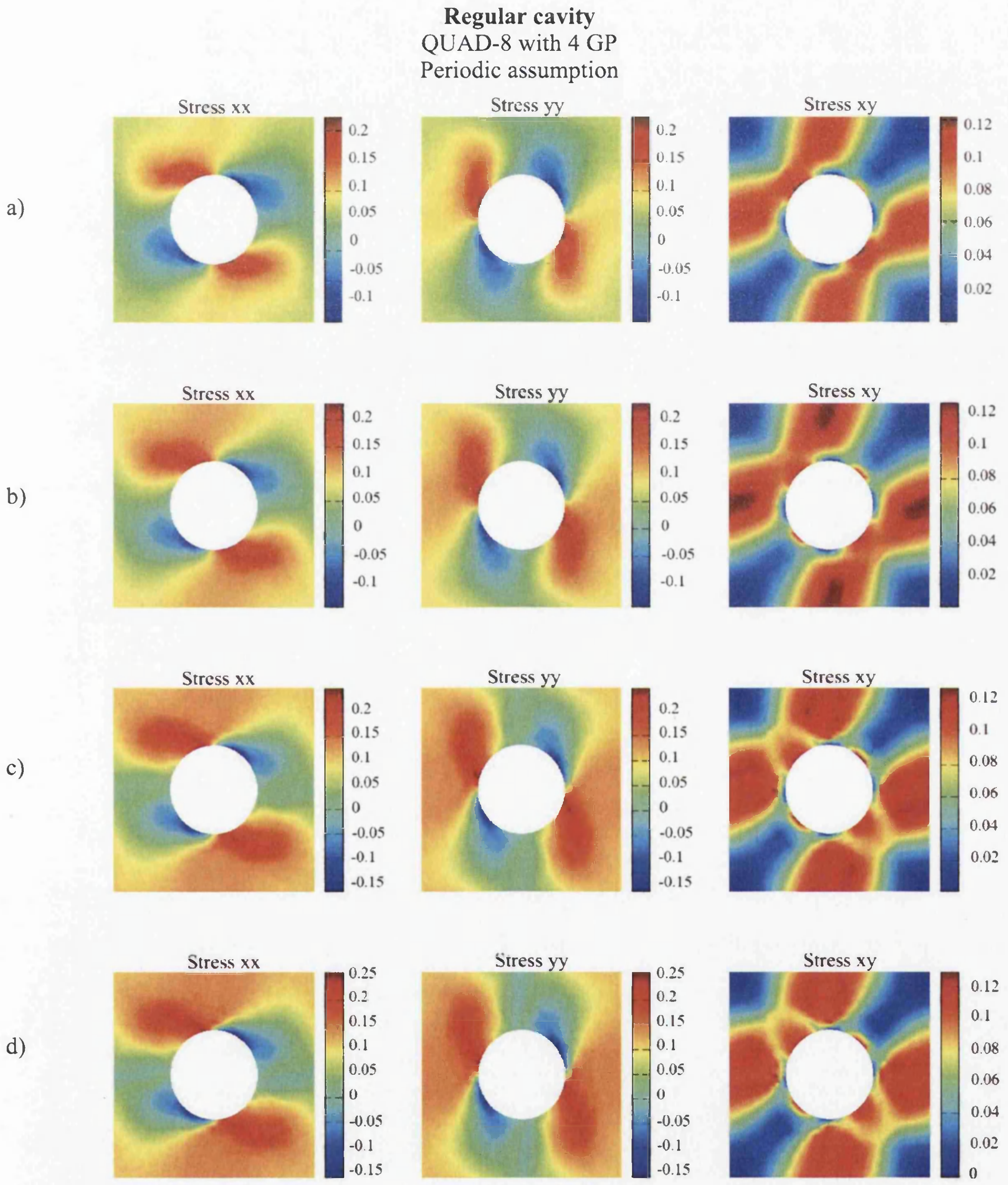

Figure 8.20: Stress contour plots for the regular model under the periodic boundary displacement fluctuations assumption.

8.6.3 Regular cavity model under the uniform boundary traction assumption

For the last boundary condition over the regular cavity model we consider the results obtained from the uniform boundary traction assumption. Figure 8.21 shows the normal stress components against the strain norm. From Figure 8.21 it can be seen that the homogenised stress components $\bar{\sigma}_{xx}$ and $\bar{\sigma}_{yy}$ show identical behaviour. The similarity of the components of the average stress is related to the symmetry of the unit cell, regular distribution of the cavities at micro-level and equal components of the imposed strain in x and y directions.

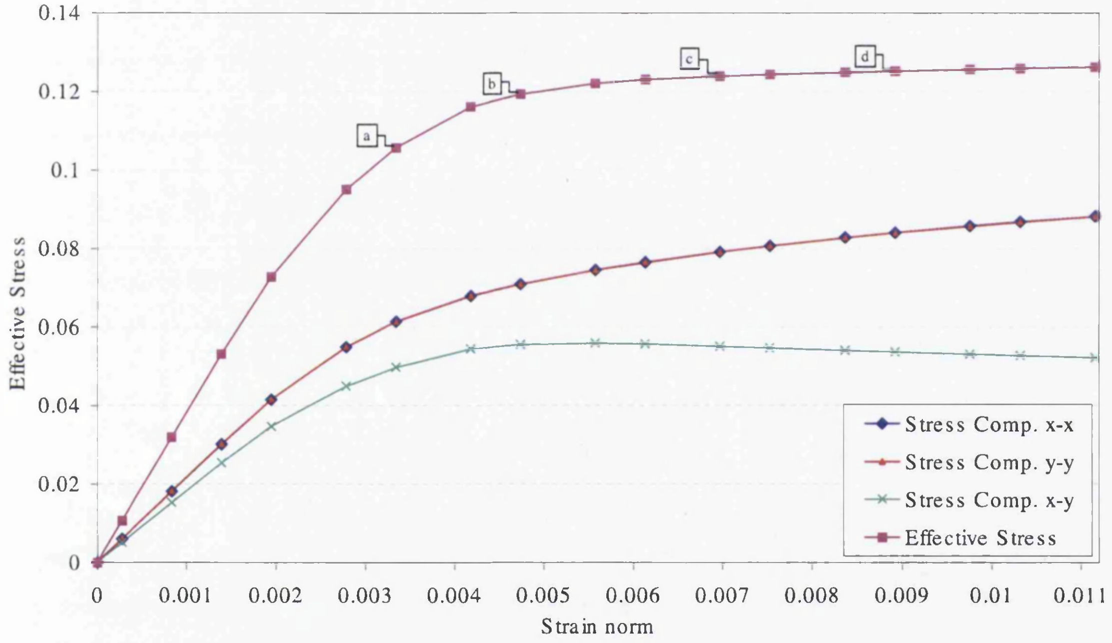

Figure 8.21: Effective stress - strain norm curves for the regular model under the uniform boundary traction assumption.

Figure 8.21 also shows a curve representing the effective stress. The data for this curve have been calculated based on the average stress components and have been plotted against the strain-norm. We chose four different snapshots on this graph to show the evolution of the plastic zone inside the unit cell (see Figure 8.22). These points are denoted as $a - d$, and are shown at different stages of the loading process before the plastic yielding point and after the plastic yielding point.

To clarify the growth of the plastic zone inside the unit cell at each stage we plot the deformed shapes of the unit cell together with the relevant effective plastic strain contours at each stage. From Figure 8.22, it can be seen that the growth path of the plastic zone follows the deformed shape of the unit cell and resembles hyperbolic curves in similarity to the periodic boundary displacement fluctuations assumption.

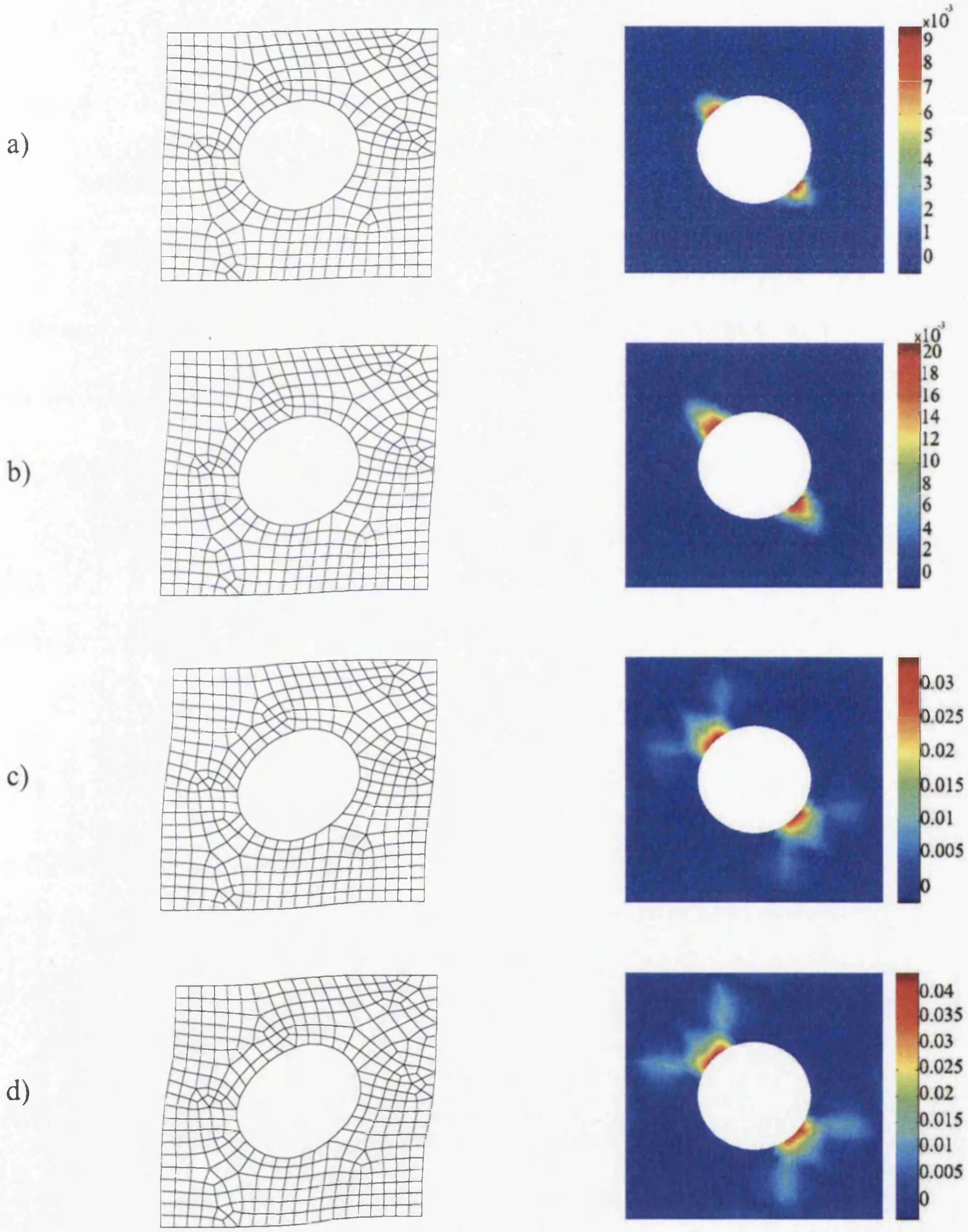

Figure 8.22: Effective plastic strain contour plots for the regular model under the uniform boundary traction assumption.

Figure 8.23 shows the growth of the overall normal stress components $\bar{\sigma}_{xx}$, $\bar{\sigma}_{yy}$ and $\bar{\sigma}_{xy}$.

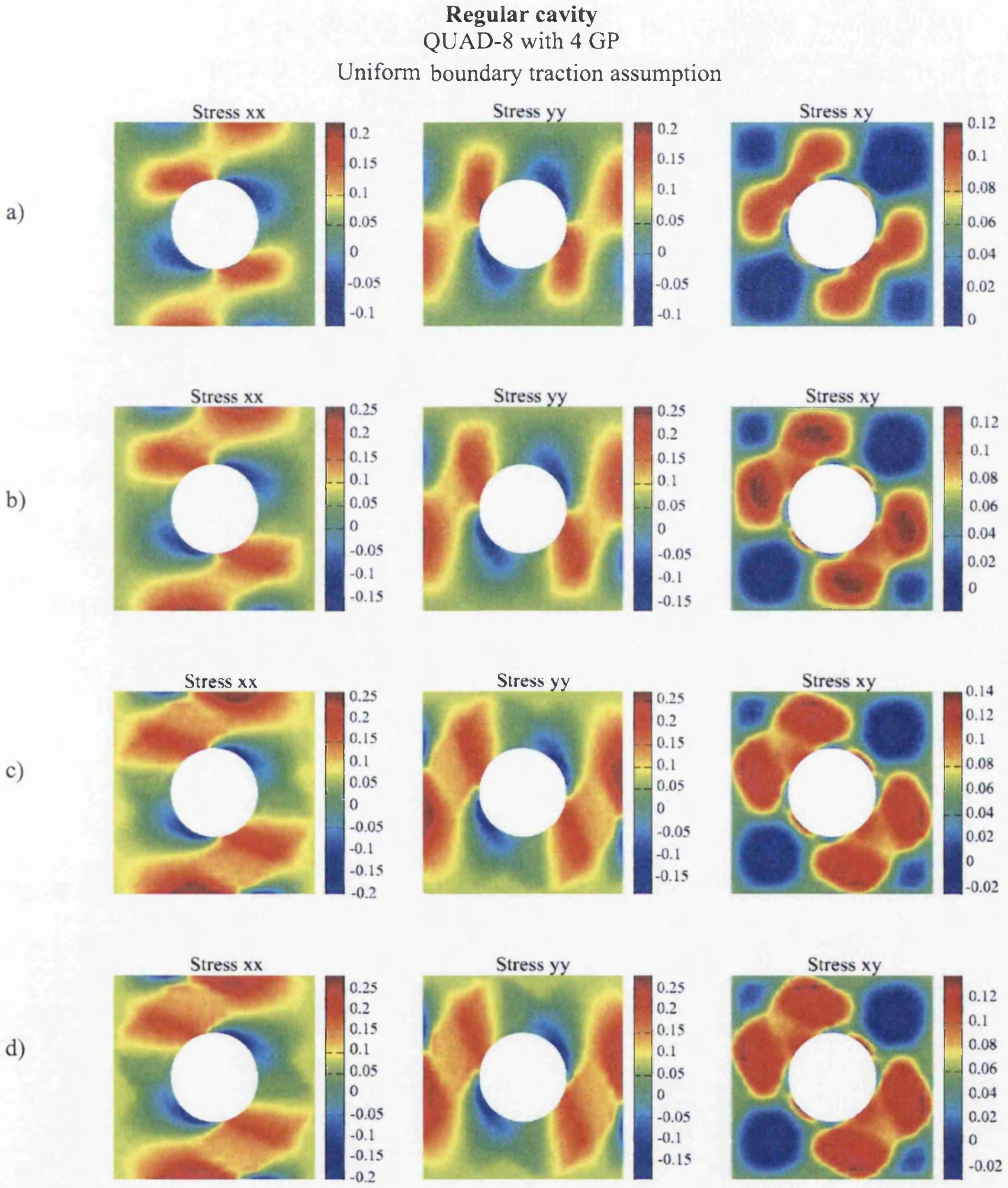

Figure 8.23: Stress contour plots for the regular model under the uniform boundary traction assumption.

With regard to the contour plots obtained for different boundary condition we can consider the effect of the various boundary conditions on the internal variables such as stress components and effective plastic strain. As can be seen these effects are crucial in plastic failure. It is clear from effective plastic strain contour plots and imposed strain pattern, that plastic failure starts from boundary of the inner void and develops up to the boundary of the unit cell.

8.6.4 Irregular cavities model-5 under the linear displacement boundary assumption.

To show the difference between the regular distribution of the cavities and random distribution of the cavities we chose to study the irregular model-5. As in previous tests for the regular model, firstly we consider the problem under the linear displacement boundary condition. The obtained results based on this boundary condition have been depicted in Figure 8.24.

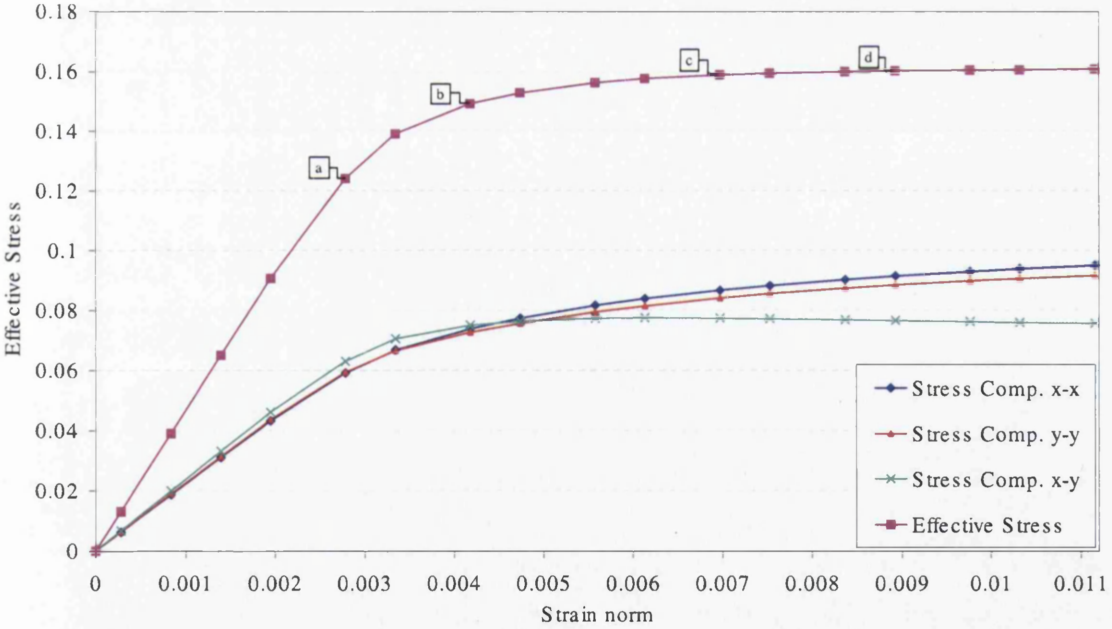

Figure 8.24: Effective stress - strain norm curves for the irregular model-5 under the linear displacement boundary assumption.

Figure 8.24 shows the average stress components against the strain norm. Although the imposed strain has the same components in x and y directions, in this model the stress components of the average stresses $\bar{\sigma}_{xx}$ and $\bar{\sigma}_{yy}$ are not identical with each other. The difference in the values of the components of the average stress in this model is caused by the random distribution of the cavities in the unit cell.

Figure 8.24 also shows the effective stress curve for this model. The data for this graph have been calculated from the average stress components and have been plotted against the strain-norm. As can be seen from Figure 8.24 we chose four different stages to show the evolution of the plastic zone inside the unit cell (see Figure 8.25). These points are denoted as $a - d$, and are shown at different stages of the loading process before the plastic yielding point and after the plastic yielding point.

To clarify the evolution of the plastic zone inside the unit cell at each stage we plot the deformed shapes of the unit cell together with the relevant effective plastic strain contour plots. From Figure 8.25 it can be seen that the evolution path of the plastic zone follows the deformed shape of the unit cell.

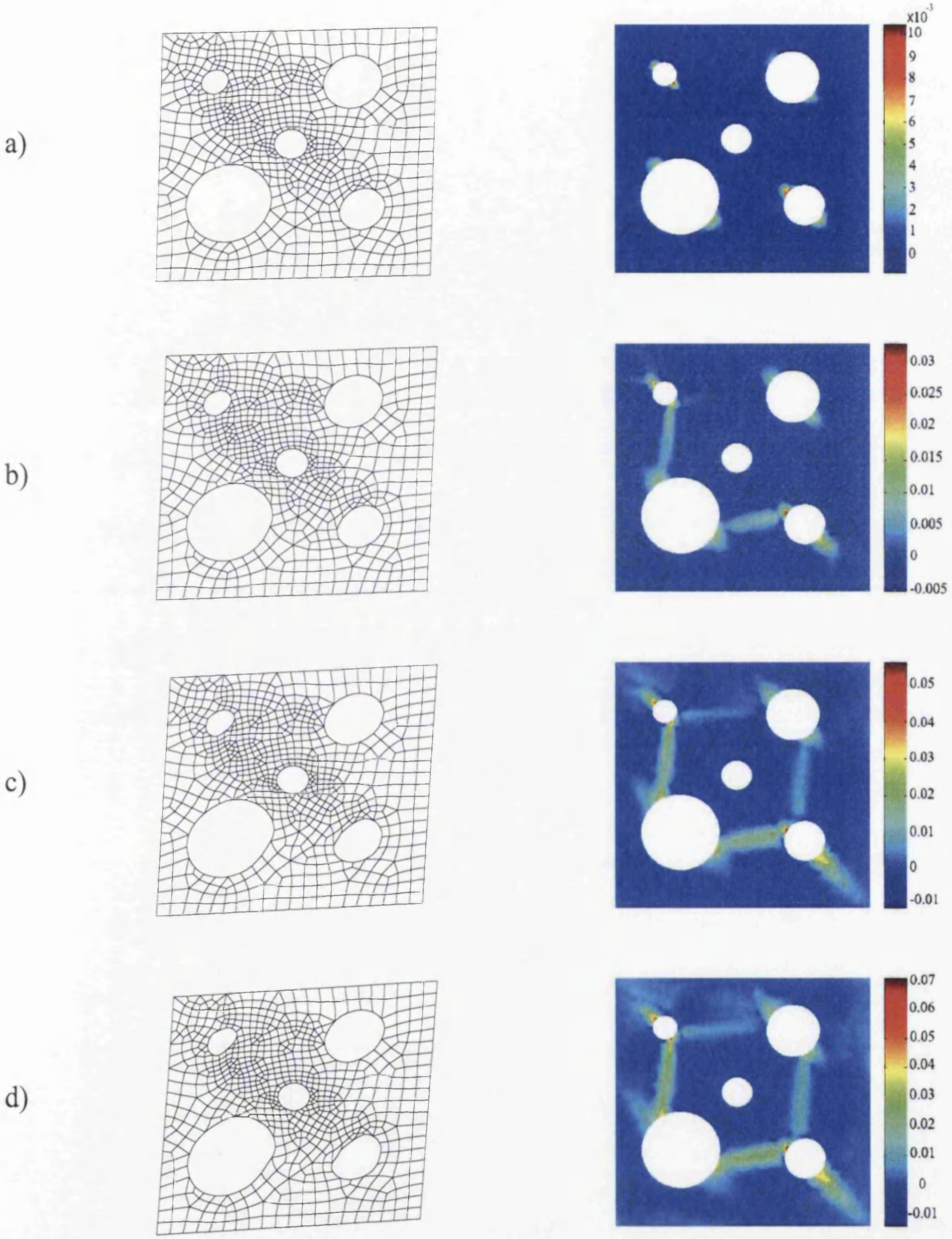

Figure 8.25: Effective plastic strain contour plots for the irregular model-5 under the linear displacement boundary assumption.

Figure 8.26 shows the evolution of the homogenised normal stress components $\bar{\sigma}_{xx}$, $\bar{\sigma}_{yy}$ and $\bar{\sigma}_{xy}$.

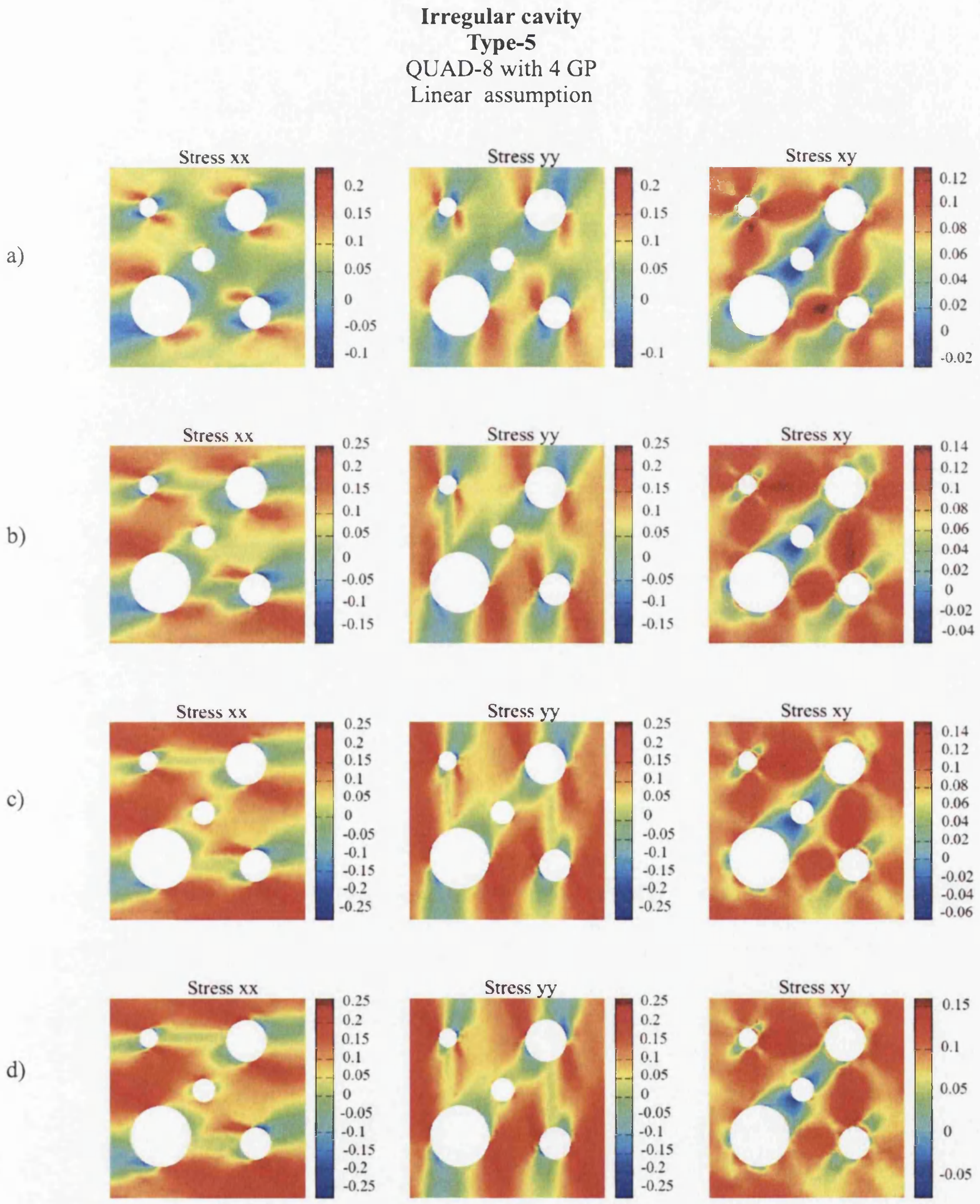

Figure 8.26: Stress contour plots for the irregular model-5 under the linear displacement boundary assumption.

8.6.5 Irregular cavities model-5 under the periodic boundary displacement fluctuations assumption

In addition to the linear displacement boundary assumption we also provide results based on the periodic boundary displacement fluctuations condition. Figure 8.27 shows the homogenised stress components against the strain norm. Although the imposed strain has the same components in x and y directions, from Figure 8.27 it can be seen that the average stress components in different directions are not identical with each other. The difference of the components of the average stress components in this model is caused by of the random distribution of the cavities in the unit cell.

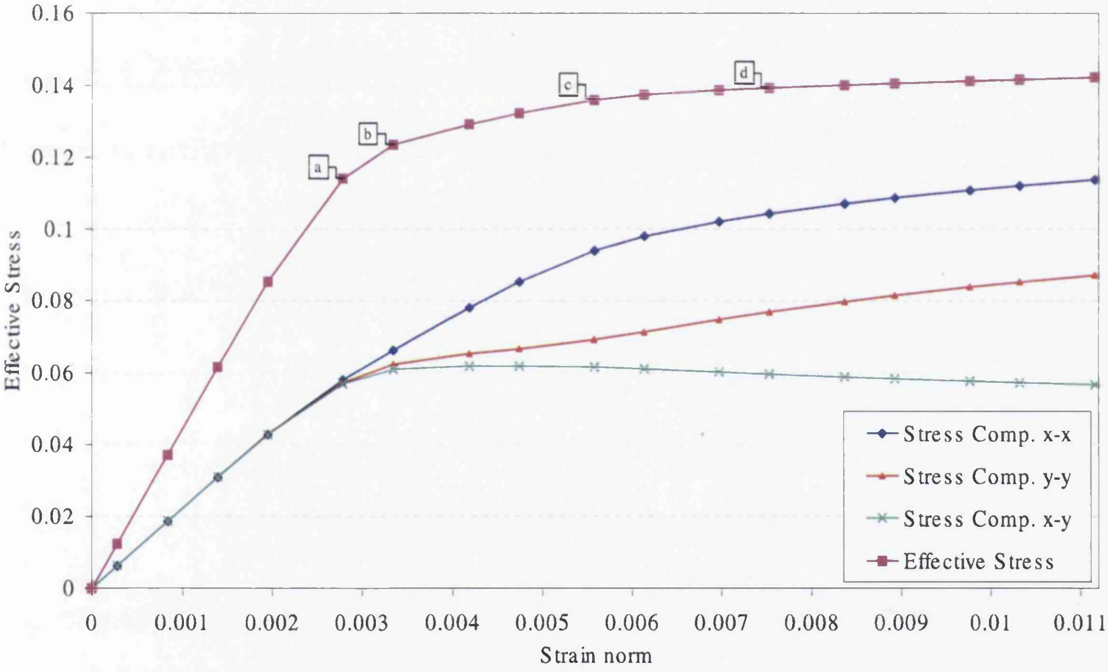

Figure 8.27: Effective stress - strain norm curves for the irregular model-5 under the periodic boundary displacement fluctuations assumption.

Figure 8.27 also shows the homogenised effective stress plot. The data for this graph have been calculated based on the average stress components and have been plotted against the strain-norm. As can be seen from Figure 8.27 we chose four different stages of this graph to show the evolution of the plastic zone inside the unit cell (see Figure 8.28). These points are denoted as $a - d$, and are shown at different stages of the loading process before the plastic yielding point and after the plastic yielding point.

To illustrate the evolution of the plastic zone inside the unit cell at each stage, we depict the deformed shapes of the unit cell together with the relevant effective plastic strain contour plots at each stage. From Figure 8.28 it can be seen that the evolution of the plastic zone follows the deformed shape of the unit cell.

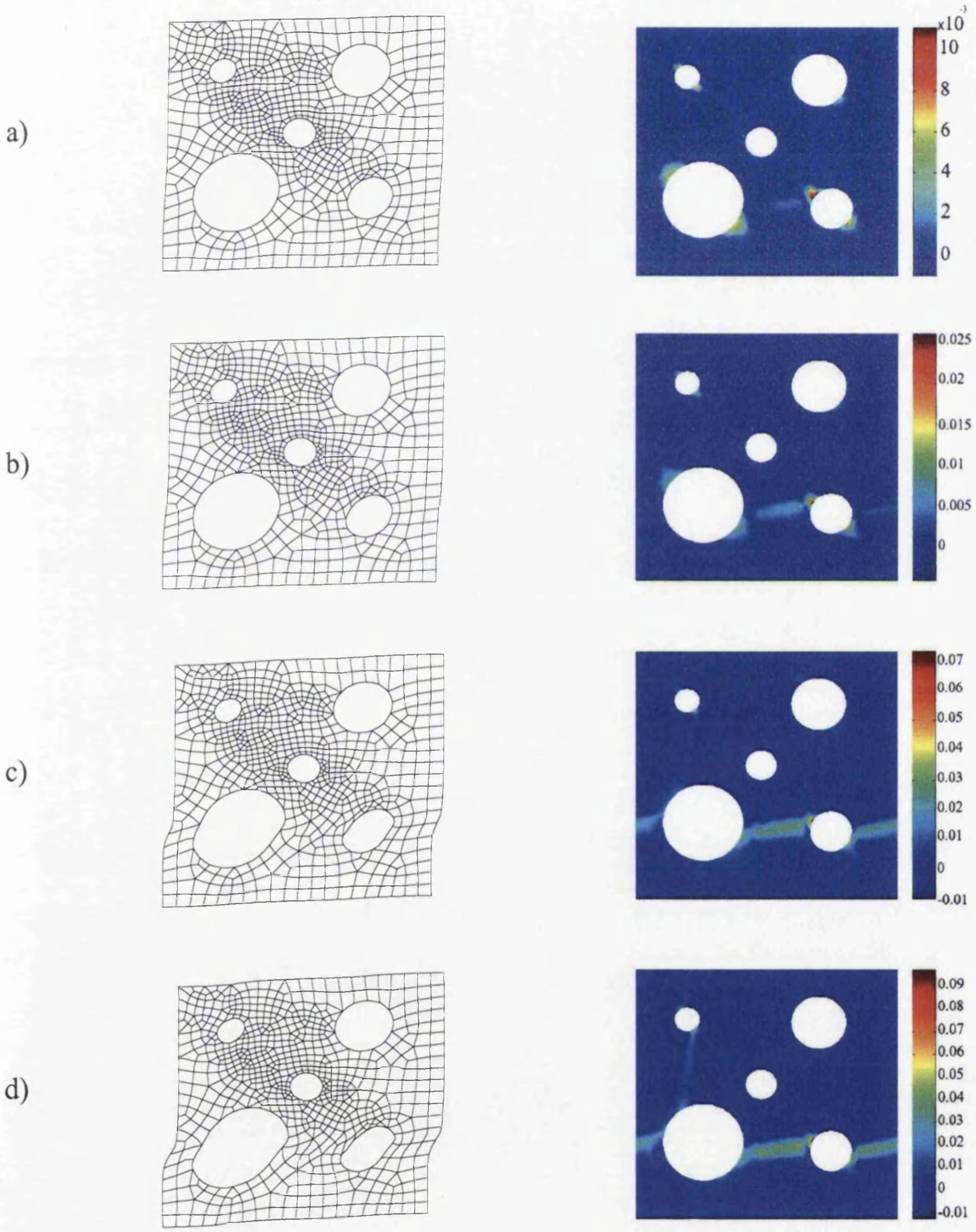

Figure 8.28: Effective plastic strain contour plots for the irregular model-5 under the periodic boundary displacement fluctuations assumption.

Figure 8.29 shows the evolution of the overall normal stress components $\bar{\sigma}_{xx}$, $\bar{\sigma}_{yy}$ and $\bar{\sigma}_{xy}$.

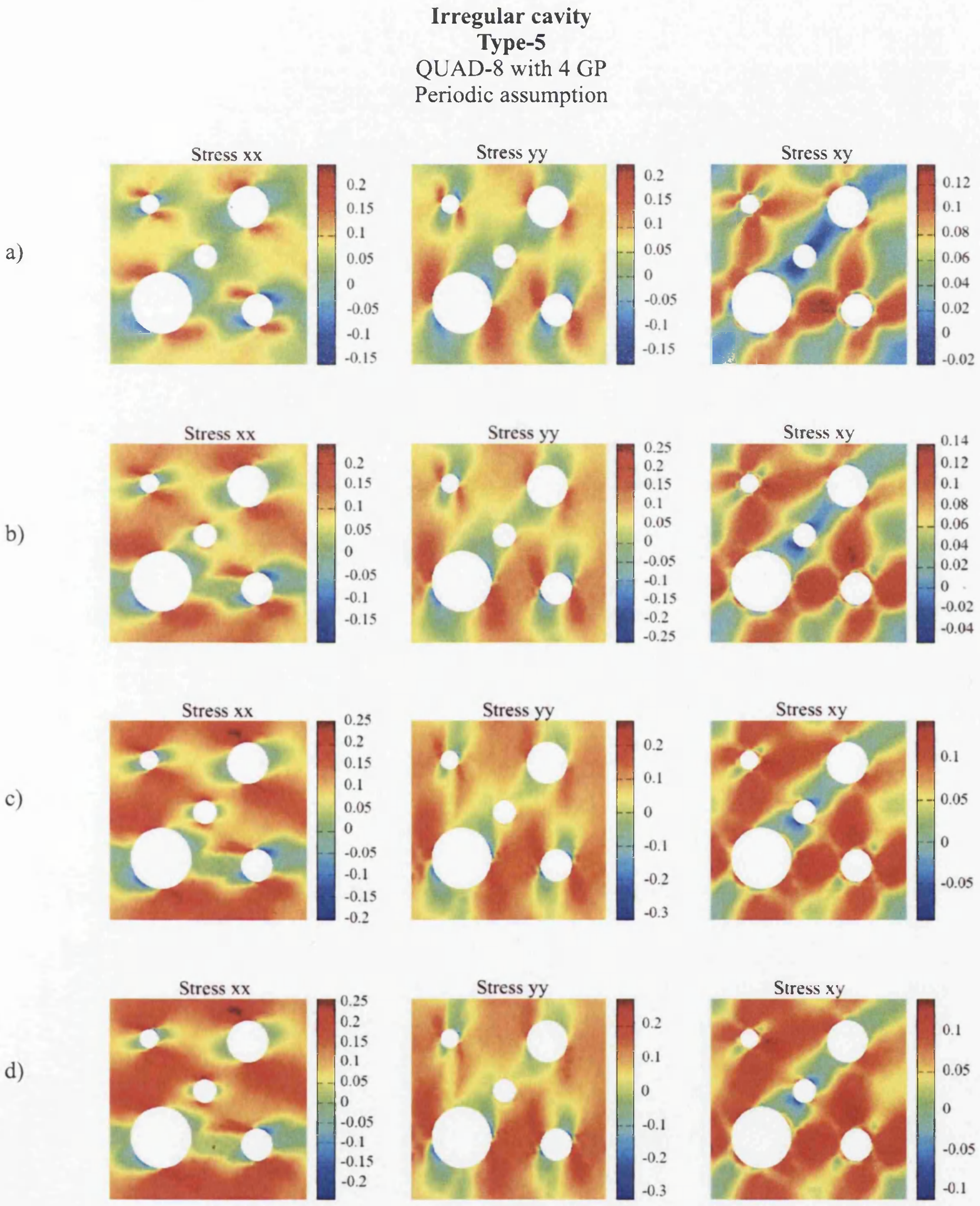

Figure 8.29: Stress contour plots for the irregular model-5 under the periodic boundary displacement fluctuations assumption.

8.6.6 Irregular cavities model-5 with uniform boundary traction assumption.

The irregular cavity model-5 has been considered under the uniform boundary traction assumption. Figure 8.30 shows the homogenised stress components against the strain norm.

Although the imposed strain has the same components in x and y directions, from Figure 8.30 it can be seen that the average stress components in differnt directions are not identical with each other. The difference in the values of the average stress components in this model is caused by the random distribution of the cavities in the unit cell.

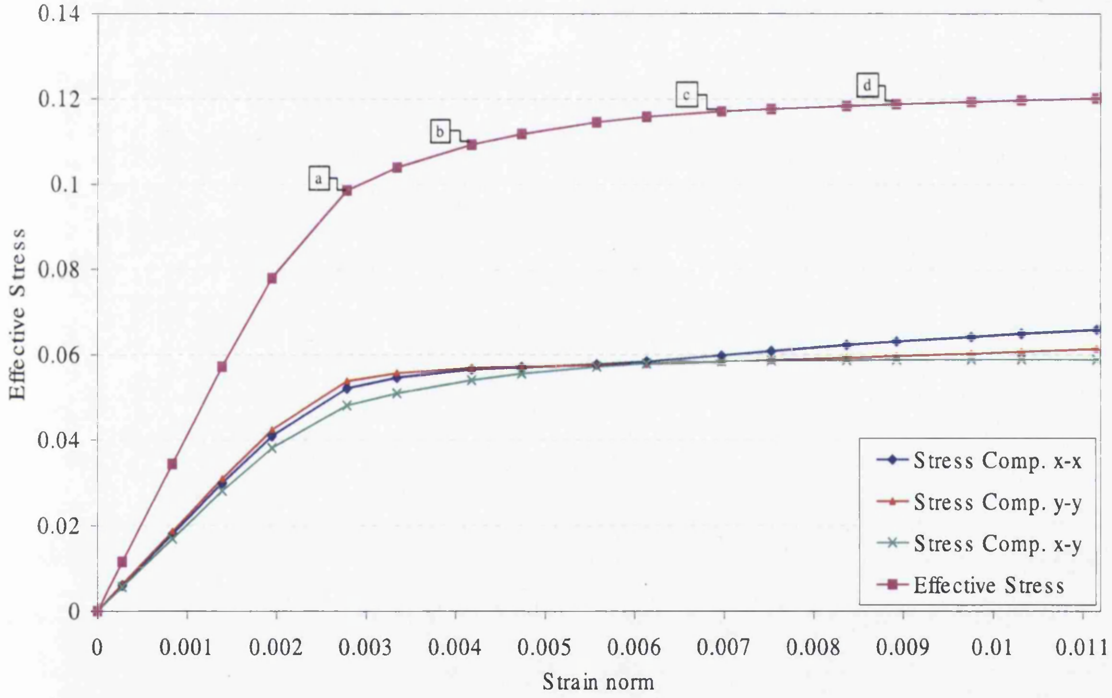

Figure 8.30: Effective stress - strain norm curves for the irregular model-5 under the uniform boundary traction assumption.

Figure 8.30 also shows the effective stress curve for this model. As can be seen from Figure 8.30 we chose four different stages of this graph to show the evolution of the plastic zone inside the unit cell (see Figure 8.31). These points are assigned as $a - d$, and are shown at different stages of the loading process before the plastic yielding point and after the plastic yielding point.

To clarify the evolution of the plastic zone inside the unit cell at each stage, we plot the deformed shapes of the unit cell together with the relevant effective plastic strain contour plots. From Figure 8.31, it can be seen that the evolution path of the plastic zone follows the deformed shape of the unit cell.

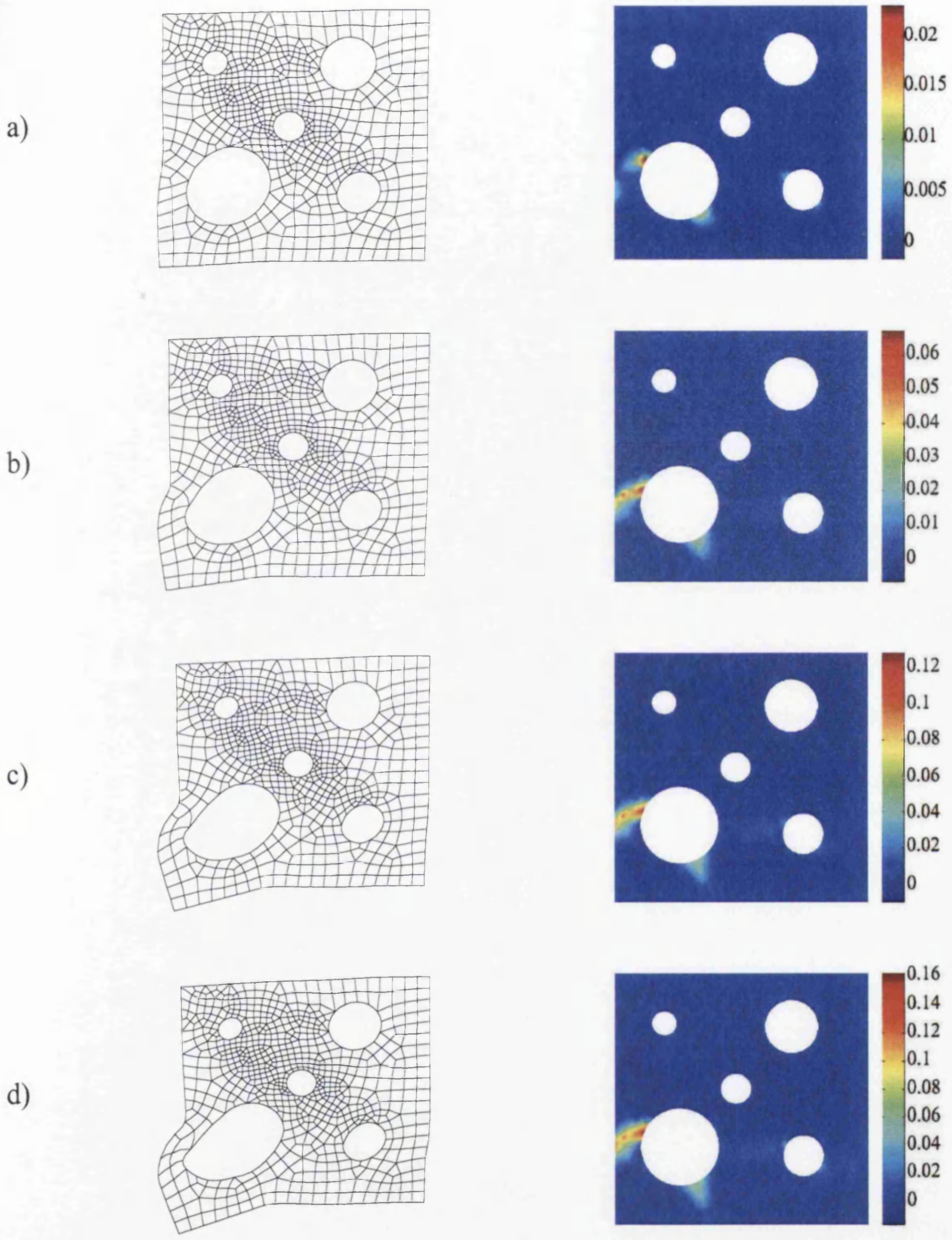

Figure 8.31: Effective plastic strain contour plots for the irregular model-5 with uniform boundary traction assumption.

Figure 8.32 shows the evolution of the homogenised normal stress components $\bar{\sigma}_{xx}$, $\bar{\sigma}_{yy}$ and $\bar{\sigma}_{xy}$.

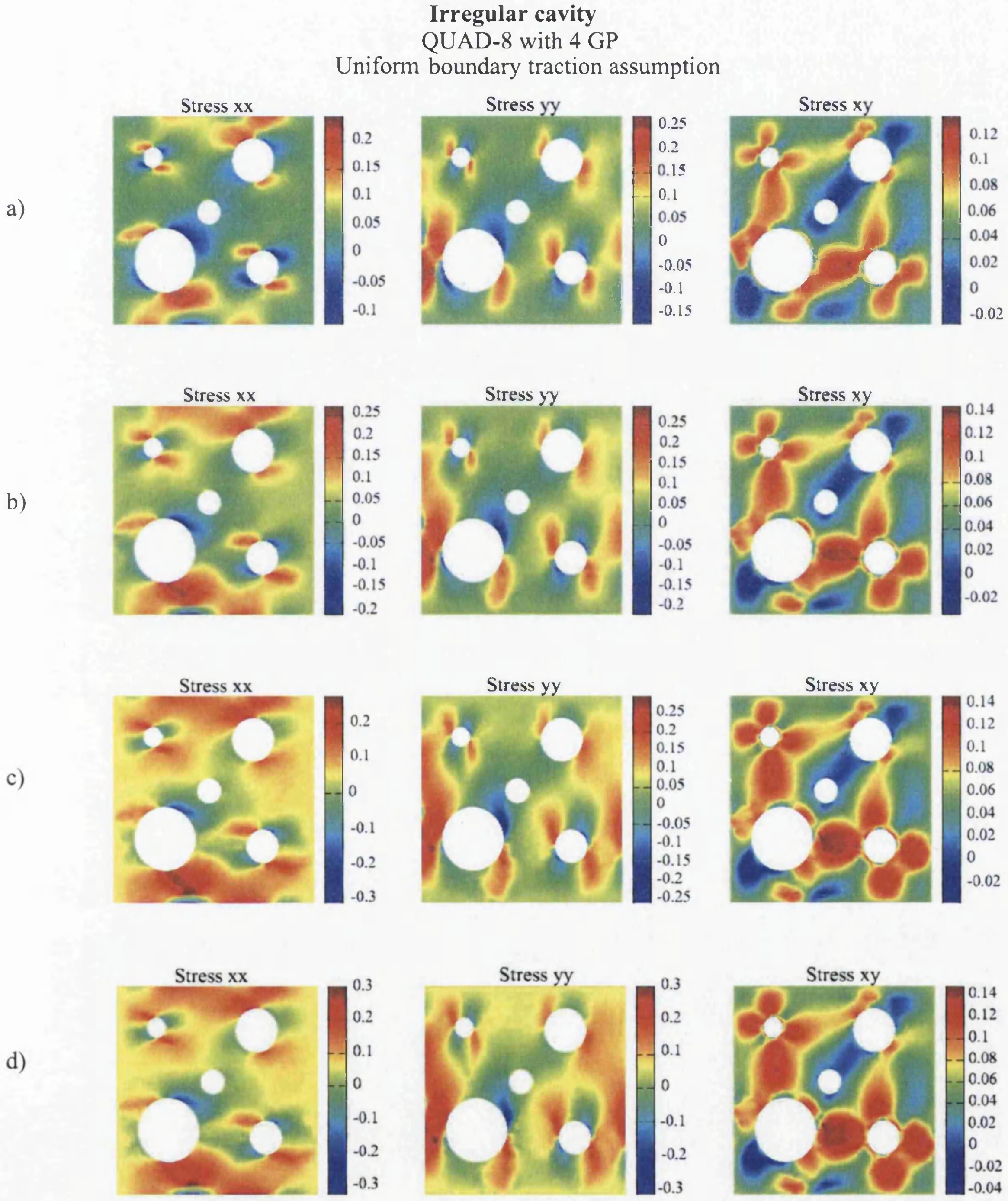

Figure 8.32: Stress contour plots for the irregular model-5 with uniform boundary traction assumption.

With regard to the different contour plots obtained from the linear displacement boundary condition, the periodic boundary displacement fluctuations condition, and the uniform boundary traction assumption, we can consider the effect of the various boundary conditions on the internal variables such as stress components and effective plastic strain. As can be seen these effects are crucial in plastic failure. It is clear from effective plastic strain contour plots and imposed strain pattern, that plastic failure starts from a critical loaded ligament between two voids and develops up to the boundary of the unit cell.

8.7 The RVE with dense area of voids

The last test in this chapter is a unit cell of side length equal to $1\mu m$ and the void volume fraction value equal to 15%. In this model we consider a large unmber of cavities and consequently discretize a model by a dense mesh (see Figure 8.33). 3-node linear triangular element is employed. This model is considered as a plane-stress problem and under three boundary conditions; (i) the linear displacement boundary condition, (ii) the periodic boundary displacement fluctuations condition and (iii) the uniform boundary traction assumption. Imposed macro-strain and material properties for this model are identical to previous examples in this chapter.

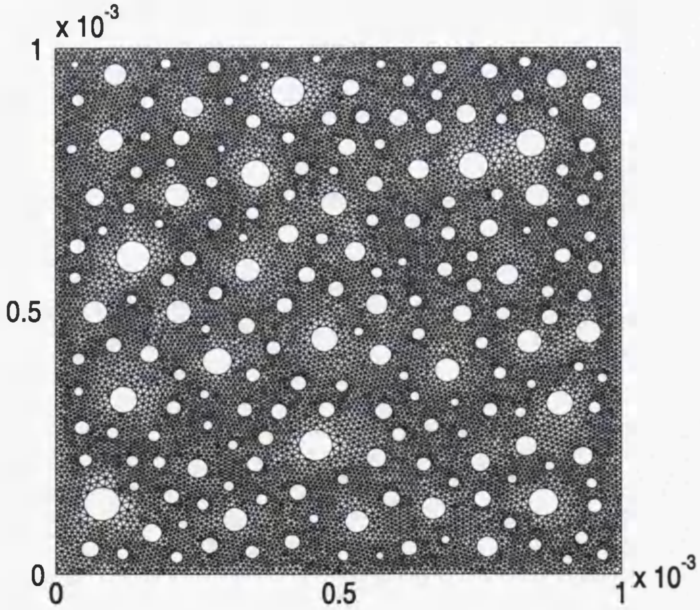

Figure 8.33: Unit cell with dense distribution of voids.

The effective average stress for the model under the cited boundary conditions is shown in Figure 8.34 against the norm of the strain.

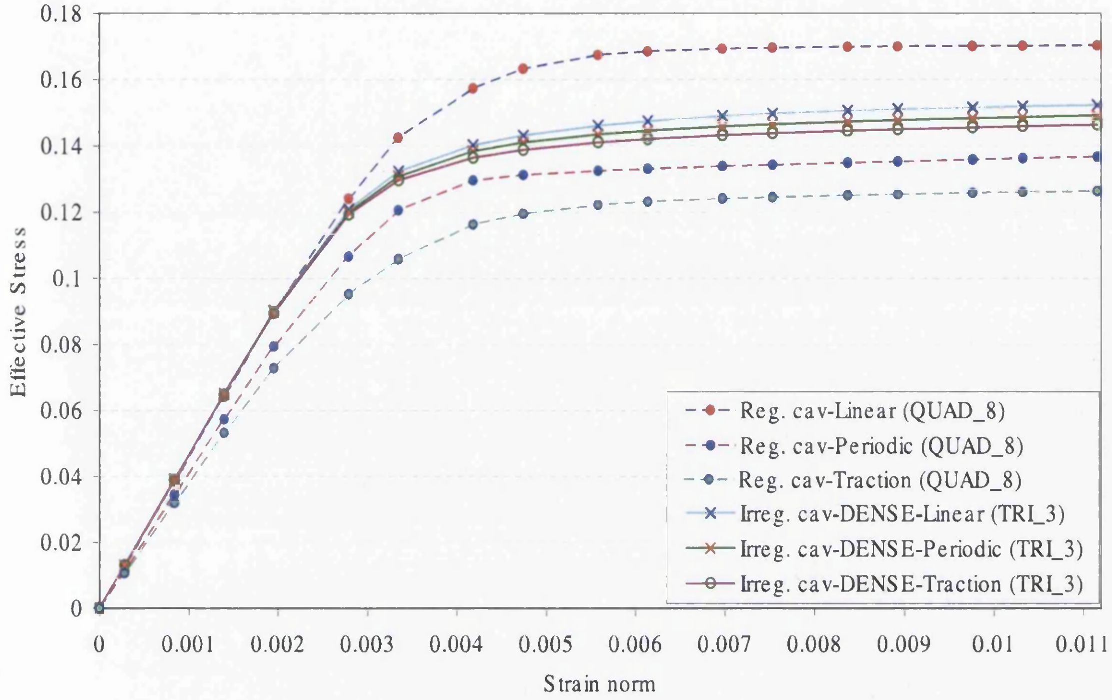

Figure 8.34: Effective stress - Strain norm curves for dense model under three boundary conditions.

Figure 8.34 illustrates comparison between the overall properties of the regular model with single void inside the unit cell and the dense model. This figure clearly indicates the convergence of the average properties with increase of the statistical sample representing the heterogeneities at the micro-level. As can be seen from Figure 8.34, although the homogenised responses of the dense model under the three different boundary conditions become close to each other, the linear displacement boundary condition shows upper bound while the uniform boundary traction presents the lower limit for the overall behaviour of the dense model.

Figure 8.35 shows the effective plastic strain contour plots for the dense mesh under the linear displacement boundary condition, the periodic boundary displacement fluctuations condition and the uniform boundary assumption. It is generally accepted that the growth path for the effective plastic strain follows the certain path inside the cell (see Figure 8.35). This path usually is known as 'rupture path', which in practice with further increase in load usually gives the failure pattern. The density of the cavities, the distance between the neighbouring cavities and the size of the cavities are crucial factors to form this critical failure ligament at micro-level.

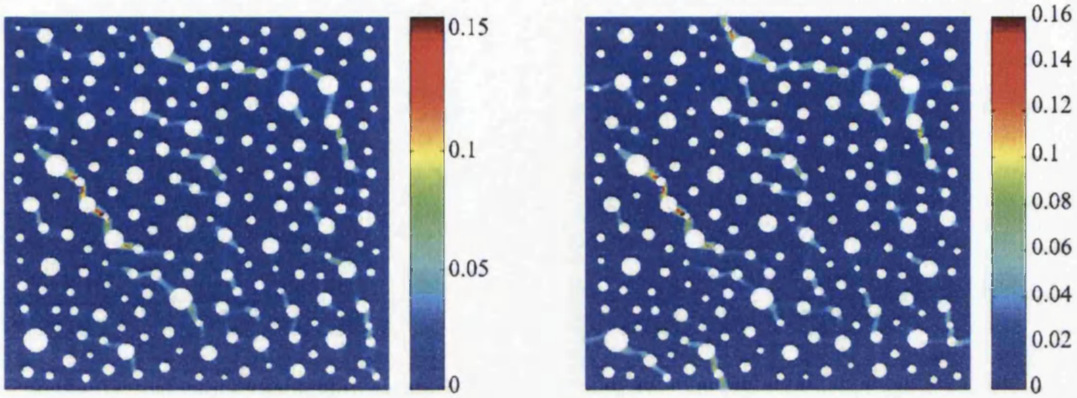

Linear displacement assumption. Periodic displacement assumption.

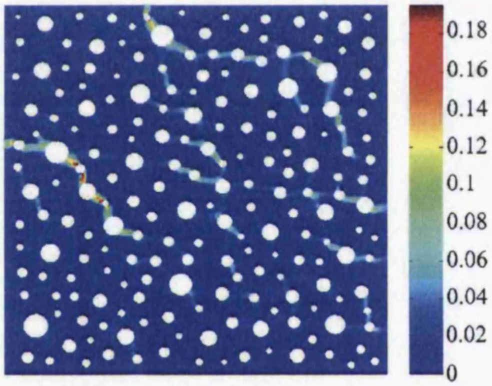

Uniform boundary traction assumption.

Figure 8.35: Effective plastic strain contours for dense model under three boundary conditions.

8.8 Conclusion

In the first part of this chapter, it was shown that the implementation of the multi-scale code satisfies the basic requirements for the heterogeneous media with a periodic micro-structure. To this end numerical simulations were performed to benchmark the overall behaviour of the cell remains unchanged when the imposed constraint over the RVE is the periodic boundary displacement fluctuations.

In the second part of this chapter we have focused on the effect of the distribution of the cavities in the unit cell. For this aim we have defined one regular cavity model and ten different models with random distribution of the cavities. Firstly we have obtained the overall response of the models by imposing the macro-strain over the unit cells. The analyses were considered under three boundary conditions. For obtaining these results we used linear triangle element and 8-node quadrilateral element with full and reduced number of integration points. Based on the effective stress - strain norm graphs, for the linear displacement boundary condition we observed that the regular model shows yielding at higher stresses compared with the other models. In contrast, the uniform boundary traction shows the softest overall behaviour. Based on the obtained results for the periodic boundary displacement fluctuations condition we could accept the regular model as a good estimate for other irregular models with reasonably small error.

We have selected two models; the regular cavity model and the irregular model-5 with 8-node quadrilateral element with 4-Gauss points, and reviewed the behaviour of the models in more detail. Based on the stress components graphs we concluded that the randomly and regular distribution of the cavities make an effect in the overall behaviour of the unit cell in two main directions, x and y. Moreover, based on contour plots, the distribution of the cavities had critical role in plastic behaviour of the unit cell.

We showed the relation between growth of the effective plastic strain and displacement of the unit cell with respect to the defined boundary assumptions. The irregularity of the micro-structure is reflected in the yield process, which occurs as a sequence of shear part of the imposed strain, distributed over the whole micro-structure. A shear process typically involves the development of shear bands in, for example, a critically loaded ligament between two voids.

Finally, the last test has illustrated that increasing in density of pores cause the overall properties of the RVE under the three different boundary conditions converge towards each other. Still the results obtained by the linear displacement boundary condition give the upper limit, and the results obtained under the periodic boundary displacement fluctuations condition show a softer response. The lower limit for the homogenised properties has been given under the uniform boundary traction assumption.

Chapter 9

Study of the effective yield surface of porous media

9.1 Introduction

The object of this chapter is the study the homogenised elasto-plastic behaviour of porous media based on the computational homogenisation methodology presented in earlier chapters.

Several authors proposed models for porous material behaviour in which the real material is replaced by an '*equivalent*' homogeneous material with an additional internal parameter describing the material porosity. Among these models, Gurson's [83] is the most widely accepted. This model was developed by considering porous material with a single cavity in a unit cell composed of a rigid plastic von Mises material. The resulting yield surface is obtained as [83]

$$\Phi = \frac{\bar{\sigma}_{eqv}^2}{\sigma_y^2} + 2f\cosh\left(\frac{\sqrt{3}}{2}\frac{\bar{\sigma}_h}{\sigma_y}\right) - 1 - f^2 = 0, \tag{9.1}$$

where $\bar{\sigma}_{eqv} = \sqrt{3J_2(\boldsymbol{s})}$, is the von Mises equivalent stress, $\boldsymbol{s}$ is deviatoric stress, f is void volume fraction and σ_y is microscopic equivalent tensile yield stress. In equation (9.1), due to axial symmetry assumption, $\bar{\sigma}_h = \frac{\bar{\sigma}_{11}+\bar{\sigma}_{22}}{2}$.

Gurson's model was later modified by Tvergaard [84] (Gurson-Tvergaard equation), by introducing additional parameters resulting in

$$\frac{\bar{\sigma}_{eqv}^2}{3\sigma_y^2} + 2q_1 f^* cosh\left(q_2\frac{\sqrt{3}\bar{\sigma}_m}{2\sigma_y}\right) - 1 - q_1^2 f^{*2} = 0, \tag{9.2}$$

where, q_1 and q_2 are additional parameters and the hydrostatic pressure $\bar{\sigma}_m$ is expressed by,

$$\bar{\sigma}_m = \sum_{i=1}^{3} \bar{\sigma}_{ii}/3. \tag{9.3}$$

They were found to be in agreement with numerical studies of materials containing periodically distributed circular cylindrical or spherical voids by using $q_1 \approx 1.5$ and $q_2 \approx q_1^2$.

In this chapter, we consider the effect of the porosity of material on the effective yield surface. The porosity is varied in terms of the void volume fraction, distribution of cavities, and the regularity of distribution of cavities at micro-level. The effect of different boundary conditions over the RVE on the homogenised yield surface is also considered.

9.2 Models specification

In this section, we chose a unit cell with side length equal to $1\mu m$ and a single cavity in the middle of the cell. This model is denoted the 'regular cavity model'. The unit cell has been modeled with two different cavity types represented by circular and square hole. The 8-noded quadrilateral element with 4-GP has been selected for finite element mesh model. Figure 9.1 shows two different unit cells with 15% cavity.

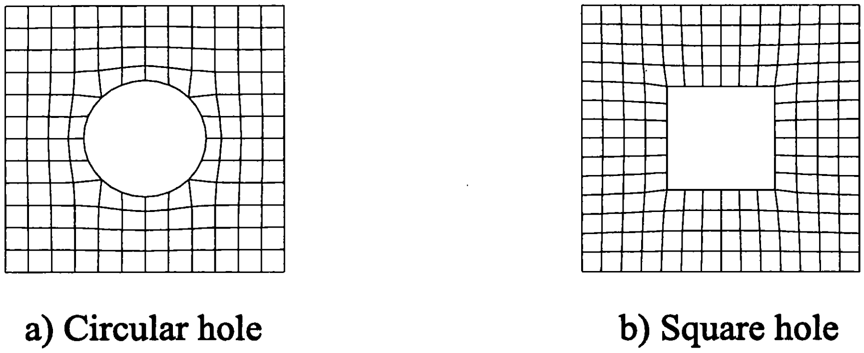

a) Circular hole **b) Square hole**

Figure 9.1: Two different unit cells' mesh models. a) Circular hole. b) Square hole.

Table 9.1 shows the relevant information about the number of elements and nodes for different unit-cell models with a circular hole, and Table 9.2 gives the same information for square cavity models.

Model Type	*Number of Elements*	*Number of Nodes*
Regular 5%	126	438
Regular 10%	128	448
Regular 15%	128	448
Regular 20%	124	444
Regular 30%	92	348

Table 9.1: Different unit-cells with circular hole.

Model Type	*Number of Elements*	*Number of Nodes*
Regular 5%	128	448
Regular 10%	128	448
Regular 15%	160	560
Regular 20%	192	672
Regular 30%	224	784

Table 9.2: Different unit-cells with square hole.

The von Mises elastic perfectly plastic material model has been selected for the matrix. The material properties assigned to these models are; Young's modulus: $E = 70\ GPa$, Poisson ratio: $v = 0.2$ and uni-axial tensile yield stress equal to $\sigma_{y_0} = 0.243\ GPa$.

9.3 Analysis approach

All examples have been carried out by employing the computational homogenisation under the plane-stress assumption as a single scale analysis. The average stress is obtained by imposing the macro-strain over the unit cell and solving the problem for defined boundary condition over the RVE. The generic imposed macro-strain tensor is expressed by the following form:

$$\bar{\varepsilon} = [\bar{\varepsilon}_{11}, \bar{\varepsilon}_{22}, 0] = [0.01, 0.01, 0]. \tag{9.4}$$

The load factors multiplied to the above strain tensor are defined by:

$$[0, 0.1, ..., 4].$$

To cover the whole range of the macro-strains without shear component, we specified a general pattern for all examples in this chapter. This pattern follows the angular parameter **λ**, which could be obtained from the reference strain-circle shown in Figure 9.2 and multiplied by the original strain tensor.

$$\bar{\varepsilon} = [\lambda_1 \bar{\varepsilon}_{11}, \lambda_2 \bar{\varepsilon}_{22}, 0], \tag{9.5}$$

where $\lambda_1 = Cos\theta$, $\lambda_2 = Sin\theta$ and θ is an angle of the reference line with respect to the *1-1* axis in strain space (see Figure 9.2).

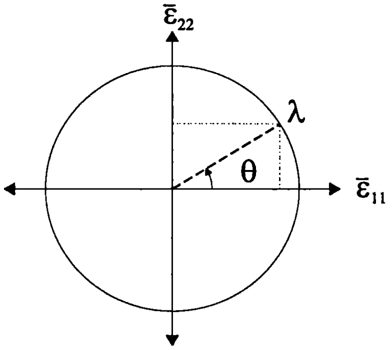

Figure 9.2: Macro-strain path at strain space circle.

The values for θ are,

$$\theta = [0°, 5°, 10°, 15°, ..., 360°].$$

Initially, uniaxial test is used in which $\theta = 0$ and macro-strain tensor defined only by one component, $\bar{\varepsilon}_{11}$, in *1-1* direction. By increasing the value of θ, new combinations of the macro-strain components create different deformed configurations over the RVE such as stretching, compressing and shear deformation. Figure 9.3 shows different loading paths regarding to the different imposed macro-strains over an RVE with 15% circular cavity under the linear displacement boundary condition. As can be seen from this figure the yield surface, for this particular model, can be achived by connecting the ultimate nodes from different loading paths.

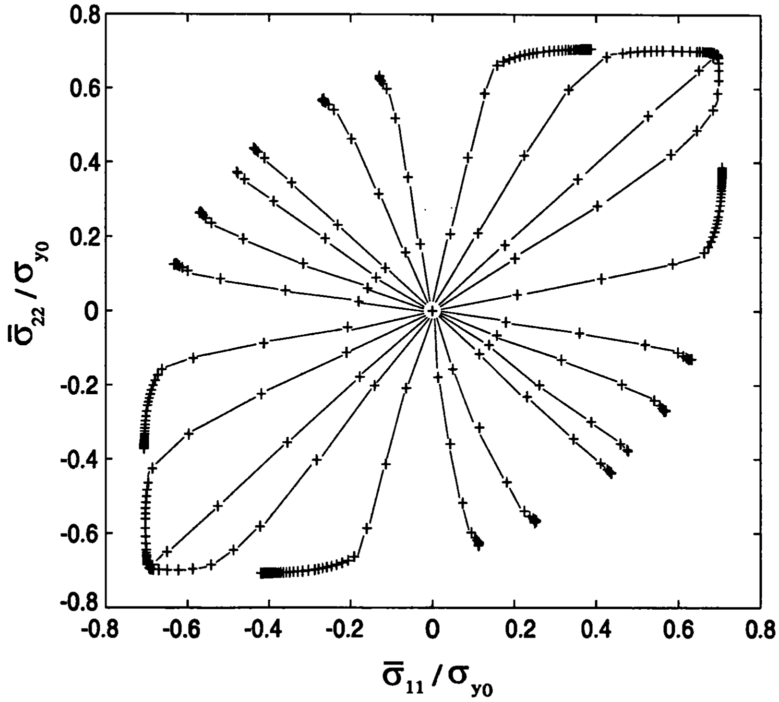

Figure 9.3: Loading path for different imposed macro-strains over the cell

9.4 Overall yield stress surfaces for regular models

This section is divided into two parts. The first part is related to the study of the homogenised yield surfaces of the micro-structures with cylindrical cavities and the next part is the same study but instead of the unit-cells with circular hole, the regular unit cell models with square cavities have been considered.

9.4.1 Taylor assumption over the RVE with circular hole

We start by showing predicted yield surface under the Taylor assumption which is the upper bound for homogenised material models. This assumption shows the stiffest behaviour of all kinematical assumptions.

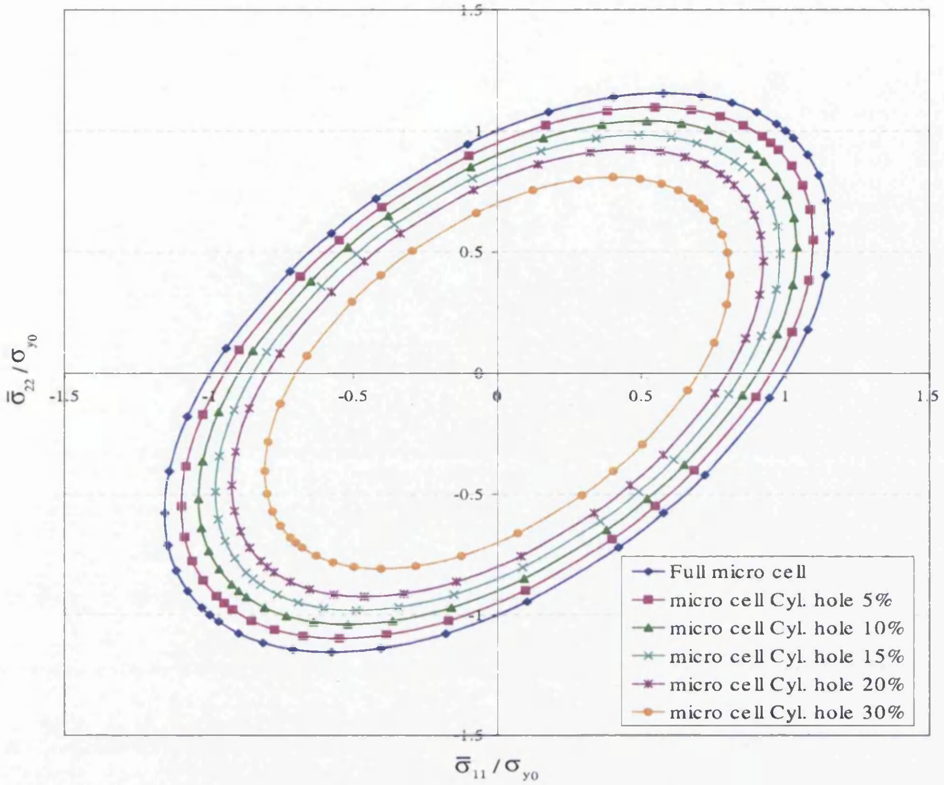

Figure 9.4: Overall yield surfaces for the Taylor assumption.

Figure 9.4 shows different yield surfaces for different micro cavities under the Taylor assumption. These graphs have been plotted in homogenised principal stress space ($\bar{\sigma}_{11} - \bar{\sigma}_{22}$). For more convenience in the interpretation of the results, axes have been normalized with respect to the microscopic equivalent tensile yield stress, σ_{y0}. As can be seen from these graphs, by increasing the void volume fraction, unit cells show softer response, in other words, they lose their load-bearing capacity with respect to the unit cell without cavity. From the definition of the Taylor assumption it can be concluded that by increasing the size of the cavity – in this case up to 30% of the cell's volume – the new micro cell loses more than 30% of its original load capacity in biaxial test. It should be mentioned that because of stiff response of the Taylor assumption, in shear deformation, we have smooth ellipse shapes for all overall yield surfaces with different void volume fractions. In the next sections it will be shown that this behaviour is not always valid for other boundary conditions, and unit cells show different behaviour especially in the biaxial stress region.

9.4.2 Linear displacement boundary condition over the RVE with circular hole

The linear displacement boundary condition is the next boundary condition which is considered. In this boundary condition, different macro-deformations have been imposed over the RVE under the linear displacement boundary condition. The homogenised responses for different unit-cells have been plotted in Figure 9.5.

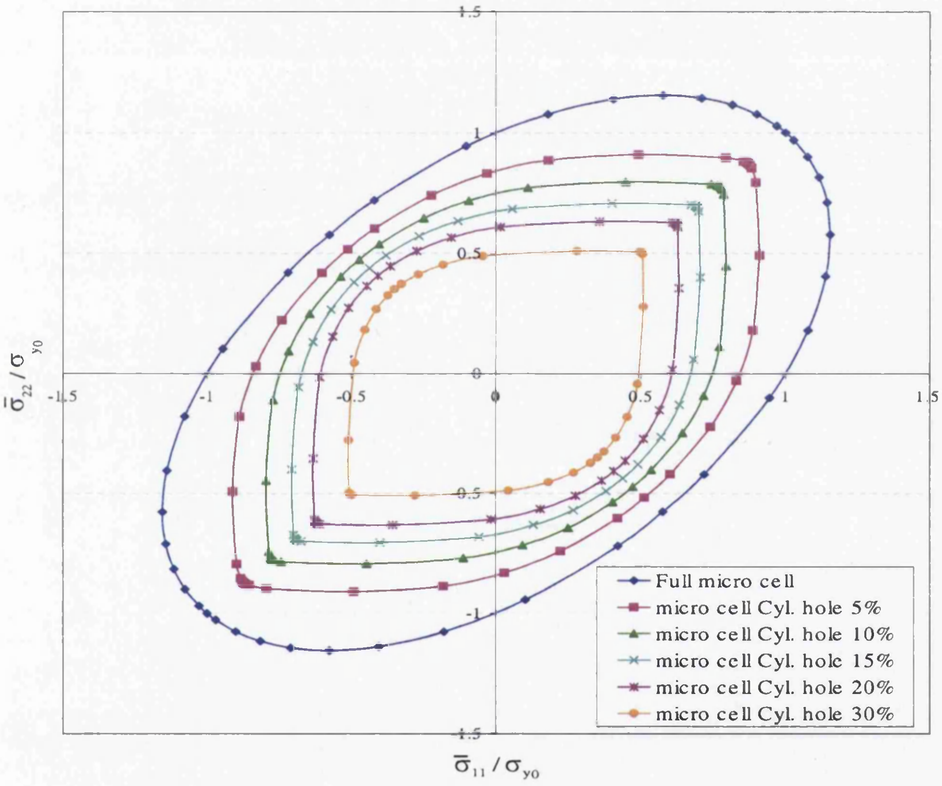

Figure 9.5: Overall yield surfaces for the Linear displacement boundary condition.

As can be seen from Figure 9.5, under this boundary condition the overall yield surfaces show completely different shapes with respect to the yield surfaces obtained from the Taylor assumption. These variations are clearly shown by sharp edges which are the results obtained from biaxial deformation tests and smoother side lines for shear deformation responses. In addition, as we expected, this boundary condition shows softer response in comparison to the Taylor assumption. This means that in this boundary condition, by increasing the void volume fraction of the micro-cell, the unit cell loses more strength in comparison with the same void volume fraction model under the Taylor assumption. For example from Figure 9.5 it may be seen that, in the biaxial test, a unit cell with 30% cavity under linear displacement boundary condition has lost 50% of its original load-bearing capacity.

9.4.3 Periodic displacement boundary condition over the RVE with circular hole

Study of the homogenised yield surface under the Periodic displacement boundary condition is more valuable due to its closest response to the real material behaviour. The imposed macro-strains are the same as those in the previous test.

Figure 9.6 shows different homogenised yield surfaces under the periodic displacement fluctuations boundary condition for different void volume fractions. The most interesting point in these graphs, is the overall response of the unit-cells in biaxial tensile deformation. The homogenised yield surfaces of the unit-cells under the periodic displacement fluctuations boundary condition in this region result in straight lines. The reason for this behaviour according to Ponte Castaneda [85], is that the yield surfaces exhibit 'flat sectors' at or near some weak point modes. The corresponding weak modes, in this example, belong to the imposed macro-strains which cause shear deformations over the unit-cell. In other words, unit-cells do not show enough strength for imposed macro-shear deformations. The range of this behaviour varies. It is less for the unit-cells with smaller void volume fraction value and by increasing the void volume fraction value this range is increased. As we mentioned earlier, the periodic displacement fluctuations boundary condition is one of the most reliable boundary conditions that can be used to predict the real behaviour of the composite materials. The limit range of the response for this boundary condition is lower than linear displacement boundary condition and is higher than the uniform boundary traction condition. Therefore, by increasing the void volume fraction at micro-level we expect that the RVE loses more of its original load capacity. This fact has been shown in Figure 9.6. From these graphs it may be concluded that, in the biaxial test, a unit-cell with 30% cavity under the periodic displacement fluctuations boundary condition will lose its original load-bearing capacity by a value of around 60%.

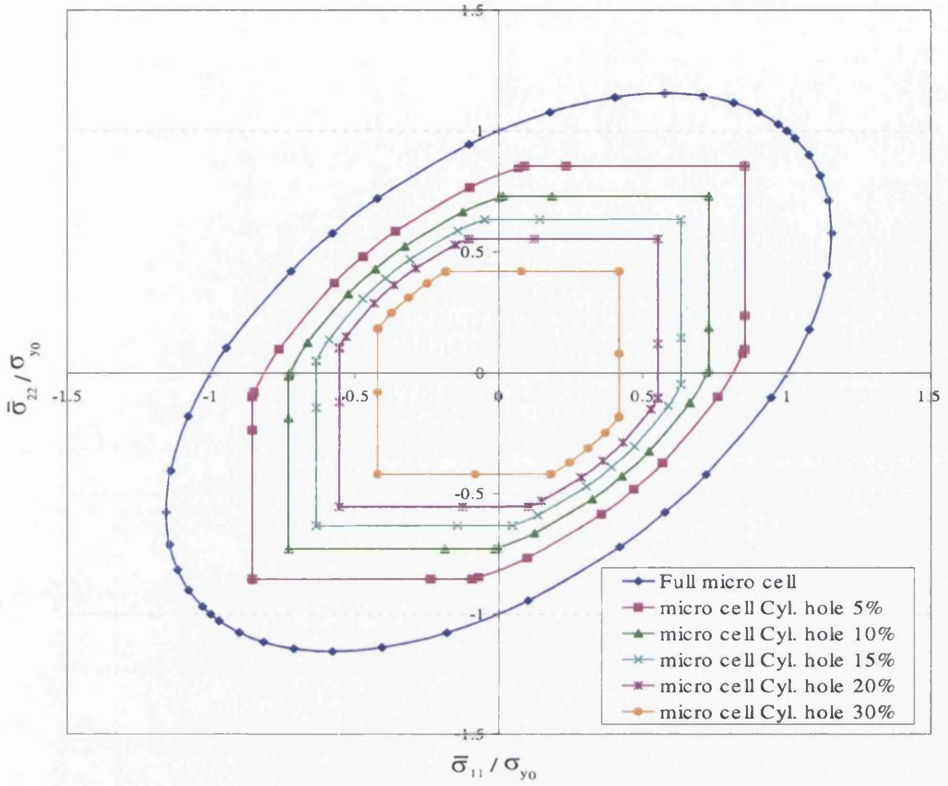

Figure 9.6: Overall yield surfaces for the Periodic displacement fluctuations boundary condition.

9.4.4 The uniform boundary traction condition over the RVE with circular hole

In contrast to the Taylor assumption, uniform boundary traction condition presents lower bound for the overall behaviour of the RVE. The predicted homogenised behaviour of the micro-cell under the uniform boundary traction condition shows a softer response with respect to the periodic displacement fluctuations boundary condition or linear displacement boundary condition. Softening of the overall yield surfaces is one of the expected effects of the uniform boundary traction condition over the RVE.

The effect of the boundary condition has been shown in Figure 9.7. Comparing the resulting homogenised yield surfaces (Figure 9.7) with other overall yield surfaces which obtained from other boundary conditions (Figures 9.4 - 9.6) confirms that the homogenised response from micro-cell is much softer than other boundary assumptions. For example for a unit-cell with 30% cavity, in the biaxial test, its load bearing capacity reduces to the 40% of its original load capacity and in the uni-axial test, its load capacity reduces to 20% of the original one.

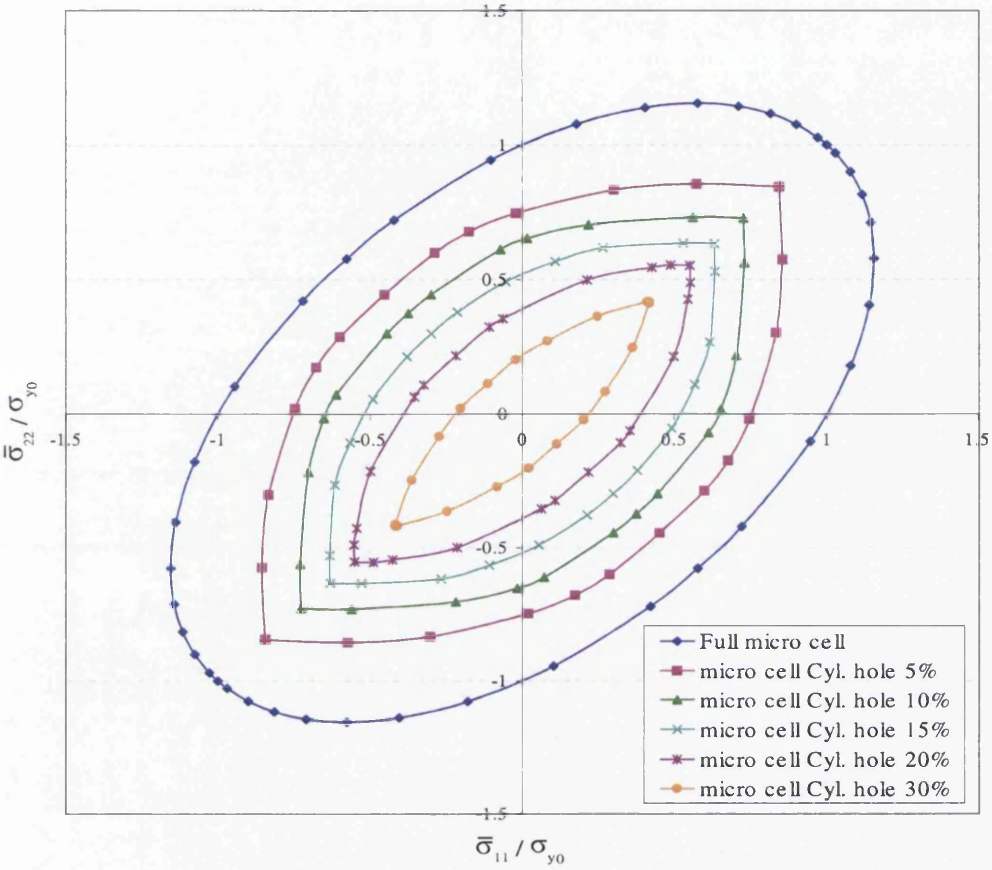

Figure 9.7: Overall yield surfaces for the uniform boundary traction condition.

Figure 9.8, shows the load-bearing capacity of the regular micro-cell model against the void volume fraction under the equal biaxial conditions. As can be seen from Figure 9.8, by increasing the percentage of the void volume fraction of micro-cell, load capacity of the micro-cell decreases with respect to the different prescribed boundary conditions over the RVE. From Figure 9.8, it is clear that a unit cell with 30% cavity, has the most load-bearing capacity under the Taylor assumption because of rigidity overall response of this boundary condition, and the lowest load-bearing capacity is obtained from uniform boundary traction condition over the unit-cell.

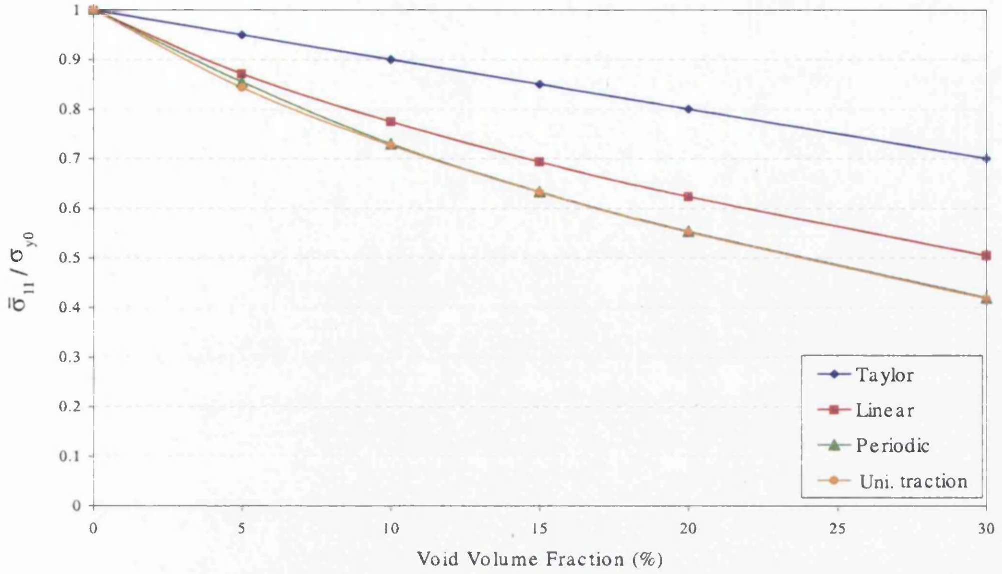

Figure 9.8: Load capacity in biaxial test for different boundary conditions.

9.4.5 Taylor assumption over the RVE with square hole

In the second part of our homogenised yield surface study, regular cell models with a square hole in the middle of the cell have been considered. We start our tests with the Taylor assumption. The results for the overall yield surfaces have been plotted in Figure 9.9.

9.4.6 Linear displacement boundary condition over the RVE with square hole

The next boundary condition is the Linear displacement boundary condition. In this boundary condition, different macro-deformations have been imposed over the RVE under the linear displacement boundary condition. The homogenised response for different unit-cells with square cavity has been plotted in Figure 9.10. From this figure it may be seen that, in the biaxial test, a unit cell with 30% square cavity under the linear displacement boundary condition has lost almost 48% of its original load-bearing capacity. The difference between square cavity and cylindrical hole has not dominated the overall response of the unit-cell in the linear displacement boundary condition.

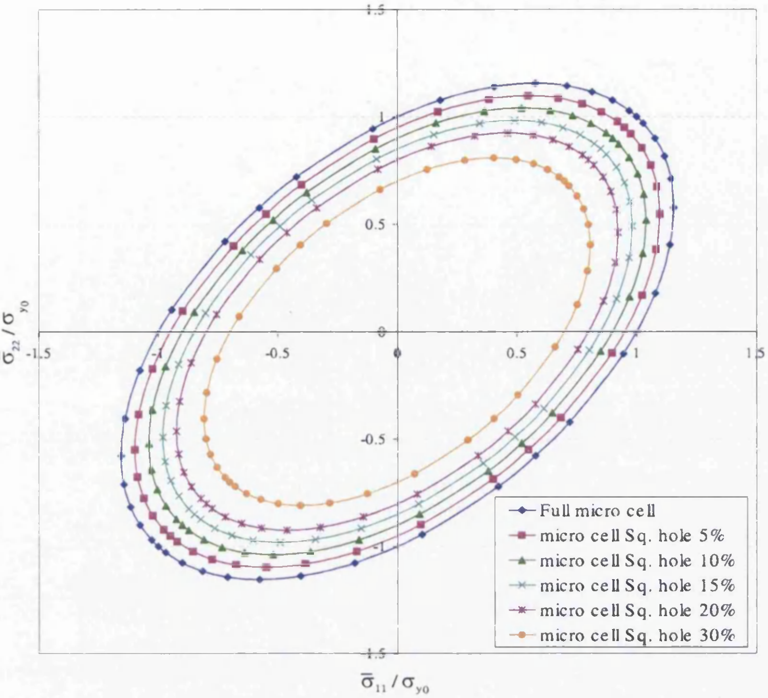

Figure 9.9: Overall yield surfaces for the Taylor assumption.

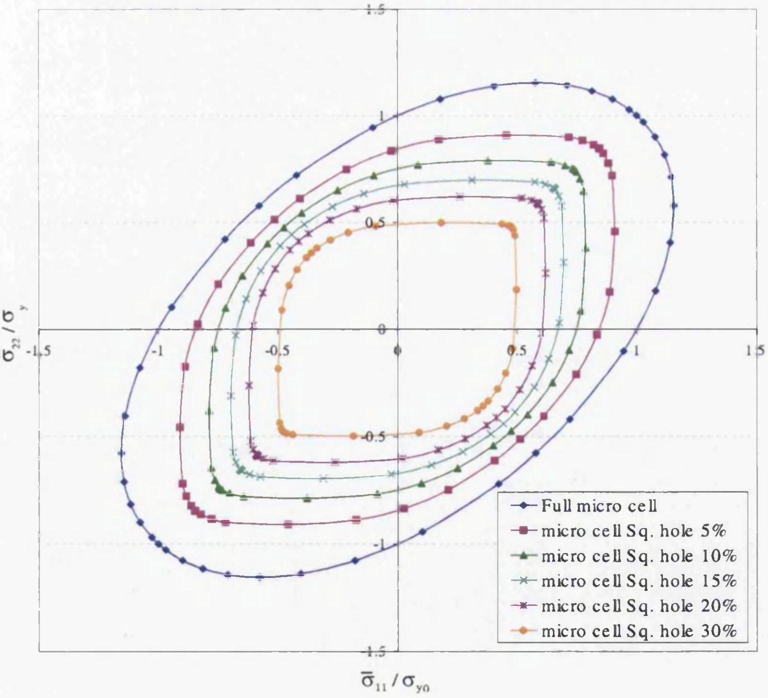

Figure 9.10: Overall yield surfaces for the Linear displacement boundary condition.

9.4.7 Periodic displacement boundary condition over the RVE with square hole

The effect of the shape of cavity, square or cylindrical hole, becomes more obvious under the periodic displacement fluctuations boundary condition. Figure 9.11 shows different yield surfaces under the periodic displacement fluctuations boundary condition. From Figure 9.11 the same observations are made as the behaviour of the RVE with a circular hole in the case of the imposed biaxial deformation.

From these graphs it may be concluded that, in the biaxial test, a unit-cell with 30% cavity under the periodic displacement fluctuations boundary condition will lose its original load-bearing capacity by a value of around 45%. The obtained load-bearing capacity value for a cell with a square cavity shows stiffer overall response as compared to the same model with circular cavity.

9.4.8 The uniform boundary traction condition over the RVE with square hole

Figure 9.12 shows the overall yield surfaces for an RVE with a square hole under the uniform boundary traction assumption. Comparing the homogenised uniform boundary traction yield surfaces in Figure 9.12 with other overall yield surfaces obtained from other boundary conditions (Figures 9.9 - 9.11), confirms that the homogenised response from micro-cell is much softer than other boundary assumptions. For example, for a unit-cell with 30% cavity, in the biaxial test, its load bearing capacity reduces to 33% of the original load capacity.

By comparing the homogenised yield surfaces which have been obtained from the regular square cavity models, shown in Figure 9.12, with the overall yield surfaces obtained from the regular circular cavity models (Figure 9.7) it may be concluded that the regular micro-cell models with square cavity shows softer response in equi-biaxial tests, while the same model shows stiffer behaviour for imposed shear deformation.

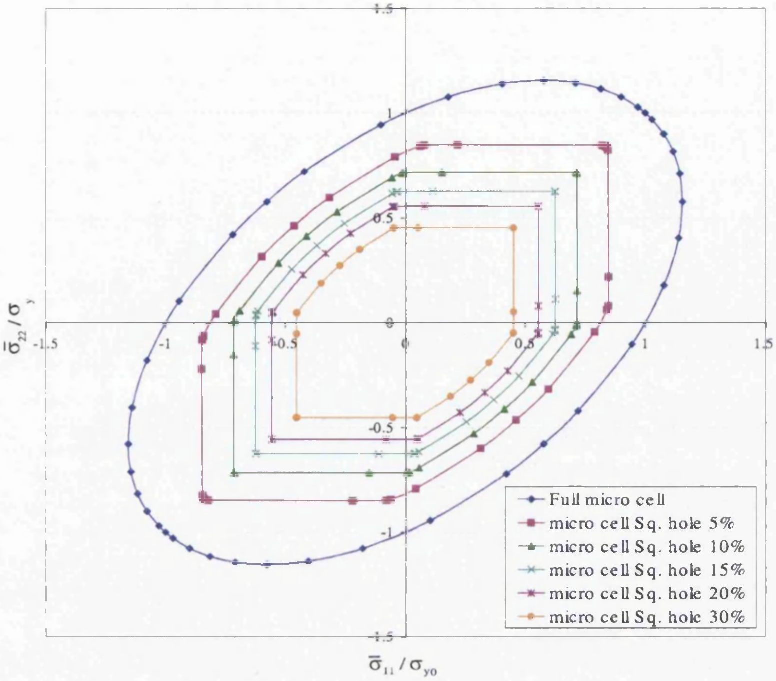

Figure 9.11: Overall yield surfaces for the Periodic displacement fluctuations boundary condition.

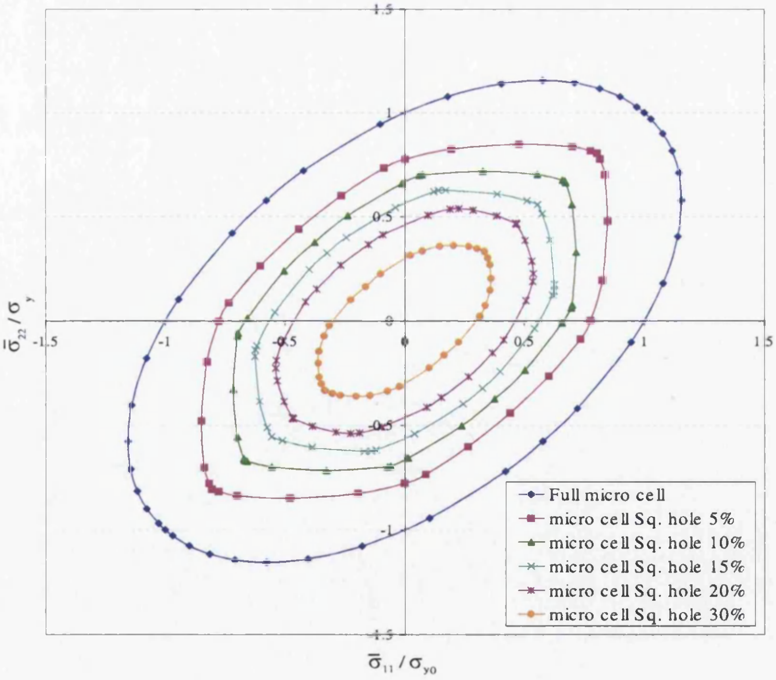

Figure 9.12: Overall yield surfaces for the uniform boundary traction condition.

Figure 9.13 shows two contour plots of the equivalent plastic strain over the micro-cell with 30% square cavity and 30% circular hole under the uniform boundary traction condition. These contour plots have been plotted at the same stage of the imposed macro-strain when $\theta = 45°$ in equation (9.5).

As can be seen from Figure 9.13 (*a*), concentration of the maximum value for plastic flow at the corners of the square cavity implies that this model shows softer response in comparison with the same model with a circular hole (Figure 9.13 (*b*)). Shear bands in Figure 9.13 (*a*), start from corners of the square hole and develop up to the outer boundary of the unit-cell – from inside of the cell to the outside of the cell – while in the circular cavity model, Figure 9.13 (*b*), the maximum values for shear bands start from outside of the micro-cell (sides of the boundary) and develop to the surface of the circular hole.

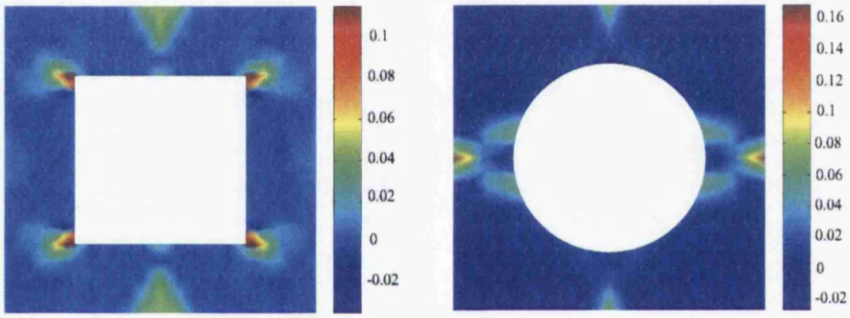

a) 30% square cavity

b) 30% circular cavity

Figure 9.13: Effective plastic strain contour plots for: a) Square cavity, and b) circular hole.

Figure 9.14 shows the load-bearing capacity of the regular micro-cell models against the void volume fractions under equi-biaxial condition. As can be seen from Figure 9.14, by increasing the percentage of the void volume fraction of the micro-cell, load capacity of the micro-cell decreases, with respect to all prescribed boundary conditions over the RVE. From Figure 9.14, it is clear that a unit cell with 30% cavity has the highest load-bearing capacity under the Taylor assumption, and the lowest load-bearing capacity is obtained from uniform boundary traction condition over the unit-cell.

As can be seen from Figure 9.14, the effect of the uniform boundary traction becomes more obvious in comparison with the other boundary conditions. By comparing the normalized values of the homogenised stress, $\bar{\sigma}_{11}/\sigma_{y_0}$ (Figure 9.14 and

Figure 9.8) it may be concluded that for both square and circular cavity models the Taylor assumption gives the same response in biaxial tests. In the linear displacement boundary condition, an RVE with a circular cavity shows stiffer response in comparison with the RVE with square cavity. On the other hand, the periodic displacement fluctuations boundary condition estimates stiffer overall behaviour for a unit-cell with square cavity. Finally, the most significant difference is in the uniform boundary traction assumption in which the square regular model shows softer overall behaviour with respect to the micro-cell with a circular cavity.

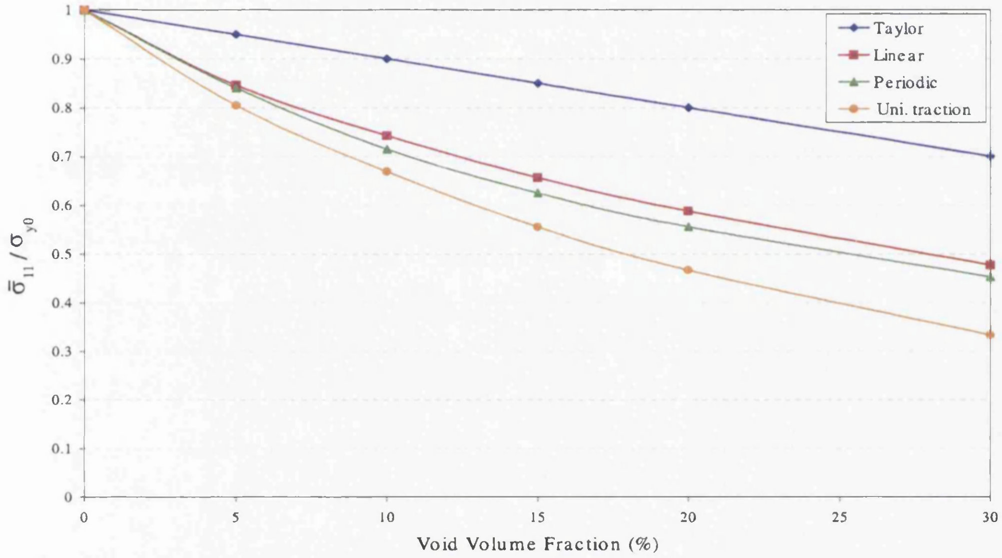

Figure 9.14: Load capacity in biaxial test for different boundary conditions.

9.4.9 Study of the effect of shape of cavities at RVE on the homogenised yield surface

In this part, we consider the effect of the shape of the cavities in the micro-cell on the overall yield surfaces under the periodic displacement fluctuations boundary condition. As discussed before, shape of the cavity affects the overall behaviour of the micro-cell. For instance in the periodic displacement fluctuations boundary condition, we showed that by increasing the void volume fraction of the unit-cell with a square cavity, the overall response of the RVE shows stiffer behaviour in comparison with the same RVE with circular hole at the micro-cell. This behaviour changes for the linear displacement boundary condition and the uniform boundary traction assumption, in which, by increasing the size of the cavity a unit-cell with a circular hole shows stiffer homogenised behaviour in comparison with the RVE with a square cavity.

Figures 9.15 and 9.16 show the comparison between the normalized values of the homogenised stress component, $\bar{\sigma}_{11}/\sigma_{y_0}$, in biaxial tests for a regular micro-cell model with a circular and square cavity model under the periodic displacement fluctuations boundary condition and uniform boundary traction assumption. As can be seen from figures 9.15 - 9.16, the effect of the shape of the cavity becomes more pronounced with increase of the size of the void under the uniform boundary traction assumption.

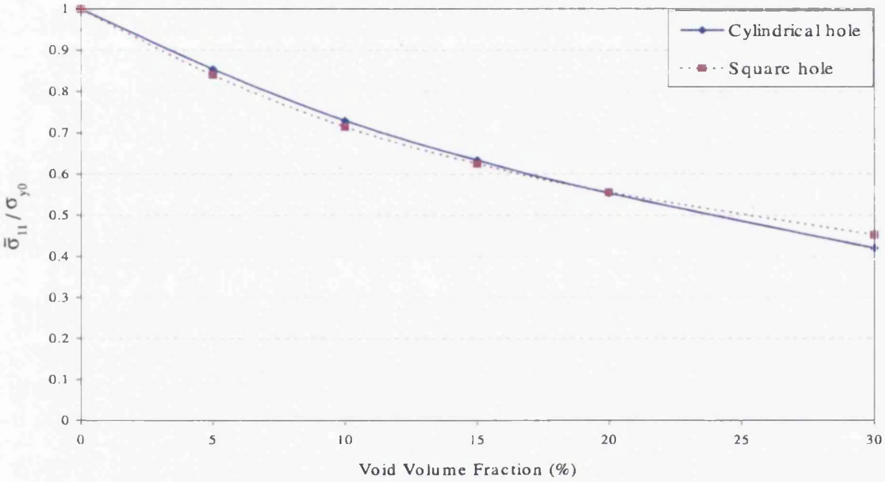

Figure 9.15: Load capacity in equi-biaxial test for different cavities - Periodic displacement B.C.

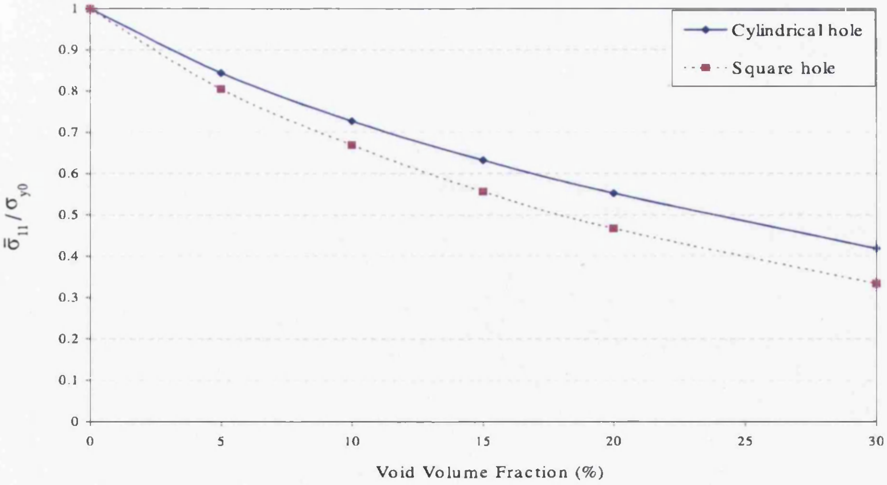

Figure 9.16: Load capacity in equi-biaxial test for different cavities - Uniform boundary traction assumption.

To illustrate the effect of the shape of the cavities on the overall yield surface we have plotted the relevant yield surfaces for a regular micro-cell model with 30% void volume fraction and different cavity shape. Figure 9.17 shows two diffrent graphs; the first one is the homogenised yield surfaces for an RVE with a circular and square cavity model under the periodic displacement fluctuations boundary condition and the second one the overall yield surfaces for different shape of the cavities under the uniform boundary traction assumption.

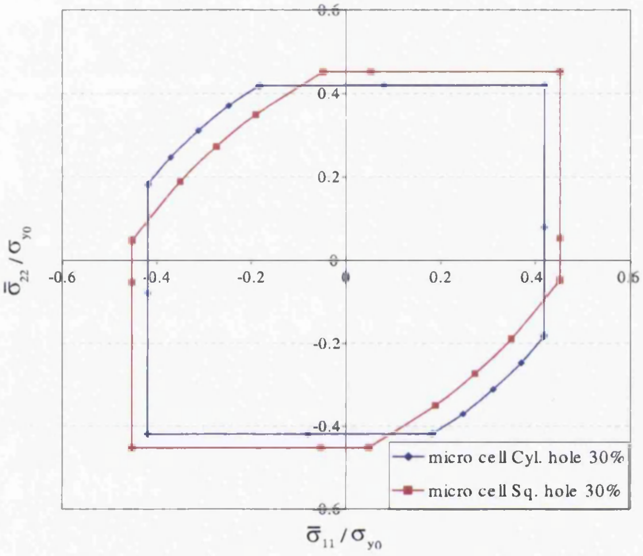

a) Periodic displacement BC.

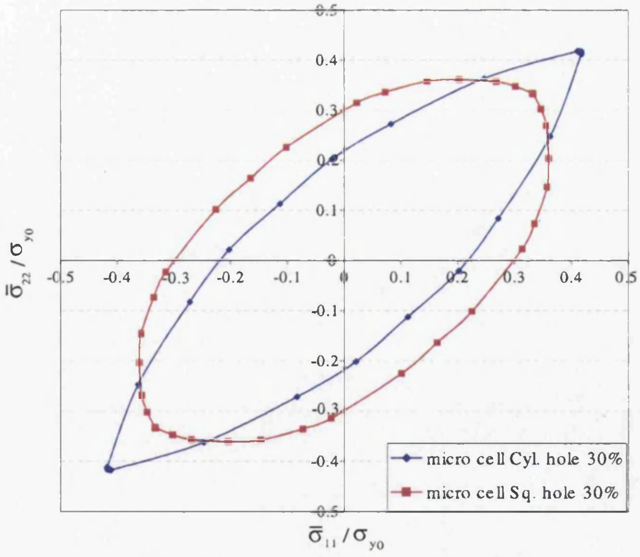

b) Uniform boundary traction assumption

Figure 9.17: The effect of the cavity shape on the overall yield surface. a)Periodic displacement boundary condition. b)Uniform boundary traction assumption.

9.4.10 Projection of the stress components on the deviatoric stress space

This part presents the projection of the overall yield surfaces on the deviatoric stress space. The homogenised normal stress components are obtained from different boundary conditions: Taylor assumption, Linear displacement boundary condition, periodic displacement fluctuations boundary condition and uniform boundary traction assumption. The stress components have then been projected to the deviatoric stress space, s_{xx} and s_{yy}.

Devitoric stress components are obtained by,

$$s = \boldsymbol{\sigma} - \sigma_{hyd}\mathbf{I}, \tag{9.6}$$

where σ_{hyd} is hydrostatic pressure which is equal to $\frac{1}{3}trace(\boldsymbol{\sigma})$ and $\boldsymbol{I}$ is the identity tensor.

In the following the effect of the regular cylindrical cavity model and square cavity model on the overall yield surfaces in deviatoric space will be considered.

Figure 9.18 shows the homogenised yield surfaces for the regular micro-cell cavity model with a circular cavity under the Taylor assumption in deviatoric stress space. As can be seen from these graphs, an increasing in size of the cavity at micro-cell affects the overall deviatoric stress components. The outer yield surface represents the behaviour of the unit-cell without any cavity and the inner yield surface shows the homogenised behaviour of a unit-cell with 30% void volume fraction. These yield surfaces in deviatoric space follow the same ellipsoidal shape but with different sizes which are dependent on the size of the cavity.

Figure 9.19 shows the projection of the overall yield surfaces obtained from the micro-cells with a square cavity in the deviatoric stress space. The comparison between the square and circular cavity regular models shows that in the Taylor assumption there is no difference between the micro-cells with circular and square cavities.

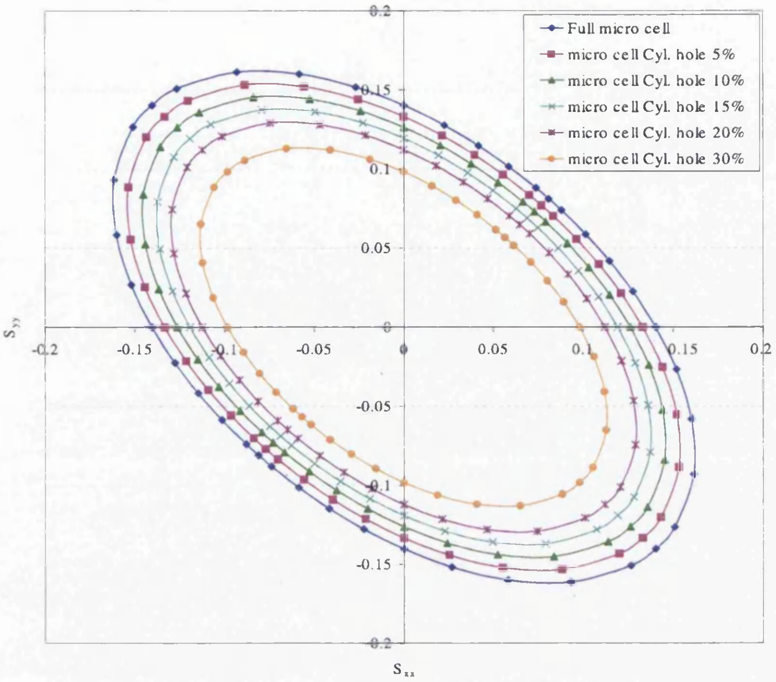

Figure 9.18: Overall yield surfaces for circular cavity models in deviatoric space for the Taylor assumption.

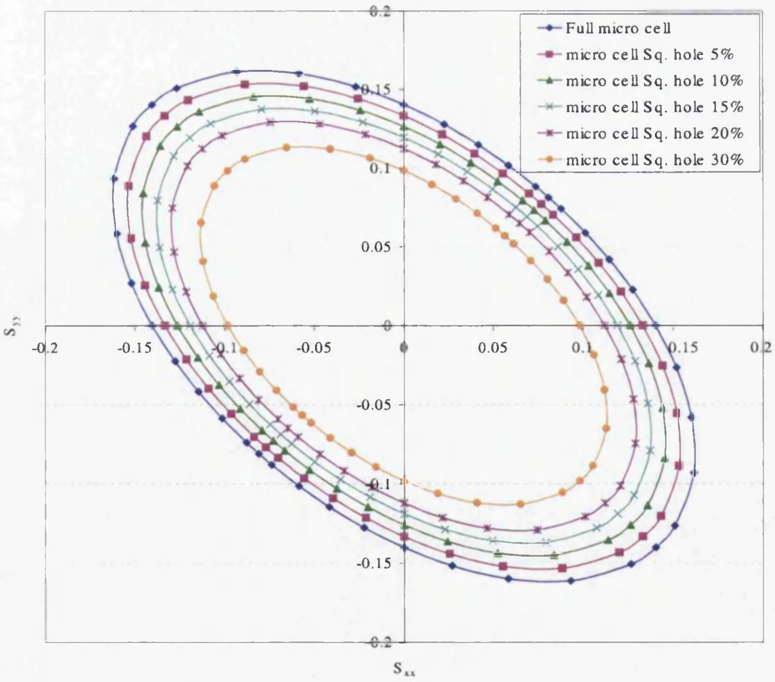

Figure 9.19: Overall yield surfaces for square cavity models in deviatoric space for the Taylor assumption.

Figure 9.20 presents different overall yield surfaces for the circular cavity models under the linear displacement boundary condition. The effect of the linear displacement boundary condition appears in the change of shape of yield surfaces in comparison with the Taylor assumption. Smooth curvatures of the corners in the Taylor assumption change to spindle shapes in the linear displacement boundary condition. From this figure it can be seen that by increasing the void volume fraction of the micro-cell, the smaller overall yield surface is obtained in deviatoric stress space.

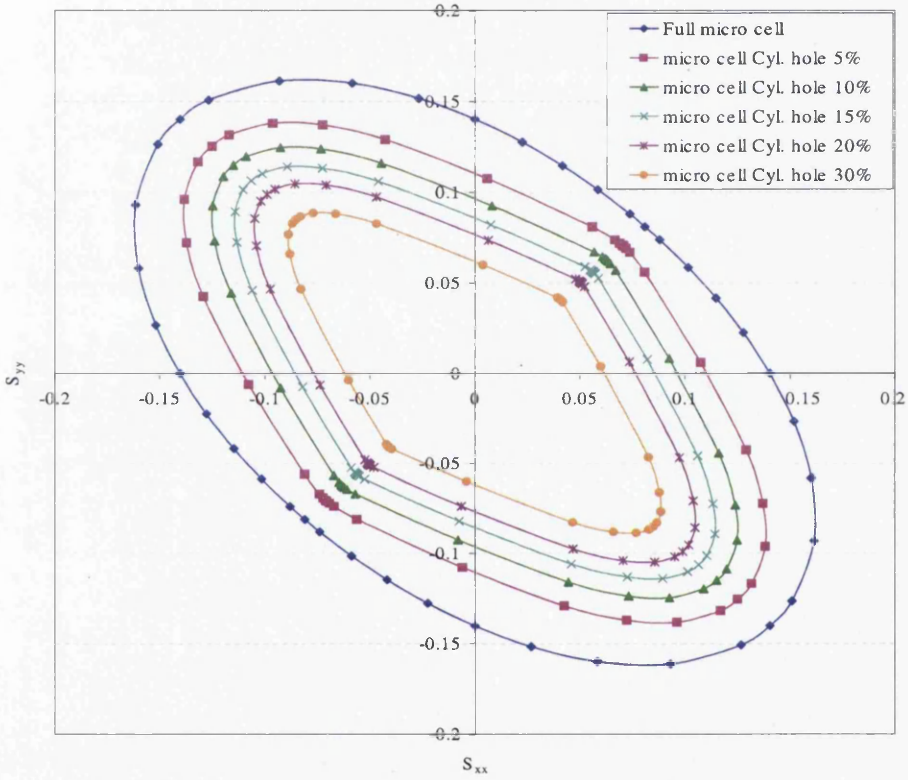

Figure 9.20: Overall yield surfaces for circular cavity models in deviatoric space for the Linear displacement boundary condition.

In addition, Figure 9.21 shows the homogenised yield surfaces for the plane stress problem for the regular micro-cell models with a square cavity. The effect of the square shape of the cavity models under the linear displacement boundary condition is not clear in comparison with the circular cavity models. In both models the value of s_{xx} varies from 0.14 GPa from a uniform micro-cell without any cavity to 0.06 GPa for the micro model with 30% cavity.

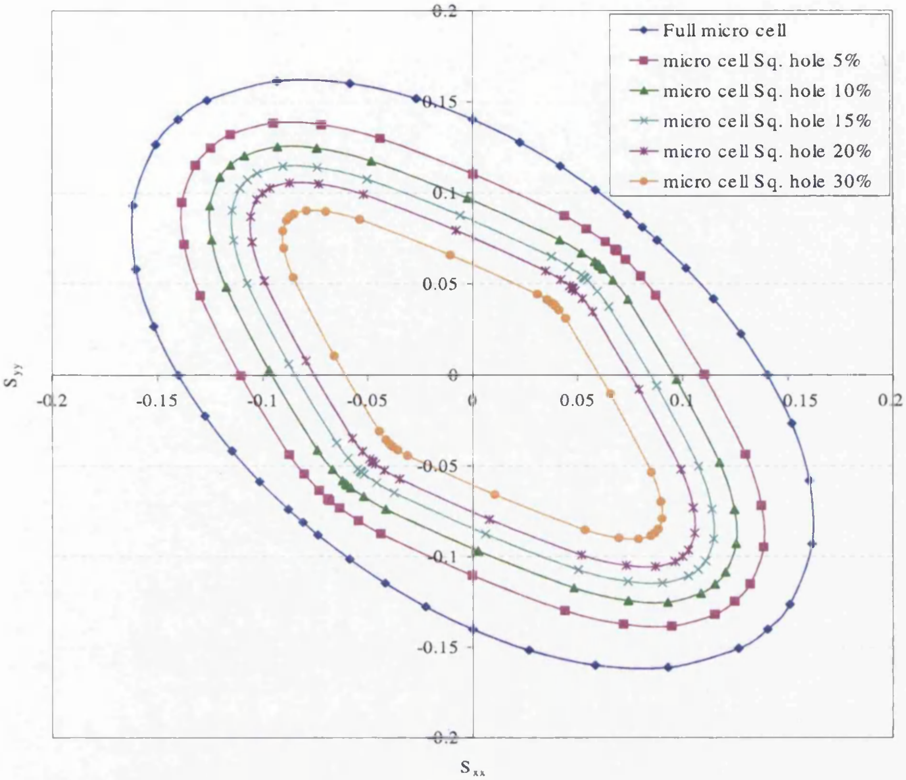

Figure 9.21: Overall yield surfaces for square cavity models in deviatoric space for the Linear displacement boundary condition.

Figure 9.22 shows the overall yield surfaces based on the homogenised deviatoric stress components under the periodic displacement fluctuations boundary condition. Smooth side lengths in yield surfaces are the effect of the periodic displacement fluctuations boundary condition. The softness of the periodic displacement fluctuations boundary condition is clear with respect to the Taylor assumption or the linear displacement boundary condition, in which s_{xx} varies from 0.1 GPa in the Taylor assumption to 0.05 GPa in the periodic displacement fluctuations boundary condition.

Figure 9.23 shows the overall yield surfaces for the micro-cells with a square cavity under the periodic displacement fluctuations boundary condition. The overall shape of the yield surfaces is the same as the homogenised yield surfaces obtained from the micro-cells with a circular hole. Softer response of the micro models under the periodic displacement fluctuations boundary condition in the case of imposed macro-shear deformation is the same for both circular and square cavity.

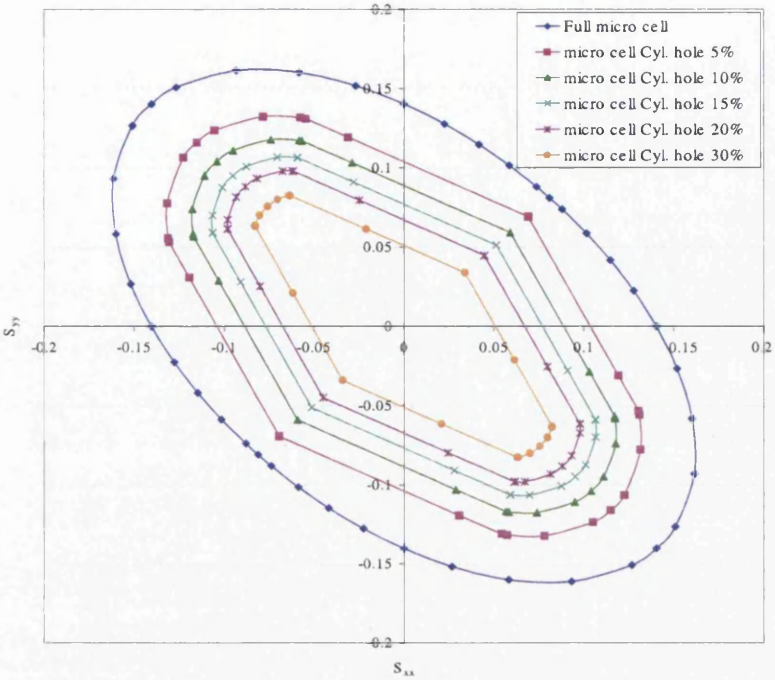

Figure 9.22: Overall yield surfaces for circular cavity models in deviatoric space for the periodic displacement fluctuations boundary condition.

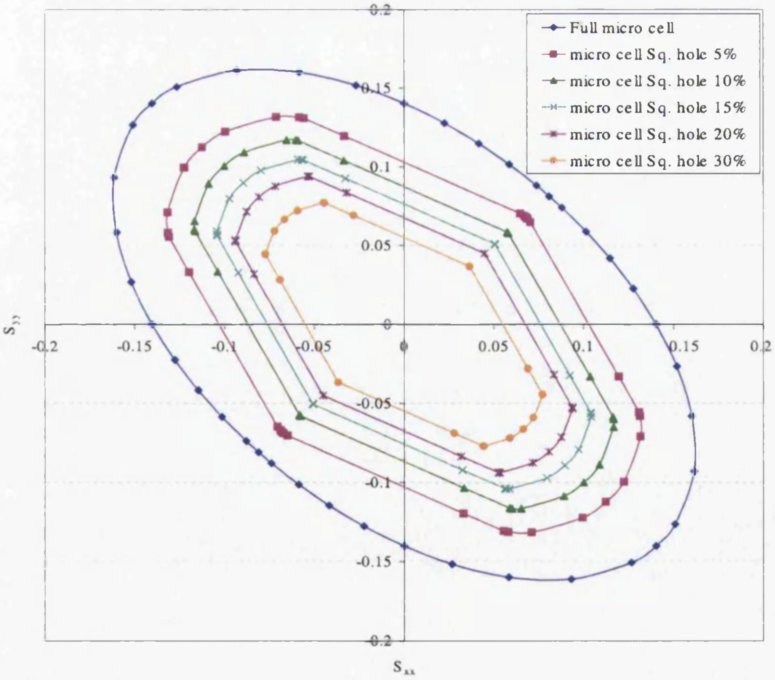

Figure 9.23: Overall yield surfaces for square cavity models in deviatoric space for the periodic displacement fluctuations boundary condition.

The effect of the shape of the cavity under the periodic displacement fluctuations boundary condition is almost evident in these two figures (Figures 9.22 - 9.23). This effect appears in uni-axial and biaxial tests in which the overall response of the RVE with square cavity shows yielding at higher stresses compared with the same model with a circular hole. As can be seen from figures 9.22 and 9.23, by increasing the void volume fraction, the difference between two shapes of the cavities is more apparent with s_{xx} in a 30% circular cavity model has a value around 0.05 GPa. However, for the same micro-cell with a square cavity and 30% void volume fraction s_{xx} has a value of more than 0.05 GPa. This effect confirms that by increasing the void volume fraction at micro-level and under the periodic displacement fluctuations boundary condition, the RVE with a square cavity shows yielding at higher stresses compared with the same RVE with a circular hole.

Finally the overall response of the micro-cell with a circular cavity is illustrated in Figure 9.24 under the uniform boundary traction condition. The graphs in this figure confirm that this boundary condition shows the softest overall response for the homogenised load-bearing capacity of the micro-cell, in comparison with the other boundary conditions. Significant contraction in the yield surface, obtained from the unit-cell with 30% void volume ratio, shows the softness of the deformation at micro-cell, and weakness of the overall response of the regular unit-cell model under imposed macro-shear deformations in the uniform boundary traction assumption.

Figure 9.25 shows the homogenised yield surfaces for the regular micro-cell models with a square cavity. As can be seen from these graphs, the effect of the square cavity and circular hole has dominated the overall yield surface of the micro-cells with different void volume fractions. The effect of the shape of the cavity at micro-cell implies different shape of the homogenised yield surface for a unit-cell model with the same void volume fraction.

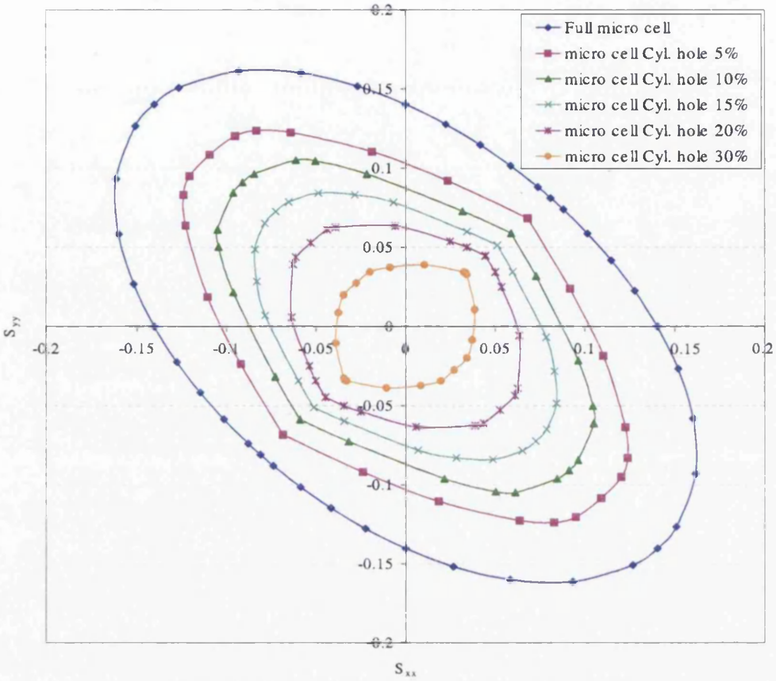

Figure 9.24: Overall yield surfaces for circular cavity models in deviatoric space for the uniform boundary traction assumption.

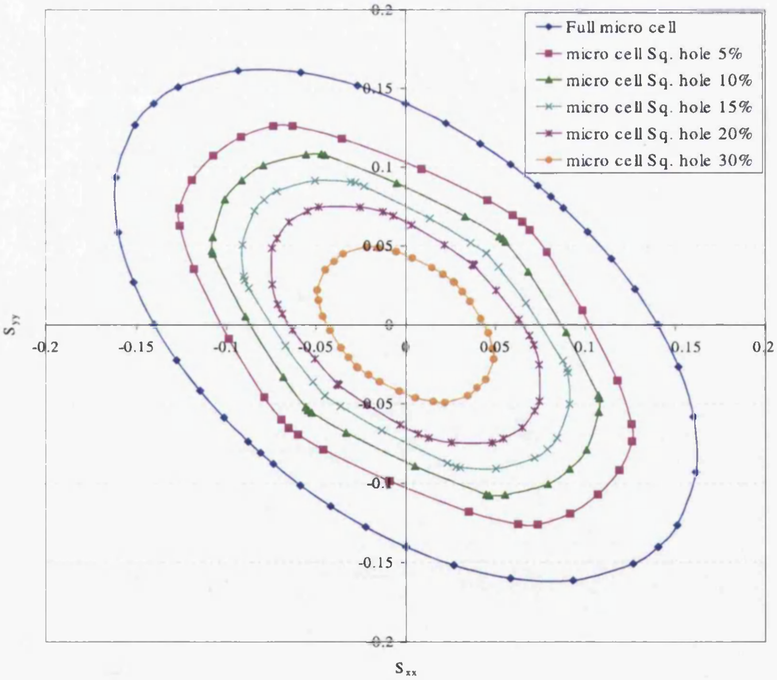

Figure 9.25: Overall yield surfaces for square cavity models in deviatoric space for the uniform boundary traction assumption.

9.5 Homogenised yield surfaces for irregular models

In this section the effect of the randomness of the distribution of the cavities in the unit cell on the homogenised yield surface will be discussed.

Irregular models in this section have the same size and specification as the regular models' tests in the previous section. The 8-noded quadrilateral element with 4-GP has been selected for finite element mesh model.

In order to be consistent with other irregular mesh models, we chose two different irregular micro-cell models with 15% void volume ratio: irregular cavity model type-5 and irregular cavity model type-10. Figure 9.26 is a schematic representation of the irregular micro-models.

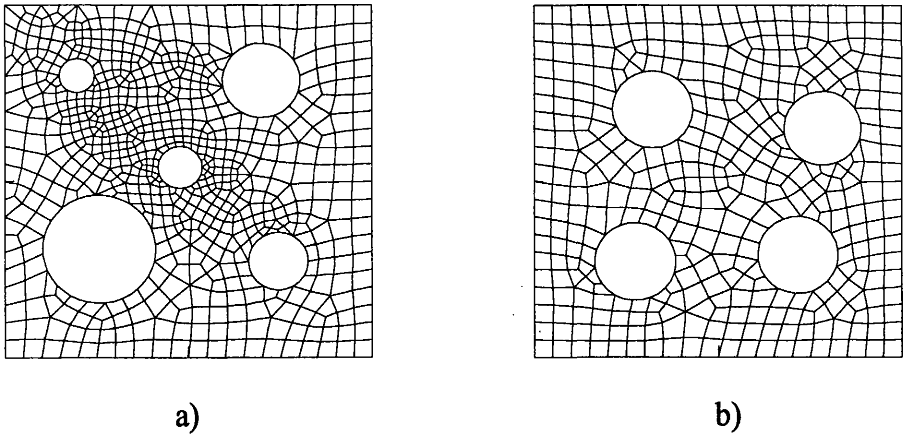

Figure 9.26: Two different unit cells' mesh models. a) Irregular cavity model Type-5. b) Irregular cavity model Type-10.

As in other tests, different macro-strains have been imposed over the micro-cells. In order to study the real behaviour of the micro models in composite materials, the only boundary condition which has been considered in this study is the periodic displacement fluctuations boundary condition.

The main difference between the irregular models' behaviour and regular model's behaviour is that the irregular models do not show an isotropic overall response, and because of randomly distributed cavities, the homogenised behaviour of the RVE may result in an anisotropic response. This fact will be demonstrated on the overall yield surfaces obtained from the irregular unit cell models.

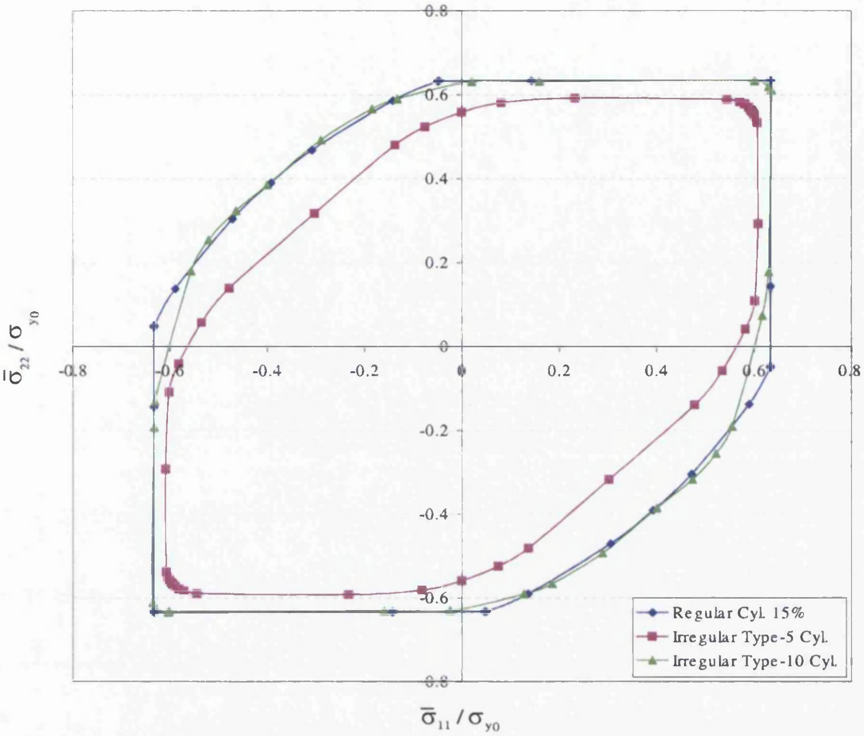

Figure 9.27: Homogenised yield surfaces for different irregular cavity models.

Figure 9.27 shows different homogenised yield surfaces obtained from different irregular and regular cavity models. These graphs have been plotted in the normalized homogenised stress components space. To compare the effect of the regularity and irregularity of distributed cavities in micro-cell on the overall behaviour of composite materials in the same graph, we have plotted the overall yield surface obtained from the regular cavity model with 15% cavity as a reference isotropic response of the micro-cell.

As can be seen from Figure 9.27, although the obtained overall yield surface from the irregular cavity model type-10 is quite close to the homogenised yield surface obtained for the regular cavity model, it has been distorted with respect to the regular cavity model's behaviour. This distortion in shape of the yield surface could be interpreted as an anisotropic response of the micro-irregular model type-10. On the other hand, the homogenised behaviour of the irregular cavity model type-5 demonstrates a completely different behaviour with respect to the regular cavity model and irregular cavity model type-10. This dissimilarity and softening of the overall response from micro-cell type-5 confirms the effect of the shape and the distribution of cavities of the unit-cell.

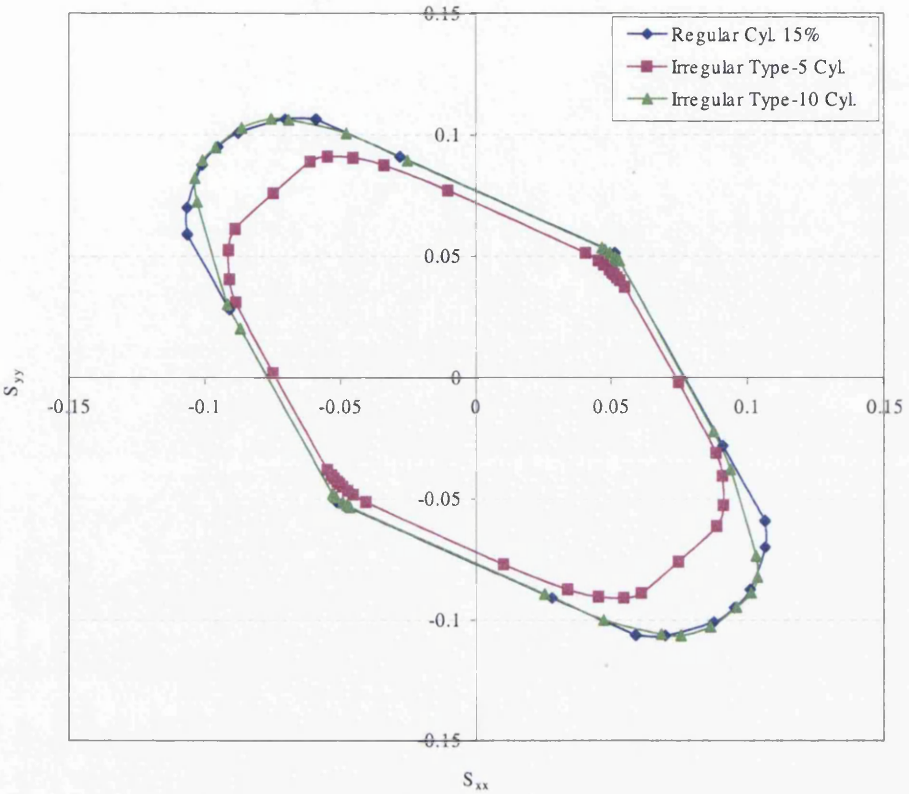

Figure 9.28: Overall yield surfaces for different irregular cavity models in deviatoric stress space.

Figure 9.28 shows the effect of the irregularity of cavities on the overall yield surfaces in deviatoric stress space. As can be seen from Figure 9.28, the obtained yield surface from irregular cavity model type-10 shows the nearest response to the regular cavity model's yield surface, and the homogenised yield surface obtained from the irregular cavity model type-5 shows softer behaviour with respect to the other models and has been located inside all other yield surfaces.

9.6 Discussion

In this section, we refer to some literature corresponding to evaluation and study of the homogenised yield surface for porous media. Following the order of the tests conducted, first we review some papers related to the regular cavity models at micro-level, followed by some technical reports and papers dealing with the effect of the distribution and the shape of the cavities on the overall response of the composite material models.

As mentioned at the begining of this chapter, Gurson [83] is one of the pioneers who estimated the overall behaviour of the composites with regular cavities. H. Li *et al.* [86], have used homogenisation theory, and the kinematic limit theorem for determining the plastic limit loads of ductile composites, such as metal matrix composites in plane stress problem. According to this paper, the macroscopic strength of perforated materials monotonically decreases with the increase in the radius of holes. In addition, the obtained behaviour for an RVE with 19.3% regular cavity shows similar behaviour to the experimental results presented by Litewka [87]. Litewka [87], has assumed different penetration patterns for perforated metal sheets and by imposing different loads has caracterized the overall behaviour of the perforated sheet with respect to the penetration pattern.

O'Donnel and Porowski [88], have investigated an analytical method to obtain the yield surface for the sheet perforated with a uniform triangular pattern of round holes and subjected to in-plane stress of arbitrary biaxial force. In his paper, based on the different characterization of the cavities, lower and upper bounds for the overall yield surface for a perforated plate were presented. The presented limits for the overall yield surfaces may be located between the results obtained from the linear displacement boundary condition and the periodic displacement fluctuations boundary condition from our numerical homogenisation analysis.

The effect of size of the cavity on the overall yield surface has been mentioned by many authors, among them Winnicki *et al.* [89] have defined a coefficient based on the perforation pattern to present the distribution of the cavity. The relation between this coefficient and the overall shape of the yield surfaces has been shown. By increasing the coefficient, the size of the yield surface becomes smaller. Instead of the effect of size of the cavity on the homogenised yield surface of multiphase materials, Ponte Castaneda and Zaidman [85] have shown the effect of size of the inclusion on the overall response of the RVE.

Finally we refer to the paper written by Ghosh S. [90]. Examples described in this paper are mostly in plane strain problem and the analysis method is based on the Voroni Cell Finite Element Method. The influence of microscopic heterogeneities on the overall behaviour has been shown to depend on morphological characteristics like size, shape orientation and spatial distribution of constituent phases (inclusion/void).

Bilger *et al.* [91] deals with the effect of the irregularity of cavities on the homogenised yield surface, particularly with the specific role played by porosity fluctuations inside an RVE. Three types of micro-structures have been specified: random micro-structures with no void clustering, micro-structures with a connected cluster of voids and micro-structures with disconnected void clusters. Results show that the random micro-structures without clusters and micro-structures with a connected cluster are the hardest and the softest configurations, respectively, whereas micro-structures with disconnected clusters lead to intermediate responses.

The anisotropy of sheet metal during sheet forming is a combination of the initial anisotropy due to its previous history of thermomechanical processing and to the plastic deformation during the stamping operation [92]. The former leads to a symmetry with the orthotropic character while the latter, called deformation-induced anisotropy, can destroy this symmetry when principal material symmetry and deformation axes are not superimposed [92].

The following papers refer to the effect of the irregularity of cavities on the overall isotropic and anisotropic behaviour of the models: F. Barlat [93] [94] (a pioneer in studying the overall behaviour of anisotropic metal sheets and the effect of anisotropy on the overall yield surface who has pursued research by modifying the proposed yield function for anisotropic materials' behaviour and has performed this concept in a wider area). F. Barlat and J. Lian [95], J. Lian F. Barlat and B. Baudelet [96], Yoon J. Barlat F. Dick R. Chung K. and Kang T [92], Barlat F. Brem J.C. Yoon J.W. Chung K. Dick R.E. Lege D.J. Pourboghrat F. Choi S. and Chu E. [97], H. Artez [98] and R. Hill [99].

9.7 Conclusion

In this chapter we studied the effect of pores on the elasto-plastic response of porous media. It has been shown that the shape of the cavity at micro-level and the prescribed assumption over the RVE are two important factors which affect the prediction of the overall yield surface of the composite material. For example it has been shown that for an RVE with a given percentage of voids, under the linear displacement boundary condition the cell with circular hole shows yielding at higher stresses compared with the cell with square cavity. On the other hand, the homogenised response of the RVE with square cavity under the periodic displacement fluctuations boundary condition shows yielding at higher stresses compared with the same regular model with circular hole. Finally for the uniform boundary traction the yielding at lower stresses are presented from a unit-cell with square cavity while for the same model circular hole presents yielding at higher stresses.

The effect of the boundary conditions and increasing the size of the cavity (circular/square) was another topic which has been investigated in this chapter. In general by increasing the size of the cavity at micro-cell; the higher yielding stresses have been obtained from the Taylor assumption followed by linear displacement boundary condition. The periodic displacement fluctuations boundary condition shows yielding at lower stresses compared with the linear displacement boundary condition. Finally the uniform boundary traction assumption gives the lower bound for the homogenised behaviour of composite material models.

In the following we also presented the same effect in the deviatoric stress space. It has been illustrated that the same considerations can be drawn in this case as under the plane stress conditions.

At the end of this chapter the effect of randomness distribution of the cavities in the unit cell on the homogenised yield surfaces was discussed. Based on the distribution and the shape of the cavities, the overall yielding stresses of the micro-cell could be lower compared with the regular cavity model and in some cases the homogenised behaviour could be anisotropic.

Chapter 10

Study of the effect of anisotropy of the RVE on homogenised elastic material properties

10.1 Introduction

Composites with short and randomly distributed fibres or particulates have in general isotropic properties. For such composites, conventional theories combined with some knowledge on material characteristics are normally acceptable for analysis and design. Often, the maximum specific strength and stiffness can be obtained when long straight fibres with appropriate orientation are along the main direction of loading. This produces highly anisotropic composites. Most composite material structural components are in the form of laminated beam, plate or shell elements.

The basics of anisotropic linear elastic constitutive material models has been reviewed in chapter 3. In the present chapter we show numerical examples where the overall elastic properties of strongly anisotropic composites are obtained by means of the computational homogenisation procedure. The obtained numerical results are compared with using analytical results.

10.2 Numerical examples

In this section, we show the effectiveness of the multi-scale analysis procedure in simulation of the RVE with orthotropic material properties such as laminate materials. We define one layer of stiff fibres in a plane embedded in a soft matrix. A unit-cell has been selected in the plane of the longitudinal fibres.

The first set of the numerical examples is concerned with a cantilever beam made from an elastic laminate material under plane stress assumption. The numerical results from the multi-scale analysis are compared with the obtained results from the FORTRAN code (MPAP) [42]. This numerical example demonstrates the application of the multi-scale analysis in the prediction of the homogenised behaviour of the orthotropic laminate composites.

In the second part of this section, the effect of fibre orientation on the overall laminate composite material properties is considered. Analytical methods are used to check the validity of the numerical results.

First we provide a brief explanation of the mixture rule in micro-mechanics context. Mixture rule, will be used to predict the overall material properties of linear elastic composites based on the volume fraction of the matrix and the fibres.

10.2.1 Micro-mechanics of composites. Mixture rule

A structural engineer, when designing a structure, tends to rely almost entirely on mechanical test results for the properties of the materials to be used. However, since the application of composite materials for general purpose structures and the range of composite formulation are so diversified, a design engineer must be able to estimate the properties of composites to be used from the properties of the constituent materials, and may also have either to specify the property requirements or direct the manufacturing process to obtain the required properties. Unlike the traditional engineers, new generation engineers may have to be able to design the material as well as the structure. In any case, it is important for a design engineer to be able to obtain expected mechanical properties of a composite chosen for a specific structural element, from given constituent materials. This will enable comparison of overall design concepts, including structural efficiency, material cost, long term economy of the structure and so on [47].

For orthotropic materials in a plane stress state, four engineering constants are necessary to completely define the composite material behaviour. These are the Young's moduli in the longitudinal direction, E_{11}, and in the transverse direction, E_{22}, Poisson's ratio, v_{12} and the shear modulus G_{12} [47].

There are two groups of methods to obtain such properties. One is the empirical method which is often called the rule or law of mixtures, and the other is the 'exact' method. The rule of mixture, which is often sufficiently accurate for many micromechanical problems, is based on the statement that the composite property is the sum of the properties of each constituent multiplied by its volume fraction. The 'exact' method involves the mechanics of materials and theory of elasticity approaches [47].

The assumption for both methods are that both the matrix and the fibres are homogeneous, isotropic and linearly elastic, and the fibre is, in addition to the above, regularly spaced and aligned. An additional important assumption is that the fibre, matrix and composite have the same amount of strain in the same direction [47].

We should notice that for each of the following variables, the subscripts, f, and m, refer to fibre and matrix, respectively. In this section, we only present part of the relations corresponding to longitudinal and transverse elastic modulus, Poisson's ratio and shear modulus. Further details can be found in some of the reference books [45–47]. The main relations are the followings:

1. *Longitudinal modulus of elasticity*;

$$E_{11} = E_m V_m + E_f V_f, \tag{10.1}$$

   where V_f and V_m, represent the volume of the constituents, respectively.

2. *Transverse modulus of elasticity*;

$$E_{22} = \frac{E_f E_m}{E_f V_m + E_m V_f}. \tag{10.2}$$

3. *Poisson's ratio, v_{12}, v_{21}*;

   Poisson's ratio, v_{12}, is defined as the strain developed in the 2-direction when the laminate is stressed in the 1-direction [47],

$$v_{12} = \frac{-\varepsilon_{22}}{\varepsilon_{11}}. \tag{10.3}$$

   The strain ε_{22} is a function of two components, namely, the fibre components, $-v_f\varepsilon_{11}$, and the matrix component, $-v_m\varepsilon_{11}$. The lateral strain, in the 2-direction, ε_{22}, is $-(v_f\varepsilon_{11}V_f + v_m\varepsilon_{11}V_m)$. Therefore,

$$v_{12} = \frac{-\varepsilon_{22}}{\varepsilon_{11}} = v_f V_f + v_m V_m. \tag{10.4}$$

The other Poisson's ratio, v_{21}, can be obtained from,

$$v_{21} = v_{12}\frac{E_{22}}{E_{11}}. \tag{10.5}$$

4. *Shear modulus, G_{12};*

$$G_{12} = \frac{G_f G_m}{G_f V_m + G_m V_f}, \tag{10.6}$$

where G_f and G_m, represent the shear modulus of the matrix and the fibres, respectively.

10.2.2 Cantilever beam subjected to a point load

Figure 10.1, shows a homogeneous cantilever beam at macro-level subjected to a point load, P. The geometry of this model is defined by l = 80 *mm*, h = 40 *mm*, t = 1 *mm* and the point load is equal to 300 KN. To avoid occurrence of stress concentration around the point of the imposed point load, we changed a point load with a distributed load along the free edge of the cantilever beam.

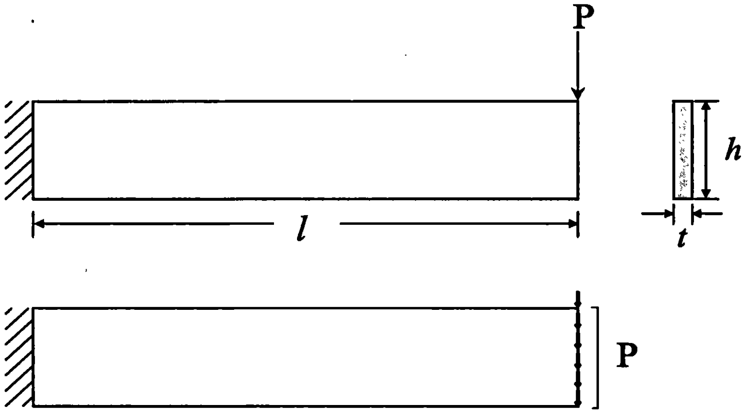

Figure 10.1: Cantilever beam subjected to a point load.

At micro-level three different cells have been considered. The side length of these cells are equal to 1 μm and the matrix and the fibres are two different constituents of these cells. The volume fraction of the fibres is assumed to be 15% of the volume of the RVE. Figure 10.2 shows three different cells with three different fibre orientation angles. By rotating the reference cell's local axes (11-22) with respect to the global axes ($xx - yy$), new cell models have been created (see Figure 10.3).

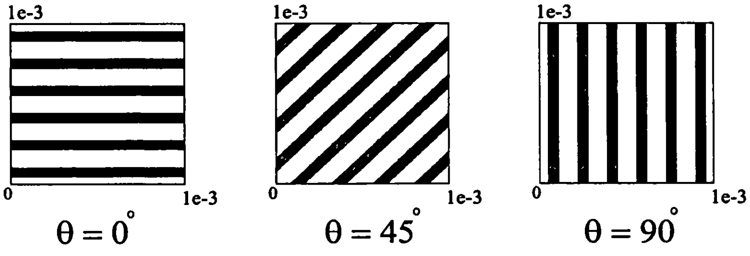

$\theta = 0^\circ$ $\theta = 45^\circ$ $\theta = 90^\circ$

Figure 10.2: Three different cells at micro-level.

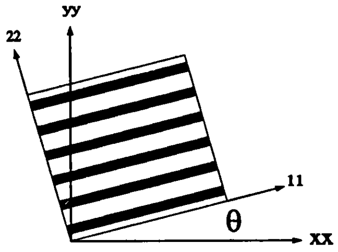

Figure 10.3: Rotation of the reference cell.

Material properties which have been used for the matrix and the fibre are expressed by,

Matrix specifications	*Fibre specifications*
$E_m = 3.4 \ GPa$	$E_f = 110 \ GPa$
$v_m = 0.35$	$v_f = 0.22$
$V_m = 85 \ \%$	$V_f = 15 \ \%$

Table 10.1: Material specifications for the matrix and the fibre.

By substituting the constituents' material properties into the mixture rule, equations (10.1)-(10.6), we can estimate the overall material properties for the laminate composite to be

$$\begin{aligned} E_{11} &= 19.39\,GPa, \\ E_{22} &= 3.9783\,GPa, \\ v_{12} &= 0.3305, \\ G_{12} &= 1.4742\,GPa, \\ D_{iso} &= 4.87, \end{aligned}$$

where D_{iso}, represents the degree of the isotropy for the composite. This value is obtained from the ratio of the longitudinal modulus of elasticity with respect to the transverse modulus of elasticity for the composite

$$D_{iso} = \frac{E_{11}}{E_{22}}. \tag{10.7}$$

10.2.3 Finite element discretization of the problem

To exploit the finite element method for this example, the cantilever beam at macro-level has been discretized with 392, 4-noded quadrilateral elements with 4 Gauss Points. At micro-level the unit cell has been defined with 1092 quadrilateral 8-noded elements with 4 Gauss Points. Figure 10.4 illustrates the FE mesh and boundary condition for cantilever beam at macro-level with imposed nodal loads on the free edge of the beam and the unit cell at micro-level.

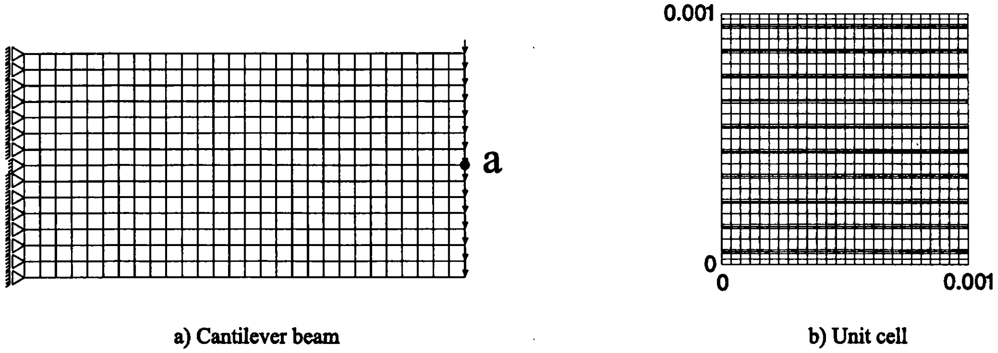

a) Cantilever beam

b) Unit cell

Figure 10.4: FE mesh illustration for cantilever beam and unit cell.

To obtain the displacement of the middle free end of the beam, **a**, the finite element analysis is performed under plane stress condition. The linear elastic materials have been assumed for matrix and fibres at micro-level.

The obtained results are illustrated in Figure 10.5. This figure shows the displacements of the beam at node, **a**, against the fibre orientation angles for two different analysis and three different assumptions; First, single-scale numerical results for orthotropic cantilever beam are obtained by MPAP code [42] by using the material properties obtained from the mixture rule for laminate composite. Second, multi-scale analysis results are obtained under three different boundary conditions at micro-level: the linear displacement boundary condition, the periodic boundary displacement fluctuations condition and the uniform boundary traction assumption. The homogenised material properties, in the multi-scale analysis, are obtained from the homogenisation procedure.

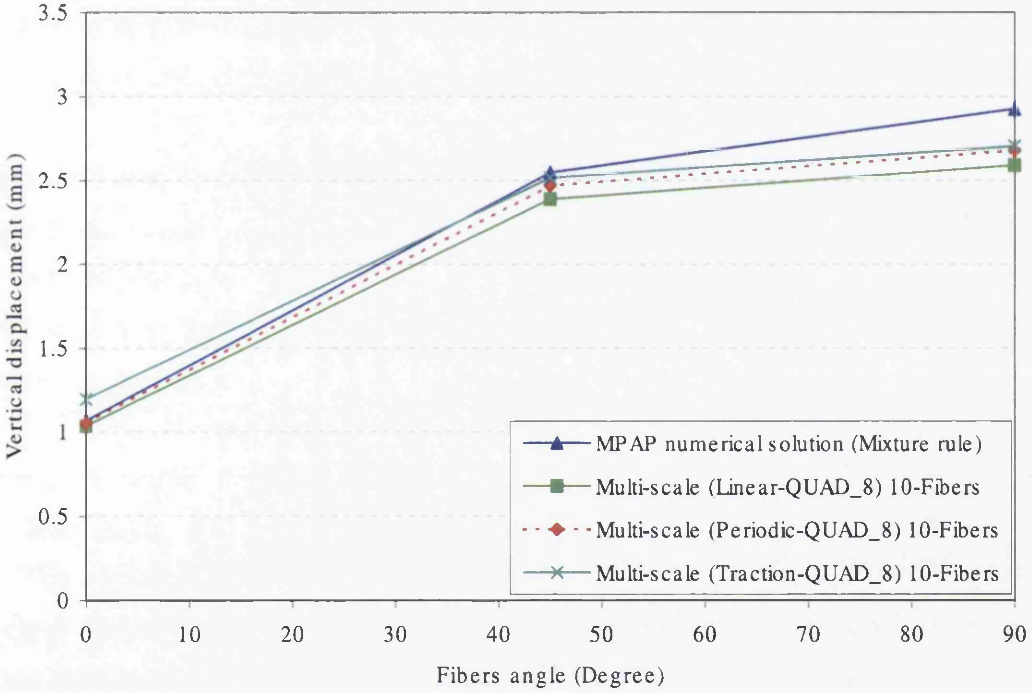

Figure 10.5: Comparison between the multi-scale and single-scale analysis for nodal displacement of the node a . Degree of isotropy=4.87.

Figure 10.5 shows that the displacements on the free edge of the cantilever beam have been affected by the fibre orientation angles. In other words, this effect could be interpreted such as, the minimum and the maximum displacements of the cantilever beam occur when the fibres orientation angles are zero and 90 degree, respectively. Figure 10.5 also shows, the effect of the boundary conditions at micro-level. As can be seen from Figure 10.5, when the fibre orientation angle is zero, the maximum displacement of the beam is observed under the uniform boundary traction assumption. On the other hand, when the fibre orientation angle is 90 degree the maximum deflection of the beam occurs under the single-scale analysis (MPAP).

It should be mentioned that to benchmark the multi-scale analysis for this particular example, the overall material properties were extracted from the overall tangent moduli and the obtained results form the single-scale analysis showed the similar displacements to the obtained results from the multi-scale analysis. The symmetry of the cell, micro-mesh and orthotropy of micro-cell materials are the basis of this observation.

10.2.4 Effect of fibre orientation

In this section, the effect of the fibre orientation angles on the homogenised material properties will be considered. The validity of the results from the multi-scale analysis is assessed by comparing the numerical results with the analytical results from the equations (3.14). An isotropic material behaviour has been assumed for the constituent materials at micro-level (matrix and fibres).

For this example we defined an RVE with side lengths equal to 1 μm. The volume fraction of the fibres is assumed to be 15% of the volume of the RVE. The material properties for this section are identical to the previous example (see Table 10.1).

To obtain the effect of the fibre orientation angles on the overall material properties, the multi-scale analysis has been used for different cells with the variation of the fibre angles from 0 to 90 degree.

The material properties have been extracted directly from the obtained overall tangent modulus from multi-scale analysis. The analysis has been performed for three different boundary conditions, the linear displacement boundary condition, the periodic boundary displacement fluctuations condition and the uniform boundary traction assumption. Equations (3.14) have been used to assemble the analytical overall elasticity tensor.

Graphs in Figure 10.6 show the ratio between the transformed Young's modulus and shear modulus with respect to the reference properties - refer to the principal material axes - of the lamina (fibre orientation $\theta = 0°$).

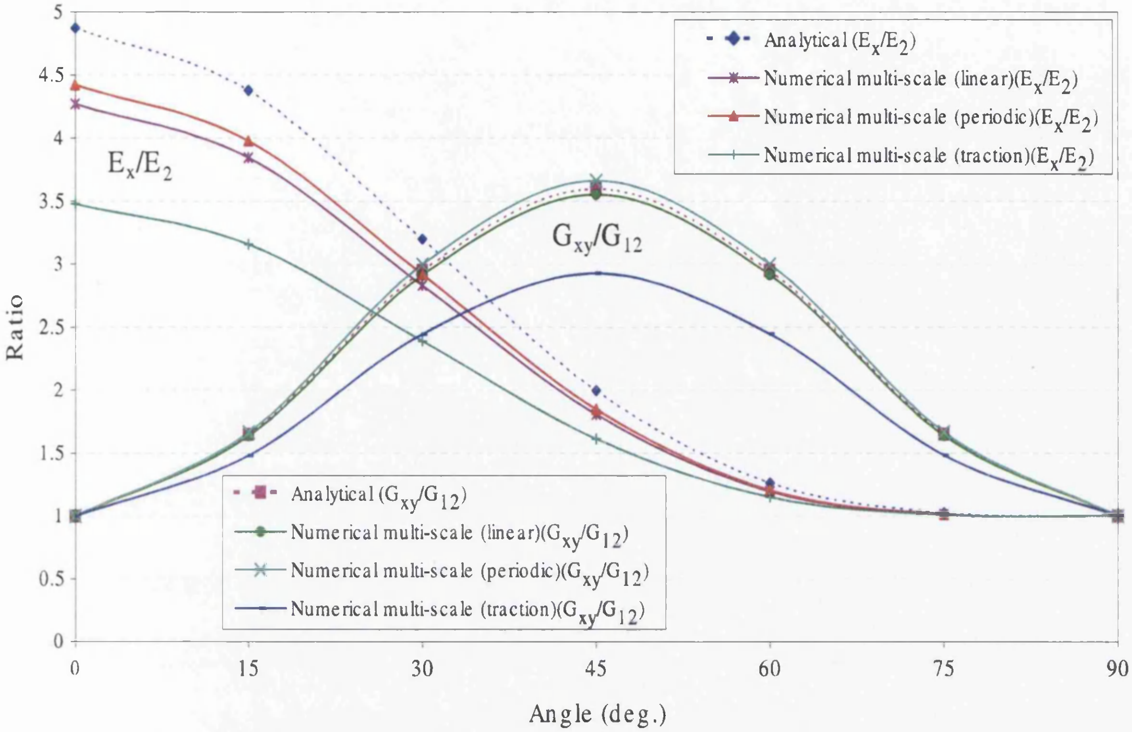

Figure 10.6: Ratio between the transformed and the original material properties.

In Figure 10.6 the dashed lines are used to illustrate the analytical results. In contrast the continuous lines show the numerical results for the different boundary conditions. It is seen that the effect of the boundary condition at micro-level becomes significant for the Young's modulus ratio when the fibre orientation is in its reference position $\theta = 0°$. On the other hand, by changing the fibre orientation to 45 degree with respect to the horizontal axis, the effect of the boundary condition on the shear modulus ratio becomes significant.

The same procedure has been performed to show the variations of the Poisson's ratio achieved from the analytical and the numerical analysis with respect to the fibres orientations. The obtained results are illustrated in Figure 10.7. As can be seen from this figure, changes in fibre orientation angles and the prescribed boundary condition over the micro-cell are two dominant factors for the multi-scale simulation of the overall behaviour of the fibre oriented composite materials.

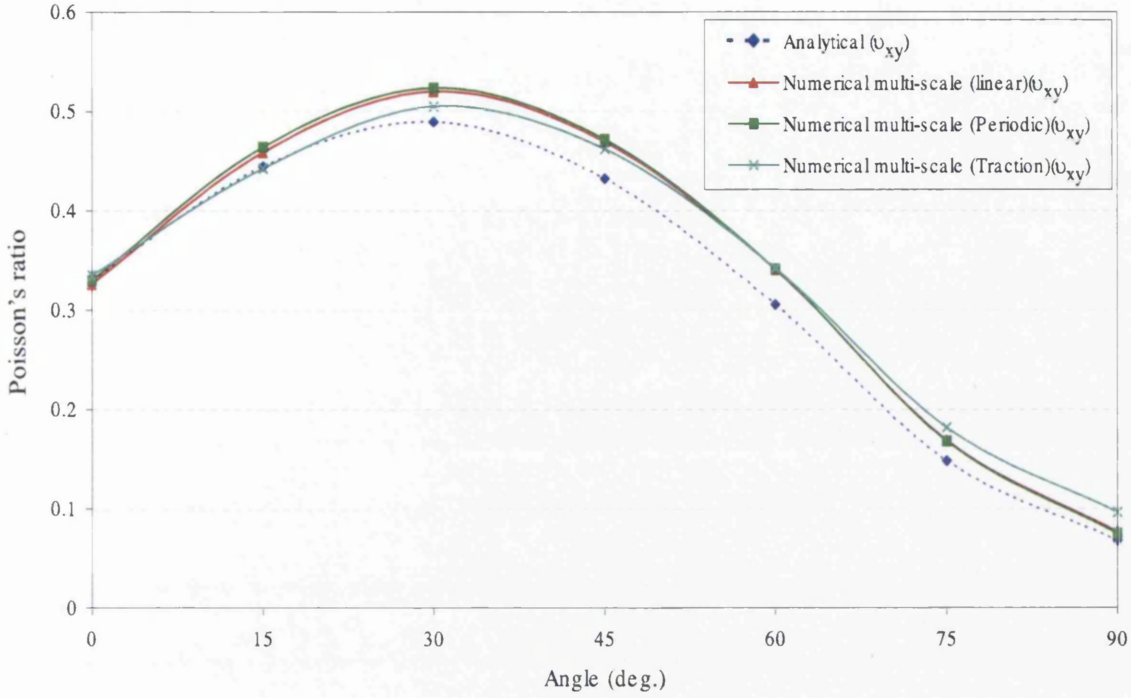

Figure 10.7: Variations of the Poisson's ratio with respect to the transformed material properties.

Based on the presented results in Figures 10.6 and 10.7, it may be concluded that, among the presented bounds for the overall material properties based on the different boundary conditions, the periodic boundary displacement fluctuations condition predicts the better results for the overall material properties Figures 10.8, show the variation of the obtained components of the overall tangent stiffness matrix from the analytical solution with respect to the multi-scale analysis results under the periodic boundary displacement fluctuations condition. The figures show the variation of a specific component of the tangent modulus with respect to the changes of the fibre angles.

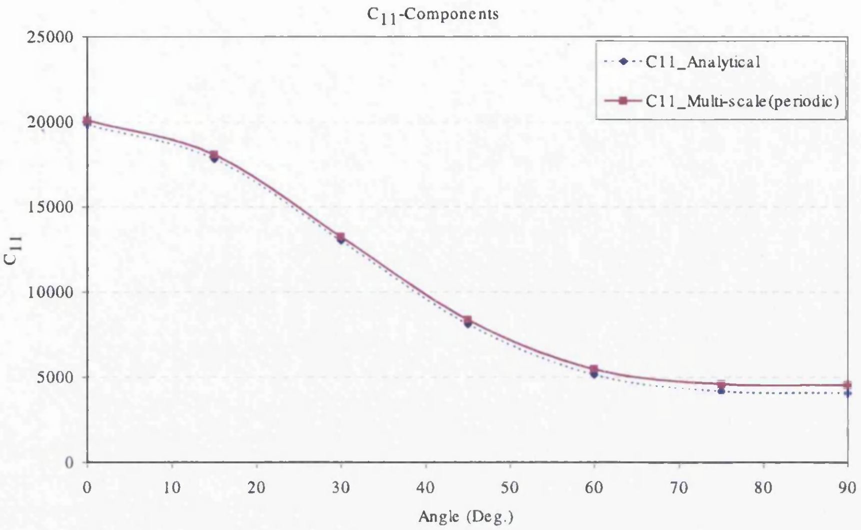
C_{11}-Components
C11_Analytical
C11_Multi-scale(periodic)
C_{11}
25000
20000
15000
10000
5000
0
0
10
20
30
40
50
60
70
80
90
Angle (Deg.)

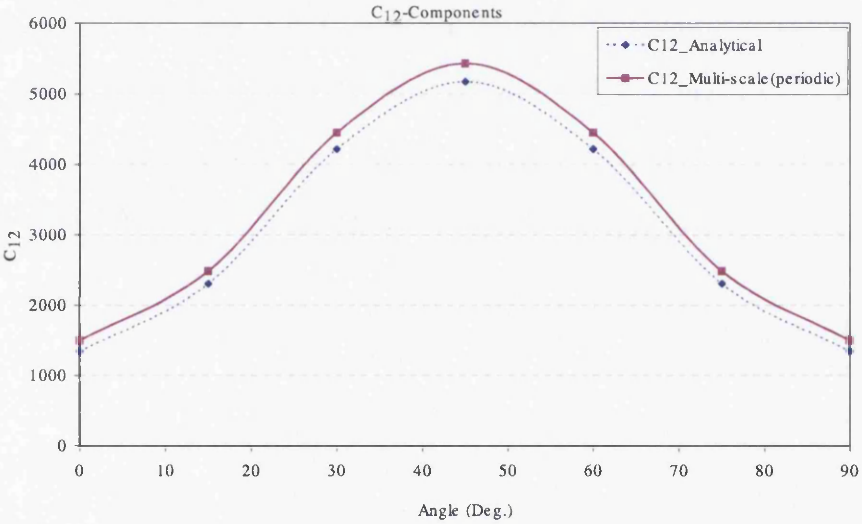
C_{12}-Components
C12_Analytical
C12_Multi-scale(periodic)
C_{12}
6000
5000
4000
3000
2000
1000
0
0
10
20
30
40
50
60
70
80
90
Angle (Deg.)

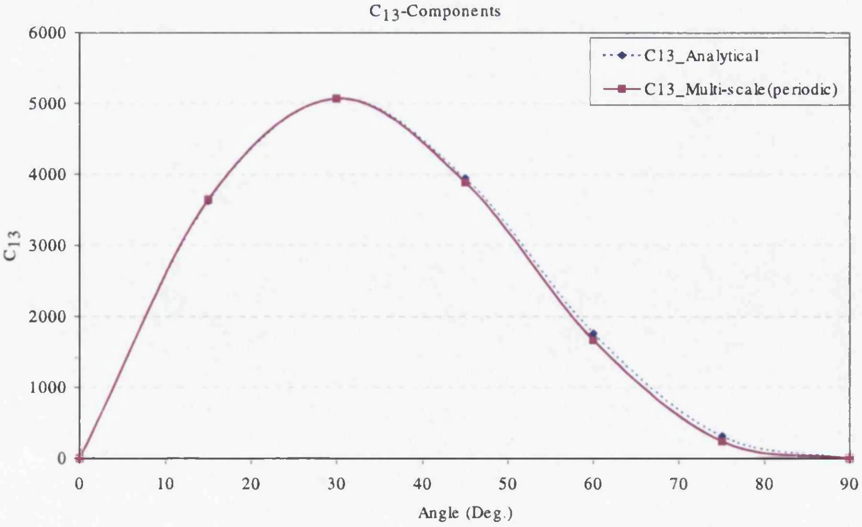
C_{13}-Components
C13_Analytical
C13_Multi-scale(periodic)
C_{13}
6000
5000
4000
3000
2000
1000
0
0
10
20
30
40
50
60
70
80
90
Angle (Deg.)

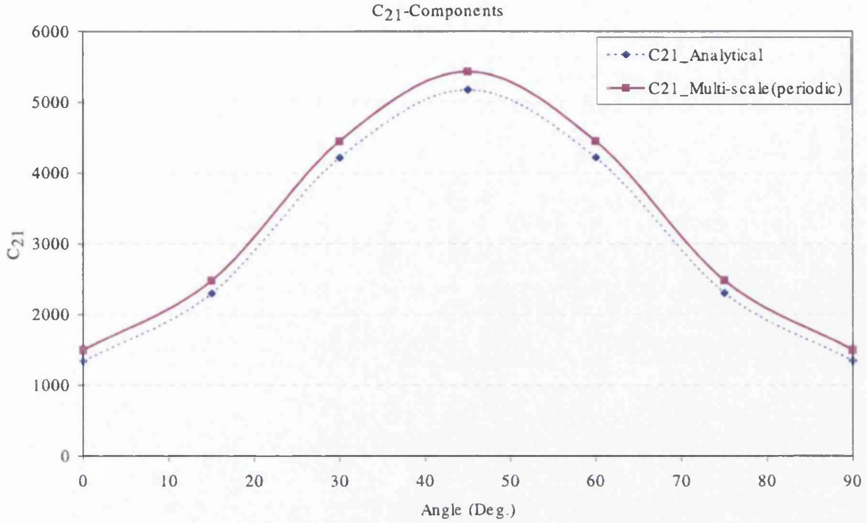
C_{21}-Components
C21_Analytical
C21_Multi-scale(periodic)
C_{21}
6000
5000
4000
3000
2000
1000
0
0
10
20
30
40
50
60
70
80
90
Angle (Deg.)

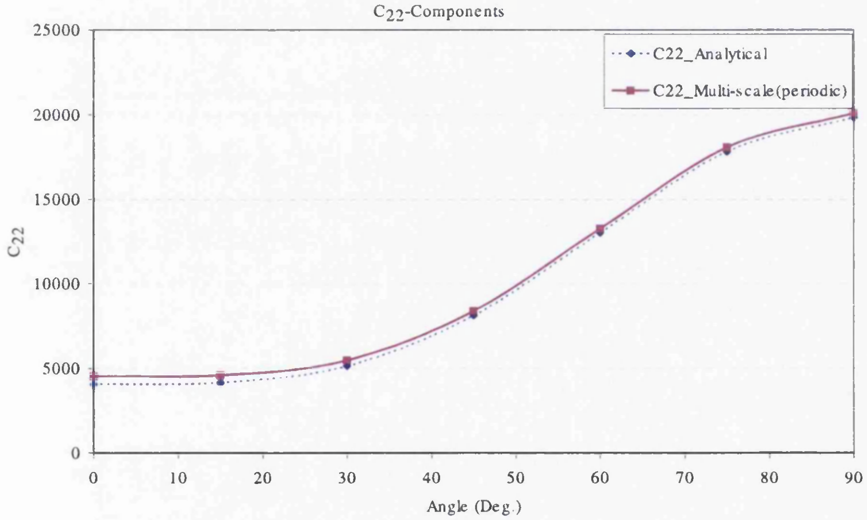
C_{22}-Components
C22_Analytical
C22_Multi-scale(periodic)
C_{22}
25000
20000
15000
10000
5000
0
0
10
20
30
40
50
60
70
80
90
Angle (Deg.)

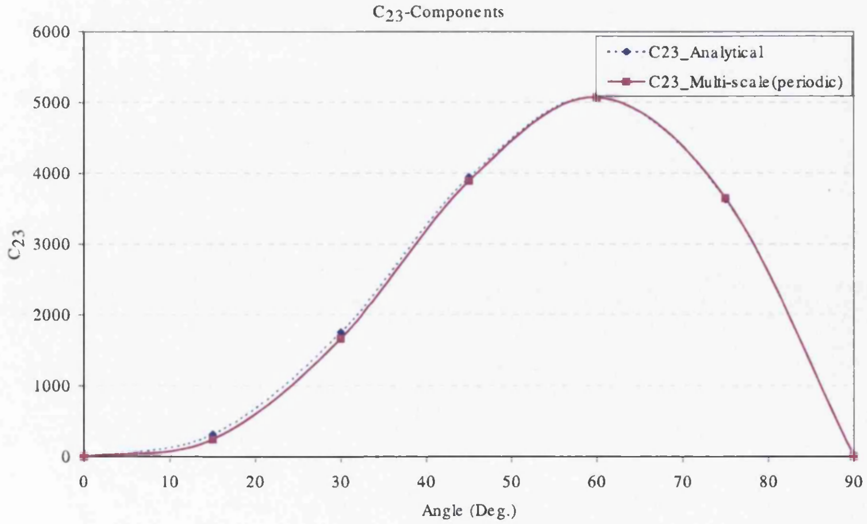
C_{23}-Components
C23_Analytical
C23_Multi-scale(periodic)
C_{23}
6000
5000
4000
3000
2000
1000
0
0
10
20
30
40
50
60
70
80
90
Angle (Deg.)

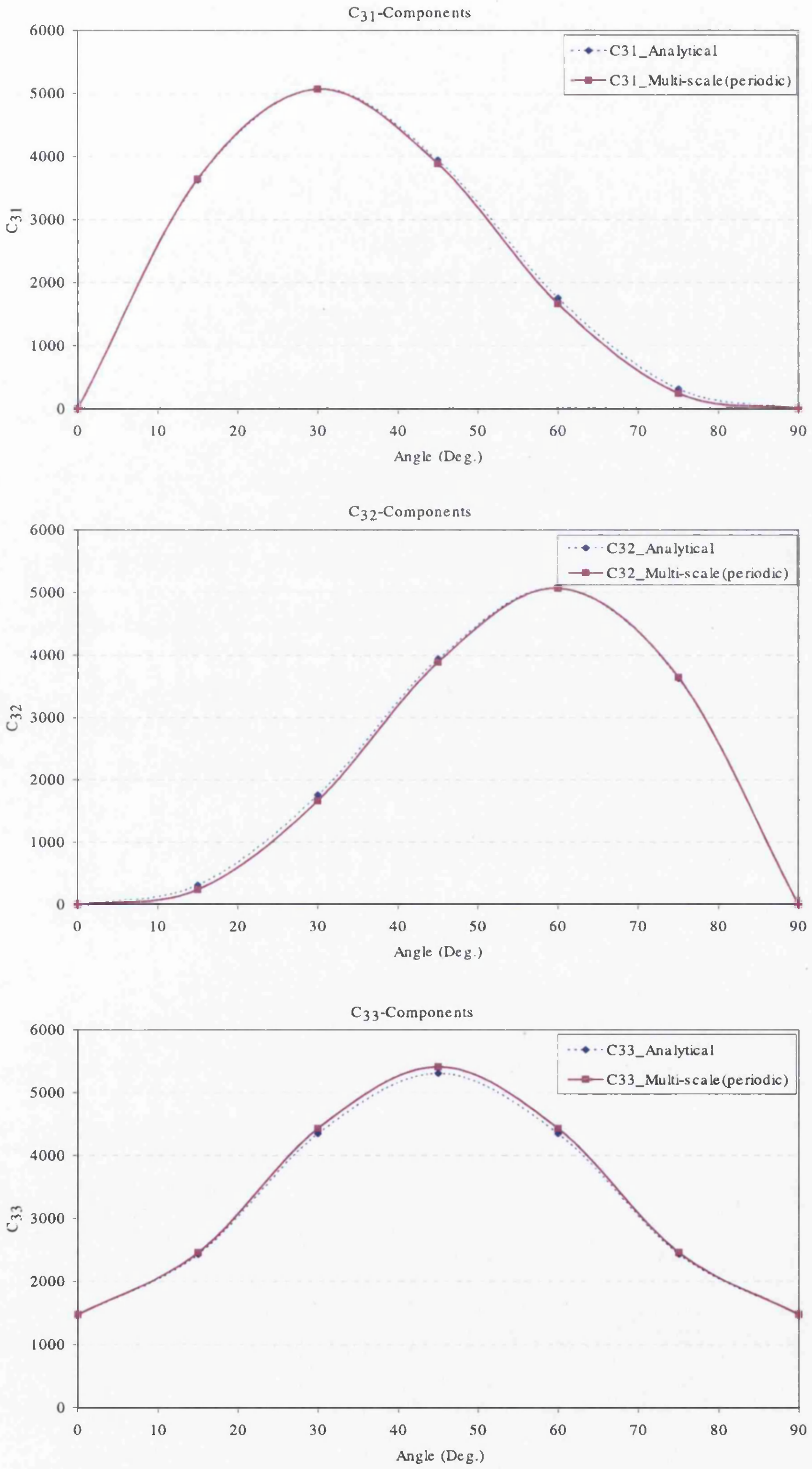

Figure 10.8: Comparison between the components of the overall tangent stiffness.

10.3 Conclusion

In this chapter, we focused on the overall behaviour of the continuous fibre reinforced composite materials. We considered the effect of the fibre orientation angles on the overall elastic material properties.

In the numerical tests, we compared the single-scale analysis for anisotropic cantilever beam with the multi-scale analysis. The overall elastic material properties for the single-scale analysis were obtained from the mixture rule. In the multi-scale analysis and at micro-level we defined an RVE with two different isotropic materials, fibre and matrix. The homogenisation procedure was performed under the various boundary conditions: (*i*) the linear boundary displacement, (*ii*) periodic boundary displacement fluctuations, and (*iii*) the uniform boundary traction assumption. The obtained results for the cantilever beam displacement, illustrated that, by changing the angle of the fibres orientation, the maximum displacement was obtained as expected from the uniform boundary traction assumption.

The effect of the fibre orientation angle on the homogenised Young's modulus and Poisson's ratio was shown in the second part of the tests. To illustrate that, we studied the effect of the fibres angles at the micro-level on the homogenised tangent modulus. The results for the overall tangent modulus obtained from the computer analysis were compared with the results obtained from the analytical method.

Chapter 11

Boundary value problem examples

11.1 Introduction

This section presents the solution of elastic and elasto-plastic single- and two-scale boundary value problems. The application of the formulation presented in chapter 5, is demonstrated by the series of numerical examples. In the elastic part of the boundary value problem test, the multi-scale analysis has been performed for a perforated plate at macro-level and two types of micro-structures (dilute distribution of cavities in the cell and dilute distribution of fibres in the cell) at micro-level. The validity of the numerical results for the perforated plate in the elastic zone have been considered with the single-scale analysis for the perforated plate with the reduced material properties obtained from the analytical solution presented by Nemat-Nasser [1], and the damage theory (see section 5.2). In addition, we consider the multi-scale analysis for the elasto-plastic material models. Because of lack of the analytical solution for non-linear models, we used our obtained results in the elastic zone as our point of reference. In the multi-scale analysis we considered different boundary assumptions at micro-level: (*i*) the Taylor, (*ii*) the linear boundary displacement, (*iii*) the periodic boundary displacement fluctuations and (*iv*) the uniform boundary traction assumption.

11.2 Perforated plate - Problem specification

A perforated strip is chosen with a uniform thickness. The calculation was performed by imposing uniform displacement control at the upper edge. For obvious symmetry considerations, only one-quarter of the specimen was analysed. The 3-D view and 2-D geometry are shown in Figure 11.1.

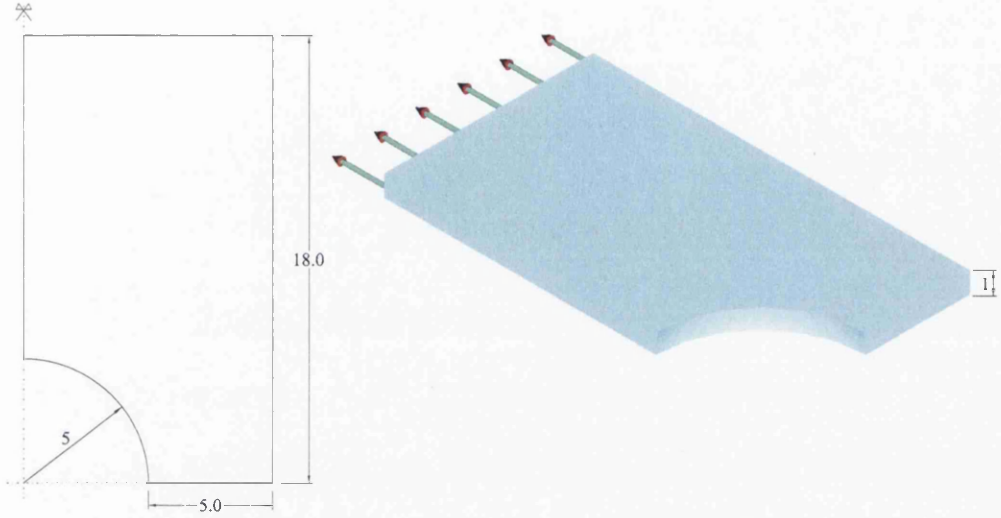

a) b)

Figure 11.1: Plane-stress strip with a circular hole. a) Undeformed 2-D geometry. b) 3-D view.

We defined four types of macro-structure and for each macro-structure we defined four types of micro-structure with different void volume fractions of the RVE. The three-noded linear triangular element has been chosen for this example.

Firstly, the problem is solved for the elastic behaviour and the results for the homogenised responses are compared with analytical methods, which were cited in section 5.3. In the last part of this example, the simulation is performed for one selected macro and micro-structure with elasto-plastic material model with isotropic hardening behaviour. Numerical tests are performed under *plane-stress* condition.

The macro-boundary condition, which is considered for this plate, is illustrated in Figure 11.2. Dimensions for the symmetric quarter of the strip, as shown in Figure 11.1 (a), are: 10 mm, width, 18 mm, length and 1 mm uniform thickness along the strip (see 11.1 (b)). Material properties for this example are, $E = 70\ GPa$, $v = 0.2$, for matrix and $E = 210\ GPa$, $v = 0.3$, for inclusion, which are respectively Elastic or Young's modulus and Poisson's ratio (see section 7.3 for different types of micro-models).

A von Mises yield condition with linear isotropic hardening for the matrix is obtained by,

$$\sigma_y(\bar{\varepsilon}^p) = 0.2\bar{\varepsilon}^p + 0.243, \tag{11.1}$$

where, $\bar{\varepsilon}^p$, is the effective plastic strain and, σ_y, is the von Mises yield stress value at relevant point. Hardening curve for this example is illustrated in Figure 11.3.

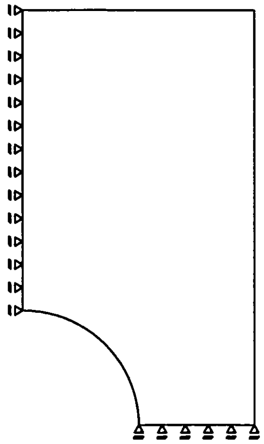

Figure 11.2: Boundary condition for macro-structure.

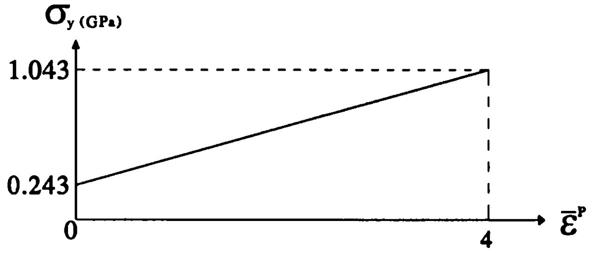

Figure 11.3: Linear isotropic hardening curve.

In the multi-scale analysis, we considered the strip as a macro-structure and discretized it by different meshes. Table 11.1, contains the relevant information for different meshes of the plate. These divisions are based on the number of the finite element meshes, (coarse to fine mesh). Figure 11.4, shows four different macro-structures with four different types of mesh, which are used at the multi-scale analysis.

Macro groups	Number of Elements	Number of Nodes
Mesh 1	39	28
Mesh 2	96	62
Mesh 3	378	217
Mesh 4	886	486

Table 11.1: Different meshes for macro-structure.

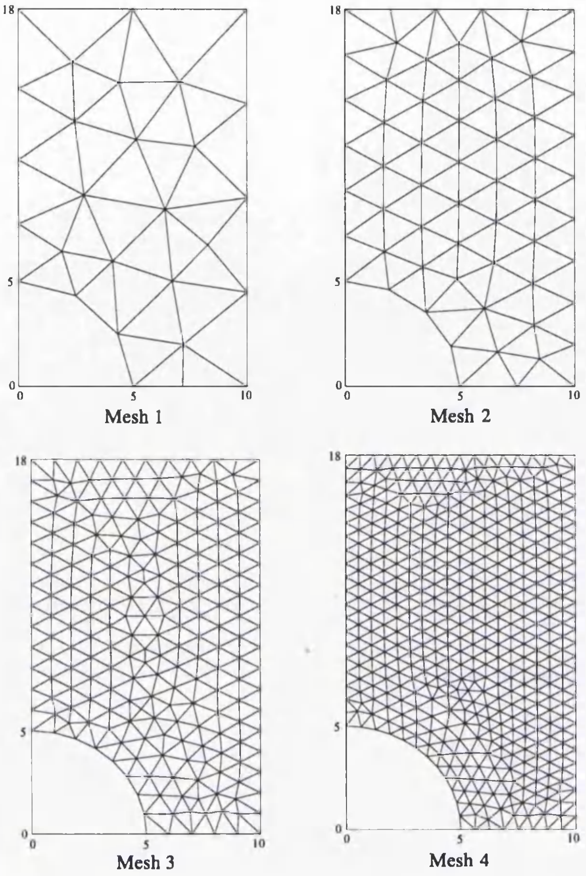

Mesh 1

Mesh 2

Mesh 3

Mesh 4

Figure 11.4: Different types of macro-structure.

In multi-scale analysis, all groups of micro-structures are implemented for each macro-structural mesh at integration points (Gauss points). The macro-structure mesh for both groups of micro-structures are, schematically, shown in Figure 11.5.

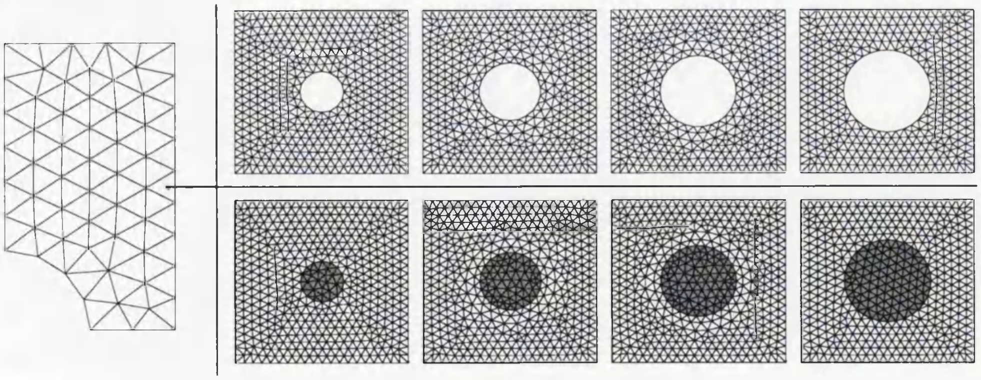

Figure 11.5: Micro-structures in each Gauss point of macro-structural meshes. Micro-structures with cavities and inclusions.

11.2.1 Elastic tests for perforated plate

In the first elastic test we considered the first group of micro-structures (micro-cavities). The analyses were restricted to the elastic range. So far, by using the new effective material properties, which are obtained from the cited theories in section 5.3 for micro-cavities, we ran similar example as a single-scale model. In this part our aim is to check the accuracy of the homogenised numerical results against the analytical results in elastic zone.

The following is based on the homogenisation assumption. By using different micro-structures for each macro-structure, we can analyze the multi-scale model for our specimen. This analysis is based on the initial material properties' values. In multi-scale analysis and at micro-level we focused on; the Taylor assumption, the linear displacement assumption, the periodic boundary displacement fluctuations condition and uniform boundary traction assumption.

To show the accuracy of the numerical homogenised results (multi-scale analysis) with the obtained results from the analytical theories (single-scale), we have obtained the elastic behaviour of the specimen at the both single-and multi-scale models.

Table 11.2 contains the reactions of the perforated plate obtained from the applied displacements. The numerical multi-scale analysis results have been compared against the single-scale analysis and analytical solutions.

According to the obtained results (see Table 11.2) increasing the void volume fraction makes the macro-structures softer. From Table 11.2 it may be concluded that the void volume fraction theory, which has been represented in [1] under the macro-stress prescribed assumption, gives a closest estimate with respect to the periodic boundary displacement fluctuations assumption at the multi-scale analyses. On the other hand, the obtained overall behaviour from the damage theory shows the similar behaviour to the Taylor assumption at the multi-scale analysis. Above all we should note that all of those comparisons have been done in elastic zone.

<table>
<tr><th colspan="5">Macro-structure Type-1</th></tr>
<tr><th>Reactions for applied Displacement</th><th>Micro-structure Type-1 (5% hole)</th><th>Micro-structure Type-2 (10% hole)</th><th>Micro-structure Type-3 (15% hole)</th><th>Micro-structure Type-4 (20% hole)</th></tr>
<tr><td>Single-scale analysis-Filled micro-structure</td><td>0.035943</td><td>0.035943</td><td>0.035943</td><td>0.035943</td></tr>
<tr><td>E-reduced (Nemat-Nasser/Pre-strain)</td><td>0.030525</td><td>0.025059</td><td>0.019515</td><td>0.013807</td></tr>
<tr><td>E-reduced (Nemat-Nasser/Pre-stress)</td><td>0.031247</td><td>0.027637</td><td>0.024776</td><td>0.022451</td></tr>
<tr><td>E-reduced (Damage-66.5,63,59.5,56)</td><td>0.034144</td><td>0.032347</td><td>0.030551</td><td>0.028754</td></tr>
<tr><td>Multi-scale analysis (Taylor)</td><td>0.03419</td><td>0.0324</td><td>0.030603</td><td>0.028811</td></tr>
<tr><td>Multi-scale analysis (Linear)</td><td>0.03162</td><td>0.027965</td><td>0.024955</td><td>0.022366</td></tr>
<tr><td>Multi-scale analysis (Periodic)</td><td>0.031568</td><td>0.02781</td><td>0.024695</td><td>0.022009</td></tr>
<tr><td>Multi-scale analysis (Traction)</td><td>0.030925</td><td>0.025476</td><td>0.020231</td><td>0.01546</td></tr>
<tr><th colspan="5">Macro-structure Type-2</th></tr>
<tr><th>Reactions for applied Displacement</th><th>Micro-structure Type-1 (5% hole)</th><th>Micro-structure Type-2 (10% hole)</th><th>Micro-structure Type-3 (15% hole)</th><th>Micro-structure Type-4 (20% hole)</th></tr>
<tr><td>Single-scale analysis-Filled micro-structure</td><td>0.035051</td><td>0.035051</td><td>0.035051</td><td>0.035051</td></tr>
<tr><td>E-reduced (Nemat-Nasser/Pre-strain)</td><td>0.029773</td><td>0.024452</td><td>0.019049</td><td>0.013487</td></tr>
<tr><td>E-reduced (Nemat-Nasser/Pre-stress)</td><td>0.030477</td><td>0.026959</td><td>0.02417</td><td>0.021905</td></tr>
<tr><td>E-reduced (Damage-66.5,63,59.5,56)</td><td>0.033297</td><td>0.031545</td><td>0.029793</td><td>0.028041</td></tr>
<tr><td>Multi-scale analysis (Taylor)</td><td>0.033341</td><td>0.031597</td><td>0.029844</td><td>0.028096</td></tr>
<tr><td>Multi-scale analysis (Linear)</td><td>0.030838</td><td>0.027276</td><td>0.02434</td><td>0.021812</td></tr>
<tr><td>Multi-scale analysis (Periodic)</td><td>0.030789</td><td>0.027125</td><td>0.024087</td><td>0.021468</td></tr>
<tr><td>Multi-scale analysis (Traction)</td><td>0.030165</td><td>0.024862</td><td>0.019756</td><td>0.015109</td></tr>
<tr><th colspan="5">Macro-structure Type-3</th></tr>
<tr><th>Reactions for applied Displacement</th><th>Micro-structure Type-1 (5% hole)</th><th>Micro-structure Type-2 (10% hole)</th><th>Micro-structure Type-3 (15% hole)</th><th>Micro-structure Type-4 (20% hole)</th></tr>
<tr><td>Single-scale analysis-Filled micro-structure</td><td>0.034032</td><td>0.034032</td><td>0.034032</td><td>0.034032</td></tr>
<tr><td>E-reduced (Nemat-Nasser/Pre-strain)</td><td>0.028909</td><td>0.023743</td><td>0.018497</td><td>0.013092</td></tr>
<tr><td>E-reduced (Nemat-Nasser/Pre-stress)</td><td>0.029592</td><td>0.026179</td><td>0.02347</td><td>0.02127</td></tr>
<tr><td>E-reduced (Damage-66.5,63,59.5,56)</td><td>0.03233</td><td>0.03063</td><td>0.028928</td><td>0.027225</td></tr>
<tr><td>Multi-scale analysis (Taylor)</td><td>0.032373</td><td>0.030679</td><td>0.028977</td><td>0.02728</td></tr>
<tr><td>Multi-scale analysis (Linear)</td><td>0.029942</td><td>0.026482</td><td>0.023628</td><td>0.021173</td></tr>
<tr><td>Multi-scale analysis (Periodic)</td><td>0.029892</td><td>0.026327</td><td>0.023367</td><td>0.02081</td></tr>
<tr><td>Multi-scale analysis (Traction)</td><td>0.029293</td><td>0.024146</td><td>0.019189</td><td>0.014675</td></tr>
<tr><th colspan="5">Macro-structure Type-4</th></tr>
<tr><th>Reactions for applied Displacement</th><th>Micro-structure Type-1 (5% hole)</th><th>Micro-structure Type-2 (10% hole)</th><th>Micro-structure Type-3 (15% hole)</th><th>Micro-structure Type-4 (20% hole)</th></tr>
<tr><td>Single-scale analysis-Filled micro-structure</td><td>0.033775</td><td>0.033775</td><td>0.033775</td><td>0.033775</td></tr>
<tr><td>E-reduced (Nemat-Nasser/Pre-strain)</td><td>0.028693</td><td>0.023564</td><td>0.018356</td><td>0.012992</td></tr>
<tr><td>E-reduced (Nemat-Nasser/Pre-stress)</td><td>0.02937</td><td>0.025981</td><td>0.023294</td><td>0.021109</td></tr>
<tr><td>E-reduced (Damage-66.5,63,59.5,56)</td><td>0.032086</td><td>0.030396</td><td>0.028709</td><td>0.027019</td></tr>
<tr><td>Multi-scale analysis (Taylor)</td><td>0.032129</td><td>0.030447</td><td>0.028757</td><td>0.027073</td></tr>
<tr><td>Multi-scale analysis (Linear)</td><td>0.029716</td><td>0.02628</td><td>0.02345</td><td>0.021011</td></tr>
<tr><td>Multi-scale analysis (Periodic)</td><td>0.029664</td><td>0.026125</td><td>0.023184</td><td>0.020643</td></tr>
<tr><td>Multi-scale analysis (Traction)</td><td>0.029072</td><td>0.023964</td><td>0.019044</td><td>0.014564</td></tr>
</table>

Table 11.2: Nodal reactions obtained from the elastic analysis of the imposed displacement (micro-cavity model).

In the second elastic test we considered the second group of micro-structures (micro-inclusions). Same as the previous test on the BVP, the analyses were restricted to the elastic range. So far, by using the new effective material properties, which are obtained from the cited theories in section 5.3 for micro-inclusions, we ran similar example as a single-scale model. In this test we focused on the micro-structures with micro inclusions for which the damage theory is not applicable. In fact in this test we compared the numerical results, which are obtained from the multi-scale analysis with two analytical solutions, which are based on the macro-stress and macro-strain prescribed.

Table 11.3 contains the results of seven different types of elastic behaviour of perforated plate; the multi-scale behaviour of specimen under the Taylor assumption, the linear displacement boundary assumption, the periodic boundary displacement fluctuations assumption, and the uniform boundary traction assumption and micro-inclusion volume fraction theory under two macro-stress and macro-strain prescribed assumptions. In addition the overall behaviour of the perforated plate has been analysed before reinforcement with inclusion. Therefore the effect of the inclusion at micro-level for the reinforced composites has been considered with respect to the homogeneous model.

Macro-structure Type-1				
Reactions for applied Displacement	Micro-structure Type-1 (5% inclusion)	Micro-structure Type-2 (10% inclusion)	Micro-structure Type-3 (15% inclusion)	Micro-structure Type-4 (20% inclusion)
Single-scale analysis-Filled micro-structure	0.035943	0.035943	0.035943	0.035943
E-reduced (Nemat-Nasser/Pre-strain)	0.037501	0.03906	0.040617	0.042173
E-reduced (Nemat-Nasser/Pre-stress)	0.037573	0.03936	0.041325	0.043496
Multi-scale analysis (Taylor)	0.03949	0.043098	0.044321	0.04723
Multi-scale analysis (Linear)	0.037555	0.039311	0.041219	0.043266
Multi-scale analysis (Periodic)	0.037549	0.039289	0.041174	0.043192
Multi-scale analysis (Traction)	0.037498	0.039095	0.040756	0.042487
Macro-structure Type-2				
Reactions for applied Displacement	Micro-structure Type-1 (5% inclusion)	Micro-structure Type-2 (10% inclusion)	Micro-structure Type-3 (15% inclusion)	Micro-structure Type-4 (20% inclusion)
Single-scale analysis-Filled micro-structure	0.035051	0.035051	0.035051	0.035051
E-reduced (Nemat-Nasser/Pre-strain)	0.036573	0.038094	0.039615	0.041133
E-reduced (Nemat-Nasser/Pre-stress)	0.036643	0.038387	0.040306	0.042427
Multi-scale analysis (Taylor)	0.038515	0.042041	0.04557	0.049081
Multi-scale analysis (Linear)	0.036625	0.038339	0.040202	0.042198
Multi-scale analysis (Periodic)	0.036618	0.038318	0.040157	0.042127
Multi-scale analysis (Traction)	0.036569	0.03813	0.039752	0.041443
Macro-structure Type-3				
Reactions for applied Displacement	Micro-structure Type-1 (5% inclusion)	Micro-structure Type-2 (10% inclusion)	Micro-structure Type-3 (15% inclusion)	Micro-structure Type-4 (20% inclusion)
Single-scale analysis-Filled micro-structure	0.034032	0.034032	0.034032	0.034032
E-reduced (Nemat-Nasser/Pre-strain)	0.035512	0.036988	0.038465	0.039939
E-reduced (Nemat-Nasser/Pre-stress)	0.035578	0.037273	0.039137	0.041195
Multi-scale analysis (Taylor)	0.037397	0.040821	0.044249	0.04766
Multi-scale analysis (Linear)	0.03556	0.037225	0.039033	0.040972
Multi-scale analysis (Periodic)	0.035555	0.037204	0.03899	0.0409
Multi-scale analysis (Traction)	0.035507	0.037024	0.038599	0.040242
Macro-structure Type-4				
Reactions for applied Displacement	Micro-structure Type-1 (5% inclusion)	Micro-structure Type-2 (10% inclusion)	Micro-structure Type-3 (15% inclusion)	Micro-structure Type-4 (20% inclusion)
Single-scale analysis-Filled micro-structure	0.033775	0.033775	0.033775	0.033775
E-reduced (Nemat-Nasser/Pre-strain)	0.035242	0.036709	0.038174	0.039635
E-reduced (Nemat-Nasser/Pre-stress)	0.03531	0.036993	0.03884	0.040884
Multi-scale analysis (Taylor)	0.037115	0.040511	0.043915	0.047298
Multi-scale analysis (Linear)	0.035292	0.036942	0.038739	0.040662
Multi-scale analysis (Periodic)	0.035285	0.036922	0.038694	0.04059
Multi-scale analysis (Traction)	0.035237	0.036743	0.038307	0.039937

Table 11.3: Nodal reactions obtained from the elastic analysis of the imposed displacement (micro-inclusion model).

As expected, increasing the micro-inclusion volume fraction makes the macro-structures stiffer (see Table 11.3). Moreover, it may be concluded that a dilute distribution of micro-inclusions which has been represented in [1] under the macro-stress and macro-strain prescribed assumptions, gives a good estimate respectively, for the periodic boundary displacement fluctuations assumption and the uniform boundary traction assumption at the multi-scale analyses.

Another point to mention is the rate of convergence with respect to the size of the macro mesh models. Figure 11.6, shows the rate of convergence for total reactions under four boundary assumptions at the multi-scale analysis with respect to increasing the number of elements in the macro-structural meshes for one type of micro-structures. Vertical axes show the total reactions along global, Y, axis and horizontal axes show increasing the number of the macro-structures' meshes. Figure 11.6, is for micro cavity model type-3.

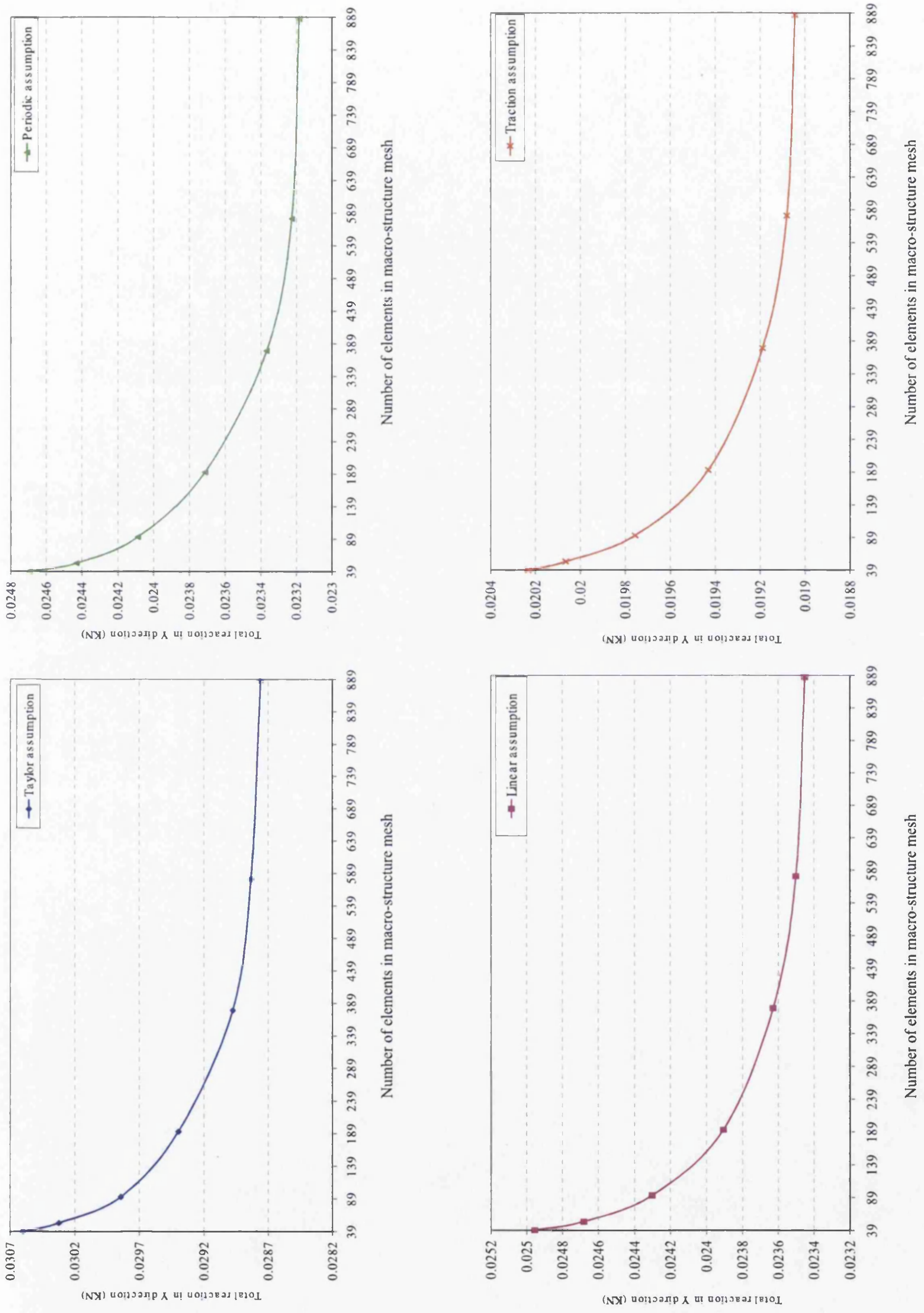

Figure 11.6: Rate of convergence with respect to increasing the number of elements at macro-structure.

Finally the important observation made in the elastic part of the test for microstructures with cavities is the CPU time for analysis. In general, multi-scales analyses are very time-consuming. This point has been illustrated in Figure 11.7, for macrostructure type-3. In this test we analyzed the same specimen as a multi-scale model in elastic zone for four different boundary assumptions by using all types of microstructures with cavities. Figure 11.7 shows the highest analysis time for the uniform boundary traction assumption at micro-level. The reason for this observation may be expressed by imposing the minimum kinematical constraint on the RVE and difficulty in obtaining the converged solution for the multi-scale problem.

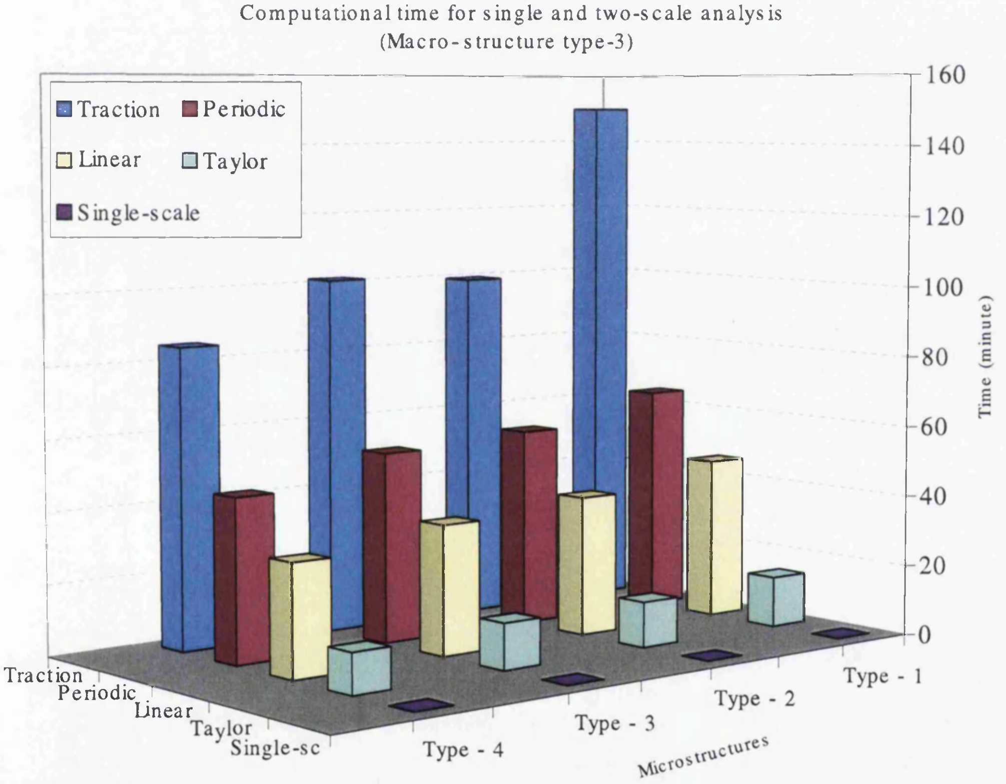

Figure 11.7: Computational time for elastic multi-scale analysis.

11.2.2 Elasto-plastic tests for perforated plate

In the second part of our numerical tests, we analyzed the perforated plate under the multi-scale assumption by defining the elasto-plastic von Mises material model with isotropic hardening at micro-level. The results are obtained under different boundary assumptions.

To validate and check the obtained results from the multi-scale analysis, we referred to the relevant papers. The effect of the different boundary conditions over the RVE in the multi-scale analysis has been presented by Kaczmarczyk [100]. Moreover, the homogenised elasto-plastic curves for the multi-phase materials have been demonstrated by [23, 24, 27]. The effect of the multi-scale analysis on the macro-to-micro transition for the elasto-visco-plastic material models under the periodic boundary displacement fluctuations condition has been demonstrated by Kouznetsova [59]. The Voroni cell finite element method has been used based on the periodic boundary displacement fluctuations condition by Ghosh et al [90] to analyse the multi-phase material models.

Firstly we consider the porous material models. For this example, a perforated plate has been considered with the same geometry as defined in section 11.2. The finite element mesh which has been used in this model is quadrilateral 8-noded element with 4 Gauss points, at both macro- and micro-levels.

Figure 11.8, shows the Finite Element meshes used for this example. Because of time consideration in multi-scale analysis, a coarse mesh has been selected at macro-level (24 quadrilateral 8-noded elements and 89 nodes) while, at micro-level, relatively, fine mesh has been defined (350 quadrilateral 8-noded elements and 1158 nodes).

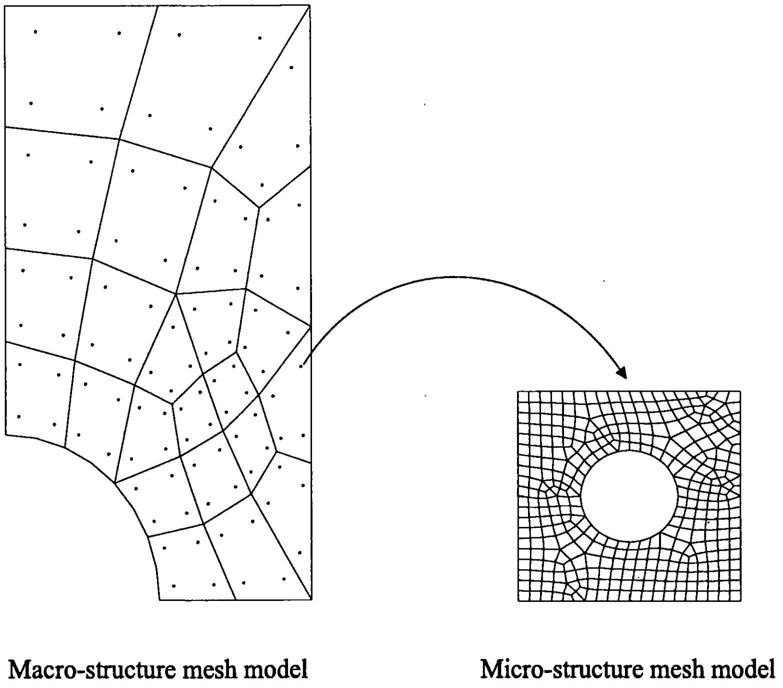

Figure 11.8: Finite element mesh at macro- and micro-level.

Figure 11.9 shows the behaviour predicted under different boundary conditions at micro-level. The vertical axis shows total nodal reactions while, the horizontal axis presents the applied displacement in Y direction. Different boundary conditions have been implemented at micro-level such as: Taylor assumption, linear displacement boundary condition, periodic boundary displacement fluctuations condition and uniform boundary traction assumption. Figure 11.9 illustrates the variety of the homogenised responses from the perforated plate.

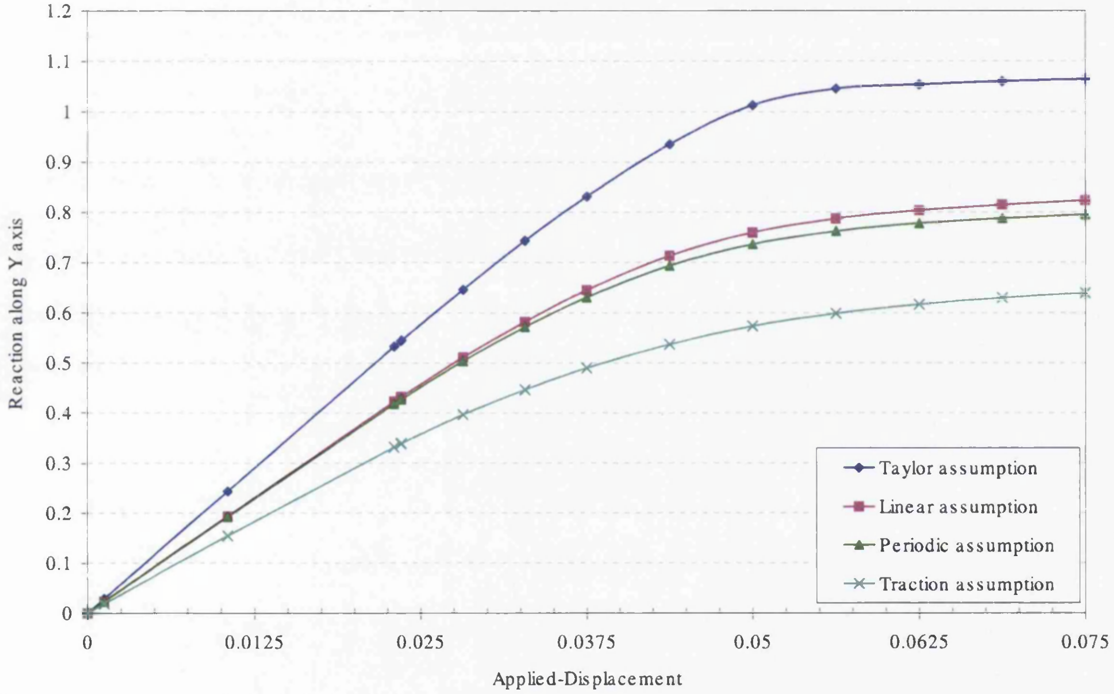

Figure 11.9: Plastic behaviour for multi-scale analysis under two boundary assumptions. Micro-structures with micro-cavities.

Figure 11.9 shows that, actual homogenised behaviour for the perforated plate has been located between the results obtained from the Taylor assumption (as an upper limit) and the uniform boundary traction assumption (as a lower limit). In the next sections we will show that between the linear displacement boundary condition and the periodic boundary displacement fluctuations condition, the homogenised behaviour of the heterogeneous material models under the periodic boundary displacement fluctuations condition gives the closest behaviour with respect to the numerical single-scale analysis and experimental results.

For comparing the homogenised plastic behaviour of the perforated plate under different boundary conditions, the obtained results from the single-scale analysis have been plotted against the multi-scale analysis. (see Figure 11.10).

As showed in section 5.2.1, the void volume fraction theory, which is represented in [1], is only valid for the linear elastic material models. To have an estimation in case of replacing the elastic material properties with the obtained analytical overall elastic properties from the void volume theory, the homogenised elasto-plastic behaviour of the perforated plate with reduced elastic material properties but with the same yielding condition (see equation 11.1) have been plotted in the same figure.

Figure 11.10 shows that, by changing the material type for the perforated plate from the homogeneous to the porous media (heterogeneous material model), the overall behaviour of the plate, shows a decrease in stiffness with increase of the percentage of the cavity at micro-level. Moreover, by prescribing different boundary conditions over the RVE the homogenised behaviour of the plate varies from the stiffest behaviour (obtained from the Taylor assumption) to the softest behaviour (obtained from the uniform boundary traction) for the homogenised behaviour of the heterogeneous material.

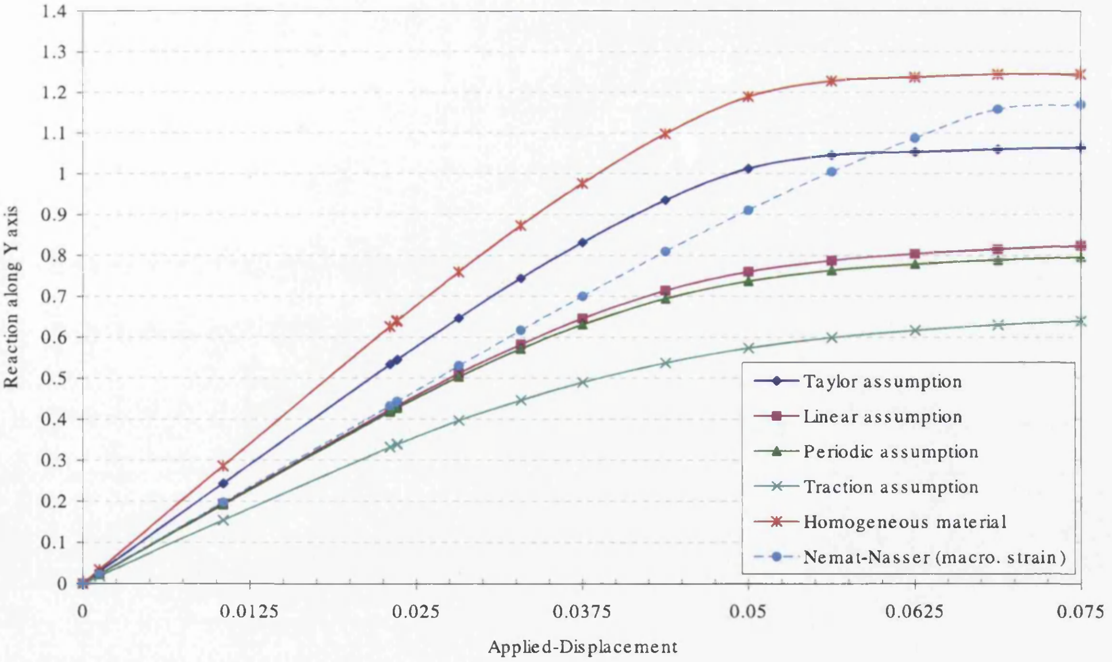

Figure 11.10: Plastic behaviour for different assumptions. Micro-structures with micro-cavities.

In the following, the elasto-plastic test with micro-inclusion has been considered. The multi-scale analysis format has the same procedure as the elasto-plastic test for the micro-structure with micro-cavity. We analyzed the perforated plate under the multi-scale assumption by defining the elasto-plastic von Mises materials with isotropic hardening for matrix and linear elastic material for micro-inclusion. The material properties at both levels are the same as the defined material properties for the macro-structures and the micro-structures with inclusion (see section 11.2).

Figure 11.11, is a schematic representation for the finite element mesh, quadrilateral 8-noded element with 4 Gauss points, in two scales. Because of time consideration in multi-scale analysis, coarse mesh has been selected for macro-structure while, at micro-level, relatively fine mesh has been defined. The number of the elements at macro-structure are: 24 quadrilateral 8-noded elements with 89 nodes while, the number of the elements at micro-structure are: 418 quadrilateral 8-noded elements and 1335 nodes.

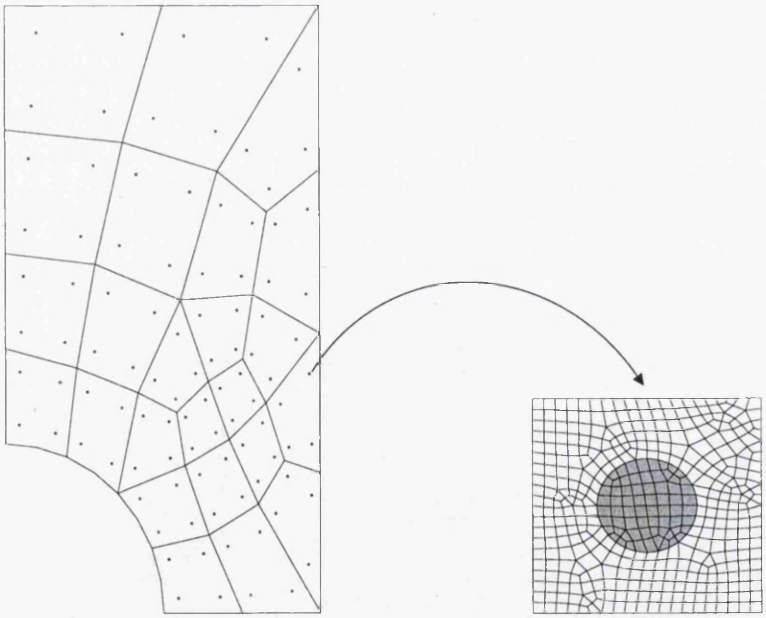

Macro-structure mesh model **Micro-structure mesh model**

Figure 11.11: Schematic representation of the finite element mesh at macro- and micro-level.

The results have been obtained under four different boundary conditions at micro-level: the Taylor assumption, the linear displacement boundary condition, the periodic boundary displacement fluctuations condition and the uniform boundary traction assumption in context of plane-stress.

Figure 11.12, shows the homogenised material behaviour for the multi-scale analysis in which, the vertical axis shows total nodal reactions and the horizontal axis presents the applied displacement from top of the plate. Different curves are the representative of different assumptions over the RVE.

From Figures 11.10 and 11.12, it can be seen that, the elastic material properties at micro-inclusion, dominate the overall behaviour of the cell. As a result, the overall reactions on the boundary nodes at macro-structure show higher values in comparison with the obtained reactions from the multi-scale analysis for the macro-structure with micro-cavity cell model.

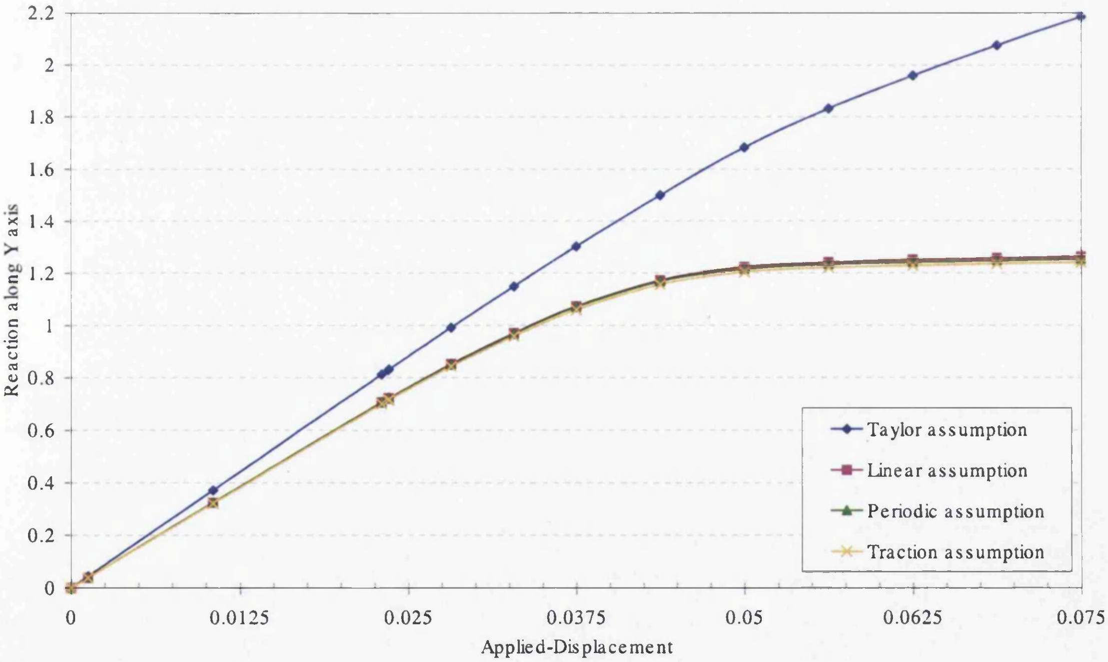

Figure 11.12: Plastic behaviour for multi-scale analysis under four boundary assumptions. Micro-structures with micro-inclusions.

For comparing the homogenised material behaviour obtained from multi-scale analysis with the single-scale analysis, the obtained results from single-scale analysis have been plotted against the multi-scale analysis in Figure 11.13. The analytical solution for a dilute distribution of micro-inclusions theory presented by Nemat-Nasser [1] has been used to modified and replaced the elastic material properties for the single-scale analysis. Although the theory presented by Nemat-Nasser is valid for the linear elastic material models, the elasto-plastic behaviour of the modified material models has been plotted in the same figure. Figure 11.13, illustrates five different curves in the elasto-plastic zone. The axes are the reactions against applied displacement.

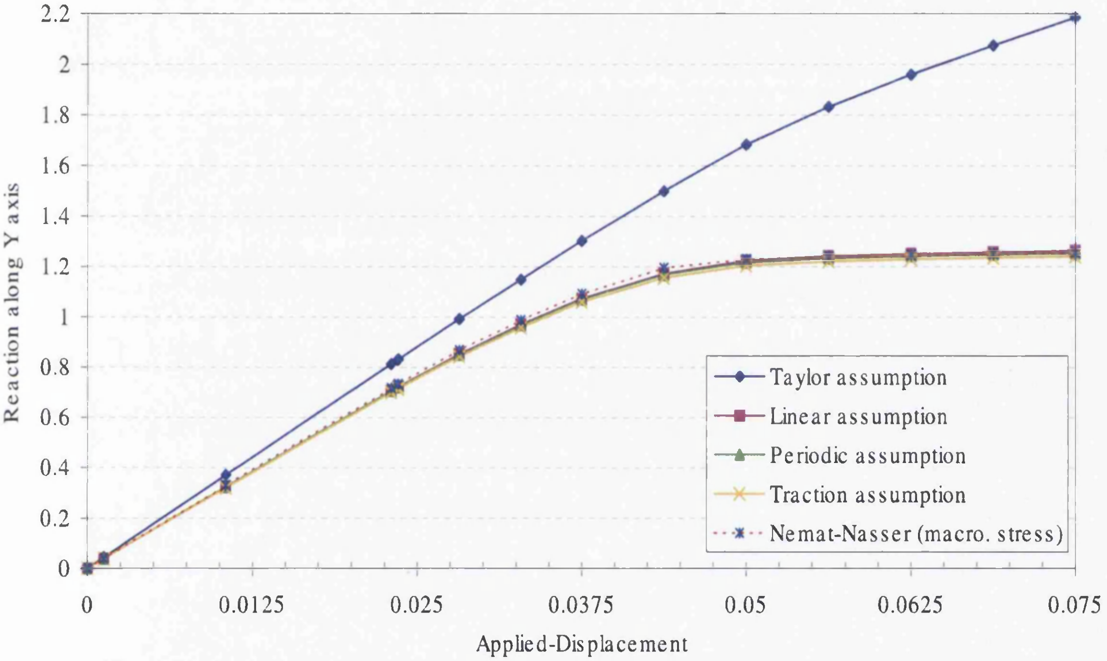

Figure 11.13: Homogenised material behaviour for different assumptions. Micro-structures with micro-inclusions.

As can be seen from Figure 11.13, the obtained overall responses from the multi-scale analysis for an RVE with micro-inclusion, follow the same order as the material model with cavity. The stiffest behaviour obtained from the Taylor assumption and the softest response obtainied from the uniform boundary traction assumption. The curve obtained from the reduced material properties for the single-scale analysis, based on the Nemat-Nasser presented theory, shows stiffer behaviour with respect to the linear displacement boundary assumption but after the yielding point, this curve converges to the periodic fluctuations displacement boundary assumption.

Computational time is the most important factor in elasto-plastic multi-scale analysis. The estimated computational times for the multi-scale and the single-scale tests have been illustrated in Figure 11.14. The multi-scale tests have been performed with the micro-cavity model under: the Taylor assumption, the linear displacement boundary condition, the periodic boundary displacement fluctuations condition and the uniform boundary traction assumption. The estimated analysis time for the single-scale model has been obtained from the proposed theory by Nemat-Nasser and based on the macro-prescribed strain assumption. The estimated computational times for the multi-scale tests (macro-structure with micro-cavity) have been illustrated in Table 11.4.

Model	Required Time (Hour)
Single-scale	0.022538
Linear assumption (Multi-scale)	35
Periodic assumption (Multi-scale)	86
Traction assumption (Multi-scale)	119

Table 11.4: Computational time for multi-scale model with micro-cavity.

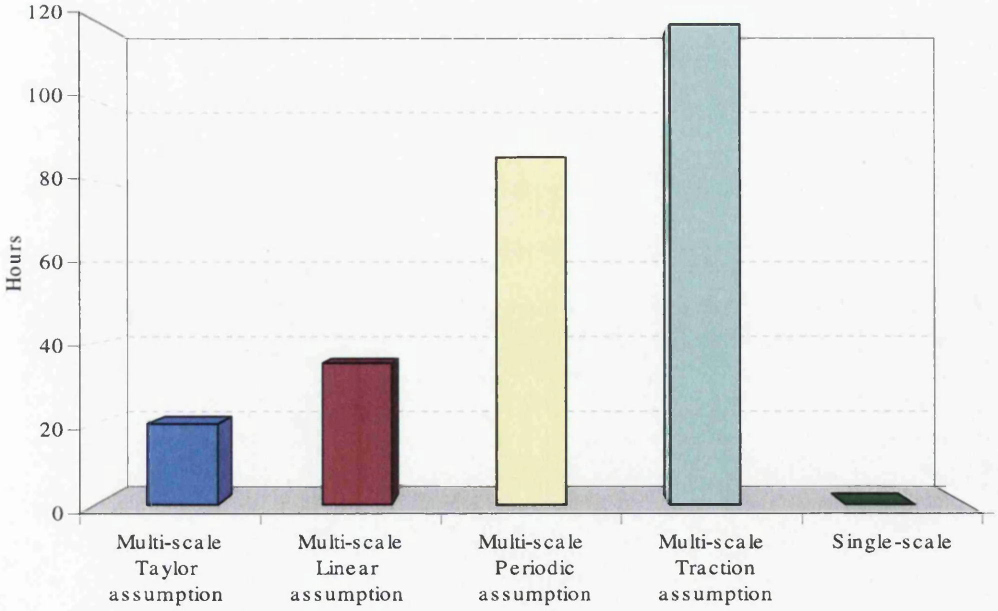

Figure 11.14: Computational time for elasto-plastic multi-scale analysis - macro-structure with micro-cavity model.

11.3 Comparison between multi-scale and single-scale analysis

Validity of the homogenised behaviour of the multi-phase material models is considered in this chapter. In order to do this, we compared the multi-scale analysis with the single-scale analysis. For the multi-scale model, a homogeneous perforated strip has been considered, same as the model in section 11.2, for the macro-structure. For the single-scale FE analysis, a perforated plate has been defined as a heterogeneous structure. Two types of element have been used for the FE mesh; (*i*) linear 3-noded triangle element with one Gauss point and (*ii*) 4-noded quadrilateral element with 4 Gauss points (see Figure 11.15).

The macro-structure mesh for single-scale analysis has been generated with 18527 linear triangle elements and 10240 nodes. The second macro-mesh model has been generated with 11216 4-node quadrilateral elements and 12147 nodes.

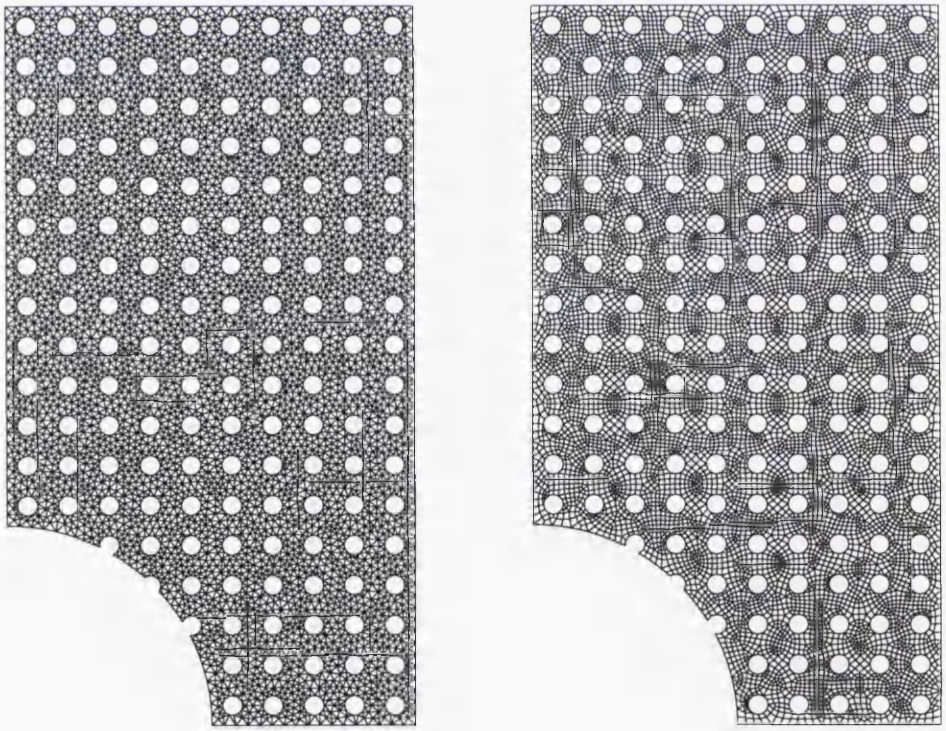

a) Triangle element

b) 4-node quadrilateral element

Figure 11.15: Macro-structures with different types of element for single-scale analysis.

For the multi-scale FE analysis we defined a perforated plate as a macroscopic homogeneous structure and at micro-level we defined a unit cell with side length equal to 1 *mm* and void volume fraction equal to 50% of the RVE. For the multi-scale alalysis and because of time and memory consideration, we used linear 3-noded triangle element for both macro and micro-structures models (see Figure 11.16). The number of elements and nodes for macro-structure are 25 and 21 respectively, while, at micro-structure we generated the FE mesh for the unit cell with 603 elements and 352 nodes.

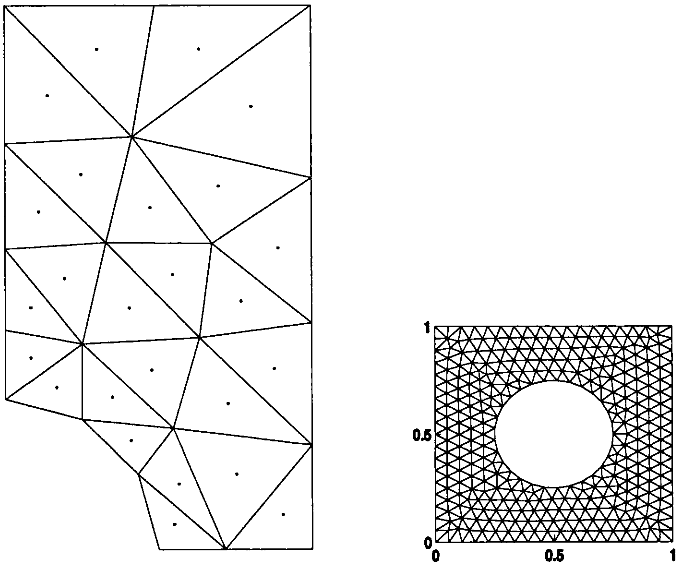

Macro-structure **Micro-structure**

Figure 11.16: Macro-mesh and micro-mesh for multi-scale analysis.

The single-scale analysis is performed for the applied displacement from top of the strip by the FEM software *ELFEN*. Figure 11.17 shows the reactions along Y direction against the applied displacements from top.

The overall results obtained from the multi-scale analysis have been considered under four different conditions at micro-level; (*i*) the Taylor assumption, (*ii*) the linear displacement boundary condition, (*iii*) the periodic boundary displacement fluctuations condition and (*iv*) the uniform boundary traction assumption. The overall responses obtained from different boundary conditions over the unit cell have been illustrated in Figure 11.17.

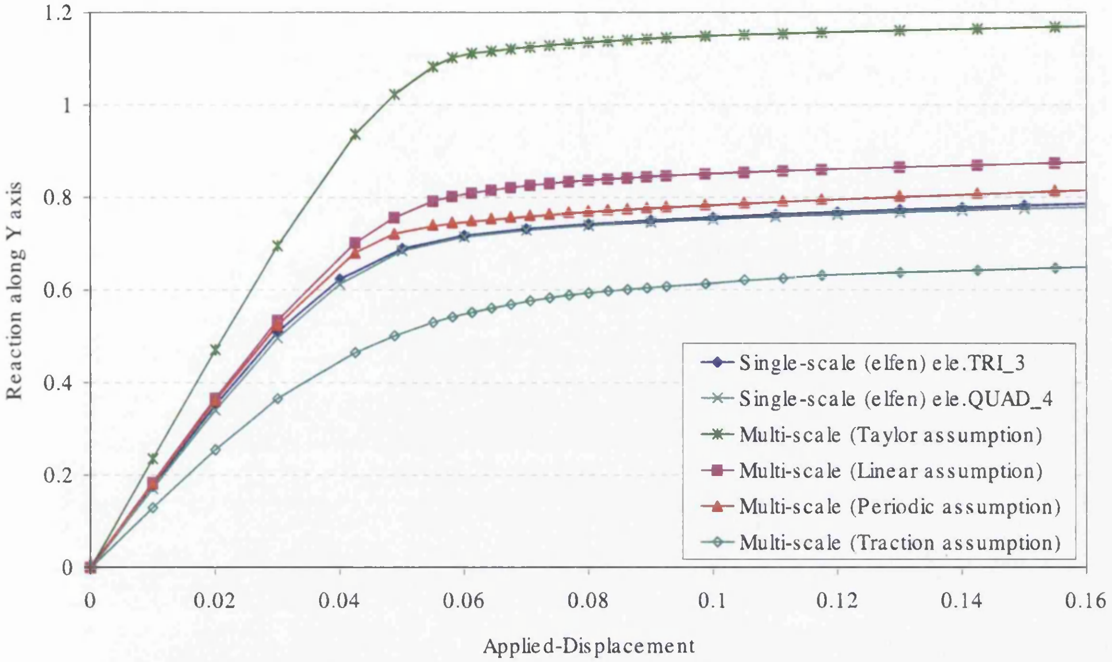

Figure 11.17: Reaction along Y direction against the applied displacement.

From Figure 11.17 it can be seen that, the obtained results form the single-scale analysis for the both models (linear triangle element, and 4-noded quadrilateral element) show the similar behaviour with respect to each other. On the other hand, the plotted graphs from the multi-scale analysis show different behaviour under different boundary conditions. The Taylor assumption shows stiffer behaviour in comparison with other boundary assumptions and it can be assumed as an upper bound for the homogenised behaviour of the perforated plate. Between the linear displacement boundary condition and the periodic boundary displacement fluctuations condition it is clear from Figure 11.17 that, the periodic boundary displacement fluctuations condition shows closer behaviour to the single-scale analysis curves. Finally, the obtained results from the uniform boundary traction present the lower bound for the homogenised behaviour of the perforated plate.

Figure 11.18, shows the evolution of the effective plastic strain at single-scale analysis.

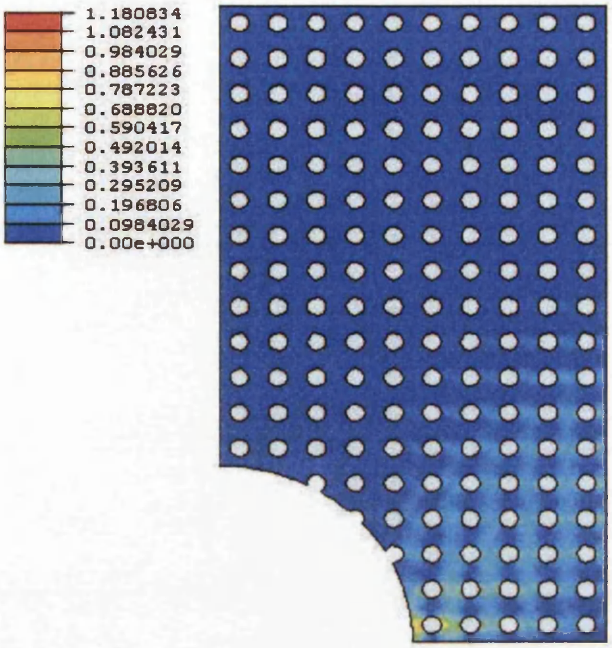

Figure 11.18: Effective plastic strain contour plot at last converged stage.

11.4 Conclusion

In this chapter a boundary value problem consisting of the stretching of a perforated plate has been discussed in detail. Different numerical simulations have been performed in the context of multi-scale analysis. For these tests, four different macro-structures were defined ranging from coarse to dense meshes. For each Gauss point at macro-level, four types of micro-structures were defined. The micro-structures were categorized based on the different percentage of the micro-cavities and the unit cell with different size of the micro-inclusions from 5% to 20% of the volume of the cell.

Firstly, the multi-scale analysis was performed for the four different boundary conditions at micro-level in the elastic zone. For comparison between multi-scale analysis and single-scale analysis, the single-scale tests were performed based on the reduced material properties from the theory presented by Nemat-Nasser [1] and damage theory for the elastic material model. The obtained results showed that the homogenised response of the perforated plate depends on the prescribed boundary condition at micro-level and the size of the cavity/inclusion at RVE.

The rate of convergence was another point which was considered in this chapter. The number of the elements in mesh model made a direct effect on the accuracy of the results. This fact and the effect of different boundary assumptions at micro-level were illustrated in separate graphs. In general, increasing in number of the elements at macro- and micro-structures cause the increase in accuracy of the homogenised results.

The elasto-plastic test was another part of this chapter. In the first test we focused on porous micro-structure modelled as a von Mises elasto-plastic material. In the following test we considered a heterogeneous micro-structure with micro-inclusions modelled as an elastic material and the matrix as a von Mises elasto-plastic materials with isotropic hardening.

The computational time estimation was considered. The multi-scale analysis is generally time consumer. If we want to simulate the whole attributes of micro-structures, apart of memory of computers, time is one of the main factors in analysis which should be considered during the procedure.

Finally, we checked the validity of the multi-scale analysis by comparing a single-scale model analysis with two-scale material model analysis. We showed that the periodic boundary displacement fluctuations assumption shows closer overall behaviour with respect to the single-scale analysis for a periodic macro-structure.

Chapter 12

Conclusion

12.1 Summary

In conclusion, the objective of this research was the computational implementation and assessment of multi-scale constitutive modelling strategies based on the volume averaging of the strain and stress tensors over a representative volume element (RVE) under infinitesimal strains assumption.

In the computational homogenisation procedure, definition of RVE, micro equilibrium, formulation of two-scale boundary value problem, micro-to-macro transition, and the Hill-Mandel principle were explained. In addition, by defining a suitable functional space of virtual displacements of the RVE, four classes of multi-scale constitutive models were considered, corresponding to: the Taylor, the linear boundary displacement, the periodic boundary displacement fluctuations and the uniform boundary traction assumptions. The corresponding finite element formulation was described in detail including the derivation of the homogenised tangent moduli which are crucial for the use of the Newton-Raphson method in the iterative solution of non-linear macro-scale problems.

A recursive hierarchical structure was developed for the multi-scale code. The advantage of implementation of this structure is the main equilibrium procedure calls itself when, at a Gauss point on the macroscopic level, computational homogenisation is used to describe the material behaviour.

A comprehensive set of numerical examples was presented. Application of the multi-scale methodology to materials with linear elastic microscopic constituents was considered first. Existing analytical methods were used to benchmark the numerical results. The effect of the distribution of cavities on the homogenised elasto-plastic material properties was studied. It was shown that increasing in density of pores cause the overall properties of the RVE under the three different boundary conditions converge towards each other. In this case, unlike the single cavity model all boundary conditions give similar distribution of the plastic strain. The effect of pores on the elasto-plastic response of porous media was studied. It was shown that the shape of the cavity at micro-level and the prescribed assumption over the RVE are two important factors which affect the prediction of the overall yield surface of the heterogeneous material. In addition, anisotropic homogenised behaviour was shown due to randomness distribution of the cavities in the RVE. The effect of the fibre orientation at micro-cell and anisotropy of the RVE, with linear elastic constituents, on the homogenised material properties was discussed. The obtained overall material properties from the mixture rule were compared with the obtained homogenised material properties from the computational homogenisation analysis. Finally, a materially non-linear fully coupled two-scale boundary value problem was solved numerically, demonstrating the suitability of the developed framework to large-scale simulations.

12.2 Future directions

It is obvious that the computational homogenisation still needs to be further explored to simulate the more realistically behaviour of multi-phase materials. According to our research the presented code and concept of multi-scale material model should be developed in many aspects, which are:

1. To simulate an accurate behaviour of heterogeneous materials, implementation of 3D elements is required in many situations.

2. To capture size effects on the homogenised material properties, implementation of the second order computational homogenisation is essential.

3. Different types of material models have been defined in the multi-scale code, including, the linear elastic, von Mises elastic perfectly plastic and von Mises elasto-plastic with isotropic hardening, mixed hardening and visco-plastic material model. The structure of the code has been defined in a manner that new material models can be easily implemented. To this end, new material routines

should be added to the relevant sub-functions for estimating tangent modulus and stress updating routines.

4. Different behaviour of the material models at micro-cell is another point which needs to be considered. Among them, cohesion between inclusion and matrix, micro-cracking, fatigue, pressurized fluid embedded by matrix, free surface interaction and many more material related behaviour are needed to be implemented, developed and studied.

5. Finally, mainly due to ease of implementation and debugging the MATLAB language has been used to develop the code. This language is not suitable for large-scale simulations or parallel analysis as it is usually extremely slow; therefore, transferring this code to other powerful platform such as, C or C++ is an important step.

In general, the overall behaviour of the heterogeneous materials are affected by many factors at micro-level, such as: the shape, spatial distribution and mechanical properties of the micro-structure. Although from the computational point of view, the multi-scale analysis is very expensive in terms of time and memory, the lack of accurate constitutive material models for more complex materials such as biological materials i.e. human tissue, justifies the performance of the multi-scale analysis to determine the overall response of this group of materials. This is the one of clear potential application of the methodology studied in this thesis.

To sum up, This research has provided some insight into the behaviour of computational homogenisation methods. The computational homogenisation is a very active research field at present and many developments are underway, especially in context of implementation of concurrent computer analysis in multi-scale models.

Bibliography

[1] Nemat-Nasser S. and Hori M. *Micromechanics: overall properties of heterogeneous materials.* Elsevier, Amsterdam, 1999.

[2] Gilormini P. and Bréchet Y. Mechanical properties of heterogeneous media. *Modelling and Simulation in Materials Science and Engineering.*, 7:805–816, 1999.

[3] Hashin Z. The elastic moduli of heterogeneous materials. *Journal of Applied Mechanics*, 29:143–150, 1962.

[4] Budiansky B. On the elastic moduli of some heterogeneous materials. *Journal of the Mechanics and Physics of Solids*, 13:223–227, 1965.

[5] Mori T. and Tanaka K. Average stress in the matrix and average elastic energy of materials with misfitting inclusions. *Acta Metallurgica*, 21:571–574, 1973.

[6] Hill R. A self-consitent mechanics of composite materials. *Journal of the Mechanics and Physics of Solids*, 13:213–222, 1965.

[7] Christensen R.M. and Lo K.H. Solutions for effective shear properties in three phase sphere and cylinder models. *Journal of the Mechanics and Physics of Solids*, 27:330–1979, 1979.

[8] Kröner E. Bounds for effective elastic moduli of disordered materials. *Journal of the Mechanics and Physics of Solids*, 25:137–155, 1977.

[9] Torquato S. Modeling of physical properties of composite materials. *International Journal of Solids and Structures*, 37:411–422, 2000.

[10] Christensen R. and Lo K.H. Solutions for effective shear properties in three-phase sphere and cylinder models. *Journal of the Mechanics and Physics of Solids*, 27:315–330, 1979.

[11] Hill R. Continuum micro-mechanics of elasoplastic polycrystals. *Journal of the Mechanics and Physics of Solids*, 13:89–101, 1965.

[12] Hashin Z. and Shtrikman S. A variational approach to the theory of the elastic behaviour of multiphase materials. *Journal of the Mechanics and Physics of Solids*, 11:127–140, 1963.

[13] Hashin Z. Analysis of composite materials. A survey. *Journal of Applied Mechanics*, 50:481–505, 1983.

[14] Moulinec H. and Suquet P. A numerical method for computing the overall response of non-linear composites with complex microstructure. *Computer Methods in Applied Mechanics and Engineering*, 157:69–94, 1998.

[15] Sanchez-Palencia E. and Zaoui A. *Homogenization techniques for composite media.* Springer, New York, 1987.

[16] Tolenado A. and Murakami H. A high-order mixture model for periodic particulate composites. *International Journal of Solids and Structures*, 23:989–1002, 1987.

[17] Guedes J.M. and Kikuchi N. Preprocessing and postprocessing for materials based on the homogenization method with adaptive finite element methods. *Computer Methods in Applied Mechanics and Engineering*, 83:143–198, 1990.

[18] Raghavan P. and Ghosh S. Concurrent multi-scale analysis of elastic composites by a multi-level computational model. *Computer Methods in Applied Mechanics and Engineering*, 5,4:311–384, 1998.

[19] Hinton E. and Hassani B. A review of homogenization and topology optimization I- homogenization theory for media with periodic structure. *Computers and Structure*, 69:707–717, 1998.

[20] Ghosh S., Lee K., and Moorthy S. Multiple scale analysis of heterogeneous elastic structures using homogenisation theory and Voronoi cell finite element method. *International Journal of Solids and Structures*, 32:27–62, 1995.

[21] Ghosh S., Lee K., and Moorthy S. Two scale analysis of heterogeneous elasticplastic materials with asymptotic homogenisation and Voronoi cell finite element model. *Computer Methods in Applied Mechanics and Engineering*, 132:63–116, 1996.

[22] Terada K. and Kikuchi N. A class of general algorithms for multi-scale analysis of heterogeneous media. *Computer Methods in Applied Mechanics and Engineering*, 190:5427–5464, 2001.

[23] Miehe C., Schotte J., and Schröder J. Computational micro-macro transitions and overall moduli in the analysis of polycrystals at large strains. *Computer Methods in Applied Mechanics and Engineering*, 172:109–143, 1999.

[24] Miehe C., Schröder J., and Schotte J. Computational homogenization analysis in finite plasticity. Simulation of texture development in polycrystalline materials. *Computer Methods in Applied Mechanics and Engineering*, 171:387–418, 1999.

[25] Feyel F. and Chaboche J.-L. FE2 multiscale approach for modelling the elastoviscoplastic behaviour of long fiber SiC/Ti composite materials. *Computer Methods in Applied Mechanics and Engineering*, 183:309–330, 2000.

[26] Ghosh S., Lee K., and Raghavan P. A multi-level computational model for multi-scale damage analysis in composite and porous materials. *International Journal of Solids and Structures*, 38:2335–2385, 2001.

[27] Miehe C. and Koch A. Computational micro-to-macro transition of discretized microstructures undergoing small strain. *Archive of Applied Mechanics*, 72:300–317, 2003.

[28] Smit R.J.M., Brekelmans W.A.M., and Meijer H.E.H. Prediction of the mechanical behaviour of non-linear heterogeneous systems by multi-level finite element modeling. *Computer Methods in Applied Mechanics and Engineering*, 155:181–192, 1998.

[29] Michel J.C., Moulinec H., and Suquet P. Effective properties of composite materials with periodic microstructure: a computational approach. *Computer Methods in Applied Mechanics and Engineering*, 172:109–143, 1999.

[30] Matsui K., TeradaK E., and Yuge K. Two-scale finite element analysis of heterogeneous solids with periodic microstructures. *Computers and Structures*, 82:593–606, 2004.

[31] de Souza Neto E.A., Perić D., and Owen D.R.J. *Computational plasticity:Small and large strain finite element analysis of elastic and inelastic solids.* 2006. (to be published).

[32] Wood R. D. and Bonet J. *Nonlinear continuum mechanics for finite element analysis.* Cambridge University Press, Cambridge, 1997.

[33] Michael Lai W., Rubin D., and Krempl E. *Introduction to continuum mechanics.* Pergamon, New York, 1974.

[34] Belytschko T., Liu W.K., and Moran B. *Nonlinear Finite Elements for Continua and Structures.* John Wiley & Sons., England, 2000.

[35] Holzapfel G. A. *Nonlinear Solid Mechanics: A Continuum Approach for Engineering.* John Wiley & Sons., England, 2000.

[36] Lemaitre J. and Chaboche J.-L. *Mechanics of solid materials.* Cambridge press, Cambridge, 1990.

[37] Crisfield M. A. *Nonlinear Finite Elements Analysis of solids and Structures (Volume 2).* John Wiley & Sons., England, 1997.

[38] Marsden J. E. and Hughes T. J. R. *Mathematical foundations of elasticity.* Prentice-Hall., New Jersey, 1983.

[39] Timoshenko S.P. and Goodier J.N. *Theory of Elasticity.* MacGraw-Hill, 1970. Third edition.

[40] Truesdell C. *Rational Thermodynamics.* MacGraw-Hill., New York, 1969.

[41] de Souza Neto E.A. and Feijoo R.A. *Variational Foundations of Multi-scale Constitutive models of Solid: Small and Large Strain Kinematical Formulation.* National Laboratory for Scientific Computing (LNCC/MCT), Brazil, 2006. Internal Research and Development Report. 16/2006, LNCC.

[42] Juzaila A. L. M. Numerical modelling of anisotropic elastic material at small and finite strain. MRes Thesis, Civil and computational engineering centre University of Wales Swansea school of engineering, 2005.

[43] Christensen R.M. *Mechanics of Composite Materials.* A Wiley-Interscience Publication., New York, 1979.

[44] de Souza Neto E.A. *Finite element computational analysis. Lecture note.* Civil and computational engineering centre. University of Wales Swansea. school of engineering., 2003.

[45] Daniel I. M. and Ishai O. *Engineering Mechanics of Composite Materials.* Oxford University Press., New York, 1994.

[46] Mallick P.K. *Fiber Reinforced composites.* Marcel Dekker., New York, 1993.

[47] Kim D.-H. *Composite structures for civil and architectural engineering.* E and FN SPON, London, 1995.

[48] Chakrabarty J. *Theory of plasticity.* MacGraw-Hill, New York, 1987.

[49] Perić D. *Computational plasticity. Lecture note.* Civil and computational engineering centre. University of Wales Swansea. school of engineering., 2003.

[50] Lubliner J. *Plasticity theory.* Macmillan, New York, 1990.

[51] Owen D.R.J. and Hinton E. *Finite Elements in Plasticity - Theory and Practice.* Pineridge Press Limited., Swansea, U.K., 1980.

[52] Simo J.C. and Hughes T.J.R. *Computational Inelasticity.* Springer-Verlag, New York, 1998.

[53] Jones R.M. *Mechanics of Composite Materials.* Scrpta book company., Washington, D.C., 1975.

[54] Chandrupatla T. R. and Belegundu A. D. *Introduction to finite elements in engineering.* Prentice-Hall, New Jersey, 1997.

[55] Cook R. D., Malkus D. S., and Plesha M. E. *Concepts and applications of finite element analysis.* John Wiley & Sons, New York, 1989.

[56] Crisfield M. A. *Nonlinear Finite Elements Analysis of solids and Structures (Volume 1).* John Wiley & Sons., England, 1997.

[57] Doghri T. and Friebel C. Effective elasto-plastic properties of inclusion-reinforced composited. Study of shape, orientation and cyclic response. *Mechanics of Materials.*, 37:45–68, 2005.

[58] Swan C. C. Techniques for stress- and strain-controlled homogenization of inelastic periodic composites. *Computer Methods in Applied Mechanics and Engineering*, 117:249–267, 1994.

[59] Kouznetsova V. G. *Computational homogenization for the multi-scale analysis of multi-phase materials.* PhD Thesis, University of Technology The Netherlands Eindhoven, 1998.

[60] de Souza Neto E.A., Perić D., and Owen D.R.J. Continuum modelling and numerical simulation of material damage at finite strains. *Archive of Computational Methods in Engineering*, 193:497–538, 2004.

[61] Eshelby J.D. The determination of the elastic field of an ellipsodal inclusion and related problems. *Proceedings of the Royal Society of London.*, 241:376–396, 1957.

[62] Voigt W. Über die Beziehung zwischen den beiden Elastizitätskonstanten isotroper Körper. *Wied. Ann. Physik*, 38:573–587, 1889.

[63] Taylor G.I. Plastic strain in metals. *Journal of Institute of Metals*, 62:307–324, 1938.

[64] Swan C. C. and Kosaka I. Voigt-Reuss topology optimization for structures with nonlinear material behaviour. *International Journal for Numerical Methods in Engineering*, 40:3785–3814, 1997.

[65] Reuss A. Berechnung der Fliessgrenze von Mischkristallen auf Grung der Plastizitätsbedingung für Einkristalle. *Z. Angew. Math. Mech.*, 9:49–58, 1929.

[66] Hill R. Elastic properties of reinforced solids: Some theoretical principles. *Journal of the Mechanics and Physics of Solids*, 11:357–372, 1963.

[67] Gurtin M. E. *An Introduction to Continuum Mechanics.* Academic Press., London, 1981.

[68] Carneiro Molina A.J., de Souza Neto E.A., and Perić D. *Multiscale finite element simulation for heterogeneous materials with reference to the effective tangent modulus computation.* Eighth International Conference on Computational Structures Technology., 2006. Conference paper.

[69] Partovi M. Computational implementation of multi-scale non-linear solid material models . MRes Thesis, Civil and computational engineering centre University of Wales Swansea school of engineering, 2004.

[70] Lee K. and Ghosh S. A microstructure based numerical method for constitutive modeling of composite and porous materials. *Materials Science and Engineering.*, A272:120–133, 1999.

[71] Zahil D.B., Schmauder S., and McMeeking R.M. Transverse strength of metal matrix composites reinforced with strongly bonded continues fibers in regular arrangement. *Acta Metallurgica at Materialia.*, 42:2983–2997, 1994.

[72] Taliercio A. and Carvelli V. A micromechanical model for the analysis of unidirectional elastoplastic composites subjected to 3D stresses. *Mechanics Research Communications.*, 26:547–553, 1999.

[73] Torquato S., Gibiansky L.V., Silva M.J., and Gibson L.J. Effective mechanical and transport properties of cellular solids. *International Journal of Mechanical Sciences.*, 40:71–82, 1998.

[74] Ladeveze P., Nouy A., and Loiseau O. A multiscale computational approach for contact problems. *Computer Methods in Applied Mechanics and Engineering*, 191:4869–4891, 2002.

[75] Foye R.L. Stress Concentration and Stiffness Estimates for Rectangular Reinforcing Arrays. *Journal of Composite Materials.*, 4:562–566, 1970.

[76] Zecca A.R., Wu X., and Matsuda T. Homogenized properties of elastic-viscoplastic composites with periodic internal structures. *Journal of Composite Materials.*, 4:556–561, 1970.

[77] Zohdi T.I. and Wriggers P. Aspects of computational testing of the mechanical properties of microheterogenous material samples. *International Journal for Numerical Methods in Engineering.*, 50:2573–2599, 2001.

[78] Ohno N. and Wriggers P. Aspects of computational testing of the mechanical properties of microheterogenous material samples. *International Journal of Mechanical Scineces.*, 42:1519–1536, 2000.

[79] Nan C.W. and Clarke D.R. The influence of particle size and particle fracture on the elastic/plastic deformation of metal matrix composites. *Acta Metallurgica at Materialia.*, 44:3801–3811, 1996.

[80] Moulinec H. and Suquet P. A numerical method for computing the overall response of nonlinear composites with complex microstructure. *Computer Methods in Applied Mechanics and Engineering*, 157:69–94, 1998.

[81] Michel J.C., Moulinec H., and Suquet P. Effective properties of composite materials with periodic microstructure: a computational approach. *Computer Methods in Applied Mechanics and Engineering*, 172:109–143, 1999.

[82] Smit R.J.M., Brekelmans W.A.M., and Meijer H.E.H. Prediction of the large-strain mechanical response of heterogeneous polymer systems: local and global deformation behvaiour of a representative volume element of voided polycarbonate. *Journal of the Mechanics and Physics of Solids*, 47:201–221, 1999.

[83] Gurson A.L. Continuum theory of ductile rupture by void nucleation and growth: Part I Yield criteria and flow rules for porous ductile media. *Journal of Engineering Materials and Tech*, 99:2–15, 1977.

[84] Tvergaard V. Material failure by void growth to coalescence . *Journal of Advance Applied Mechanics.*, 27:83–147, 1990.

[85] Ponte Castaneda P. and Zaidman M. The finite deformation of nonlinear composite materials-I. Instantaneous constitutive relations. *International Journal of Solids and Structures*, 33:1271–1286, 1996.

[86] Li H., Liu Y., Feng X., and Cen Z. Limit analysis of ductile composites based on homogenization theory. *Proceedings of the Royal Society of London.*, 459:659–675, 2003.

[87] Litewka A. Experimental study of the effective yield surface of perforated materials. *Nuclear Engineering and Design.*, 57:417–425, 1980.

[88] O'donnel W.J. and Porowski J. Yield surfaces for perforated materials. *Journal of Applied Mechanics*, March:263–270, 1973.

[89] Winnicki L., Kwiecnski M., and Kleiber M. Numerical limit analysis of perforated plates. *International Journal for Numerical Methods in Engineering.*, 11:553–561, 1977.

[90] Moorthy S. and Ghosh S. A model for analysis of arbitrary composite and porous microstructures with Voroni Cell Finite Elements. *International Journal for Numerical Methods in Engineering.*, 39:2363–2398, 1996.

[91] Bilger N., Auslender F., Bornert M., Michel J., Moulinec H., Suqet P., and Zaoui A. Effect of nonuniform distribution of voids on the plastic response of voided materials: a computational and statistical analysis. *International Journal of Solids and Structures*, 42:517–538, 2005.

[92] Yoon J., Barlat F., Dick R., Chung K., and Kang T. Plane stress yield function for aluminum alloy sheets-part II: FE formulation and its implementation. *International Journal of Plasticity.*, 20:495–522, 2004.

[93] Barlat F. Crystallographic Texture, Anisotropic Yield Surfaces and Forming Limits of Sheet Metals. *Material Science and Engineering.*, 91:55–72, 1987.

[94] Barlat F. Prediction of Tricomponents Plane Stress Yield Surfaces Yield Surfaces and associates Flow and Failure Behaviour of Strongly Textures F.C.C. Polycrystalline Sheets. *Material Science and Engineering.*, 95:15–29, 1987.

[95] Barlat F. and Lian J. Plastic behaviour and stretchability of sheet metals. Part I: A yield function for orthotropic sheets under plane stress conditions. *International Journal of Plasticity.*, 5:51–66, 1989.

[96] Lian J., Barlat F., and Baudelet B. Plastic behaviour and stretchability of sheet metals. Part II: Effect of yield surface shape on sheet forming limit. *International Journal of Plasticity.*, 5:131–147, 1989.

[97] Barlat F., Brem J.C., Yoon J.W., Chung K., Dick R.E., Lege D.J., Pourboghrat F., Choi S., and Chu E. Plane stress yield function for aluminum alloy sheets-part I: theory. *International Journal of Plasticity.*, 19:1297–1319, 2003.

[98] Artez H. A non-quadratic plane stress yield function for orthotropic sheet metals. *Journal of Materials Processing Technology.*, 168:1–9, 2005.

[99] Hill R. A user-friendly theory of orthotropic plasticity in sheet metals. *International Journal of Mechanical Sciences.*, 35:19–25, 1993.

[100] Kaczmarczyk L. *Generalized micro-to-macro transitions of micro-structures for the first and second order continuum.* Third MIT Conference on Computational Fluid and Solid Mechanics., 2005.